

Particle Breakage in Agitated Drying Conditions

François S. Hallac

Submitted in accordance with the requirements for the degree of

Doctor of Philosophy

The University of Leeds

School of Chemical and Process Engineering

Centre for Doctoral Training in Complex Particulate Products and Processes

March 2022

The candidate confirms that the work submitted is his own, except where work which has formed part of jointly authored publications has been included. The contribution of the candidate and the other authors to this work has been explicitly indicated below. The candidate confirms that appropriate credit has been given within the thesis where reference has been made to the work of others.

Chapter 4 on The Breakage Strength of Elongated Organic Crystals is based on work from a jointly authored publication:

Micro-mechanical Properties of Single High Aspect Ratio Crystals

François S. Hallac, Ioannis S. Fragkopoulos, Simon D. Connell and Frans L. Muller
CrystEngComm, 2019, 21, 5738-5748

All experimental work and data analysis has been performed by François Hallac. Ioannis Fragkopoulos has supervised the work of François Hallac, performed the beam bending simulations (section 2.8 in the paper), and reviewed the paper for journal submission. Simon Connell has supervised the experimental work and trained François Hallac to the use of the atomic force microscope. Frans Muller has supervised the work of François Hallac and reviewed the paper for journal submission.

This copy has been supplied on the understanding that it is copyright material and that no quotation from the thesis may be published without proper acknowledgement

The right of François S. Hallac to be identified as Author of this work has been asserted by François S. Hallac in accordance with the Copyright, Designs and Patents Act 1988.

Acknowledgements

I would like to express my deepest gratitude to Professor Andrew Bayly for his wise supervision during my PhD. His expertise in the domain of particle processing and distinct element modelling methods has been crucial in determining the framework of my project and the progression of my research.

I am also grateful to Professor Frans Muller for co-supervising my PhD and providing such stimulating research environment and discussions. His advice have been essential in the development of new analytical techniques, especially in data science and coding.

I am indebted to Doctor Claire MacLeod for her close industrial co-supervision throughout my thesis and for her thoughtful support during my research placement at AstraZeneca on the Macclesfield site.

Doctor Yi He has played an important role in developing my understanding of the limitations and good practice of DEM simulation work. Doctor Ioannis Fragkopoulos' guidance was valuable during the first stage of my PhD and in the writing of my first publication. They accompanied me during my first conferences and have become mentors and friends.

My greatest thanks to Doctor Simon Connell who co-supervised my first research study in Leeds. He provided a fantastic lab environment for me to receive training to use atomic force microscopy.

I would like to thank the University of Leeds, EPSRC and AstraZeneca for sponsoring my PhD and giving me the wonderful chance to complete a research degree in the UK.

Finally, I would like to express gratitude from the bottom of my heart to my parents for their unconditional support through my life and encouraging me throughout my PhD.

Abstract

Particle breakage is an undesired phenomenon in the production chain of the pharmaceutical industry as it can strongly impact the product quality of an active pharmaceutical ingredient (API) e.g. dissolution rate and bioavailability. Moreover, most of the API crystals are organic and of high aspect ratio, thus more prone to break in agitation-based drying processes.

A novel methodology combining experimental and modelling techniques is presented to predict the breakage of elongated particles in an agitated bed from the process environment and the particles properties.

The breakage of glutamic acid crystals in their elongated form (β -LGA) is observed experimentally in lab-scale agitated filter dryer (AFD). Measurements of particle size distribution allows to quantify the fragmentation of crystals throughout agitation in both wet and dry beds. The breakage strength distribution of the β -LGA crystals is assessed introducing a novel 2-point bending method using atomic force microscopy. In total, 52 individual crystals are broken.

A shear cell is built using distinct element modelling (DEM) to mimic the stress conditions in an agitated dryer and filled with particles modelled utilising the experimentally measured physical and mechanical properties of the β -LGA crystals. After optimising the simulation setup, a full-factorial study of uniaxial compressions and Couette flows for different normal stresses and particle elongation is performed allowing the calculation of the particles internal stress. Correlations between key variables are examined to understand the behaviour of the particle bed to its mechanical environment, and mathematical models are then created to estimate the particles internal stress and calibrated against simulation data.

Lastly, a breakage kernel is built using a probabilistic approach combining the obtained breakage strength of β -LGA crystals and the particles internal stress. The breakage of the crystals in a lab-scale AFD is estimated with a designed population balance model and the results are validated against experiments. The calibrated model is finally used to predict particle breakage for the scale-up of agitation.

Table of Content

Acknowledgements	I
Abstract	II
Table of Content	III
List of Tables	XV
List of Figures	XVIII
List of Appendixes	XXX
Abbreviations	XXXII
Nomenclature	XXXIII
Greek Characters	XXXIII
Latin Characters	XXXIII
1 Introduction.....	1
1.1 Background Context.....	1
1.2 Aims and Objectives	2
1.3 Research Methodology.....	2
2 Literature Review	5
2.1 The Particles.....	5
2.1.1 Physical Properties	5
2.1.2 Mechanical Properties	5
2.1.3 Breakage Mechanisms	7
2.1.4 Dry Granules	8
2.2 The Solvents.....	8
2.2.1 Solvents in Pharmaceutical Industry	8
2.2.2 Liquid Bridges	8
2.2.2.1 Forces	9

2.2.2.2	Mechanical Properties.....	10
2.2.2.3	Kinetics	10
2.2.2.4	Morphology	10
2.2.3	Wet Granules	11
2.2.3.1	Binding Forces.....	12
2.2.3.2	Saturation	12
2.2.3.3	Mechanical Properties.....	12
2.3	Drying Process Conditions.....	13
2.3.1	Equipment	13
2.3.2	Wetness	14
2.3.3	Bed Flow.....	15
2.3.4	Drying Kinetics	17
2.3.5	Stresses at Scale	18
2.3.6	Impact on PSD.....	20
2.3.6.1	Agitation.....	20
2.3.6.2	Scale Effect	22
2.3.6.3	Dryers Geometry.....	22
2.3.6.4	Moisture Content.....	23
2.3.6.5	Temperature	24
2.3.6.6	Particle Properties.....	24
2.3.6.7	Strategies and Solutions	24
2.4	Distinct Element Method (DEM).....	25
2.4.1	Particles	26
2.4.1.1	Shape.....	26
2.4.1.2	Size.....	27

2.4.1.3	Mechanical Properties	27
2.4.2	Models	27
2.4.2.1	Particle Interaction	27
2.4.2.2	Cohesion	28
2.4.2.3	Flexible Particles	29
2.4.2.4	Particle Breakage	30
2.4.2.4.1	Particle Internal Stress	30
2.4.2.4.2	Breakage Mechanisms	31
2.4.2.4.3	Breakage Rate	31
2.4.2.4.4	Location of Breakage	32
2.4.2.4.5	Population Balance Model	32
2.4.3	Shear Cell	33
2.4.3.1	Types of Cells	33
2.4.3.2	Periodic Boundaries	34
2.4.3.3	Domain Size	35
2.4.3.3.1	Cell Dimensions	35
2.4.3.3.2	Number of Partides	35
2.4.3.4	Mechanical Aspects	36
2.4.3.4.1	Strain and Strain Rate	36
2.4.3.4.2	Bed Dilatancy and Densification	37
2.4.3.4.3	Stress Environment	38
2.4.3.4.4	Bed Flow	40
2.4.3.4.5	Packing	41
2.4.3.4.6	Force Chains	42
2.4.3.5	Gravity	43
2.4.4	DEM Validation	44
2.5	Concluding Remarks	44
3	The Breakage of Elongated Organic Crystals in Agitated Filter Dryers	47
3.1	Introduction	47

3.2	Materials and Methods	47
3.2.1	Crystallisation.....	47
3.2.2	Filtration	48
3.2.3	Agitated Drying Process.....	49
3.2.3.1	Dry Bed	49
3.2.3.2	Wet Bed	50
3.2.4	Measurements	51
3.2.4.1	Particle Sampling	51
3.2.4.2	Particle Size Distribution	52
3.2.4.3	Moisture Content.....	53
3.2.4.4	Microscopy	53
3.3	Results and Discussion	54
3.3.1	Moisture Content	54
3.3.2	Laser Diffraction	54
3.3.3	Optimisation of Script Analysis for Morphologi G3 Data	57
3.3.4	Morphologi G3	59
3.4	Conclusion	67
4	The Breakage Strength of Elongated Organic Crystals	68
4.1	Introduction.....	68
4.2	Background Context.....	68
4.3	Materials and Methods	71
4.3.1	Materials	71
4.3.1.1	Organic Crystals	71
4.3.1.2	Metallic Support.....	72
4.3.1.3	Glue	73

4.3.2	Preparation.....	74
4.3.2.1	Crystal Mounting	74
4.3.2.2	AFM Calibration.....	75
4.3.2.3	Sample Cleaning	75
4.3.3	Measurements	76
4.3.3.1	Crystal Dimensions	76
4.3.3.2	Force Calculation	77
4.3.3.3	Broken Crystal Measurement.....	80
4.3.3.4	Mechanical Properties.....	81
4.3.4	Beam Bending Simulations.....	82
4.4	Results and Discussion	83
4.4.1	Preliminary Observations	83
4.4.2	Model Fitting.....	85
4.4.3	Correlations	87
4.4.4	Potential Improvements and Future Work.....	89
4.5	Conclusions	89
5	Optimisation of Simulation Setup and Methods	91
5.1	Introduction.....	91
5.2	Initial Simulation Setup	92
5.2.1	Particles	92
5.2.1.1	Physical Properties	92
5.2.1.2	Mechanical Properties.....	93
5.2.1.3	Interactions.....	94
5.2.1.3.1	Contact Model	94
5.2.1.3.2	Model Parameters.....	96
5.2.2	Shear Cell.....	97

5.2.2.1	Domain.....	97
5.2.2.2	Bed Filling.....	98
5.2.2.3	Compression and Shearing	99
5.2.3	Simulator Settings	100
5.2.3.1	Time Step	100
5.2.3.2	Simulator Grid.....	100
5.3	Preliminary Observations	101
5.3.1	Velocity Profile	101
5.3.2	Particle Alignment	103
5.3.2.1	Calculation Method	103
5.3.2.1.1	Order Tensor.....	103
5.3.2.1.2	Eigenvalues and Order Parameter.....	105
5.3.2.1.3	Eigenvectors and Order Director	106
5.3.2.2	Order Parameter	108
5.3.3	Bed Densification	110
5.4	Particles Internal Stress.....	111
5.4.1	Calculation Methods	111
5.4.1.1	Analytical Solving of Simple Beam Bending	111
5.4.1.2	Euler Equation of Motion.....	117
5.4.2	Discretisation of Location for Euler Equation of Motion Method.....	119
5.4.2.1	Radius	119
5.4.2.2	Length	120
5.4.2.3	Angle	121
5.4.2.4	Concluding Remarks	122
5.4.3	Comparison of Methods	123
5.5	Optimisation of Parameters	124

5.5.1	Wall Mass	124
5.5.2	Strain Rate and Flow Regime	127
5.5.3	Young's Modulus	128
5.6	Wall Effect	131
5.6.1	First Layer	132
5.6.2	Second Layer	136
5.7	Conclusions	139
6	Particles Internal Stress for Agitated Drying Conditions	140
6.1	Introduction	140
6.2	Modelling of Distributions	140
6.2.1	Weibull Fitting for Distribution of Particles Internal Stress	140
6.2.2	Gaussian Fitting for Distribution of Maximum Stress Location	141
6.3	Simulation Setups	142
6.3.1	Particles and Domain Size	142
6.3.2	Stress Environment	143
6.3.2.1	Shearing Phase	143
6.3.2.2	Uniaxial Compression	144
6.3.3	Data Recording	145
6.4	Shearing Phase	145
6.4.1	Number of Core Particles	145
6.4.2	Bed Conformation	146
6.4.2.1	Particle Alignment	146
6.4.2.2	Bed Densification	149
6.4.2.3	Particle Contacts	151
6.4.3	Stress Ratio	154

6.4.4	Contact Force	159
6.4.5	Inter-Contact Distance on Particle	162
6.4.6	Particles Internal Stress	164
6.4.6.1	Predominance of Bending Stress Component	164
6.4.6.2	Weibull Fit Parameters	167
6.4.6.2.1	Scale Parameter	167
6.4.6.2.2	Shape Parameter.....	169
6.4.6.2.3	Coefficient of Determination.....	171
6.4.6.3	Location of Maximum Stress on Particles	173
6.5	Uniaxial Compression	176
6.5.1	Number of Core Particles.....	176
6.5.2	Bed Conformation	177
6.5.2.1	Particle Alignment	177
6.5.2.2	Bed Densification	178
6.5.2.3	Particle Contacts	180
6.5.3	Contact Force	181
6.5.4	Particles Stability	183
6.5.5	Inter-Contact Distance on Particle	184
6.5.6	Particles Internal Stress	186
6.5.6.1	Predominance of Bending Stress Component	186
6.5.6.2	Weibull Fit Parameters	186
6.5.6.2.1	Scale Parameter	187
6.5.6.2.2	Shape Parameter.....	188
6.5.6.2.3	Coefficient of Determination.....	190
6.5.6.3	Location of Maximum Stress on Particles	191
6.6	Conclusions	192
7	Prediction of Particles Internal Stress for Agitated Drying Conditions	195

7.1	Introduction.....	195
7.2	Theoretical Model for Prediction of Particle Internal Stress.....	195
7.2.1	Mean Contact Force	196
7.2.1.1	In Uniaxial Compression	196
7.2.1.2	In Shearing Phase	199
7.2.1.3	Model Fitting	201
7.2.1.4	Discussion.....	203
7.2.2	Particles Bending Stress	203
7.2.2.1	In Uniaxial Compression	205
7.2.2.2	In Shearing Phase	206
7.2.2.3	Model Fitting	206
7.2.2.4	Discussion.....	208
7.2.3	Bending Stress Ratio	209
7.2.4	Particles Internal Stress	210
7.2.5	Conclusion.....	211
7.3	Prediction of Weibull Scale Parameter	213
7.3.1	From Predictive Theoretical Model of Mean Particles Internal Stress ..	213
7.3.2	Empirical Model from Simulation Data.....	214
7.3.2.1	Linear Correlation with Sum of Forces on Particle	214
7.3.2.2	Linear Correlation with Particle Aspect Ratio	215
7.3.2.3	Discussion.....	217
7.3.3	Empirical Model from Bulk Parameters	218
7.3.3.1	Linear Correlation with Stress Environment	218
7.3.3.2	Power correlation with Particle Aspect Ratio.....	219
7.3.3.3	Discussion.....	221

7.4	Prediction of Weibull Shape Parameter	222
7.4.1	Empirical Model from Simulation Data	222
7.4.1.1	Power Correlation with Standard Deviation of Sum of Forces on Particle	222
7.4.1.2	Linear Correlation between Power Parameters	223
7.4.1.3	Correlation with Particle Aspect ratio	225
7.4.1.4	Discussion	226
7.4.2	Empirical Model from Bulk Parameters	227
7.5	Prediction of Maximum Stress Location on Particle	228
7.5.1	Empirical Model from Simulation Data	229
7.5.1.1	Power Correlation with the Mean Number of Contacts	229
7.5.1.2	Linear Correlation with Particle Aspect Ratio	230
7.5.1.3	Linear Correlation with Particle Size	231
7.5.1.4	Discussion	232
7.5.2	Empirical Model from Bulk Parameters	233
7.5.2.1	Linear Correlation with Solid Fraction	233
7.5.2.2	Linear Correlation with Particle Aspect Ratio	234
7.5.2.3	Logarithmic Correlation with Normal Stress	236
7.5.2.4	Discussion	238
7.6	Conclusion	239
8	Prediction of Particle Breakage for Agitated Drying Conditions	242
8.1	Introduction	242
8.2	Probabilistic Approach to Particle Breakage	242
8.2.1	Extent of Breakage	242
8.2.2	Breakage Rate	244

8.2.3	Population Balance Model	245
8.3	Model Application	247
8.4	Model Validation against Experiments	251
8.4.1	Bed Division into Zones	251
8.4.2	Particle Properties	252
8.4.2.1	Breakage Strength	252
8.4.2.2	Particle Aspect Ratio Distribution	253
8.4.3	Breakage Model	253
8.4.3.1	Mechanical Environment in Zones	253
8.4.3.1.1	Strain per Impeller Rotation	253
8.4.3.1.2	Normal Stress	254
8.4.3.1.3	Stress Ratio	255
8.4.3.2	Particle Internal Stress Distribution	255
8.4.3.2.1	Weibull Scale Parameter	256
8.4.3.2.2	Weibull Shape Parameter	257
8.4.3.2.3	Gaussian Standard Deviation	257
8.4.3.3	Extent of Breakage	258
8.4.3.4	PARD by Impeller Rotation	259
8.4.4	Model Calibration	260
8.4.5	Prediction for Process Scale-up	261
8.4.6	Discussion	263
8.4.6.1	Particle Properties	264
8.4.6.1.1	Selected Crystals for AFM Experiments	264
8.4.6.1.2	Polydispersity	265
8.4.6.1.3	Particle Size	266
8.4.6.1.4	Mechanical Properties	266
8.4.6.2	Models Used in PBM	267
8.4.6.3	Experimental Error	268

8.4.6.4	Breakage Mechanisms	270
8.4.6.5	Mechanical Environment.....	270
8.4.6.6	Particle Flow	271
8.4.6.7	Future Work	272
8.5	Conclusion	273
9	Conclusions and Future Work	274
10	References	278
	Appendixes.....	302
	Figures	302
	Tables.....	306
	Derivations.....	323

List of Tables

Table 3.2.1: List of samples during AFD experiment of dry bed with performed analysis.	49
Table 3.2.2: List of samples during AFD experiment of wet bed with performed analysis.	51
Table 3.3.1: Measured moisture content of the different samples of wet agitation experiment (see Table 3.2.2).	54
Table 4.2.1: Literature values of mechanical properties for organic materials.	69
Table 4.4.1: Weibull fitting parameters of breakage strength distribution of the β -LGA crystals.	87
Table 4.4.2: Spearman correlation analysis. The shaded columns have p-values larger than the significance limit $\alpha = 0.05$	88
Table 5.2.1: Mechanical properties of simulation objects	94
Table 5.2.2: Interaction properties of simulation objects	96
Table 6.3.1: Number of element spheres composing the different aspect ratio particles and their corresponding shear cell width.	143
Table 6.3.2: Strain levels applied in compression case simulations for different aspect ratios.	144
Table 7.2.1: Fitting parameters of Equation 7.2.11 on all simulation data.	202
Table 7.2.2: Mean error for prediction of F_c using Equation 7.2.11 and parameters in Table 7.2.1 for different aspect ratios and stress environments.	202
Table 7.2.3: Fitting parameters of Equation 7.2.19 on all simulation data.	207
Table 7.2.4: Mean error for prediction of σ_p, ZZ using Equation 7.2.19 and parameters in Table 7.2.3 for different aspect ratios and stress environments.	208
Table 7.2.5: Fitting parameters of Equation 7.2.21 on all simulation data.	209
Table 7.2.6: Mean error for prediction of mean bending stress ratio $\alpha\sigma, ZZ$ using Equation 7.2.21 and parameters in Table 7.2.5 for different aspect ratios and stress environments.	210
Table 7.2.7: Mean error for prediction of mean particles internal stress σ_p using Equation 7.2.24 for different aspect ratios and stress environments.	211

Table 7.3.1: Mean error between Weibull scale parameter λ and predicted mean particles internal stress σ_p for different aspect ratios and stress environments.	214
Table 7.3.2: Mean a (in $m - 2$) as given in Equation 7.3.2 for the different aspect ratios and stress environments.	215
Table 7.3.3: Parameters of linear regression between a and aspect ratio α_p such as $a = b. \alpha_p + c$	216
Table 7.3.4: Mean error of predicted λ using Equation 7.3.3 for the different aspect ratios stress environments.	216
Table 7.3.5: Mean a as given in Equation 7.3.4 for the different aspect ratios and stress environments.	219
Table 7.3.6: Parameters of power regression between a and aspect ratio α_p such as $a = b. \alpha_p^c$	220
Table 7.3.7: Mean error of predicted λ using Equation 7.3.5 for the different aspect ratios stress environments.	220
Table 7.4.1: Fitting parameters of Equation 7.4.1 on all simulation data.	222
Table 7.4.2: Mean error of predicted k using Equation 7.4.1 and parameters values reported in Table 7.4.1.	223
Table 7.4.3: Parameters of power regression as described in Equation 7.4.1 for the different aspect ratios and stress environments.	224
Table 7.4.4: Fitting parameters of Equation 7.4.2 on all simulation data.	225
Table 7.4.5: Mean error of predicted k using Equation 7.4.2 and parameters values reported in Table 7.4.4.	226
Table 7.4.6: Fitting parameters of Equation 7.4.3 on all simulation data.	227
Table 7.4.7: Mean error of predicted k using Equation 7.4.3 and parameters values reported in Table 7.4.6.	228
Table 7.5.1: Parameters of power regression as described in Equation 7.5.1 for the different aspect ratios and stress environments.	229
Table 7.5.2: Fitting parameters of Equation 7.5.2 on all simulation data.	231
Table 7.5.3: Fitting parameters of Equation 7.5.3 on all simulation data.	231

Table 7.5.4: Mean error of predicted σ_{dev} using Equation 7.5.3 and parameters values reported in Table 7.5.3.	232
Table 7.5.5: Parameters of linear regression as described in Equation 7.5.4 for the different aspect ratios αp and normal stresses applied σ in shearing phase. The values of the coefficient of determination R^2 are in Appendix 10.	234
Table 7.5.6: Parameters of linear regression as described in Equation 7.5.5 for the different normal stresses applied σ in shearing phase.	235
Table 7.5.7: Fitting parameters of Equation 7.5.6 on all simulation data.	236
Table 7.5.8: Mean error of predicted $N_{c,p}$ using Equation 7.5.6 and parameters values reported in Table 7.5.7.	237
Table 7.5.9: Mean error of predicted σ_{dev} using Equation 7.5.7 and parameters values reported in Table 7.5.3 and Table 7.5.7.	238
Table 7.6.1: Summary of theoretical and empirical models created with the associated overall mean error. The list of variable description is in Chapter No.	240
Table 8.4.1: Strain per impeller rotation γ_{rot} in the 9 zones of Hare's AFD [108] and calculated for the studied AFD.	254
Table 8.4.2: Strain per impeller rotation γ_{rot} in the 9 zones of Hare's AFD [108] and calculated for the scale-up Maxi Lab AFD.	262

List of Figures

Figure 1.3.1: Methodology for the prediction of crystal breakage in agitated filter dryer.	4
Figure 3.2.1: Agitated filter dryer (1) Minilab GFD from PSL used for filtration and agitation of β -LGA crystals. The nitrogen flow is applied in the vessel via flexible tubing (2) and controlled using a Humidifier P-50 from Cellkraft (3). The AFD controller (4) allows the selection of the impeller rotation speed.	48
Figure 3.2.2: Particle sample collected using a soft cut plastic pipette.	52
Figure 3.2.3: HR73 Halogen Moisture Analyser oven from Mettler Toledo used for moisture content measurement of β -LGA crystal samples.	53
Figure 3.3.1: Laser diffraction data of the different samples of dry agitation experiment with the particle size at 10%, 50% and 90% of the PSD.	55
Figure 3.3.2: Laser diffraction data of the different samples of wet agitation experiment with the particle size at 10%, 50% and 90% of the PSD.	56
Figure 3.3.3: Laser diffraction data in agitation phase given by the number of impeller rotations. The particle size is given at 10%, 50% and 90% of the PSD.	57
Figure 3.3.4: PSD data of the different samples (see Chapter 3.2.3) performed using Morphologi G3 and analysed using script parameterised with no minimum neighbour.	58
Figure 3.3.5: PSD data of the different samples of dry agitation experiment (see Table 3.2.1) performed using Morphologi G3 and analysed using script [294] parameterised with 2 minimum neighbours.	60
Figure 3.3.6: PSD data of the different samples of wet agitation experiment (see Table 3.2.2) performed using Morphologi G3 and analysed using script [294] parameterised with 2 minimum neighbours.	61
Figure 3.3.7: Particle size distributions of the different samples collected in the dry case for particle length (a) and width (b), and in the wet case for particle length (c) and width (d). The PSD data is obtained from script analysis [294].	62
Figure 3.3.8: Volume fraction of fines ($\alpha_p = 1, L < 15\mu m$) and long particles ($\alpha_p \geq 6$) for the different samples collected for G3 analysis in dry and wet cases.	63
Figure 3.3.9: Probability density function of aspect ratio of the different samples during dry (a) and wet (b) agitation experiment. The data is displayed for $\alpha_p \leq 10$ (full distribution values in Appendix 14).	64

Figure 4.3.1: Light microscope image of the re-crystallised β -LGA crystals.	72
Figure 4.3.2: Metallic support: the red corner is placed at the centre of the AFM stub. 6 crystals can be mounted as cantilevers on positions A to F.	73
Figure 4.3.3: AFM magnetic stub. The corner of the metallic support highlighted in red is positioned at the centre of the AFM stub.	74
Figure 4.3.4: Ramp curve on Bruker Sapphire-12M used for the AFM probe calibration.	75
Figure 4.3.5: (a) Top and (b) lateral views of a mounted crystal (see <i>No</i> 38 in Appendix 5). The image was produced using a light microscope at $x5$ magnification.	76
Figure 4.3.6: Schematic representation of (a) the force application on the β -LGA cantilever and (b) the AFM probe and β -LGA cantilever deflections.	77
Figure 4.3.7: Ramp loading (blue)/unloading (red) curve of a Bruker RTESP-525 AFM probe engaged on the beta-LGA cantilever. The system spring, kT , is equal to the gradient of the loading curve ($kT = Force/\delta T$).	78
Figure 4.3.8: Top view of the AFM probe engagement at the tip of the glued crystal at different step motor deflections: a) 0 steps, b) 40 steps, c) 60 steps and d) 63 steps (when crystal breakage occurred).	79
Figure 4.3.9: Schematic representation of the crystal length before and after breakage.	81
Figure 4.3.10: Top view of the crystal after breakage. The image was produced using a light microscope at $x5$ magnification.	81
Figure 4.3.11: Predicted von Misses stress along the crystal arc length. The crystal is fixed on a support and the force applied $\sim 375\mu m$ from the edge of the support.	83
Figure 4.4.1: Crystals Young's Modulus E values against the associated probe and order of usage (individual data can be found in Appendix 5)	84
Figure 4.4.2: Distribution of breakage strength σB (see data in Appendix 7)	86
Figure 4.4.3: Distribution of Young's modulus E (see data in Appendix 8).	86
Figure 5.1.1: Stress conditions within a particle bed sheared in an agitated filter dryer.	91
Figure 5.2.1: Elongated particle modelled in EDEM.	93
Figure 5.2.2: Light microscope image of β -LGA crystals.	93

Figure 5.2.3: Shear cell designed in EDEM. Both normal and shear stress are applied on particle bed	98
Figure 5.3.1: Division of the particle bed within a shear cell along its height.	101
Figure 5.3.2: Mean velocity profile of a simulation with 10 bed divisions height-wise. The speed values are normalised over the module of wall speed. The case of a linear velocity profile is shown by the red line.	102
Figure 5.3.3: Mean particle speed during bed shearing simulation for 5 zones of the particle bed divided along the height. The speed values are normalised over the module of wall speed.	103
Figure 5.3.4: Clumped sphere particle with its neutral axis and unit vector u_p	104
Figure 5.3.5: Order parameter of a particle bed along simulation of shear cell.	108
Figure 5.3.6: Particle bed within the shear cell at a strain applied of $\gamma = 0$ and $\gamma = 30$	109
Figure 5.3.7: Absolute value of order director's coordinates of a particle bed along simulation of shear cell.	109
Figure 5.3.8: Solid fraction f_s during the shearing phase for a normal stress applied $\sigma = 6.5kPa$ and an aspect ratio $\alpha_p = 6$	110
Figure 5.4.1: Typical case of force application on a particle represented by its neutral axis u . The shear force V and the bending moment M are calculated based on the magnitude of the normal component of the forces $FX, norm$ and their application point uX with $FX, norm = 0$	112
Figure 5.4.2: Projection $FX, proj$ of the normal component $FX, norm$ of contact force on a defined plane (P) and θ_X the angle between these two vectors.	114
Figure 5.4.3: Internal stress of a particle calculated with Euler Equation of Motion at different length positions: for the particle length discretised at 100 locations and at the location of contacts.	120
Figure 5.4.4: Mean particles internal stress calculated for different length discretisation numbers and at location of contacts.	121
Figure 5.4.5: Mean particles internal stress calculated for different angle discretisation numbers.	122
Figure 5.4.6: Mean particle internal stress calculated with Simple Beam Bending and Euler Equation of Motion methods.	123

Figure 5.4.7: Internal stress of a particle along its length, calculated with Simple Beam Bending and Euler Equation of Motion methods	124
Figure 5.5.1: Normalised standard deviation of normal stress for different wall mass multipliers.....	126
Figure 5.5.2: Compressive stress during shear phase for wall mass multiplied by 1 and 10 – 5. The stress values are normalised over the target value.	126
Figure 5.5.3: Stress ratio during the shearing phase for a strain rate of 2, 20 and $200s^{-1}$	128
Figure 5.5.4: Shear cell at $\gamma = 40$ with particles at $E = 19MPa$. A few particles have penetrated the upper wall.	129
Figure 5.5.5: Stress ratio during in shearing phase for particles Young's modulus of $1.9GPa$ and $190MPa$	130
Figure 5.5.6: Number of particle contacts during the shearing phase for particles Young's modulus of $1.9GPa$ and $190MPa$	130
Figure 5.5.7: Mean particles internal stress during the shearing phase for particles Young's modulus of $1.9GPa$ and $190MPa$	131
Figure 5.6.1: Side view of particle bed in the shear cell. Wall particles are in contact with one of the two walls.	132
Figure 5.6.2: Box plots of particles internal stress for wall particles and core particles at $\gamma = 3$. The crosses indicate the mean values for the two groups of particles and the horizontal bars are (from bottom to top) the lower boundary, first quartile, median, third quartile and upper boundary. The boundaries of the whiskers is based on the $1.5 \times$ interquartile range value.....	133
Figure 5.6.3: Mean particle internal stress of wall particles and core particles in the shearing phase.	134
Figure 5.6.4: Theoretical standard deviation of particles internal stress for wall particles and core particles in the shearing phase.....	134
Figure 5.6.5: T value and critical $t_{0.975}(v)$ of null hypothesis H_0 during the shearing phase.....	135
Figure 5.6.6: Box plots of particles internal stress for 2nd layer particles and new core particles at $\gamma = 3$. The crosses indicate the mean values for the two groups of particles and the horizontal bars are (from bottom to top) the lower boundary, first quartile, median, third quartile and upper boundary. The boundaries of the whiskers is based on the $1.5 \times$ interquartile range value.	136

Figure 5.6.7: Mean particle internal stress of 2nd layer particles and new core particles in the shearing phase.	137
Figure 5.6.8: Theoretical standard deviation of particles internal stress of 2nd layer particles and new core particles in the shearing phase.	137
Figure 5.6.9: T value and critical $t_{0.975}(v)$ of null hypothesis H_0 during the shearing phase.....	138
Figure 6.2.1: Position P of maximum particle internal stress and x its projection on the particle neutral axis u	141
Figure 6.3.1: Particles shape for the different aspect ratio αp	142
Figure 6.4.1: Minimum number of core particles in shearing simulations for the different aspect ratios αp and normal stresses σ	146
Figure 6.4.2: Order parameter S during the shearing phase for the different aspect ratios αp and a normal stress at $\sigma = 4kPa$	147
Figure 6.4.3: Strain γ required to reach steady state of order parameter S for the different aspect ratios αp and normal stresses σ	147
Figure 6.4.4: Mean value of order parameter S in steady state for the different aspect ratios αp and normal stress σ	148
Figure 6.4.5: Solid fraction f_s of particle bed in shearing phase for the different aspect ratios and a normal stress at $\sigma = 1kPa$	149
Figure 6.4.6: Mean solid fraction in steady state of shearing phase, f_s , for the different aspect ratios αp and normal stresses σ	150
Figure 6.4.7: Mean number of contacts on particle, $N_{c,p}$, in shearing phase for the different aspect ratios αp and a normal stress at $\sigma = 10kPa$	151
Figure 6.4.8: Mean number of contacts on particle, $N_{c,p}$, in steady state of shearing phase for the different aspect ratios αp and normal stresses σ	152
Figure 6.4.9: Mean number of contacts on particle, $N_{c,p}$, in the shearing phase given by the solid fraction f_s for the different aspect ratios αp and a normal stress applied at $\sigma = 10kPa$	152
Figure 6.4.10: Mean number of contacts on particle $N_{c,p}$, given by the solid fraction f_s for the different normal stresses σ and an aspect ratio at $\alpha p = 6$	153

Figure 6.4.11: Mean number on contacts between two interacting particles, $N_{c,2p}$, given by the order parameter S during shearing phase for the different aspect ratios αp and a normal stress at $\sigma = 10kPa$	154
Figure 6.4.12: Stress ratio in the shearing phase, ϕ , for the different normal stresses σ and an aspect ratio $\alpha p = 6$	155
Figure 6.4.13: Strain required to reach steady state value of stress ratio ϕ for the different particles aspect ratio αp and normal stresses σ	156
Figure 6.4.14: Peak value of stress ratio ϕ during transitional state for the different aspect ratio αp and normal stresses σ	156
Figure 6.4.15: Mean stress ratio in steady state, ϕ , given by the mean number of contacts on particle $N_{c,p}$ for the different normal stresses σ . Within each σ series, $N_{c,p}$ increases with the particle aspect ratio αp set at 2; 3; 4; 5; 6.....	158
Figure 6.4.16: Mean contact force, F_c , in the shearing phase for the different aspect ratios αp and a normal stress at $\sigma = 10kPa$	159
Figure 6.4.17: Mean contact force F_c given by the mean number of contacts on particle $N_{c,p}$ for the different aspect ratios αp and a normal stress applied at $\sigma = 10kPa$. The values are given in the steady state of stress ratio.....	160
Figure 6.4.18: Mean contact force in steady state of shearing phase, F_c , for the different aspect ratios αp and normal stresses σ	161
Figure 6.4.19: Mean surface concentration of contacts in steady state, $cc, area$, for the different aspect ratios αp and normal stresses σ	161
Figure 6.4.20: Mean contact force F_c given by the surface concentration of contacts $cc, area$ for the different aspect ratios αp and a normal stress at $\sigma = 10kPa$. The data are given in the steady state of stress ratio.	162
Figure 6.4.21: Mean inter-contact distance on particle, ΔL , during the shearing phase for the different aspect ratios αp and a normal stress applied at $\sigma = 10kPa$	163
Figure 6.4.22: Mean inter-contact distance on particle, ΔL , in shearing phase given by the mean number of contacts on particle $N_{c,p}$ for the different aspect ratios αp	163
Figure 6.4.23: Mean bending stress ratio, $\alpha\sigma, ZZ$, for the different aspect ratios αp and a normal stress at $\sigma = 10kPa$	164
Figure 6.4.24: Mean bending stress ratio in steady state, $\alpha\sigma$, for the different aspect ratios αp and normal stresses σ	165

Figure 6.4.25: Mean bending stress ratio in the steady state, $\alpha\sigma_{ZZ}$, given by the number of contacts on particle $N_{c,p}$ for the different normal stresses σ and a particle aspect ratio of $\alpha p = 6$ 166

Figure 6.4.26: Proportion of particles experiencing a number of contacts $N_{c,p} \leq 5$, given by the different normal stresses σ and for a particle aspect ratio at $\alpha p = 6$. 166

Figure 6.4.27: Weibull scale parameter λ during the shearing phase for the different aspect ratios αp and a normal stress applied at $\sigma = 10kPa$ 167

Figure 6.4.28: Mean Weibull scale parameter in steady state, λ , for the different aspect ratios αp and normal stresses σ 168

Figure 6.4.29: Mean Weibull scale parameter in the steady state, λ , given by the mean contact force F_c for the different aspect ratios αp . Within each αp series, F_c increases with the normal stress applied σ set at 1; 2; 4; 6.5; 10kPa. 168

Figure 6.4.30: Weibull shape parameter k in the shearing phase for the different aspect ratios and a normal stress at $\sigma = 6.5kPa$ 169

Figure 6.4.31: Strain γ required to reach steady state value of Weibull shape parameter k for the different aspect ratios αp and normal stresses σ 170

Figure 6.4.32: Weibull shape parameter k in the steady state, given by the normalised standard deviation of the sum of absolute forces on particle σ_{norms} for the different aspect ratios αp 170

Figure 6.4.33: Mean Weibull shape parameter in steady state, k , for the different aspect ratios αp and normal stresses σ 171

Figure 6.4.34: Coefficient of determination R^2 of Weibull model fitting in the shearing phase for the different aspect ratios αp and a normal stress at $\sigma = 10kPa$ 172

Figure 6.4.35: Mean coefficient of determination R^2 of Weibull model fitting in the steady state, given by the mean number of contacts on particle $N_{c,p}$ for the different normal stresses σ . Within each σ series, $N_{c,p}$ scales with the aspect ratio αp set at 2; 3; 4; 5; 6. 172

Figure 6.4.36: Normalised standard deviation of the coefficient of determination R^2 in steady state for the different aspect ratios αp and normal stresses σ 173

Figure 6.4.37: Standard deviation σ_{dev} of Gaussian fitting of distribution of maximum stress location in the shearing phase for the different aspect ratios αp and a normal stress at $\sigma = 1kPa$ 174

Figure 6.4.38: Mean standard deviation σ_{dev} of Gaussian fitting of distribution of maximum stress location for the different aspect ratios αp and normal stresses σ .	174
Figure 6.4.39: Standard deviation σ_{dev} of Gaussian fitting of the distribution of maximum stress location in the shearing phase, given by the mean number of contacts on particle $N_{c,p}$ for the different aspect ratios αp .	175
Figure 6.4.40: Mean distance from particle centre of location of maximum stress in the shearing phase, given by the number of contacts on particle $N_{c,p}$ for the different normal stresses σ and an aspect ratio at $\alpha p = 6$.	175
Figure 6.5.1: Minimum number of core particles in uniaxial compression for the different strains γ performed in the shearing phase, normal stresses applied σ , and an aspect ratio of $\alpha p = 2$.	176
Figure 6.5.2: Minimum number of core particles in all uniaxial compression simulations for different aspect ratios αp .	177
Figure 6.5.3: Order parameter S in uniaxial compression performed at the beginning of shearing phase (i.e. strain applied $\gamma = 0$), for different normal stresses applied σ and aspect ratios αp .	178
Figure 6.5.4: Maximum variation of order parameter ΔS in uniaxial compression for different aspect ratios αp and strain applied γ .	178
Figure 6.5.5: Solid fraction f_s in uniaxial compression simulations, performed at the beginning of shearing phase ($\gamma = 0$), for different normal stresses applied σ and aspect ratios αp .	179
Figure 6.5.6: Maximum variation of solid fraction Δf_s from initial value (i.e. at normal stress applied $\sigma = 100Pa$) in uniaxial compression simulations for different aspect ratios αp and mean order parameter S of the bed.	179
Figure 6.5.7: Mean number of contacts on particle $N_{c,p}$ in uniaxial compression simulations, performed at the beginning of shearing phase (i.e. strain applied $\gamma = 0$), for different normal stress applied σ and aspect ratios αp .	180
Figure 6.5.8: Mean number of contacts on particles, $N_{c,p}$, in uniaxial compression, given by the solid fraction f_s for the different normal stresses σ and an aspect ratio at $\alpha p = 6$. Within each σ series, $N_{c,p}$ scales with the strain applied γ set at 0; 3; 5; 10; 15; 20; 25; 30.	180
Figure 6.5.9: Mean number of contacts on particles, $N_{c,p}$, in uniaxial compression, given by the solid fraction f_s for the different aspect ratios αp and a normal stress at $\sigma = 100kPa$.	181

Figure 6.5.10: Mean contact force F_c in uniaxial compression, given by the cross-sectional concentration of contacts $cc, area$ for the different aspect ratios αp and a normal stress at $\sigma = 100kPa$. Each data point corresponds to the different strain value tested..... 182

Figure 6.5.11: Mean contact force F_c in uniaxial compression, given by the mean number of contacts on particle $N_{c,p}$ for the different aspect ratios αp and a normal stress at $\sigma = 100kPa$. Each data point corresponds to the different strain value tested. 182

Figure 6.5.12: Mean contact force F_c in uniaxial compression, performed at the beginning of the shearing phase (i.e. strain applied $\gamma = 0$), for the different aspect ratios αp and normal stresses applied σ 183

Figure 6.5.13: Mean sum of absolute forces on particle s given by the number of contacts on particle $N_{c,p}$ for a strain applied $\gamma = 30$, an aspect ratio $\alpha p = 6$ and a normal stress $\sigma = 100kPa$ 184

Figure 6.5.14: Mean inter-contact distance on particle ΔL in uniaxial compression, given by the mean number of contacts on particle $N_{c,p}$ for different aspect ratios αp 185

Figure 6.5.15: Mean inter-contact distance on particle ΔL in uniaxial compression, performed at the beginning of the shearing phase (i.e. strain applied $\gamma = 0$), for the different aspect ratios αp and normal stresses σ 185

Figure 6.5.16: Mean bending stress ratio $\alpha\sigma, ZZ$ in uniaxial compression, performed at the beginning of the shearing phase (i.e. strain applied $\gamma = 0$), for the different aspect ratios αp and normal stresses σ 186

Figure 6.5.17: Weibull scale parameter λ in uniaxial compression simulations, performed at the beginning of shearing phase ($\gamma = 0$), for different normal stress applied σ and aspect ratios αp 187

Figure 6.5.18: Weibull scale parameter λ in uniaxial compression, given by the mean contact force F_c for the different strain applied γ and an aspect ratio at $\alpha p = 6$. Within each γ series, λ scales with the normal stress applied σ and the mean number of contacts on particle $N_{c,p}$ 188

Figure 6.5.19: Weibull shape parameter k in uniaxial compression, given by the normalised standard deviation of the sum of absolute forces on particle σ_{norms} for the different aspect ratios αp 189

Figure 6.5.20: Mean Weibull shape parameter k in uniaxial compression simulations, performed at the beginning of shearing phase ($\gamma = 0$), for different normal stress applied σ and aspect ratios αp	189
Figure 6.5.21: Weibull shape parameter k given by mean number of contacts on particles $N_{c,p}$ in uniaxial compression with a normal stress applied of $\sigma = 100Pa$, for different aspect ratios αp and bed ordering.	190
Figure 6.5.22: Coefficient of determination R^2 of Weibull fitting, given by mean number of contacts on particle $N_{c,p}$ in uniaxial compression for the different aspect ratios αp	191
Figure 6.5.23: Standard deviation σ_{dev} of Gaussian fitting of distribution of maximum stress location in uniaxial compression, given by the mean number of contacts on particle $N_{c,p}$ for the different aspect ratios αp	192
Figure 6.6.1: Direct correlations between main variables characterising the particle bed in the simulations. The description of the variables is listed in Chapter Nomenclature.....	193
Figure 7.2.1: Compressive stress σ distributed over contacts (black crosses) on cross-section (A) with contact forces F_c	196
Figure 7.2.2: Linear correlation between $F_c\sigma$ (in $m - 2$) and $cc, vol - 2/3$ (in $m - 2$) for the different aspect ratios αp in uniaxial compression, as described in Equation 7.2.7.	199
Figure 7.2.3: Compressive stress σ and shear stress τ distributed over contacts (black crosses) on cross-section (A) with contact forces F_c	199
Figure 7.2.4: Linear correlation between $F_c\sigma$ and $1 + \varphi^2 cc, vol - 2/3$ in the shearing phase for the different aspect ratios αp as described in Equation 7.2.8.	200
Figure 7.2.5: Linear correlation between $F_c\sigma$ and $1 + \varphi^2 cc, vol - 2/3$ for all simulation data in uniaxial compression and shearing phase as described in Equation 7.2.8.	201
Figure 7.2.6: Ratio between the theoretical and the recorded mean particles bending stress $\sigma_p, ZZ_{th}\sigma_p, ZZ_{sim}$ in uniaxial compression simulations, given by the mean number of contacts on particle $N_{c,p}$ for the different aspect ratios αp	205
Figure 7.2.7: Ratio between the theoretical and the recorded mean particles bending stress $\sigma_p, ZZ_{th}\sigma_p, ZZ_{sim}$ in shearing phase simulations, given by the mean number of contacts on particle $N_{c,p}$ for the different aspect ratios αp	206
Figure 7.3.1: Mean a (in $m - 2$) for the different aspect ratios αp and stress environments (data in Table 7.3.2).	215

Figure 7.3.2: Mean a for the different aspect ratios αp and stress environments (data in Table 7.3.5).....	219
Figure 7.4.1: Parameter a plotted against parameter b (see Equation 7.4.1) for both compression and shearing cases (data in Table 7.4.3).	224
Figure 7.4.2: Parameter b (see Equation 7.4.1) for the different aspect ratios αp and stress environments.....	225
Figure 7.5.1: Parameter a (see Equation 7.5.1) for the different aspect ratios αp and stress environments (data in Table 7.5.1). The dotted line represents the linear regression on the displayed data with an intercept at 0; 0.....	230
Figure 7.5.2: Parameter a as in Equation 7.5.4 obtained by linear regression for the different aspect ratios αp and normal stresses applied σ in shearing phase. Data available in Table 7.5.5.	235
Figure 8.2.1: Particle internal stress distribution (PISD) and breakage strength distribution (BSD). The area below the joint density function ($PISD \times BSD$) is the extent of breakage.	243
Figure 8.2.2: Aspect ratio αf of the two created fragments (circled) for the different ranges of breakage location x in the case of a particle with $\alpha p = 6$. No breakage occurs when $x \in 0, 0.5 \cup 5.5, 6$	246
Figure 8.3.1: Mean extent of breakage B averaged over all bed conformations in uniaxial compression for the different aspect ratios αp and normal stresses σ	248
Figure 8.3.2: Extent of breakage B in steady state of shearing phase for the different aspect ratios αp and normal stresses σ	249
Figure 8.3.3: Fraction of particles population in the different aspect ratio αp sub-groups, given by the strain applied γ and for a normal stress applied $\sigma = 4kPa$	250
Figure 8.3.4: Volume fraction in the different aspect ratio αp sub-groups, given by the strain applied γ and for a normal stress applied $\sigma = 4kPa$	251
Figure 8.4.1: Particle bed in agitated filter dryer divided 9 zones of equal volume and equal height.....	252
Figure 8.4.2: Weibull scale parameter λp for the different aspect ratios αp and the different zones along bed height (top, middle and bottom).	256
Figure 8.4.3: Gaussian standard deviation of maximum stress location for the different aspect ratios αp and the different zones along bed height (top, middle and bottom).	258

Figure 8.4.4: Extent of breakage B for the different aspect ratios α_p and the different zones along bed height (top, middle and bottom)..... 259

Figure 8.4.5: Coefficient of determination R^2 of the model fitting on experimental AFD data for different numbers of events of breakage per strain NB 260

Figure 8.4.6: PARD results from calibrated model (PBM) and dry AFD experiment (Exp) for an increasing number of impeller rotations I (data are displayed for $\alpha_p \leq 6$). Data for model-experiment comparison are in Appendix 14 & Appendix 15..... 261

Figure 8.4.7: PARD results from the application of the calibrated model to process scale-up for an increasing number of impeller rotations I (data are displayed for $\alpha_p \leq 6$)..... 263

Figure 8.4.8: Extent of breakage B given by the different aspect ratios for the different zones along bed height (top, middle and bottom) and a Weibull scale parameter λ_p at $27MPa$ and $2.7MPa$ 265

Figure 8.4.9: PARD results from calibrated model (PBM) and dry AFD experiment (Exp) for an increasing number of impeller rotation I (data are displayed for $\alpha_p \leq 6$). The initial PARD is taken as the one measured at $I = 30$. Data for model-experiment comparison are in Appendix 14 & Appendix 16. 269

List of Appendixes

Appendix 1: Vessel apparatus used for the crystallisation of glutamic acid in their elongated β form.	302
Appendix 2: Zeiss Axioskop 40 light microscope mounted with a Zeiss Axiocam 512 color camera used for the observation of β -LGA crystals.	303
Appendix 3: Light microscopy images of the different samples of β -LGA crystals collected during the dry agitation experiment (see Table 3.2.1).....	304
Appendix 4: Light microscopy images of the different samples of β -LGA crystals collected during the wet agitation experiment (see Table 3.2.2).	305
Appendix 5: Experimental data and calculated mechanical properties for 52 crystals.	306
Appendix 6: Descriptive statistical analysis data for the breakage experiment on the sample of 52 β -LGA crystals.	309
Appendix 7: Breakage strength distribution data.	310
Appendix 8: Young's modulus distribution data.	311
Appendix 9: Laser diffraction parameters for the different particle samples.	312
Appendix 10: Coefficient of determination R^2 of linear regressions performed using Equation 7.5.4 for the different aspect ratios and normal stresses applied in shearing phase. Values of linear parameters given in Table 7.5.5.	313
Appendix 11: Number of data points recorded in simulations of shearing phase for the different aspect ratios α_p and normal stresses applied σ	314
Appendix 12: Number of data points recorded in simulations of uniaxial compression for the different aspect ratios α_p and strain applied γ	315
Appendix 13: Statistics of particles retained and excluded for the parameters used in the script analysis of Morphologi G3 data for the different samples collected (MN: minimum neighbour).	316
Appendix 14: Probability density function of the different samples collected in dry and wet agitation experiments. The data is obtained using script analysis [294].....	317
Appendix 15: Estimation of probability density function from the calibrated model for different numbers of impeller rotations I and aspect ratios α_p (see Chapter 8.4.4).	318

Appendix 16: Estimation of probability density function from the calibrated model for different numbers of impeller rotations I and aspect ratio αp . The initial PARD corresponds to the values for the dry AFD experiments at $I = 30$ (see Chapter 8.4.6.3).	319
Appendix 17: Weibull scale parameter λp of particle internal stress distribution in Pa for the different aspect ratios αp and in the different zones of the Maxi Lab AFD (see Chapter 8.4.5).	320
Appendix 18: Gaussian standard deviation σ_{dev} of the maximum stress location distribution for the different aspect ratios αp and in the different zones of the Maxi Lab AFD (see Chapter 8.4.5).	321
Appendix 19: Extent of breakage B for the different aspect ratios αp and in the different zones of the Maxi Lab AFD (see Chapter 8.4.5).	322
Appendix 20: Derivation of Equation 4.3.2.	323
Appendix 21: Derivation of Equation 4.3.3.	325
Appendix 22: Derivation of Equation 8.2.2.	326

Abbreviations

AFD	Agitated Filter Dryer
AFM	Atomic Force Microscopy
API	Active Pharmaceutical Ingredient
BSD	Breakage Strength Distribution
β -LGA	Beta-Glutamic Acid
CDF	Cumulative Density Function
DEM	Discrete Element Method
LOD	Loss on Drying
MFB	Micro-Force Balance
MRI	Magnetic Resonance Imaging
PARD	Particle Aspect Ratio Distribution
PDF	Probability Density Function
PBM	Population Balance Model
PEPT	Positron Emission Particle Tracking
PISD	Particle Internal Stress Distribution
PIV	Particle Image Velocimetry
PSD	Particle size distribution
VBA	Visual Basic for Application

Nomenclature

Greek Characters

α_p	Particle aspect ratio (\emptyset)
$\alpha_{\sigma,ZZ}$	Bending stress ratio (\emptyset)
γ	Strain applied (\emptyset)
ΔL	Inter-contact distance on particle neutral axis (m)
λ	Weibull scale parameter (Pa)
ν	Poisson ratio (\emptyset)
ρ	Material density ($kg.m^{-3}$)
σ	Normal stress on particle bed (Pa)
σ_b	Particle breakage strength (Pa)
σ_{dev}	Gaussian standard deviation
σ_{norm}	Normalised standard deviation (\emptyset)
σ_p	Particle internal stress (Pa)
τ	Shear stress on particle bed (Pa)
φ	Stress ratio (\emptyset)

Latin Characters

A	Area (m^2)
$c_{c,area}$	Cross-sectional concentration of contacts in the bed (m^{-2})
$c_{c,vol}$	Volume concentration of contacts in the bed (m^{-3})
E	Young's modulus (Pa)
F_c	Contact force (N)

f_s	Solid volume fraction (\emptyset)
g	Gravitational acceleration on Earth ($m.s^{-2}$)
G	Shear modulus (Pa)
h	Height (m)
J_{Ic}	Crack toughness (Pa)
k	Weibull shape parameter (\emptyset)
K_{IC}	Critical stress index ($Pa.m^{1/2}$)
l_c	Crack length (m)
L	Length (m)
M_p	Particle bending moment ($N.m$)
$N_{c,p}$	Number of contacts on a particle (\emptyset)
r_p	Radius of element sphere (m)
R^2	Coefficient of determination (\emptyset)
s	Sum of absolute forces (N)
S	Order parameter (\emptyset)
T_R	Rayleigh time step (s)
w	Width (m)

1 Introduction

1.1 Background Context

The drying process in the pharmaceutical industry consists of the purification of the active pharmaceutical ingredient (API) whilst preserving its properties [1]. This is the last active step of the API production after crystallisation and filtration [2, 3]. A level of agitation is applied to the wet particle bed during the drying process to increase the drying performance. This agitation increases the stress environment within the particle bed, which has been reported as the main cause of particle breakage during the production of APIs [4]. The crystals produced in the pharmaceutical industry are in majority organic and elongated, therefore they are very sensitive to mechanical shear as their main breakage mechanism is the fragmentation by bending stress [1]. The effect of the presence of liquid within the particle bed on the extent of breakage isn't clearly defined: some observations show that the stresses on particles decrease due to lubrication [1, 5], whilst authors have observed an increase of shear stress for wet systems due to the additional cohesion created by liquid bridges [6, 7]. The reason of these contradictory observations hasn't been thoroughly investigated but it is hinted that this phenomenon is due to the nature of the material tested [1, 8, 9].

The breakage of crystals is of great concern in the pharmaceutical industry. Conservation of the desired particle size distribution (PSD) throughout downstream processing is extremely important, as PSD changes are known to affect properties such as bulk density, dissolution rate [10], flowability and content uniformity of drug product [11]. Although techniques like milling can be performed after drying to homogenise the particle size, the milling batch product exhibits slower dissolution [12].

Understanding and predicting the breakage of elongated particles in agitated drying systems remains a challenging and active area of research. Computational methods such as Distinct Element Modelling (DEM) have been employed to simulate the flow of particle beds for various stress conditions [13] and a range of particles aspect ratio [14]. Experimental tools like PIV, PEPT and annular shear cell have also been used to understand the phenomenon. However the lack of methodology and analytical techniques [15] makes the impact of drying processes on powder properties poorly understood [16] and the crystal breakage phenomenon isn't yet totally predictable at

industrial scale. For this reason, the production of pharmaceutical compound is nowadays based on a resource consuming “try-and-see” methodology. The scale-up and outsourcing of drying operations are also challenging [15] as no reliable model exists to transpose one equipment conditions to another [17].

In a sheared bed, contact forces between particles induce an internal stress which is responsible for particle breakage, with a predominance of the bending stress component [1]. Therefore, to elucidate the fracture phenomenon of elongated particles in agitated drying, the internal stress of individual crystals must be determined within an agitated bed.

1.2 Aims and Objectives

The objective of this research project is to predict the breakage of elongated organic crystals within a particle bed for agitated drying process conditions in the pharmaceutical industry.

As the main breakage mechanism of elongated particles is fragmentation due to the bending stress, it is critical to measure the impact of drying environmental conditions on the particles bending stress. An assessment of the environmental process conditions and both physical and mechanical properties of single crystals are needed as they dictate the internal stress induced within the particles and their possible breakage. The effect of moisture content, PSD and stress environment on the particles internal stress needs to be investigated to estimate the propensity of crystal to experience breakage throughout the drying process.

1.3 Research Methodology

The studied material is glutamic acid crystallised in its beta form (β -LGA). This material is representative of API crystals in the pharmaceutical industry as it is organic and of high aspect ratio, which makes it an ideal candidate for the planned studies.

Chapter 1: Introduction

The breakage of β -LGA crystals is first quantified in a lab-scale AFD for both wet and dry cases. Measurements of the PSD with Morphologi G3 methods are examined to determine the reduction of particle size in length and width with agitation time. The predominance of fragmentation and attrition mechanisms in particle breakage is then assessed for the different drying conditions.

A novel probabilistic approach is chosen for the prediction of particle breakage in agitated drying conditions using joint density function. This method requires both mechanical properties of particles, determined experimentally, and their internal stress for different mechanical environments calculated in simulations.

The breakage strength of β -LGA crystals is measured using a novel experimental method [18]. Single crystals are glued as cantilever on a metallic support and an end load is applied on them using atomic force microscopy (AFM) creating a 2-point bending situation. The load is increased until the crystal breaks allowing to calculate its breakage strength using Euler-Bernoulli Beam Theory. Overall, the breakage strength of 52 crystals is assessed creating a distribution following a Weibull equation. The Weibull fitting parameters are finally determined by regression.

A shear cell is built in DEM to mimic the mechanical environment experienced by particles in an agitated filter dryer. 2000 elongated particles are modelled using clumped spheres and periodic boundaries are set on two axes to simulate an infinite shear band. Inductive studies are undertaken to optimise the simulation setup to ensure that the particle bed behaviour is representative to reality in AFD and to decrease the computational resources needed. The validity of different methods for the calculation of particles internal stress in the studied system is also assessed and the most adequate technique is selected for the further analysis.

DEM shear cell simulations are then performed for different particle shapes and mechanical environments in monodisperse bed and the internal stress is determined for each particle. The particle aspect ratio and normal stress applied on the bed are varied in both uniaxial compression and shearing case. The simulation results allow an extensive analysis of the bed behaviour for different conditions and identify the key variables impacting the particles internal stress. The distribution of particles internal

Chapter 1: Introduction

stress within the shear cell follows a Weibull model and the fitting parameters are obtained for the different simulations by regression.

Theoretical and empirical mathematical models are then built for the prediction of the particle internal stress distribution and the location of the maximum stress on the particle neutral axis, as a function of stress environment and particle physical properties. The models are calibrated to fit the output data of the performed DEM shear cell simulations.

Lastly, the extent of breakage is calculated using the aforementioned probabilistic approach. This method allows the estimation of particle breakage for the different mechanical environments, and particle mechanical and physical properties. The created breakage kernel is implemented in a population balance model (PBM) to estimate the PSD of particles in a lab-scale AFD. The model is then validated against experimental results and subsequent model calibration is applied. The calibrated model is finally used to predict particle breakage for the scale-up of agitation.

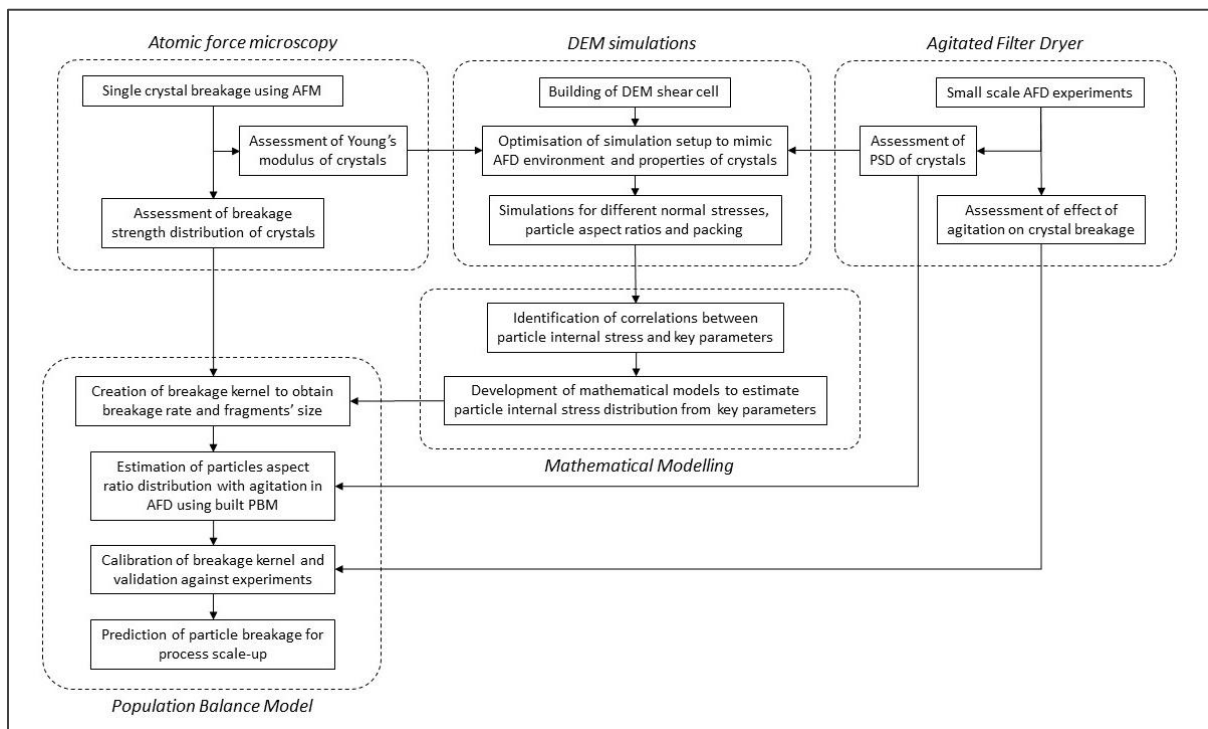


Figure 1.3.1: Methodology for the prediction of crystal breakage in agitated filter dryer.

The interactions between the different steps of the aforementioned methodology in this thesis are shown in Figure 1.3.1.

2 Literature Review

2.1 The Particles

2.1.1 Physical Properties

The physical properties of the produced crystals in the pharmaceutical industry are of great importance as they can impact the dissolution rate [10], stability, bioavailability and content uniformity of the drug product [11]. The particle shape and size are known to affect process performance in agitated dryers and is therefore given close attention to [19, 20]. Indeed, an irregular particle shape affects the quasi-static behaviour of a particle bed [20-24] e.g. via resistance to rotation and interlocking. Moreover, the reduction in particle size increases the particle surface for the same material volume, which augments the frictional energy in the bed. This phenomenon affects the particle flow and can ultimately jeopardise the entire process [25].

In the pharmaceutical industry, most of the API molecules are organic. The crystallisation process generates crystalline forms which are mostly of high aspect ratio. API crystals are mainly needle-shaped [26] and their length typically scales from tens to hundreds of micrometres at the end of crystallisation [16].

The PSD of elongated particles is generally assessed using image analysis techniques (e.g. Morphologi G3) [25, 27, 28] which can measure both width and length of particles, allowing the calculation of their aspect ratio. Scanning Electron Microscopy (SEM) can also be employed and provides insights on particles shape and surface [25]. Even though laser diffraction [1] doesn't consider the notion of particle elongation, it is generally used in addition to image analysis to provide a complete picture of particles physical properties [28-31]. Alternative methods exist to assess the PSD during manufacturing processes (e.g. drying) by applying light scattering techniques [16].

2.1.2 Mechanical Properties

The behaviour of a crystal under force application is dictated by its mechanical properties, which are dependent on the molecular crystal packing [32]. In the case of

organic crystals, their lattice is mainly formed by weak Van der Waals bonds [33], and their mechanical surface properties can vary due to the different nature of the involved molecular interactions [27, 34]. Their tensile strength is correlated to their modulus of elasticity [33].

The experimental assessment of mechanical properties of particles is time-consuming with actual methods [27]. The mechanical properties of small particles are generally assessed using nano-indentation where a hard tip is penetrated within the particle using increasing load: the Olivier-Pharr method [35] is used to assess the hardness [36] and Young's modulus [28] of single particles from the loading-unloading curves.

The three-point bending test is commonly used on elongated particles to evaluate the bending strength of a crystal [37]. This method allows the assessment of both Young's modulus and breakage strength of elongated crystals using a derivative of Euler-Bernoulli beam theory [26, 38]. The breakage strength of organic crystal typically scales at tens of MPa [26] and their Young's modulus at the magnitude of GPa [34, 39-42].

Even though the mechanical properties of a material can now be predicted from the crystal structure with good accuracy [32, 43-45], organic crystals still exhibit a heterogeneity in their measured mechanical properties [34, 42, 46]. The phenomenon is believed to be caused by the greater presence of defects within organic crystals. A Weibull model [47, 48] is typically fitted on the distribution of mechanical properties of these particles. The Weibull equation is also found to be more appropriate for the analysis of the mechanical properties data than a normally distributed function [47].

The link between particles size and mechanical properties is not clearly established. No correlation has been found for milled powder made of organic crystals [27] whilst it has been observed that the a decrease in size of elongated inorganic crystals increases their bending strength [49].

2.1.3 Breakage Mechanisms

There are different types of breakage: the attrition where a particle is chipped creating small fragments and fines, and the fragmentation which results in the rupture of a primary particle into at least two secondary particles [50, 51].

The breakage of a crystal results from a combination of both geometric (i.e. particle shape) and thermodynamic (i.e. molecular bonding) mechanisms. The fracture occurs preferably along crystallographic slip planes which are a source of defects and disorder during crystal deformation and fatigue [52], unless the elongation of the particle is sufficient to give predominance to geometric effect [27] e.g. for high aspect ratio particles [52]. Therefore, fragmentation is the main breakage mechanism of elongated particles [1, 26] and mainly occurs along the shortest axis of the crystals [52].

Euler-Bernoulli beam theory [26, 38] shows that the bending stress experienced by a particle scales linearly with the separation distance of force application contacts. The bending stress is the main cause of breakage for elongated particles [1]: the higher the aspect ratio of a particle, the more rapidly it breaks [53-55].

The bending and breakage behaviour of crystals are dependent on their mechanical properties [56-58]. Particles with low hardness are expected to deform plastically rather than experience chipping [16, 26, 58]. Organic crystals with high Young's modulus are stiffer, i.e. bend less for the same applied force [59], and have a higher breakage strength [33].

There are three modes characterising the fracture of homogenous continuum solids: ductile which refers to a fracture where significant plastic deformation takes place, brittle that denotes no plastic deformation before fracture, and semi-brittle which corresponds to a mode of fracture where brittle fracture happens at the limit of a plastically deformed zone [60]. Organic API are generally brittle materials [61].

In the case of crystalline materials a cleavage can also occur spontaneously in the crystal lattice which changes de facto its morphology [16]. The purity of the crystal, possible existing defects (e.g. cracks) and fatigue experienced also affect its bending and breakage behaviour [27].

2.1.4 Dry Granules

A granule is an assembly of particles held together by various types of forces [62]. Inter-molecular and electrostatic forces (i.e. Van der Waals, coulombic and hydrogen bonds) are related to crystal surface chemistry and increase with reducing the inter-particulate distance. These forces are only significant for small dry particles ($< 1\mu m$) and short separation distance such as in the case of strong compaction. On a larger scale, mechanical interlocking occurs between rough surfaces of particles, especially in the case of elongated crystals, and is dependent on the packing density. Solid bridges can also be created from sintering, chemical reaction, melting, hardening bonding agents or crystallisation of dissolved materials. This last type of bonding is the strongest of all [63].

2.2 The Solvents

2.2.1 Solvents in Pharmaceutical Industry

Different types of solvents are used in the pharmaceutical industry. The most popular ones are alcohols, acetone, THF, ketones and alkanes. Once the crystals are formed after the crystallisation process, they are filtered from the mother liquor and dried. The properties of the solvent influence the efficiency of the drying process, the flowability of the materials and the agglomeration mechanism [15]. Most importantly, they affect the polymorphic form of the crystal [64].

2.2.2 Liquid Bridges

Liquid bridges are created in presence of liquid at inter-particulate contact [62, 65, 66]: the capillarity attracts the liquid to the particles surfaces [67] whilst the cohesion of the liquid bridge results from both the surface tension and hydrostatic pressure within the liquid [68].

2.2.2.1 Forces

The capillary forces determine the static behaviour of a liquid bridge. There are two ways to determine the static forces in a liquid bridge between two identical spheres. In the first one, the force is determined at the neck of the bridge [69]:

$$F_n = 2\pi R \gamma_L - \pi R^2 \Delta P \quad 2.2.1$$

And the second method focuses on the solid-liquid interface [70]:

$$F_b = 2\pi R \sin \beta \gamma_L \sin(\beta + \theta) - \pi R^2 \sin^2 \beta \Delta P \quad 2.2.2$$

Where θ is the contact angle, β the angle between the axis linking the two spheres centres and the axis of the sphere centre and the vapour-liquid-solid interface, R the sphere radius, γ_L the liquid surface tension and ΔP the pressure differential.

If the spheres are not identical then the geometric average radius can be used:

$$\bar{R} = \frac{2R_A R_B}{R_A + R_B} \quad 2.2.3$$

Where R_A and R_B are the radii of the two particles.

The contact angle is the angle that the binder droplet does when it is put in contact with a particle at the vapour-liquid-solid interface. The contact angle plays an important part in determining the frictional forces between particles [71].

The viscous force F_{vis} of a liquid bridge between moving identical spheres is given by the following equation:

$$F_{vis} = \frac{3}{2} \pi \eta R^2 \frac{da}{a \cdot dt} \quad 2.2.4$$

Where η is the viscosity of the liquid and a the distance between the two spheres.

The viscous force can be neglected in the case of static behaviour (low strain rate) [71] and low moisture content (low capillary number) [72].

2.2.2.2 Mechanical Properties

The calculation of liquid bridge properties (e.g. contact angle, rupture distance) using the previous models have shown good agreement with experimental observations [73]. It is possible to measure the strength of liquid bridges between particles using force-displacement curves from techniques like micro force balance [74]. Up to a certain distance, shorter liquid bridges have a greater adhesion force [74-76]. A greater liquid volume also participates to a stronger cohesion of a liquid bridge [77].

If the inter-particle distance exceeds a certain separation, then the liquid bridge experiences rupture. For identical spherical particles, the higher the volume of the liquid bridge, the further it can be stretched before rupture [78]. In case of rupture of a mobile liquid bridge, the cohesion force of the liquid is generally overcome, and a volume of liquid resides on the surface of the particle. It is assumed that the quantity of liquid on each particle corresponds to the volume of liquid bridge divided at its thinnest point. The viscous component of immobile liquid bridges can change their mode of rupture and the particle-liquid adhesion may be overcome before liquid cohesion depending on their strength.

2.2.2.3 Kinetics

The creation of mobile liquid bridges is promoted by lower binder viscosity, particle diameter or higher particle surface energy. Their forces are due to the surface tension at solid-liquid-gas interface (directed along the liquid surface) and negative capillary pressure within the liquid. Immobile liquid bridges can also be created: they are composed of a thin layer of viscous binder between particles.

2.2.2.4 Morphology

Various morphologies have been observed for a liquid bridge depending on the shape of the particles, geometrical configuration of particles and liquid properties (e.g.

contact angle, volume) [79]. Gravitational effect is considered insignificant compared to surface tension effects [80], which is confirmed by a low Bond number [81], on the shape of the liquid bridge.

In the case of cylindrical fibres, the liquid bridge can take the shape of a column, a drop or a mix of the two [82-85]. These different states have been studied for wetting liquid, i.e. where the contact angle is below 90°, at different volume and fibres configurations (crossing angle and separation).

The shape of a liquid bridge can also be approximated by the calculation of its liquid-vapour surface area using energy balance equation: the system finds equilibrium at its lowest free energy [83]. The Young-Laplace equation [86, 87] can be used to model a toroidal liquid bridge [76]:

$$\Delta P = \gamma_L \left(\frac{1}{r_1} - \frac{1}{r_2} \right) \quad 2.2.5$$

Where ΔP is the difference in hydrostatic pressure across the vapour-liquid interface, r_1 and r_2 the local radii [73], and γ_L the interfacial tension between the liquid bridge and the external medium [70].

2.2.3 Wet Granules

The phenomenon of granulation is of great concern for the pharmaceutical industry as it can affect the bioavailability of the obtained product [8]. In most cases, granules are heterogeneous particles and their strength is governed by inter-particle bonding rather than the strength of the individual crystals within [73].

The shape of the primary particles is critical as it provides a surface area for effective contact between particles and thus increases the likelihood of agglomeration [1]. This phenomenon has been observed along the main axis of particles in presence of liquid, especially for high aspect ratio crystals (e.g. rod-shaped and needle-shaped) [9].

2.2.3.1 Binding Forces

In the case of static or quasi-static conditions (i.e. low strain rate), the inter-particulate forces within a wet granule is mainly due to the forces of their liquid bridges [62, 63, 65, 66]. All other types of forces [77] can be neglected. Viscous forces become significant at high strain rate [71] and the dynamic behaviour of viscous immobile liquid bridges can be approximated by the Frenkel model [88]. Typically, a higher viscosity limits the motion of the liquid within a granule and offers more resistance to compaction [89-92]. It also creates small granules [93] whilst a lower viscosity allows a better wettability of the particles and produces more spherical granules [92, 94].

2.2.3.2 Saturation

There are three existing states of contact network in wet granules (from low to high moisture content) [62, 95, 96]: pendular where each liquid bridge links two particles together, funicular where a liquid bridge can hold cohesive more than two particles, and capillary where the liquid fills the whole granule and where the surface of the granule shows both solid and liquid. If the moisture content increases again, the network becomes a droplet which shows only liquid at its surface. A moisture content of 1 – 4.5 v/v % is reported as representative of a pendular regime for spherical particles [97, 98]. Another study reported the following values of moisture content for the different saturation regime with spherical particles [99]: 0 – 13.6 v/v % for pendular regime, 13.6 – 100 v/v % for funicular regime and 100 v/v % for capillary regime.

2.2.3.3 Mechanical Properties

The cohesiveness of a granule increases with its moisture content and creates stronger pellets as the liquid fills the granule and lowers the porosity [91, 100, 101]. The higher the moisture content the stronger and more numerous the liquid bridges [102] that are able to transmit the experienced stress through the granule [62]. Also a higher binder content decreases the Young's modulus of a granule [103]: it becomes

more flexible as the lubrication effect reduces friction and interlocking between particles. The hardness of a wet granule is related to the liquid surface tension, viscosity and friction between primary particles [104], whilst the tensile strength of the granule is mainly due to its saturation level [7]: positively correlated in the pendular and funicular state, and inversely proportional in capillary state [105].

A granule experiences rupture if the applied stress exceeds a critical value. According to the Rumpf's theory [63] the breakage of a granule happens by simultaneous rupture of the bonds along the breakage plane, which means that the tensile strength of a granule is the sum of the intra-granular bonds along the breakage plane. Alternatively, Kendall's theory [106] assumes that there is a crack nucleation and a chain reaction of bond rupture along the breakage plane (i.e. crack propagation).

2.3 Drying Process Conditions

The drying conditions are selected to meet a certain drying performance in the pharmaceutical industry. The process environment is mostly the result of dryer's geometry, temperature and agitation, which induces different types of stresses and affects the PSD within the particle bed by agglomeration, fragmentation and attrition. The behaviour of the particle bed mainly depends on the particle properties and moisture content.

2.3.1 Equipment

The pharmaceutical industry uses various drying equipment to evaporate the solvent from the filtered wet particle bed and obtain a dry powder. In 1999, more than 200 dryer variations were produced by more than 150 manufacturer [107]. API crystals are very sensitive to drying conditions and therefore pharmaceutical companies need to find specific equipment and settings to minimise the impact on the product quality.

The most popular drying equipment is the agitated filter dryer (AFD) [8, 9, 65, 108, 109]. This dryer type is highly appreciated as it allows the processes of filtration and drying without the need to change equipment: it limits the exposure of the API between

the two processes [1]. Despite of a limited mass/heat transfer compared to the other dryers, its containment is appreciated, especially regarding some specific APIs [110]. The AFD is a cylindrical vessel equipped with a rotating impeller. The impeller is composed of two or four blades that create different level of agitation on the particle bed. The geometry of the blade can have an impact on the drying performance since the use of curved impeller blades results in smoother and more spherical granules whilst plane ones give more irregular shaped pellets [111]. A filter is present at the bottom of the cylinder to allow the pressure filtration stage. At the beginning of the drying process, the impeller rotates and moves vertically to agitate the particle bed [15]. This agitation is made under vacuum and a heat transfer is performed by either a set jacket temperature or a gas temperature. The AFD is in the category of contact dryers and these dryers are preferred for the drying of elongated particles because of their drying performance, even if they generate a high degree of attrition [12].

The conical screw dryer performs the agitation of the particle bed with the rotation of a screw that lift the particles to the bed surface to allow the evaporation of the solvent. The shape of the bed container is conical which places a bigger percentage of the particles close to the bed surface. A large scope study has shown that conical screw dryer has the best drying performance and the highest overall heat transfer coefficient. This technique also generates attrition and agglomeration (attrition being dominant) resulting in a bimodal particle size distribution (PSD) [17].

2.3.2 Wetness

During the drying process an amount of liquid is present within the particle bed. This moisture content links particles together with liquid bridges and creates a particle network. The cohesion between particles can be regarded as the interstitial cohesion within a wet granule [73]. The additional forces created by the presence of liquid influence the behaviour of the particle bed when agitated and impact the PSD changing throughout the drying process. Therefore, an understanding of the wet granule state and the liquid bridges within is critical to simulate the drying conditions computationally.

2.3.3 Bed Flow

A minimum stress is needed to initiate the flow of the particle bed. The agitation provided within the dryer has to overcome this yield stress of a particle bed otherwise the bed remains stationary [112]. The produced work to initiate the flow can be observed as a spike in the torque signal of the impeller at the beginning of the agitation and generally lasts a few seconds [1, 113]: this behaviour is typical for visco-plastic fluid.

The agitator torque can also give information on the flow regime of the particle bed. In the case of industrial scale AFD, with a low shear rate, the agitator torque is constant regardless of the impeller speed [1]: it shows a quasi-static bed behaviour where the momentum transfer is governed by frictional forces between particles [114] and is independent of the shear rate [115, 116]. The agitator torque may vary throughout drying because of a densification of the bed due to particle breakage [1]: the attrition of particles generally creates a poor flowability of the particle bed [8, 17]. This happens because of a greater number of frictional contacts present between particles, which increases the impeller torque [1, 117]. If recorded on a specific bed location, the torque signal shows periodic fluctuation as the blade passes: the bed compresses at the approach of the blade, and then the particles are lifted up due to the angle of the impeller blade before avalanching behind the blade which causes a dilatation of the bed [118]. This phenomenon is confirmed in DEM simulation of AFD where particles in front of impeller experience shear and fall behind the blade to a region where the bed is dilated [119]. Other torque fluctuation can be observed and are due to the “slip-and-stick” behaviour of particles flow [1, 116].

Another way to define the flow regime is the calculation of the Froude number associated with the dimensionless shear rate [118]: it allows the definition of the flow regime as static (or quasi-static), intermediate or granular [116]. Indexes have also been created to define the flowability of a fluid or assembly [62].

Various methods exist to track the motion of individual particles: Positron Emission Particle Tracking (PEPT) which locates an irradiated particle within a particle bed, Magnetic Resonance Imaging (MRI), and Particle Imaging Velocimetry (PIV) that records the motion of particles at the surface of a particle bed [118].

The behaviour of a system is also dependent on the total moisture content within and its distribution [120-125]. A high moisture content decreases the mixing performance because of the formation of agglomerates that can resist the shear from agitation without being broken (in the case of spherical particles). This behaviour has been confirmed by the observation of a lower radial and vertical particle velocities [80]. Indeed the lubrication effect of the liquid reduces the number of inter-particulate collisions as the liquid films on particles have to drain before the contact of particles surfaces [8]. This effect increases the mobility of the particles because of an increased particle-particle distance and reduces their frictional contacts [118]: it has per consequence the dilatation of the particle bed and the increase of its porosity [80]. In industrial scale dryers the mass of the particle bed generates a normal stress that partly compensate the dilatation of the bed. A way to know if the induced shear from agitation overcomes the cohesiveness of the bed consists on observing changes in the bed height for different agitation speed: if the height decreases then the dilatation of the bed due to the liquid bridges is compensated by the shear induced [118]. During drying the moisture content decreases which makes the liquid bridges shorter and stronger, increasing the cohesion of the particle bed [77]. Therefore the agitator torque and the fluctuation in the shear produced can monitor the particles agglomeration and the wet-to-dry transition [118]. PIV experiments have also been performed on a particle bed in an AFD with the variation of the moisture content [118]: the velocity of spherical particles changes when the liquid content is above 0.5% and holds cohesive the particles in a "correlated regime".

The flowability of powder is reduced with particle elongation [126-129], which can affect hopper discharge [130, 131] and die filling [132] in the industry. During agitation, the particle size reduction changes the shape and surface properties of the crystals, and influences the flow properties of the bulk material [25, 52, 126, 133]. On the one hand, the fragmentation of elongated particles reduces the interlocking and increases the powder flow [25]. On the other hand, the attrition of particles and the creation of small fines increase the overall surface area [25], which augments the number of frictional contacts within the bed. Moreover, the surface energy of organic crystals increases with breakage [134-137] which augments the cohesiveness of the powder [133]. This phenomenon induces sticking of particles to wall, and fines are likely to accumulate near the blade and container base in AFD operations.

2.3.4 Drying Kinetics

The drying rate is one of the most important aspects to assess the drying performance of a system. Therefore, the pharmaceutical industry aims to optimise the liquid mass transfer during the drying process.

To improve the liquid mass transfer, heat is conducted to the particle bed, either by gas or by contact with dryer walls. In the case of contact drying, a level of agitation is needed to promote the heat transfer by convection which reduces the drying time [1, 8]: the higher the agitation the greater the heat and mass transfer [125]. Here, the agitation homogenises the liquid content through the bed which participates to the increase of the drying rate [138]. To preserve the stability of heat-sensitive materials, a reduced pressure can be applied using the vacuum within the dryer, which allows drying at low temperature [17]. If the set absolute pressure of the system is lower than the vapour pressure of the solvent, given by Antoine's equation, then it increases the drying rate of the particle bed [139].

Thus the drying rate is proportional to the heat and mass transfer coefficient, the temperature and the surface area [17], the latter being scale-dependant [140]. Other models correlate the loss on drying (moisture weight loss) to the enthalpy [140] and involve the use of the Arrhenius equation [141, 142]. The Newton's law for fluid-wall heat transfer, the Darcy formula for vapour transfer and the energy balance equation can also model the vaporisation of a solvent in a vacuum contact dryer [138].

The drying process can be divided into three different stages [65]: the preheating where the temperature increases in the bed until a constant "wet bulb temperature" is reached, then the constant rate phase where the heat initiates the evaporation of the solvent, and finally the falling rate where the drying rate decreases because of the low moisture content which increases the thermal resistance of the bed. When the drying rate becomes constant the diffusion can be assimilated to a Fickian diffusion [143, 144].

The modelling of heat transfer and drying rate have been performed for various materials in tray dryers [145], rotary dryers [146, 147] and agitated dryers [138, 148].

As the agitation promotes particle breakage and agglomeration, models have also been developed to determine the drying performance for intermittent agitation [138].

2.3.5 Stresses at Scale

The weight of a bed and the agitation provided by the rotation of the impeller induces various stresses on the particles through the drying process. Typical hydrostatic pressure experienced by particles in agitated dryers are: $0.2kPa$ at laboratory scale (bed weight at $50g$), $1.4kPa$ at pilot scale ($150kg$) and $3kPa$ at commercial scale ($500kg$) [1]. Several experimental setups exist to simulate the pressure and shearing experienced by the particles in industrial scale dryers [16, 62].

The hydrostatic pressure P within a homogenous material (e.g. liquid) is given by the following equation:

$$P = \rho gh \quad 2.3.1$$

Where ρ is the material density, g the acceleration of gravity and h the normal distance from the material surface.

The pressure P can be related to the average of the normal stress in all directions as followed [80, 149]:

$$P = \frac{1}{3}(\sigma_{\theta\theta} + \sigma_{rr} + \sigma_{yy}) \quad 2.3.2$$

Where $\sigma_{\theta\theta}$ is the normal stress in the tangential direction, σ_{rr} in the radial direction and σ_{yy} in the vertical direction. The choice of the cylindrical coordinates is adapted to most of the dryers' geometries.

The normal stress on particles cannot be predicted from the hydrostatic pressure for all APIs and equipment configurations. Indeed, if the bed height exceeds a certain level then the dryer walls may support partially the weight of the particles, which produces a lower pressure than expected towards the bottom of the bed. This

phenomenon has been confirmed by both experiments with torque measurements [1] and DEM simulation [150].

Particulate solids have the ability to transfer stresses from normal to shear direction [151]. In the case of quasi-static flow regime where the momentum transfer is governed by frictional contacts [112], the shear stress τ scales linearly with the normal stress σ as given in Coulomb's law of friction [152-154]:

$$\tau = \sigma \tan \theta + C_f \quad 2.3.3$$

Where θ is the angle of internal friction and C_f the cohesiveness of the material (≥ 0). This linear dependency has been verified experimentally [1]. This correlation can be observed in yield locus curves giving the shear stress by the normal stress. The angle of internal friction, the tensile strength and the cohesiveness of a material can be obtained from these curves. The yield locus curve of a cohesionless material is linear and intercepts the origin. In the case of a typical powder, the tensile strength is obtained from the yield curve when shear stress is null, and the cohesiveness is found when normal stress is null. If cohesion is added to the particle bed, e.g. by the presence of moisture content, then the yield curve shifts upward [62]. In quasi-static flow regime, the shear stress scales with the pressure [112].

The shear stress can also be averaged in a cylindrical agitated bed using the Darelius equation [152]:

$$\tau_{ave} = \frac{T}{2\pi R^2 H} \quad 2.3.4$$

Where τ_{ave} is the average shear stress, T the measured torque, R the radius of the glass vessel and H the total height of the powder bed during agitation. The composition of the particle bed has an impact on the shear stress experienced by the particles. Indeed the shear stress depends on the number of frictional contacts on particles, thus the difference between the size of a given particle and the size of its neighbours (i.e. size ratio) affects the stress experienced by this particle [155].

Moreover, the cohesion between particles induced by the forces of liquid bridges influences the way the stress is transmitted through the particle bed. Indeed the torque profile changes in the presence of moisture content [113, 156]. There are different conclusions regarding the effects of moisture content on the shear stress in the literature: some papers argue that the presence of liquid makes wet particles flow by lubrication and decreases the measured torque [1, 5], whilst other authors have observed the increase of the shear stress for wet systems as the liquid allows the transfer of energy from the impeller into the particle bed [6, 7]. These different observations could be explained by the nature of the studied material [1, 8, 9].

A DEM study gives the level of normal and shear stress experienced by spherical particles in an agitated filter dryer with the variation of the moisture content [80]. It is observed that the normalised pressure (by gravity) scales linearly with the normalised height of the particle bed, and that the presence of moisture content increases the normalised shear stress (by gravity).

2.3.6 Impact on PSD

In the pharmaceutical industry, the PSD obtained after crystallisation is generally altered by uncontrollable breakage [157] and agglomeration [158, 159] throughout the drying process, which degrades the powder quality [8, 9]. An undesired PSD is typically associated with batch failure, increased costs and downstream issues (e.g. tableting) [25].

2.3.6.1 Agitation

Although the agitation is necessary to increase the drying rate, it also promotes the changing of the PSD within the particle bed [8]. Indeed, the shear induced by the agitation increases the energy and rate of particle collisions (i.e. particle-particle, particle-blade and particle-wall) [16, 17], which can lead to both agglomeration and breakage depending on the drying equipment [109, 160-162] (e.g. type of dryer,

impeller blade design) and operational parameters [8, 80, 118] (e.g. agitation rate, liquid content, temperature and pressure).

The breakage of particles densifies the particle bed and increases the number of frictional contacts. The particle bed requires then more energy to maintain the flow with the agitation. This phenomenon has been observed in an AFD for high aspect ratio particles by measuring the torque on a dry particle bed [1]. The increase in the torque corresponds to the densification of the bed due to the fragmentation of particles lengthwise [1] (particles don't agglomerate in this experiment). As the sensitivity to mechanical stress scales with particle size [16] and elongation [8, 9] for brittle materials, the particle bed stops experiencing particle breakage after a certain level of agitation.

In the case of quasi-static flow regime with no agglomeration, the particle breakage is independent of the impeller speed and is only determined by the total strain (shear deformation) experienced by the particle bed [108]. As the average shear stress can be calculated from the torque in an AFD (Darelius equation) [152], then the particle breakage phenomenon is proportional to the work provided by the impeller. This theory has been validated in AFD and shows that even if a wet bed shows a different resistance than a dry bed (observable by torque measurement), the breakage of given elongated particles is only dependant on the total work applied on the particle bed [1]. In an AFD, the work W can be calculated from the measured torque T using the following equation:

$$W = \int_0^t T \cdot \omega dt \quad 2.3.5$$

Where ω is the angular velocity of the impeller rotation and t the time.

Thus, the agitation improves the drying kinetics but also promotes the changing of PSD within the particle bed [8]. Compromises are found for the drying conditions in the pharmaceutical industry to minimise agglomeration and breakage [15]. Efforts are developed to obtain a high drying rate with minimising the agitation to preserve the materials properties [138].

2.3.6.2 Scale Effect

Particle properties are typically affected in manufacturing of API by scale-up of operations and transfer to different equipment [15, 16, 163, 164]. The breakage of particles is more extensive in industrial scale than laboratory scale drying [16]: the particles experience greater shear stress [165] because of the increase of normal stresses (pressure) in high scale equipment. Indeed, the normal stress is reported as the predominant factor impacting particle breakage [156].

An experimental setup allows the application of a weight on a particle bed in a laboratory scale AFD to mimic the hydrostatic pressure experienced at scale [1, 16, 156, 166]. This method has also been applied with a FT4 rheometer [156]. This apparatus allows the torque measurement on an agitated bed of elongated particles for different pressure applied [1], and shows that the torque and particle breakage increase with the pressure applied. Moreover, the time for the torque to reach a plateau increases with the pressure applied; therefore, the particle breakage phenomenon is more extensive and lasts longer in higher scales. In this experiment [1], the output density and PSD have shown good agreement with pilot scale experiments.

2.3.6.3 Dryers Geometry

The breakage of particles also depends on the geometry of the dryer. There exist zones in the dryers where the particle breakage is more extensive, and the mixing conditions change the residence time of particles in these zones. In an AFD these zones are the bottom plate [16] (beneath the impeller due to the bed compression) and near the impeller [1, 108, 165]. These zones are also known to have a higher flow velocity enhancing the particle breakage phenomenon [167]. The difference of breakage between low and high risk zones is so important that models assume the particle breakage being only dependant on the energy and frequency of the impact with the impeller [168], whilst neglecting the low risk areas.

2.3.6.4 Moisture Content

The presence of liquid within the particle bed also changes its resistance to agitation. This phenomenon is due to the adhesion and lubrication effects that liquid bridges induce between particles, which changes the nature of inter-particulate frictional contacts. The energy required to flow a given particle bed depends on its temperature and moisture content. Up to a certain level, the moisture content promotes wet granulation in a particle bed [80], and a specific region of temperature and liquid content called “sticky-point” exists where agglomeration is highly present [62, 169, 170]. The sticky-point can be observed when the torque reaches its maximum on a torque vs. moisture content graph for a given temperature [156]. The liquid properties also impact the agglomeration of particles as it is demonstrated that above a critical contact angle the resulted granules have a wider PSD and lower strength [171].

The phenomenon of adhesion in the presence of liquid can be enhanced by particle breakage as broken crystals are more cohesive and easily agglomerate [12]. Moreover a scattered PSD produces a closer particle packing and leads to denser and stronger granules, which are more difficult to break [169].

The particle breakage is also affected by the presence of moisture content. There is however no consensus in the literature on whether the presence of liquid is promoting or reducing particle breakage in a particle bed. On the one hand, authors observe more crystal breakage in a wet cake than in a dry bed with the same agitation [1, 8, 16, 156], which can be attributed to a higher pressure (due to the weight of the liquid) applied on particles that move less freely within the particle bed: a higher resistance to the flow increases the shear experienced by particle which break more easily. On the other hand, other papers show that particle breakage occurs preferably towards the end of drying when the moisture content is low [1, 8, 9]. This phenomenon is explained by a greater number of frictional contacts with a lower moisture content which induces more particle breakage [172]. The lubrication effect created by the presence of liquid [1] reduces the shear stress on particles as they move more freely and make the materials flow easier [5]. This phenomenon can be combined with the ability of elongated materials to stack lengthwise with liquid bridges which lowers their sensitivity to bending stress [9].

Authors agree on the fact that this difference in particle breakage observation with different moisture content is due to the nature of the tested crystals. Indeed, the crystal morphology and strength influence the PSD changes under agitation [9], which is confirmed by the good agreement of population balance models with AFD experiments where the Young's modulus, critical aspect ratio and crystal density are considered as input variables [168].

2.3.6.5 Temperature

A high temperature has the advantage to shorten the drying time which reduces the exposition of particles to shear [8]. In these conditions, the probability for a crystal to become more soluble and form solid bridges at the end of the drying process would increase, which would augment the strength of the resulting agglomerates. Likewise, a low pressure decreases the number of inter-particulate collisions and minimises particle breakage.

2.3.6.6 Particle Properties

The rate of PSD changing under drying conditions is partially influenced by the material properties of the crystals [9], e.g. morphology and mechanical properties. Despite of the absence of constitutive equation to describe particle breakage [173], empirical models have been created to predict the phenomenon. An equation suggests that the particle size reduction is positively correlated to the initial particle size, hardness and aspect ratio, whilst inversely proportional to the particle thickness [28]. In this study, a logarithmic curve is used to fit the particle size distribution.

2.3.6.7 Strategies and Solutions

Strategies have been elaborated to obtain desired PSD in pharma manufactures [129, 174-179]. However these solutions may not be applicable as they can affect API solubility, impurity level, toxicity, yield or environmental impact [25]. Batch

crystallisation process [10] and milling [180] are typically used to alter the obtained PSD and fit the properties required by formulators to create the desired drug product. The wet milling is then used to reduce the particle aspect ratio whilst avoiding the generation of fines [25, 135] and amorphous forms which can potentially be toxic [181-183]. This combination of re-crystallisation and wet milling used repetitively allows to reach the target mean size and a narrow PSD; however, it is generally impracticable due to number of iterations and volume required for PSD measurements [25].

Methodologies also exist to assess the attrition risk of particles. Attrition matrix have been developed and the impact of key process parameters on the particle size reduction is evaluated with small scale agitator (e.g. FT4 powder rheometer) [156]. Although this method requires a large amount of compound (10-100g per experiment), it allows the classification of the risk for a material (i.e. hard, medium, easy) and the estimation of attrition at larger scale [16, 156]. Other methods have been introduced to assess the attrition risk of a material without the need of large amount of powder by comparing initial and final PSD parameters after lab-scale AFD experiment [28].

Propensity of materials to break under specific conditions can also be determined experimentally with methods like the agitation cell, HELOS [16] and tracer granules. However it remains difficult to predict the dried materials PSD, especially in scale-up process [158] and when changing dryer equipment [140].

Other experiments allow the assessment of the mechanical properties for a bed of crystals: the annular shear cell is used to measure the shear strength of packed crystals [184]. This technique can be used to evaluate the propensity of breakage of particulate solids [108, 185, 186]

2.4 Distinct Element Method (DEM)

DEM is a computational modelling method introduced in 1971 [22] which models particles using discrete elements. The interactions between particles are ruled by contact models and particle bed can be created with mechanical behaviour similar to real assemblies. The mechanical response of assemblies can be observed in shear

cells which mimic the process conditions experienced by a particle bed when agitated in dryers.

2.4.1 Particles

2.4.1.1 Shape

DEM elements can be spherical or polyhedral depending on the software used and are assembled to create particles with desired shape [24]. Elongated particles can then be modelled with smooth surface as spherocylinders [187-191] or using spheres overlapped along an axis [192-197].

In clumped spheres approach, the particle overlap [198] generally defines the accuracy of particle modelling: for elongated particles, the higher the overlap, the greater the number of elements and the lower the roughness of the created particles. Indeed, the clumped sphere approach creates artificially rough surfaces [199-203], decreases the coefficient of restitution [202] and potentially increases the computational overhead of tracking multiple spheres. The angular measure of smoothness has been introduced to quantify the roughness of clumped-sphere particles [204], which is often considered more similar to actual granular materials compared to particles with smooth surface [205]. The overlapping ratio can be defined as the overlap distance over the radius of the sphere element [149].

The elongation of particles and granular materials is quantified with the aspect ratio [55, 206, 207] i.e. the length of the particle over its width [119, 208, 209]: The aspect ratio is high for an elongated particle (e.g. needle, rod-shaped) [191] and low (< 1) for platy particles (e.g. disk-shaped) [13]. Different shape descriptors have been introduced for more complex particle shapes such as the form, the angularity and the surface texture [210].

2.4.1.2 Size

The granular assembly is called monodisperse when composed of particles having the same size, and polydisperse otherwise. The polydispersity of particle size and shape generally has an impact on the mechanical behaviour of the bed [211]. A mathematical model, e.g. Gaussian, can be used to obtain the distribution of size or aspect ratio [191].

2.4.1.3 Mechanical Properties

Particles made of clumped spheres act like rigid body: the internal contacts between the spherical elements are ignored in the contact model calculations and internal contacts don't break [195, 212-215].

It is good practice when selecting input parameters to scale down the Young's modulus of particles as it reduces the computational cost and time of DEM simulations. This modification can only be performed after confirming that it doesn't affect the results e.g. torque in the agitated bed. The elastic modulus is generally scaled down by several orders of magnitude [55]. The rolling friction of spherical particles can also be adjusted in DEM to better model the behaviour of prismatic particles [165].

2.4.2 Models

2.4.2.1 Particle Interaction

In DEM simulations, the motion of each particle is determined discretely by solving Newton's second law of motion [210, 216]:

$$m_p \cdot \vec{a}_p = \vec{F}_{c,p} + m_p \cdot \vec{g} + \vec{F}_{f,p} \quad 2.4.1$$

$$I_p \cdot \vec{\omega}_p - (I_p \cdot \vec{\omega}_p) \times \vec{\omega}_p = \vec{T}_p \quad 2.4.2$$

With m_p the mass of particle p , a_p its acceleration, ω_p its rotational speed, $\dot{\omega}_p$ its rotational acceleration and I_p its moment of inertia tensor. The translational motion of the particle is determined from the inter-particulate contact force $F_{c,p}$, the gravitational force $m_p \cdot g$ with g the acceleration of gravity, and the fluid-particle interaction force $F_{f,p}$ in the presence of a fluid media. The torque T_p induced the particle's interactions (i.e. with walls, fluid or other particles) dictates the rotation of particle p .

Models exist to simulate the attractive, repulsive and frictional forces of particle-particle and particle-wall interactions [192, 217]. Simulations of particle shearing are generally operated with linear contact models [195] or with Hertzian models [55, 190, 218, 219]. The Mindlin-Deresiewicz [220, 221] or sliding model [55, 222] can also be used for the calculation of tangential forces. Ultimately, the contact model is selected based on the material simulated.

The advantage of using DEM with spherical element is the simplicity of the sphere-sphere contact detection which requires less computational power. In soft sphere approach, the deformation of particles in contact is simulated by the overlap of the element spheres of the two involved particles: the greater the overlap the higher the repulsive forces. The relationship between contact force and overlap distance is mainly dictated by the Young's modulus assigned to the elements.

Other existing methods allow the calculation of collisional stress by the summation of particle contact force vectors within a volume in a zonal approach of the particle bed [114]. Most of the models do not include the calculation of kinetic stresses as they are found being three order of magnitude lower than collisional stresses [80].

2.4.2.2 Cohesion

The presence of liquid is simulated by the addition of a cohesive force to the total force balance on particles [150, 218]. Viscosity models can also be used [210] where the viscosity of the fluid is likely to affect the force balance on particles e.g. for high fluid viscosity or in dynamic regime. Cohesive forces are calculated at inter-particulate contacts (pendular regime of saturation) and are effective within a chosen particle-particle distance [79] i.e. below the critical size of a liquid bridge.

Even though DEM aims for a realistic particle bed modelling, assumptions are taken to reduce the computational time needed. Concerning the modelling of moisture content effects on a particle bed, the liquid is generally assumed being only present at inter-particulate contacts and homogeneously spread with equal liquid bridge volumes [98, 223]: the total liquid volume is divided by the number of particles and average coordination number in a dry bed (around 5 for monodisperse spheres) [80]. The rupture distance of the liquid bridges is given as a function of their volume. Moreover, the capillary forces are usually presumed acting in the only normal contact direction and don't affect tangential movement [80]. The capillary force is also dependent on the contact angle which can be considered null for hydrophilic materials [223], and on the surface roughness at low moisture content [120] (not considered in first approximations [80]). In models where drying kinetics are not considered, the state transition (e.g. evaporation or condensation) isn't simulated.

Other cohesive models are based on numerical solutions of Laplace-Young equation [224], where the axial component from surface tension and the hydrostatic force due to pressure deficiency are calculated [210], and the results of static capillary forces show good agreement with experimental data [68, 225].

2.4.2.3 Flexible Particles

Flexible particles are studied in DEM simulations since 1993 [226] and consist on spheres linked together by forces that are related to the mechanical properties of the particle [192, 227]. The use of bending models allows the elongated particles to deform elastically [228]. Some models use energetic equations to rule the mechanical behaviour of fibres made of bound spheres [210]: the global kinetic energy of the fibre, the local kinetic energy of the constituent spheres and the elastic potential energy are calculated in the simulations [228].

Bending fibres in 3D Couette shear box experience similar normalised shear stress compared to rigid fibres, unless at high solid fraction and coefficient of static friction where they experience smaller normalised shear stress [14, 210, 228]. Indeed, the coordination number, shear stress and stress ratio vary with the Young's modulus of bonds within a flexible particle. A minimum Young's modulus of bonds of around

100MPa is necessary to observe the same bulk mechanical behaviour of a bed compared to rigid particles [228].

2.4.2.4 Particle Breakage

Breakage kernels are implemented in DEM simulations to compute the breakage of particles when their critical internal stress is reached. DEM is used for the prediction of particle breakage either by computing the breakage of primary particles into secondary particles within the simulation or by associating stress calculation in the model with assessing effects of stresses on the extent of breakage experimentally (e.g. annular shear cell) [165].

2.4.2.4.1 Particle Internal Stress

The internal stress of elongated particles can be calculated along the simulation using the Newton's second law of motion (see Equation 2.4.1 and Equation 2.4.2) and Euler equation of motion [55]. The particle internal normal and shear stress can also be calculated on specific planes [229], and the beam bending equation can be used in the case of flexible fibres [230].

Once the particle internal stress is calculated, the particle breakage is performed if the particle internal stress exceeds the assigned critical value. The breakage strength can be attributed homogeneously to all particles or following a Weibull distribution to reflect the heterogeneity of a particle bed due to the presence of defects within the crystals [192].

The particle internal stress calculation method can be verified by performing a DEM 3-point bending simulation [191] and compare the results with analytical solving of the simple beam bending equation [59].

2.4.2.4.2 Breakage Mechanisms

There are three types of breakage models in DEM [210]: the bound-particle model where the bonds between the constitutive elements of a particle break if their stress exceeds the material strength [191, 192, 194, 231-234], the fragment spawning model where a parent sphere generates daughter spheres with temporary overlaps, and the attrition prediction model where the attrition rate is given as a function of the strain applied.

Breakage kernels can compute both attrition and fragmentation [232-234]. Nevertheless, it is assumed that the fines have a low impact on the flow behaviour due to low attrition rates in dryers, which is why the fines are generally not accounted in the breakage kernels [191]. The corresponding mass loss is typically $< 3\%$.

2.4.2.4.3 Breakage Rate

The location of particles within the bed in an AFD highly impacts the breakage rate. In DEM agitation cell, a reduced distance between elongated particles and the impeller increases the breakage rate when using a breakage kernel [191]. Indeed, particle breakage mainly occurs in front of the impeller as it is an identified high stress region [108, 188, 191]. Likewise, a higher hydrostatic pressure [235] and strain applied increase the breakage rate of particles, which is confirmed in AFD simulations where more than 50% of the attrition of spherical particles occurs in the bottom third of the bed and towards larger radial distances [108]. The extent of breakage is actually dependent on the number of impeller rotations (i.e. the work applied) regardless of the impeller speed, which is in good agreement with the quasi-static flow regime during the drying process [1, 8, 9, 108, 156, 191, 235]. The breakage of elongated particles mainly occurs during the first impeller rotations in DEM agitated cell and then decreases with time [1, 191]. With time, particle breakage becomes more probable in the upper region of the bed as particles segregate and the smaller particles, requiring larger forces to break, migrate towards the bottom of the bed [191].

Finally, the particle physical and mechanical properties influence the breakage rate. As breakage occurs, the aspect ratio of particles is reduced which decreases their

breakage rate as they need a greater load to be broken [55, 191]. On the contrary, a lower particle yield strength or higher particle elastic modulus [55] increase the breakage rate of elongated particles [191]. A higher contact friction (i.e. particle-particle and particle-wall) is also reported to increase the breakage rate of elongated flexible particles made of bound spheres [235]. If the number of particles in the simulation is not sufficient, noise in the breakage rate can occur due to the lack of bed homogeneity [191]. Ultimately, the same steady state of PSD is achieved with sufficient work applied on the particle bed [8, 9, 28], regardless of the initial distribution [1, 191].

2.4.2.4.4 Location of Breakage

Elongated particles preferably break at their centre and the distribution of breakage location along the particle neutral axis follows a Gaussian model in both attrition cell [191] and compaction simulations [194]. The distribution parameters are the same for all aspect ratio and stress conditions, with a mean at the middle of the particle length [55, 191, 192, 194, 235] and a standard deviation at 0.11% of the length [191]. Moreover, the maximum internal stress on a particle occurs at its surface [55] where the tensile stress is at its maximum.

The probability that the particle internal stress exceeds the critical material strength on multiple location on the particle is below 1% [191]. In this case, the particle is broken on the location of the maximum stress. These models have shown good agreement with experimental extent of breakage when they use experimentally assessed mechanical properties (e.g. 3-point bending test) [192, 194].

2.4.2.4.5 Population Balance Model

The breakage rate of particles can be implemented in a population balance model (PBM) to predict the PSD of elongated particles during agitation [168, 191]. The PBM estimates the distribution of particle size or particle aspect ratio, the latter following a log-normal function if enough work is applied on a breakable particle system [191].

The PSD reduction in agitated systems is typically related to the operating conditions [157, 186, 231, 236-238]. The extent of attrition scales with the normal stress characterising the stress environment and the shear strain quantifying the deformation of the bed [157, 184]. Other models predict the extent of attrition from the work applied on the sheared particle bed [231]. The bed volume can be divided into zones and the operating conditions can be assessed within each zone [108] to increase the accuracy of the model.

The prediction of particle breakage can be performed by a combination of DEM simulation and PBM, as it has been done for elongated particles made of bound spheres in uniaxial compression [192, 194]. Alternatively, the extent of attrition can also be predicted from a combination of DEM simulations and experimental measurements allowing model calibration. A study has combined DEM simulation of lab-scale AFD, to obtain the strain and normal stress within the particle bed, with experimental measurement of attrition in annular shear cell [108]. In this paper, the particle size reduction due to breakage is considered having no effect on the strain, stresses and breakage rate of the primary particles with an aspect ratio of 2.

2.4.3 Shear Cell

A shear cell built in DEM consists of the application of shear and normal stress to a bed of particles. This method mimics the mechanistic conditions experienced by particles in an experimental annular shear cell [165] where the lower plate rotates horizontally inducing shear on the particle bed whilst the higher plate applies a scalable compression on it. Consequently, friction is generated at inter-particulate contacts and the bed deforms with particle rearranging to relieve the stress.

2.4.3.1 Types of Cells

Conventional shear test is performed using two connected boxes filled with particles. The boxes perform a translational movement in opposite directions to deform the particle bed [195]. The distance between the two boxes can be adjusted to define the

depth of the shear band i.e. the volume of the bed that experiences deformation [239, 240]. When the boxes separation is null, the shear band can be defined as a shear plane.

The Couette method consists of deforming a particle bed using rough walls instead of boxes. The shearing is induced by the translation of either one [13, 24] or the two parallel walls [21, 23, 241] in opposite directions [13, 24, 242]. The roughness of the walls is needed to ensure that no slipping occurs at the particle-wall interface: the particles in contact with the walls are dragged efficiently to avoid strain localisation at the boundaries [13, 23, 242, 243]. This phenomenon is generally simulated by increasing adhesion of particle-wall contacts (i.e. gluing particles to the walls) or modifying the walls inner surfaces to promote particle-wall interlocking. The particle bed can be compressed by reducing the distance between the two walls creating a uniaxial compression [191].

When populating the cell, particles are usually generated at random position and orientation [191] with no initial translational or rotational velocities [55]. An algorithm is used to ensure that particles are not generated where they would overlap with existing ones.

2.4.3.2 Periodic Boundaries

The use of periodic boundaries has become a standard in DEM simulations. Applied on two axes, it allows the creation of an infinite shear band with a reduced number of particles [21, 244], and thus considerably moderates the required computational power.

A shear cell can be simulated with periodic boundaries on the three spatial dimensions using Lees-Edwards boundaries [245], creating an infinite cell. The shearing is induced by assigning a velocity to particles crossing the Lees-Edwards boundaries and applying a reverse symmetry between the two involved boundaries [203]. The effect of gravity cannot be studied in this configuration as there is no wall to balance unidirectional forces.

2.4.3.3 Domain Size

2.4.3.3.1 Cell Dimensions

The shear cell volume needs to be large enough to produce consistent data and be representative of the volume of a real particle bed. The cell dimension is generally defined after the size of the studied particles. In the case of non-spherical particles, the diameter of a sphere (d_v), which volume is equivalent to the particle volume, is taken as reference to normalise simulations [119, 154]. In the case of elongated particles, the recommended specimen size is defined as a function of the particle length (i.e. particle's maximum dimension): a minimum of $\times 5$ with an ideal figure of $\times 8$ [246], and a maximum of $12 \times$ maximum particle size reported in tri-axial compression [205].

The objective of the domain definition is to minimise the number of particles generated and then increase the rapidity of the simulation, whilst conserving the consistency of the data. A comparison between a $20.16 \times 20.16 \times 10.08 d_v$ and $15.12 \times 15.12 \times 7.56 d_v$ cell size has been performed for particles aspect ratio of 6 and the results in normal stress, shear stress, kinetic and collisional components were in good agreement [203]. Further on, the smaller domain has been chosen for the study of elongated particles [228].

2.4.3.3.2 Number of Particles

A minimum number of particles is essential to obtain relevant particle bed behaviour and bed homogeneity, as the mechanical properties of assemblies (e.g. stiffness and peak shear strength) vary with sample size [247, 248]. The number of particles is generally reduced with increasing aspect ratios [55], especially for clumped-sphere particles as they require more computational power due their increased total number of elements.

The number of particles typically scales at the order of magnitude of thousands: 1170 to 3000 ellipsoids used in tri-axial compression [205, 249], 4500 clumped-sphere

particles in direct shear test [195], 2360 to 8400 elongated sphero-cylinders in DEM vertical axis mixer [55], and up to 8000 flat particles in shear box [13]. A study on 3D DEM shear cell has shown that the number of particles can be reduced from 4000 to 2000 whilst conserving identical mechanical response of the bed [203].

In simulations on two dimensions, the minimum number of particles for representative bed behaviour can be reduced: 1500 particles were sufficient in 2D Couette flow [23].

2.4.3.4 Mechanical Aspects

2.4.3.4.1 Strain and Strain Rate

The strain of a particle bed in a shear cell is defined by the relative displacement of the translating walls over the separation distance of the two parallel walls [23]. It is therefore a dimensionless number quantifying the deformation experienced by a particle bed. In shear cell simulating a Couette flow, the dimensionless strain γ is expressed as follows:

$$\gamma = \dot{\gamma} \cdot t \quad 2.4.3$$

With t the time of shearing and $\dot{\gamma}$ the strain rate given as:

$$\dot{\gamma} = \frac{|\vec{v}_{up} - \vec{v}_{low}|}{h_{(\gamma=0)}} \quad 2.4.4$$

With $|\vec{v}_{up} - \vec{v}_{low}|$ the relative velocity between the upper and lower walls, and $h_{(\gamma=0)}$ the shear cell height at the start of the shearing phase i.e. when the strain applied is null.

In Couette flow, an effective strain application is promoted by increasing the roughness of the walls. The grip factor f quantifies this effectivity as follows [155]:

$$\gamma = \frac{d}{h} f \quad 2.4.5$$

With d the relative displacement of the two walls and h the shear cell height. Here, the strain application is optimal when $f = 1$.

The velocity profile assesses the gradient of particle velocity in the shear direction across the bed [242] and a uniform strain application throughout the bed can be confirmed by a linear velocity profile [13]. To ensure a linear velocity profile, a velocity can also be assigned to particles individually according to their position along the bed height, ensuring a linear velocity gradient [203].

The magnitude of strain performed in simulations generally corresponds to the deformation needed to reach a steady state on an investigated variable. A strain of 0.15 was sufficient to reach a constant stress ratio (see Equation 2.4.6) in a 3D conventional shear cell with particles aspect ratio between 1 and 2.5 [149], whilst a strain of 2.5 was needed to study the mechanical behaviour of a bed of platy particles [13], and only 0.3 in a direct shear test with elongated clumped-sphered particles strained on a shear plane [195].

In triaxial compression, the strain required to reach a plateau of effective stress ratio increases with aspect ratio of ellipsoids [205]. The same observation is made for clumped-sphere particles in direct shear test [195]. On the contrary, the normal stress applied doesn't impact the strain needed to reach a steady state in this study, for a range of $50k - 2MPa$.

The initial acceleration of the walls, before they reach a constant velocity, has been taken in consideration, and a low acceleration can be assigned to walls to avoid initial shock disturbance on the particle bed [24].

2.4.3.4.2 Bed Dilatancy and Densification

A granular assembly dilates slightly when a shear stress is applied on it. This phenomenon is called Reynold's dilatancy [250, 251] and is due to the interlocking between particles and rearrangement of particles in an over-consolidated bed [21]. Indeed, the particles change position and rotates to release the frictional energy by breaking existing particle-particle contacts and creating new ones [252, 253].

Therefore, the choice of either constraining the bed volume by fixing the walls separation distance or constraining the normal pressure applied by adjusting the walls separation [13, 21, 23, 24, 195] throughout shearing may affect the mechanical behaviour of the particle bed [24].

2.4.3.4.3 Stress Environment

The stress environment is defined with the components of the stress tensor [13, 254, 255]. Generally, only the normal and shear stresses are taken to characterise this stress environment in DEM. The two stresses are linearly proportional in quasi-static flow regime according to the Coulomb's law of static friction [152-154] (see Equation 2.3.3).

The stress ratio φ is the main dimensionless number for the characterisation of the mechanical behaviour of a particle bed [13, 21] and is given as a function of the shear stress τ and the normal stress σ :

$$\varphi = \frac{\tau}{\sigma} \quad 2.4.6$$

The stress ratio can also be obtained by the division of the deviatoric stress by the hydrostatic pressure (see Equation 2.3.2). The deviatoric stress is then given as the major σ_1 , intermediate σ_2 and minor σ_3 principal stresses [149]:

$$\tau = \frac{\sqrt{(\sigma_1 - \sigma_2)^2 + (\sigma_1 - \sigma_3)^2 + (\sigma_2 - \sigma_3)^2}}{\sqrt{6}} \quad 2.4.7$$

In the shear cells, the average normal and shear stresses can be calculated from the sum of forces on the wall $\vec{F}_{i,w}$ divided by the wall area A [195, 256, 257]:

$$\sigma = \frac{1}{A} \sum_{i=1}^n \vec{F}_{i,w} \cdot \vec{z} \quad 2.4.8$$

$$\tau = \frac{1}{A} \sum_{i=1}^n \vec{F}_{i,w} \cdot \vec{y} \quad 2.4.9$$

With n the number of wall contacts, \vec{z} the unit vector in the normal stress direction and \vec{y} the unit vector in the shear direction.

In shear cells, the stress ratio first increases to a peak in the transitional state [13] before decreasing to reach a steady state [258]. The average value of stress ratio in steady state can be taken as a characteristic value [149].

The aspect ratio of elongated particles influences the mechanical behaviour of the bed in shear cells and affects the shear stress [203]. Observations differ on the nature of the correlation between aspect ratio and shear stress. On the one hand, the stress ratio is reported to decrease with higher particle elongation when the aspect ratio is greater than 1.5 in shear cells [149, 228]. Indeed, the angle of friction, proportional to the stress ratio [152-154] (see Equation 2.3.3), for ellipsoids is shown to slightly decrease with increasing aspect ratio [258]. This phenomenon may be attributed to particles alignment which reduces particles resistance to shear and make them slide more easily [149]. On the other hand, a bed of particles made of two clumped spheres with an aspect ratio of 2 exhibits larger shear stress than for spherical particles [154]. This observation is supported by the increase of critical direct shear angle of friction with particle elongation for aspect ratio ranging from 1.2 to 2.2 in direct shear test [195]. It is also the case in 2D simulations using clumped spheres for aspect ratio ranging from 1 to 3.3 [259]. In AFD simulations, the impeller torque, proportional to the shear stress using Darelius equation [152] (see Equation 2.3.4), scales with particle elongation up to an aspect ratio of 5 [119]. The increase of torque with non-spherical particles made of clumped spheres and with inter-particle friction is confirmed in DEM Freeman powder rheometer [193]. In the case for platy particles, the shear stress also scales with particle platyness in 3D Couette flow [13]. Finally, the peak value of stress ratio is not correlated to the particle aspect ratio when > 1.2 in direct shear test [195].

The impact of aspect ratio on shear stress can also be magnified by the bed packing and particle-particle interaction properties e.g. solid volume fraction and friction

coefficient [14, 203, 210]. Indeed, the normalised shear stress increases with solid volume fraction for particles with aspect ratio of 6 [228]. Likewise, the impeller torque increases with lower elastic modulus of sphero-cylinders in DEM vertical axis mixer. The use of realistic elastic modulus produces torque similar as experimentally observed [188].

Contrary to cylindrical-shaped particles, the spacing between elements in multi-sphere particles induces an additional particle roughness which promote interlocking and a higher shear stress in shear tests [149, 228, 260]. The flow stresses produced with these particles is greater by over one order of magnitude than with smooth particles in DEM simple shear flow [14, 203, 261].

The normal stress applied isn't reported to have an impact on the steady state value of the stress ratio, as it is the case in tri-axial compression of ellipsoids with an aspect ratio of 1.1 and the normal stress ranging from $50Pa$ to $2kPa$ [205, 262]. However, the peak value of stress ratio increases for lower normal stress in the range of $50k - 20MPa$ [195].

2.4.3.4.4 Bed Flow

Granular flow is characterised according to the correlation between the stress and the shear rate applied [203, 210]: it is called dilute when collisions are dominant and the stress scales with the square of shear rate, dense (or elastic-inertial) in the case of multiple enduring contacts where the stress scales linearly with shear rate, and quasi-static if the shear stress and shear rate are independent [116]. In the dilute flow regime, the flow stress is largely dependent on the particles aspect ratio rather than the surface roughness [14, 203, 261]: the stress is inversely proportional to the aspect ratio. In the dense flow regime, the stress increases with particles aspect ratio, friction and surface roughness.

In the case of quasi-static flow regime, most of the energy is dissipated by frictional contact rather than inter-particulate damping [24] and the kinetic energy can be considered negligible [205]. The ratio of mean unbalanced force to the mean contact force is an indicator of quasi-static flow if low enough: a value of 10^{-5} has been

reported as characteristic of quasi-static flow [263], however no maximum value is specified for this regime.

Quasi-static flow regime is characteristic of bed behaviour in industrial scale AFD [1] where the normal stress scales linearly with the shear stress [152-154] (see Equation 2.3.3). This phenomenon is confirmed in AFD simulations with the impeller torque being linearly proportional to the lid pressure [191, 235].

The particle shape affects the bed flow in DEM shear tests [264]. The velocity of sphero-cylinders in mixing simulations decreases with increasing particles elongation [188]. This phenomenon is due to a higher mass moment of inertia of elongated particles restraining their rotation, and is reported to lower the rate of volume changing in tri-axial compression [205]. Indeed, the variation of particles angular rotation decreases with increasing aspect ratio [149]. Nevertheless, their trajectories remain similar to spherical particles with vortices on horizontal plane circulating in opposite direction from blade rotation [188].

2.4.3.4.5 Packing

The particle shape is one of the key factors conditioning the packing structure [265] and this phenomenon was investigated for ellipsoids [266, 267], polyhedrons [268, 269] and cylinders [187, 189].

The coordination number of a particle is the number of particles in contact with it [270]. It is related to the structural stability of a granular assembly [271] and a coordination number greater than 4 is necessary to consider stable an assembly of polydisperse spheres [270]. The coordination number increases with particle aspect ratio [228], and a plateau is reached for an aspect ratio of 2 with ellipsoid [205]. This increase is potentially due to the obstruction of particle rotation with greater aspect ratio, forcing the creation of more particle-particle contacts for them to slide [205]. The choice of modelling ellipsoids with clumped spheres decreases their coordination number but increases the total number of contacts compared to smooth shapes [272]. When a bed of ellipsoids is strained, the coordination number decreases to reach a steady state [205, 270].

The void ratio of a bed increases with elongation of ellipsoids having an aspect ratio greater than 1.5 [119, 205]. The same observation is made for spherocylinders in DEM monodisperse system with periodic boundaries [273-276]. The sphere overlap also affects packing properties: the void ratio is observed to be larger for rough particles compared to smooth [272, 277] and affects the number of contacts [249, 258, 266, 278] which appears twice as high for rough particles [228]. Likewise, increasing the stress field with a higher compression on particles augments the coordination number and decreases the void ratio [205]. Indeed, the coordination number typically increases with reduced porosity [270].

Elongated particles have the ability to align [14] along the flow stream in sheared systems [188] and the order parameter S quantifies the uniformity of their ordering in the same direction [205, 279, 280]: the order director. A higher aspect ratio of particles is reported to increase alignment [14], decreases overall solid fraction and solid fraction uniformity within the bed [188]. In DEM vertical axis mixers, the alignment phenomenon then affects the flow and particle velocity [188]. A smaller degree of alignment, and thus solid fraction, is found in the region of higher velocity in DEM agitated cell with spherocylinders [188].

Different packing gives different resistance to the flow and can affect particle breakage [281]. Methods can be employed to generate isotropic dense assemblies, such as setting to zero the gravitational acceleration and friction coefficients of particle-particle and particle-wall interactions [205]. The use of this method resulted in the densest granular assemblies [282, 283]. Further on, the coefficients can be set back to a realistic value for the shearing phase [195, 205, 282-284].

2.4.3.4.6 Force Chains

The forces induced by the stress environment are transmitted through contacts between particles within a granular assembly. The contact network can be described as strong/weak subnetwork if normal contact force is higher/below average normal force applied [195, 285-287]. The strongest contacts support most of the stress on the assembly and form force chains across the bed [195, 285-287].

Sliding mainly occurs on weak contacts as they require less force to be broken during bed straining [205, 285, 288]: they are called sliding contacts. They behave like interstitial liquid providing stability for the force propagation along the strong contacts [205, 285]. The percentage of sliding contacts increases with the particle aspect ratio in monodisperse bed [205].

2.4.3.5 Gravity

The gravity is generally used when simulating a realistic environment [289] and becomes essential when the acceleration of gravity is likely to have an impact on the modelled phenomenon. This is especially the case in large scale where the load on particles scales with the mass of the bed, which produces a discrepancy of compressive stress within the bed due to the uni-directionality of gravity.

The use of gravity in simulations has a noticeable influence on the key properties of a particle bed when a low pressure is applied on particles in a shear cell: it particularly affects the symmetrical distribution of particles velocity, inter-particulate forces and stress tensors along the gravity axis [290]. Moreover, the behaviour of elongated particles changes with gravity as they tend to lie flat on surfaces to minimise their gravitational potential energy [205]. The influence of gravity diminishes when the applied load increases. The magnitude of the applied gravity force also has a noticeable effect on the packing of the particle bed in quasi-static flow: the density increases and the macroscopic friction decreases with a greater gravity force [291]. Moreover, powders exhibit more cohesiveness with decreasing gravity [292].

Nevertheless, the absence of gravity allows the observation of small-scale phenomenon and reduces the number of variables involved, i.e. degrees of freedom [203, 228, 241, 261]. As an example, not introducing gravity allows the creation of an homogeneous stress field within the particle bed [13].

2.4.4 DEM Validation

The angle of repose is a widely used method and consists of measuring the angle of a pile of particles been dropped on a flat surface. The angle is affected by DEM parameters such as the angle of friction, particles morphology and surface energy. The angle also generally increases with the presence of cohesion [120]. The result of this test can then be validated against experimental observations. Another method was used to validate DEM results by performing uniaxial compression on chalk sticks and compare the load vs. displacement curve with experiments [191, 235].

The flow of the particles within a bed when submitted to agitation can be compared with Particle Image Velocimetry (PIV) experiments that analyse the velocity of particles at the bed surface [80]. The use of Positron Emission Particle Tracking (PEPT) experiments has the advantage to validate particle flow through the whole bed [165].

The level of shear and normal stress that the particles experience in simulated blade mixers can also be confirmed by theory. As expected, DEM simulations have demonstrated that these stresses scale linearly with the total weight of particle bed [150]. Also it is realistic to observe in simulations that the momentum transfer is independent of shear rates in quasi-static flow regime [115].

2.5 Concluding Remarks

API crystals experience breakage during the drying process in the pharmaceutical industry. The phenomenon is of great concern as it degrades the quality of medicines and requires resource-consuming methods to obtain the desired particle properties for further product formulation.

The breakage of a crystal means that the internal stress experienced by the crystal exceeded its critical breakage strength. Therefore, two variables are needed to solve the issue of crystal breakage during agitation drying: the particle internal stress experienced in the drying environment and the particle breakage strength.

The presence of defects in organic crystals involved in the pharmaceutical industry makes their mechanical properties unpredictable from their ideal crystal lattice. An

experimental study on the crystals charged into the dryer is then essential to obtain the distribution of their breakage strength. Methods like 3-point bending are widely used in the literature and allow to assess the mechanical properties of individual crystals to obtain this distribution.

Most of these crystals are highly elongated e.g. rods or needles. Therefore, their main breakage mechanism is fragmentation from their experienced bending stress. Mechanical theory informs that the internal stress of particle is induced by external forces on its surface. In granular assembly, these forces are created from inter-particulate contacts. An in-depth knowledge of the force magnitude and number of contacts is then crucial to accurately determine the particle internal stress. This information can only be obtained using modelling tools, and DEM is an established method to simulate the behaviour of granular assemblies.

Due to the limits of computational power nowadays, it is not possible to simulate the number of particles present in an AFD with DEM. Nevertheless, it is possible to study the behaviour of a reduced number of particles using a shear cell which can mimic the mechanical process environment within an AFD: the normal stress induced by the weight of the bed and the shear stress generated from the impeller rotation. The shear stress is proportional to the normal stress due to the quasi-static flow regime of a particle bed in the AFD.

The use of DEM shear cell simulations with the different normal stresses experienced in an AFD and particle elongations represents a solution to obtain the distribution of particle internal stress. The distribution parameters can then be correlated with the particle physical properties and drying process conditions to obtain mathematical models. These models have the potential for the process operator to predict the particle internal stress distribution in dryers without the need to perform further DEM simulations which require time and computational resources.

Particle breakage is generally computed during the simulation which makes the PSD time-dependant and creates transient model. A novel probabilistic approach can be proposed to obtain the extent of breakage of particles from the joint density function of particle internal stress and particle breakage strength. It is reported that the breakage rate is proportional to the strain applied, which is dependent on the radial

Chapter 2: Literature Review

distance in AFD and number of impeller rotation. A breakage kernel can then be created and used in a population balance model to obtain the breakage rate of particles in the different zones of an AFD. This methodology would allow the prediction of PSD during the drying process in an AFD and can be validated against lab-scale experimental results.

3 The Breakage of Elongated Organic Crystals in Agitated Filter Dryers

3.1 Introduction

In this chapter, the breakage of elongated organic crystals is investigated for different agitated drying conditions. Glutamic acid is crystallised in its elongated form (β -LGA). The crystals are then filtered and agitated in a lab scale agitated filter dryer (AFD).

The effect of agitation is assessed by measuring the particle size distribution (PSD) for different level of agitation, i.e. number of impeller rotations applied to the particle bed. The impact of agitation on particle breakage is investigated on both dry and wet systems. The PSD is measured by laser diffraction and image analysis for cross-referencing. The use of image analysis method provides insights on the mode of breakage of particles according to their size and shape. As the study of individual β -LGA crystal breakage using Atomic Force Microscopy (AFM) performed in Chapter 4 confirms the brittle fracture of this material, and the agitation in AFD is applied in quasi-static flow regime, the expected principal modes of breakage of these elongated crystals are attrition and fragmentation.

3.2 Materials and Methods

3.2.1 Crystallisation

The crystallisation of glutamic acid is performed to obtain its needle-shaped β -LGA polymorph following the methodology described by Shier [293]. A 99% purity glutamic acid powder provided by Sigma-Aldrich is taken as raw material. 40g glutamic acid powder and 1L deionised water is charged into a 1L vessel (see Appendix 1) and heated up to 70°C for 60min to dissolve the solid under a 300rpm agitation throughout (the solution took approximately 30min to reach the desired temperature). The temperature of the solution was then reduced to 60°C over 30min. 1.2g LGA material is ground up using a mortar and pestle until the consistency becomes like flour and non-shiny. The crushed powder is then charged to the reactor at a batch temperature

of 60°C. The seed holds forming a thin white slurry and is cooled down to 20°C at a rate of 0.06°C/min, allowing the crystals to grow.

3.2.2 Filtration

After crystallisation, the slurry is removed from the vessel and vacuum filtered in 4 portions, each approximately 250mL, using the AFD model PSL minilab GFD (see Figure 3.2.1). The filtration is performed by nitrogen gas flow at 5L/min, room temperature and 0.4bar pressure controlled by a Humidifier P-50 from Cellkraft.

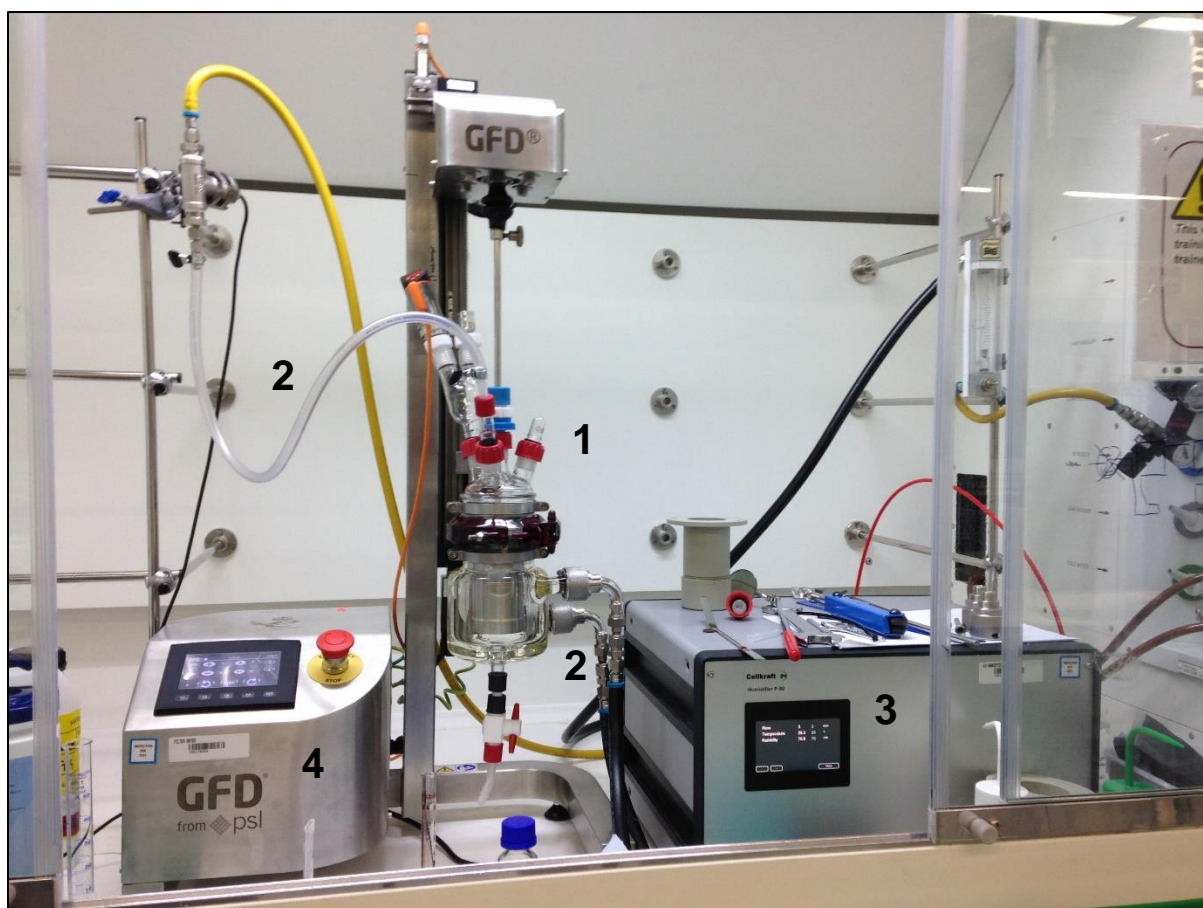


Figure 3.2.1: Agitated filter dryer (1) Minilab GFD from PSL used for filtration and agitation of β -LGA crystals. The nitrogen flow is applied in the vessel via flexible tubing (2) and controlled using a Humidifier P-50 from Cellkraft (3). The AFD controller (4) allows the selection of the impeller rotation speed.

The filtration was rapid and took less than 5s for each portion, with the filtrate collection performed after each portion filtrated. The wet cake is then directly agitated in the wet agitation experiment, whilst it is allowed to deliquor in static conditions by flow through nitrogen at $5L/min$ with a target humidity at 0% to obtain a dry bed for the further dry agitation experiment.

During the filtration process, the agitator is on its top position and outside of the wet cake for the further dry agitation experiment, whilst it is already positioned towards the bottom of the bed for the further wet agitation experiment.

3.2.3 Agitated Drying Process

3.2.3.1 Dry Bed

After crystallisation and filtration, the wet cake is left overnight in the AFD with a nitrogen flow filtration allowing the particles to fully dry in static conditions. The particle bed is considered fully dry after overnight filtration and no moisture content measurement is performed.

The impeller rotation is then activated in the forward direction at $30rpm$ and lowered into the particle bed until a $5mm$ gap separates the impeller from the bottom of the AFD. 8 rotations were performed in the forward direction into the bed whilst lowering the agitator. The agitation of the particle bed is started again at $30rpm$ for $1min$ then $100rpm$ until the end of the agitation phase.

Bed sampling is performed regularly for PSD measurements, stopping the agitation if the impeller is rotating. In total, 9 laser diffraction and 5 G3 PSD measurements are performed during the dry bed agitation experiment (see Table 3.2.1).

Table 3.2.1: List of samples during AFD experiment of dry bed with performed analysis.

Sample name	Description	Impeller rotations (cumulative)	Microscopy	Laser diffraction	Morphologi G3
-------------	-------------	---------------------------------	------------	-------------------	---------------

Chapter 3: The Breakage of Elongated Organic Crystals in Agitated Filter Dryers

Dry-A	After filtration	0	Y	Y	N
Dry-B	Overnight filtration	0	Y	Y	Y
Dry-C	8 impeller rotations	8	Y	Y	N
Dry-D	1min 30rpm	38	Y	Y	Y
Dry-E	5min, 100rpm	638	Y	Y	N
Dry-F	25min 100rpm	3.74k	Y	Y	N
Dry-G	120min 100rpm	18.8k	Y	Y	Y
Dry-H	165min 100rpm	50.4k	Y	Y	Y
Dry-I	505min 100rpm	132.4k	N	Y	Y

3.2.3.2 Wet Bed

Another crystallisation and filtration are performed. The cake height is assessed by fully immersing a spatula and measuring the portion covered with white powder. The measured cake height is 6 cm with a slight overestimate as the spatula was immersed with a slight angle.

Contrary to the dry bed agitation experiment, the agitator was already positioned 5 mm away from bottom of the AFD before filtration to avoid crushing of particles when lowering.

8 impeller rotations are then carried out in the forward direction at 30 rpm . The agitation of the particle bed is started again at 100 rpm until the end of the agitation phase.

Again, bed sampling is performed regularly for PSD and moisture content measurements, stopping the agitation if the impeller is rotating. In total, 6 moisture

Chapter 3: The Breakage of Elongated Organic Crystals in Agitated Filter Dryers

contents, 6 laser diffraction and 4 G3 PSD measurements are performed during the wet bed agitation experiment (see Table 3.2.2).

Table 3.2.2: List of samples during AFD experiment of wet bed with performed analysis.

Sample name	Description	Impeller rotations (cumulative)	Microscopy	Moisture content	Laser diffraction	Morphologi G3
Wet-A	After crystallisation	0	Y	N	N	N
Wet-B	After filtration	0	Y	Y	Y	Y
Wet-C	8 impeller rotations	8	Y	Y	Y	N
Wet-D	1min 100rpm	108	Y	Y	Y	Y
Wet-E	5min, 100rpm	708	Y	Y	N	N
Wet-F	25min 100rpm	3.81k	Y	Y	N	N
Wet-G	142min 100rpm	21.1k	Y	Y	Y	Y
Wet-H	204min 100rpm	58.8k	Y	N	Y	N
Wet-I	987min 100rpm	195.2k	Y	N	Y	Y

3.2.4 Measurements

3.2.4.1 Particle Sampling

The particle sampling is performed using a soft cut plastic pipette (see Figure 3.2.2). The cut pipette is inserted into the particle bed along the entire bed height to obtain a representative PSD and account for the possible particle segregation by size with

particle breakage and agitation. All wet samples are dried in a vacuum oven before performing microscopy, laser diffraction or Morphologi G3.

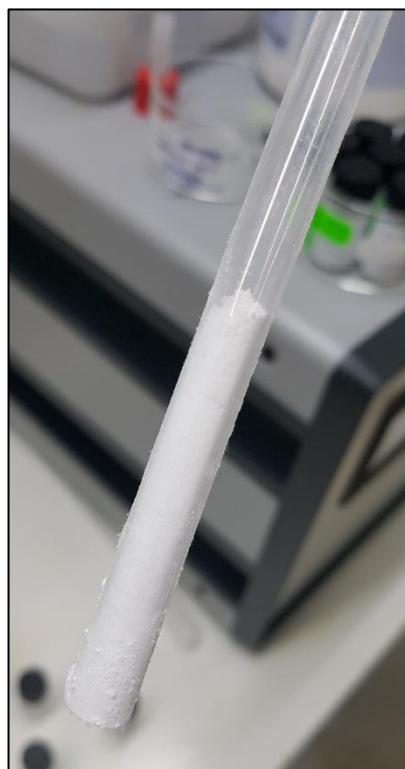


Figure 3.2.2: Particle sample collected using a soft cut plastic pipette.

3.2.4.2 Particle Size Distribution

The PSD of β -LGA crystal samples is assessed using two methods to obtain both one-dimensional and 2-dimensional particle size measures. This combination provides complete insights on the particles physical properties [28-31].

The laser diffraction [1] is performed using the Mastersizer 3000 from Malvern. The powder dispersion is operated at 2bar air pressure at a temperature of 0°C and 3 million snaps (individual data record collection instances) are demanded. The additional parameters recorded for the different samples are summarised in Appendix 9.

The measure of particles width and length is performed using the Morphologi G3 [25, 27, 28] from Malvern. The data collected is analysed using a script presented by Mahdi

et al. [294] allowing the elimination of particles having an unrealistic shape, e.g. t-shape due to superposed particles. The PSD is presented as a 31×31 cell grid being bins of particles width and length. The bins limit values are linearly divided for the input maximum values of width W_{max} and length L_{max} .

3.2.4.3 Moisture Content

The moisture content is measured for a sample mass of $0.1g$ using the HR73 Halogen Moisture Analyzer oven (see Figure 3.2.3) from Mettler Toledo at a temperature of $100^{\circ}C$ with an automatic end point detection.

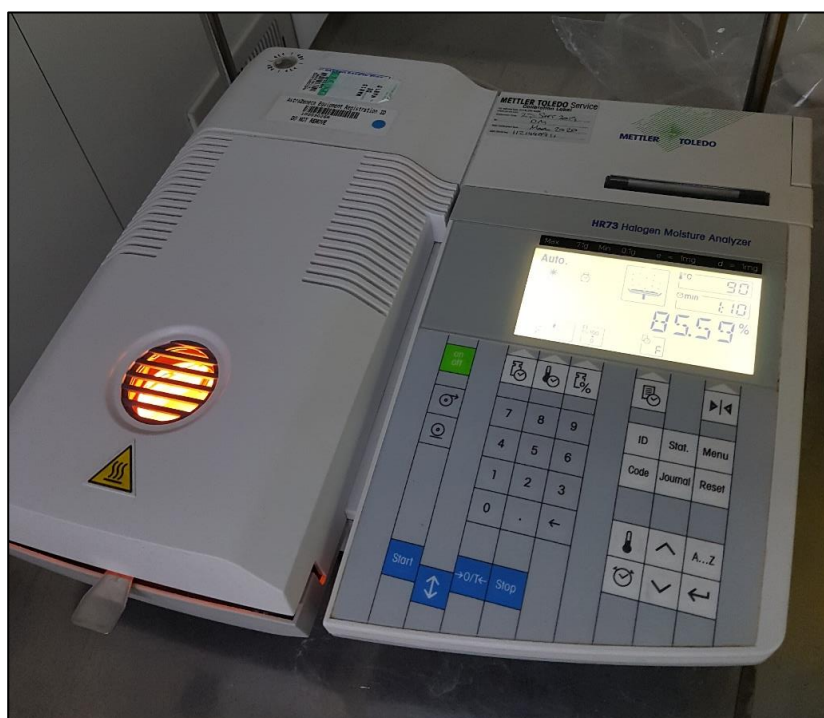


Figure 3.2.3: HR73 Halogen Moisture Analyser oven from Mettler Toledo used for moisture content measurement of β -LGA crystal samples.

3.2.4.4 Microscopy

The β -LGA crystals (see Appendix 3 & Appendix 4) are observed using an Axioskop 40 light microscope from Zeiss (see Appendix 2) and images are captured with a Zeiss AxioCam 512 color camera and the ZEN 2.5 Lite software.

3.3 Results and Discussion

3.3.1 Moisture Content

The moisture content is measured for 6 samples during the wet agitation experiment. The values range between 45.5% and 72.2% with a mean value at 59.4%. It is not expected for the moisture content to vary significantly within 142min, therefore the variability of the results is attributed to the inaccuracies in the sampling.

Table 3.3.1: Measured moisture content of the different samples of wet agitation experiment (see Table 3.2.2).

Sample name	Description	Tare (g)	Wet weight (g)	Dry weight (g)	Moisture content
Wet-B	After Filtration	8.40	9.43	8.89	52.4%
Wet-C	8 Impeller Rotations	8.45	9.15	8.69	65.7%
Wet-D	1 min 100 rpm	8.49	9.21	8.69	72.2%
Wet-E	5 min 100 rpm	8.63	9.40	8.91	63.6%
Wet-F	25 min 100 rpm	8.55	9.50	8.96	56.8%
Wet-G	142 min 100 rpm	8.41	9.40	8.95	45.5%

3.3.2 Laser Diffraction

The analysis of the laser diffraction results allows to observe the particle size reduction due to particle breakage. There is the established consensus that the flow regime in an AFD is quasi-static [1, 8, 9, 108, 156, 191, 235], which means that the impact breakage driven by particle velocity is expected to be marginal in the performed experiments. Likewise, it is expected that the viscous forces are negligible in the wet agitated particle system [71]. Therefore, there are two possible modes of particle

breakage occurring here: the attrition where a particle is chipped creating small fragments and fines, and the fragmentation which results in the rupture of a primary particle into two secondary particles [50]. Most of organic API are brittle [61] and the individual β -LGA crystal breakage study using AFM in Chapter 4 confirms the brittle fracture mode of this material. The microscope images of particles at different stages of the dry experiment suggest that no granulation is occurring in the performed agitation experiments.

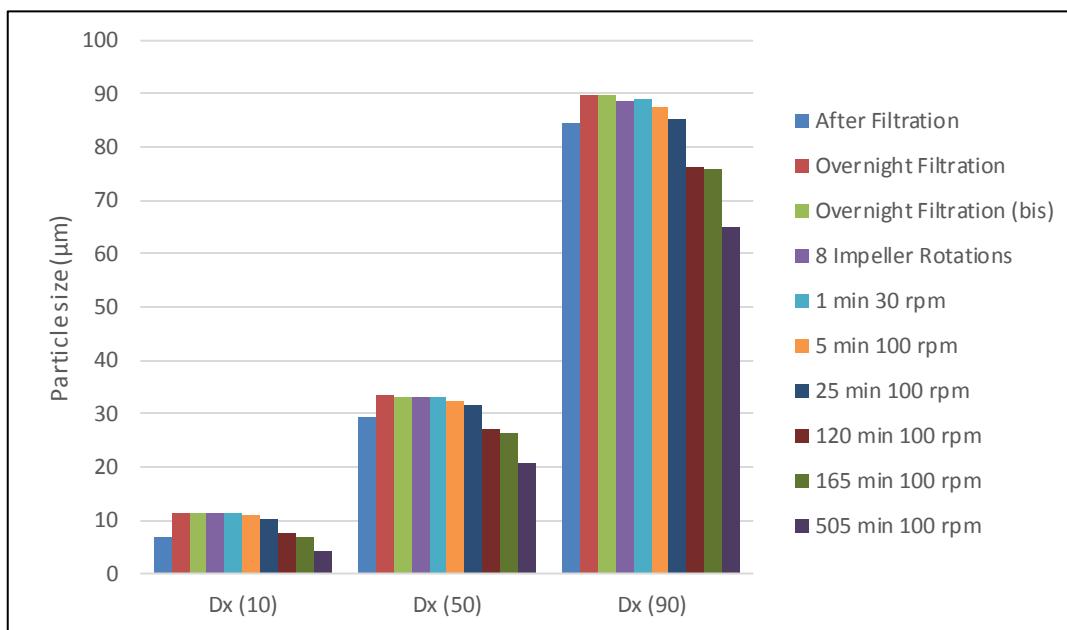


Figure 3.3.1: Laser diffraction data of the different samples of dry agitation experiment with the particle size at 10%, 50% and 90% of the PSD.

The median particle size at the beginning of the dry agitation experiment is approximately $30\mu m$, with 10% of the particles below $10\mu m$ and 10% above $90\mu m$ (see Figure 3.3.1). There's a noticeable increase of $5\mu m$ in the particle size after overnight filtration, which isn't reflected in the microscope image of the two samples "after filtration" and "overnight filtration" (see Appendix 3). A second sample is taken and confirms the PSD obtained for "overnight filtration", which indicates that there might have been a specific difference in the sampling or analysis method of the "after filtration" particles that has not been identified. The PSD decreases during the agitation phase, with an end median size at $20\mu m$. The size of the biggest particles has experienced a significant decrease down to $Dx(90) = 64\mu m$, which is also the case for the smallest particles down to $Dx(10) = 4.3\mu m$. The microscopy images show an

extensive production of fines confirming the attrition of particles. Indeed, attrition is highly present in dry particulate systems due to the frictional contacts between particles [172], especially in AFD equipment [12].

In the wet case, the particle size after filtration is higher than in the dry case with a median value at $37\mu\text{m}$, 10% of the particles below $11.3\mu\text{m}$ and 10% above $109\mu\text{m}$ (see Figure 3.3.2). This difference could only be attributed to a variability of the PSD obtained using the same crystallisation process. At the end of the agitation phase, the median size decreased down to $31.6\mu\text{m}$, which is also the case for the biggest particles down to $Dx(90) = 95.6\mu\text{m}$. At the same time, the size of the smallest particles remained quasi-constant at $Dx(10) = 10\mu\text{m}$ which is supported by the low number of fines present on the microscopy images at the end of agitation (see Appendix 4). It suggests that the crystals have predominantly broken by fragmentation along their length rather than producing fines by attrition. Indeed, the moisture content creates liquid bridges at inter-particulate contacts [62, 65, 66] and the lubrication effect of the liquid [1, 103] reduces the number of inter-particulate collisions as the liquid films on particles have to drain before the contact on particles surfaces [8]. This effect increases the mobility of the particles because of an increased particle-particle distance and reduces their frictional contacts [118].

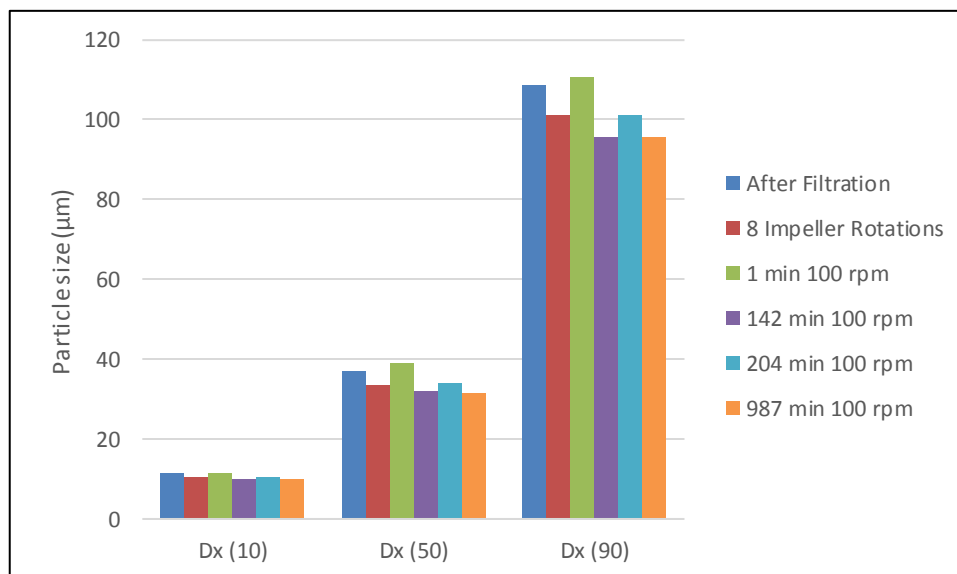


Figure 3.3.2: Laser diffraction data of the different samples of wet agitation experiment with the particle size at 10%, 50% and 90% of the PSD.

The breakage of particles increases monotonically with the strain applied in a quasi-static system [1, 108], therefore, the particle size reduction is observed as a function of the number of impeller rotations. Here, the particle size doesn't change as significantly as in the dry case (see Figure 3.3.3). An order of magnitude of 10^4 impeller rotation is needed to observe the effect a significant decrease in the particle size due to crystal breakage. The end values and trend in the dry case suggest that particle breakage would continue to occur if the agitation was carried on for a longer period: no steady state is yet observed. When kept agitated in the same conditions, the PSD is expected to reach a steady state if sufficient work is applied on the particle bed [8, 9, 28] regardless of the initial distribution [1, 191]. Indeed, the sensitivity to mechanical stress scales with particle size [16]. Therefore, it can be assumed that breakage would keep occurring if more agitation is applied to the bed.

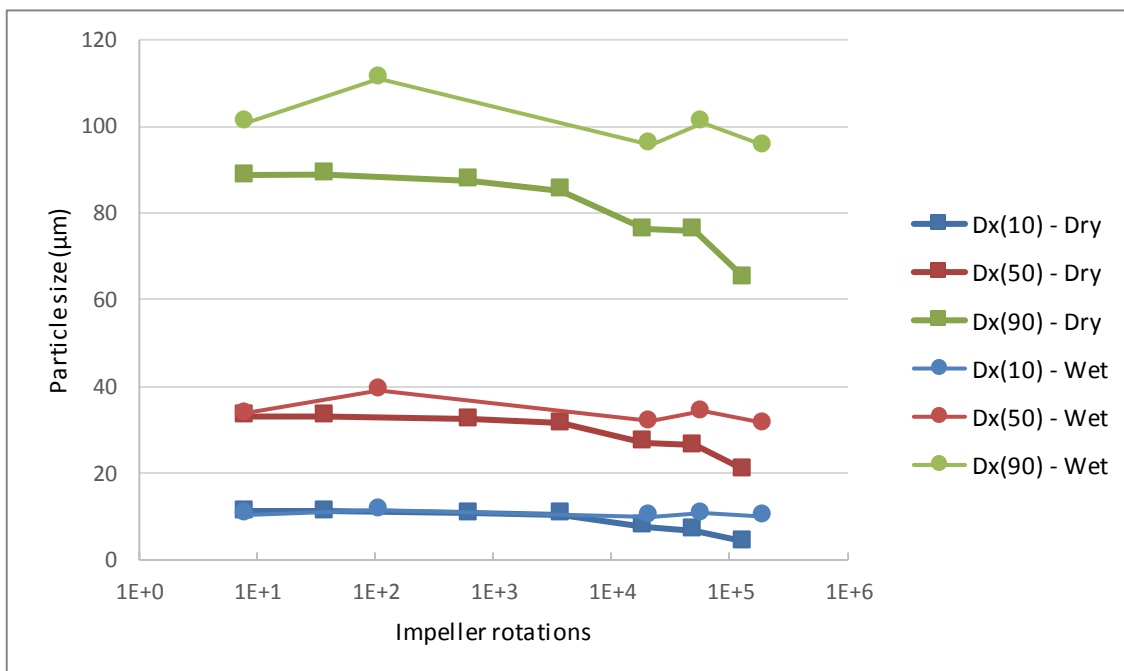


Figure 3.3.3: Laser diffraction data in agitation phase given by the number of impeller rotations. The particle size is given at 10%, 50% and 90% of the PSD.

3.3.3 Optimisation of Script Analysis for Morphologi G3 Data

Based on observation of microscopy images (see Appendix 3 and Appendix 4), the script [294] was first parameterised for an analysis of the dry case samples with

Chapter 3: The Breakage of Elongated Organic Crystals in Agitated Filter Dryers

maximum length $L_{max} = 1450\mu\text{m}$ and maximum width $W_{max} = 250\mu\text{m}$, and of the wet case samples with $L_{max} = 1200\mu\text{m}$ and $W_{max} = 220\mu\text{m}$.

The script retains 22 – 83% of the solid volume depending on the sample analysed and the proportion of particles with a shape considered as credible (see Appendix 13). The number of particles retained ranges 31k – 170k for a volume of 0.4 – 0.9mm³.

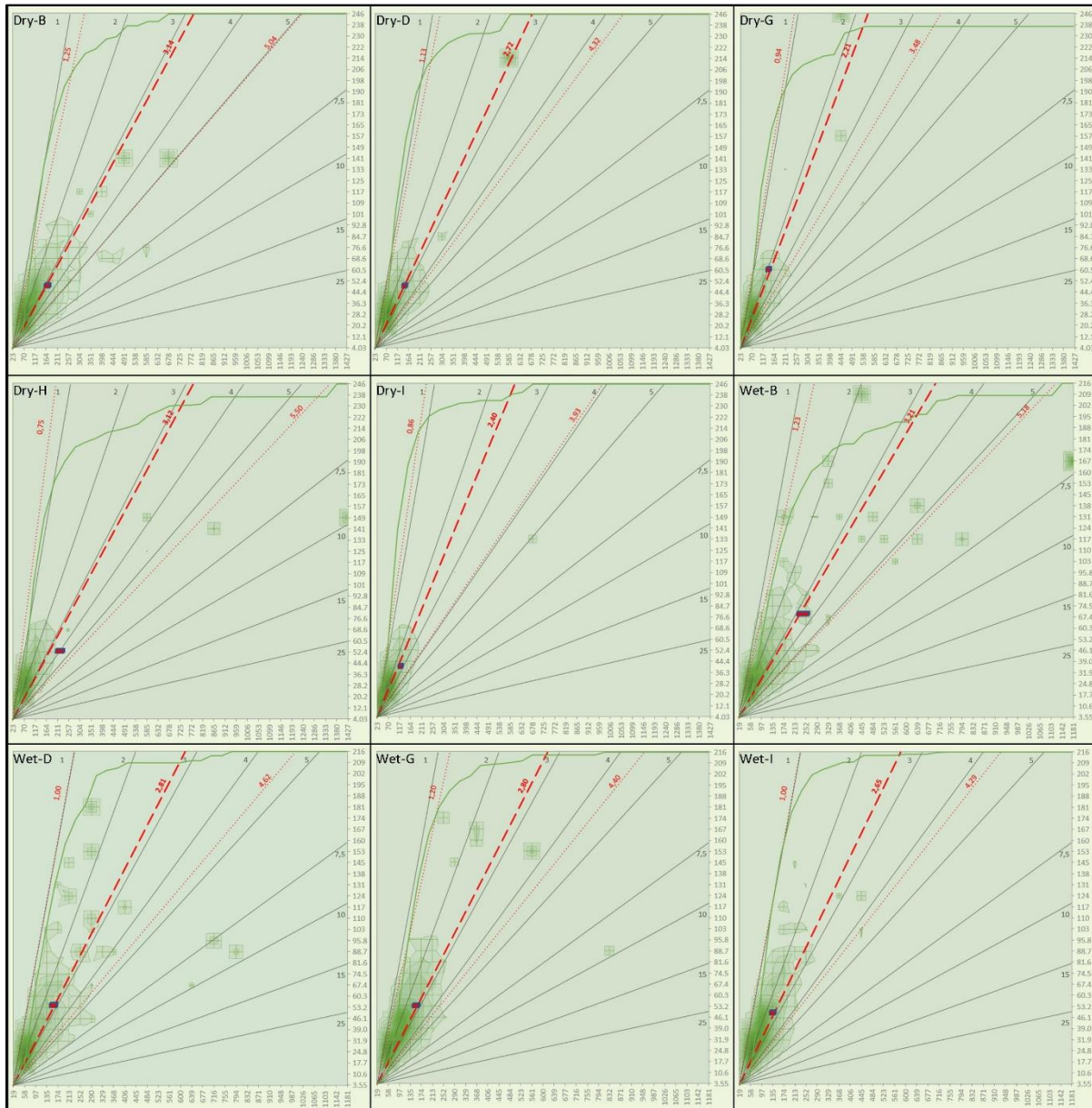


Figure 3.3.4: PSD data of the different samples (see Chapter 3.2.3) performed using Morphologi G3 and analysed using script parameterised with no minimum neighbour.

A 2-dimensional PSD is output with a graph showing the presence of particles within this grid (see Figure 3.3.4). A cumulative density function (CDF) of the particles length

is also displayed as a green curve on the graphs. The presence of a few big particles creates sudden increases in the CDF for multiple cases. For instance, 1 particle with an aspect ratio of $\alpha_p = 10$ represents 3.8% of the bed volume by itself and is isolated in the PSD grid in sample Dry-H. Another particle with $\alpha_p \approx 2$ represents 4.5% of the bed volume in sample Dry-G. These particles skew the PSD and are not considered representative of the typical particle size in the bed. To allow a liable representativeness of the PSD in the particle bed, the maximum particle sizes for the script analysis are set at $L_{max} = 600\mu m$ and $W_{max} = 150\mu m$ for both dry and wet cases. In addition, the “minimum neighbour” option is set at 2, meaning that a cell of the PSD grid containing particles must be in contact with a minimum of 2 occupied cells to be kept in the output PSD. This parameter is designed to exclude particles that are isolated on the PSD grid. The application of a minimum neighbour at 2 has excluded around 20 particles with a negligible impact on the PSD as it typically represents a volume fraction of 10^{-10} .

3.3.4 Morphologi G3

The 2D PSD graphs produced using the analysis script are superposed to present the evolution of the PSD throughout the agitation phase in an intuitive way.

The size of particles typically ranges up to $300\mu m$ long and $100\mu m$ wide before agitation in the dry case (see Figure 3.3.5). Significant particle breakage occurs as agitation is brought to the bed, which is shown by the contraction of the PSD cloud. The results for the $165min$ sample show an unexpected expansion of the PSD cloud whilst the results for $120min$ already demonstrated a significant particle breakage and decrease in size. This increase of PSD for $165min$ is not observed in the laser diffraction data (see Figure 3.3.1) which indicates that there might have been a difference in the sampling or the G3 method that has not been identified.

At the end of agitation, the particle size ranges up to $150\mu m$ long and $65\mu m$ wide, which corresponds to a loss of approximately half the particles size range.

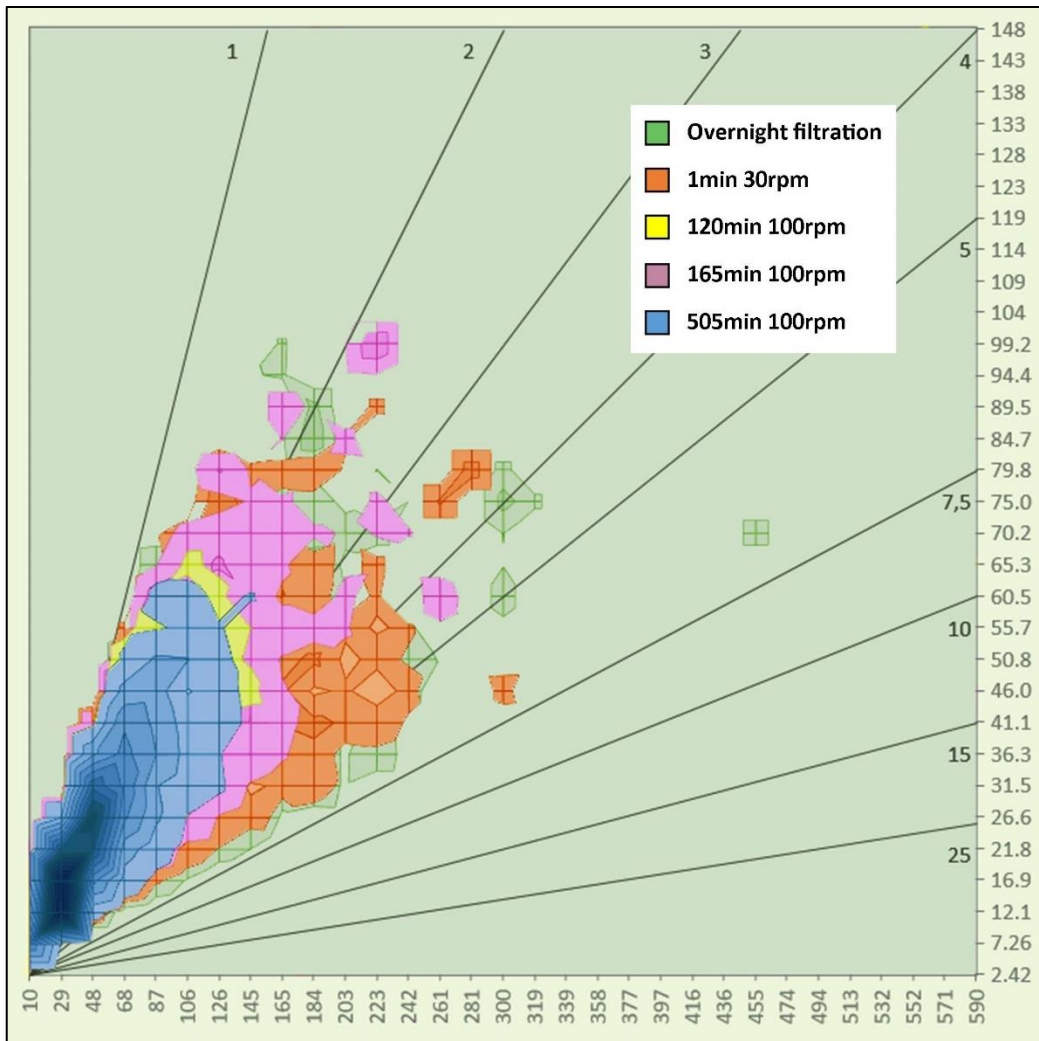


Figure 3.3.5: PSD data of the different samples of dry agitation experiment (see Table 3.2.1) performed using Morphologi G3 and analysed using script [294] parameterised with 2 minimum neighbours.

The PSD cloud obtained for the wet case is comparable to the dry case before agitation with particle size ranging on the same values of length and width (see Figure 3.3.6). Nevertheless, the contraction of the PSD cloud with agitation is not as significant with an end range of particle size up to $200\mu\text{m}$ long and $115\mu\text{m}$ wide. It confirms the observation made from the laser diffraction results where more breakage is occurring in the dry bed.

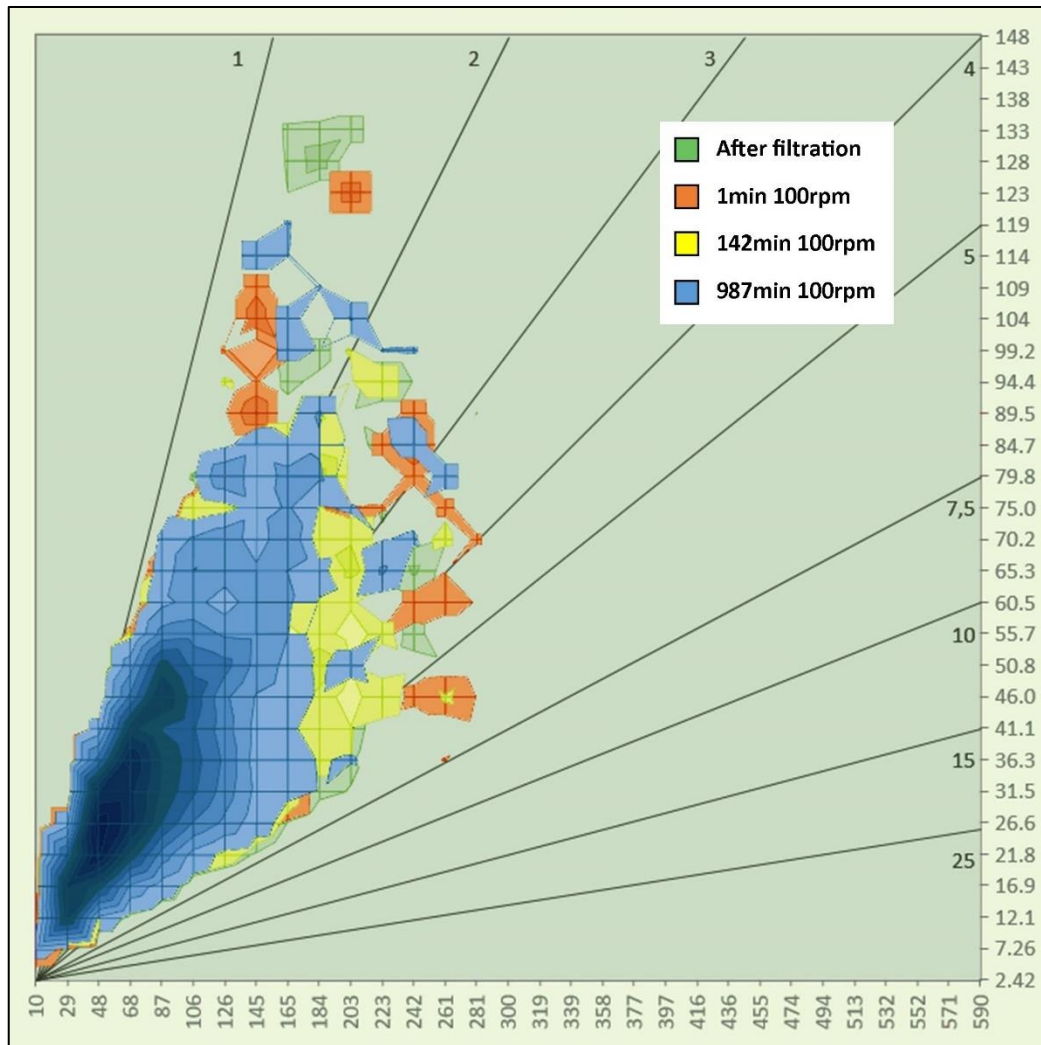


Figure 3.3.6: PSD data of the different samples of wet agitation experiment (see Table 3.2.2) performed using Morphologi G3 and analysed using script [294] parameterised with 2 minimum neighbours.

The enhanced breakage phenomenon in the dry case is also observable in the probability density functions (PDF) of particles size (see Figure 3.3.7). In both dry and wet cases, the proportion of particles with length $L > 180\mu\text{m}$ decreases. However, this breakage has the effect of narrowing the distribution and decreasing the mode of PDF in the dry case from $90\mu\text{m}$ to $30\mu\text{m}$, whilst the mode remains unchanged in the wet case at $50 - 60\mu\text{m}$. Thus, the breakage in dry conditions produces smaller fragments than in the wet case. Again, the values for 165min 100rpm sample are unexpected and are not discussed further.

The same phenomenon occurs for the particle width where the PDF mode decreases from $30\mu\text{m}$ to $15\mu\text{m}$ in the dry case. The width PDF in the wet case remains unchanged during agitation except for a little bump around $120 - 140\mu\text{m}$ in the “after filtration” sample representing 3% volume fraction for 7 particles only.

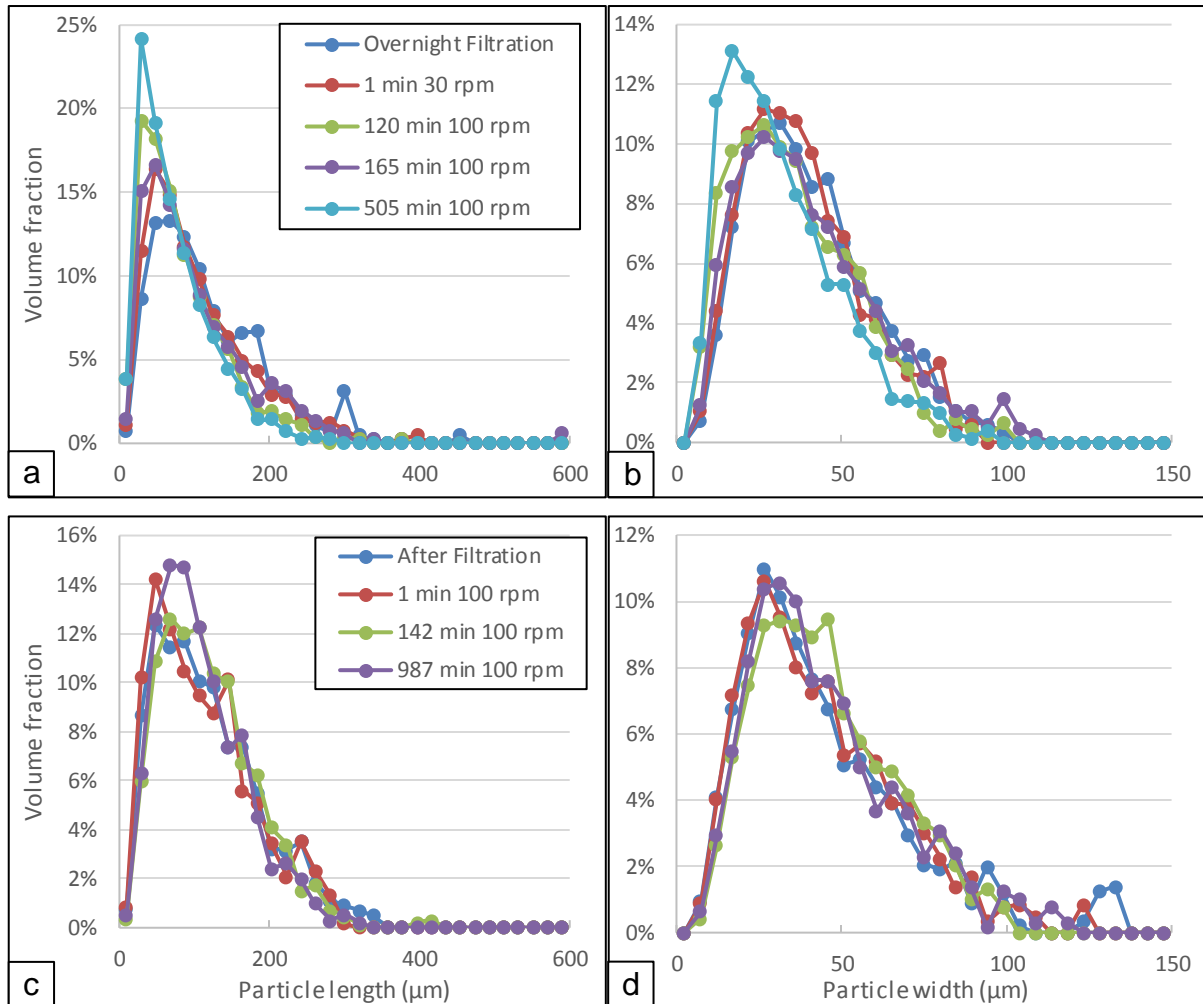


Figure 3.3.7: Particle size distributions of the different samples collected in the dry case for particle length (a) and width (b), and in the wet case for particle length (c) and width (d). The PSD data is obtained from script analysis [294].

The PDF values suggest that there are different breakage mechanisms occurring for the wet and dry cases. In both dry and wet cases, there’s a quasi-identical decrease in the volume of long particle, i.e. with an aspect ratio $\alpha_p \geq 6$, which is reduced by half, indicating a breakage of the longest particles (see Figure 3.3.8).

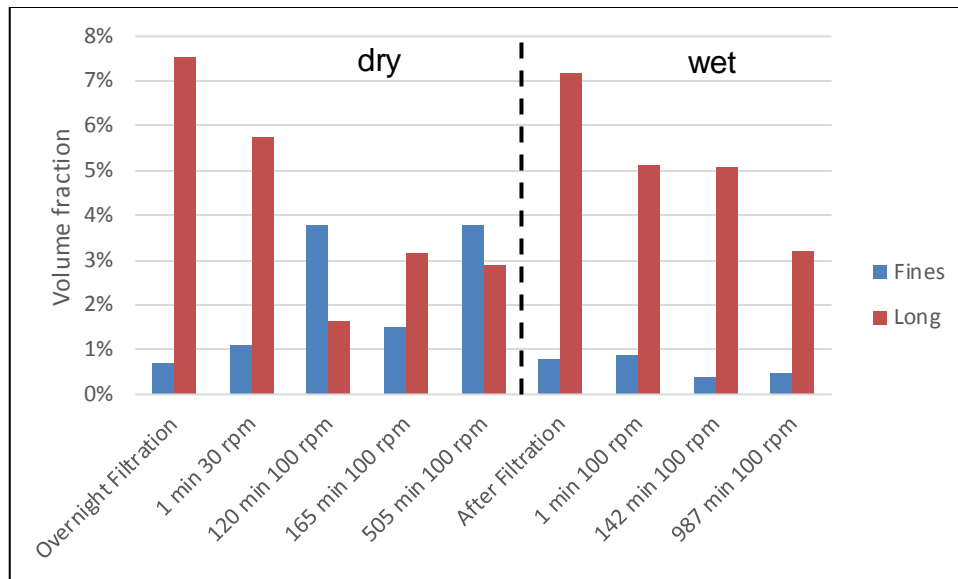


Figure 3.3.8: Volume fraction of fines ($\alpha_p = 1$, $L < 15\mu\text{m}$) and long particles ($\alpha_p \geq 6$) for the different samples collected for G3 analysis in dry and wet cases.

The volume of the fines, i.e. within the called “ $\alpha_p = 1$ ” category ($0.67 \leq \alpha_p \leq 1.5$) and $L < 15\mu\text{m}$, in the wet case remains unchanged throughout the agitation, which shows that the wet particles break preferably by fragmentation rather than attrition. Here, the liquid acts as a lubricant and reduces the probability of particles to being chopped at particle-particle contacts and decrease in size by attrition [25, 135]. The presence of the liquid also increases the weight of the bed [80] and is expected to augment the compressive force on the particles, especially towards the bottom of the bed. This increase of normal stress on the bed can facilitate the fragmentation of particles due to higher contact forces between particles.

On the contrary, the volume fraction of fines raises from 0.7% to 3.8% in the dry case indicating that an important attrition phenomenon occurred. The end volume fraction of fines is in good agreement with the reported steady state value of mass loss at 3% due to attrition in dryers [191]. The augmentation of fines matches the diminution of long particles volume fraction, however the particles with $\alpha_p \leq 6$ would also break, which indicates that the breakage of long particles is occurring by a mix of fragmentation and attrition mechanisms.

Starting here from quasi-identical volume fractions of fines and long particles, the results of agitation are significantly different, which is attributed to the action of the liquid.

These observations are confirmed by the particle aspect ratio distributions (see Figure 3.3.9), which can be output to analyse the effect of breakage on the reduction of particle elongation [191]. Indeed, the volume fraction of particles with $\alpha_p = 1$ increases in the dry case due to particle attrition and remains unchanged during the wet agitation. Inversely, the volume fraction of $\alpha_p = 3$ particles increases and reaches a steady state in the wet case, whilst it is decreasing in the dry conditions due to the combination of the two breakage mechanisms. In both cases, particles with a higher aspect ratio break and their volume fraction decreases, with more significant breakage in the dry case.

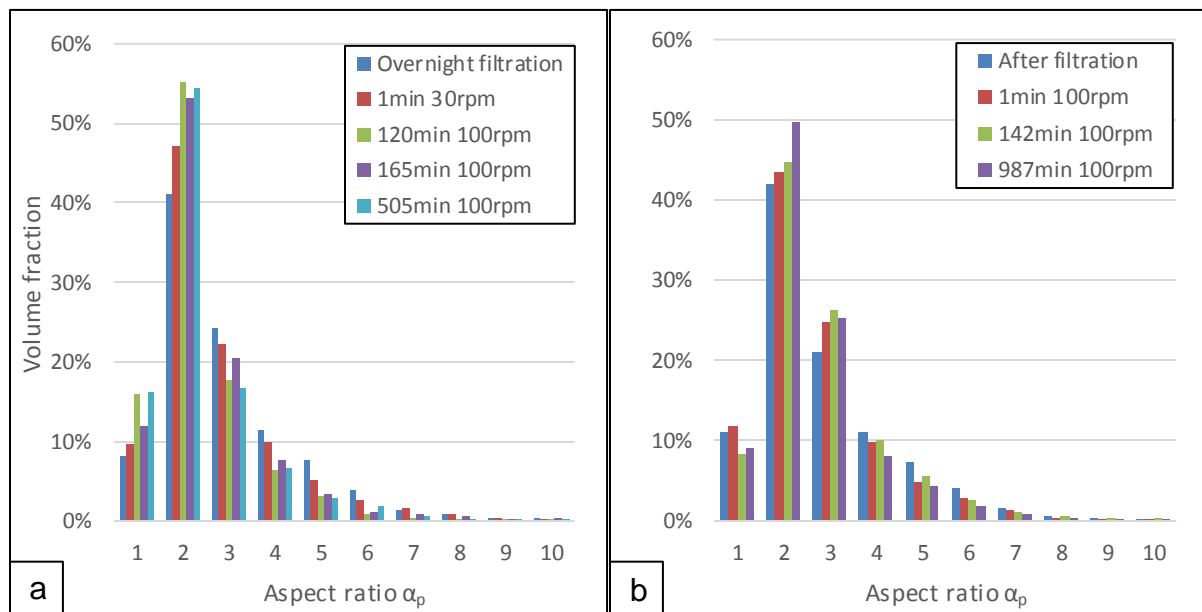


Figure 3.3.9: Probability density function of aspect ratio of the different samples during dry (a) and wet (b) agitation experiment. The data is displayed for $\alpha_p \leq 10$ (full distribution values in Appendix 14).

The effect of the first impeller rotations is also investigated by sampling the particle bed after 1min agitation in both dry (at 30rpm) and wet (at 100rpm) cases. Indeed, elongated particles are reported to mainly break during the first impeller rotations in simulations of agitated cell [1, 191]. The volume fraction of dry particles with $\alpha_p \leq 2$ increases whilst the proportion of more elongated particles decreases. A significant

change can be observed for $\alpha_p = 2$ with an augmentation of 6% in their volume fraction. The same phenomenon can be observed for wet particles with a moderate impact on the volume fractions. Indeed, the proportion of wet particles with $\alpha_p \leq 3$ increases to the detriment of more elongated ones. This result indicates the breakage of particles in the early stage of agitation, with a predominant effect in the dry case. It is noted that, contrary to the wet case, the impeller wasn't positioned towards the bottom of the AFD during filtration and the agitator was inserted into the dry bed after overnight filtration during 8 impeller rotations (see Chapter 3.2.3.1). Introducing the impeller into the bed may have crushed the particles and could be an explanation for the important breakage phenomenon observed between "overnight filtration" and "1 min 30rpm". As the particle bed remained static during drying, it is also possible that solid bridges have formed by crystallisation of the remaining dissolved LGA, which are the strongest type of bonding [63] and would have increased the yield strength of the bed that needs to be overcome to initiate the flow [112], promoting particle breakage. Nevertheless, these results need to be taken with care as no breakage phenomenon of this importance is observed in the laser diffraction data for both dry (see Figure 3.3.1) and wet cases (see Figure 3.3.2), even though laser diffraction is not as sensitive to a change in aspect ratio. Moreover, the nitrogen flow during filtration and drying was at room temperature, so the formation of solid bridges has not been promoted by a temperature effect [8]. It is therefore assumed that no solid bridge has formed in the dry bed. Besides, an experimental error needs to be considered and more agitation experiments are necessary to confirm the results obtained. Also, the use of the script with the "minimum neighbour" parameter may introduce a bias to the analysis as it casts out existing particles for their lack of representativeness on the PSD. These particles are present in the bed and are usually voluminous, which could influence further samples analysis if these particles break and if their fragments/fines are included in the analysis with the applied parameter. Elongated particles are also known for their ability to align [14] along the flow stream in sheared systems [188]. This phenomenon affects the flow and particle velocity [188] due to their higher mass moment of inertia restraining their rotation [149, 205], densifies the bed, and reduces the particle sensitivity to bending stress when stacked lengthwise with liquid bridges [9]. Indeed, at this level of moisture content, the wet bed is in funicular regime of saturation [99] and the forces in the particulate network is mainly due to the forces of their liquid

bridges [62, 63, 65, 66] which can be impacted by the morphology of the liquid bridges [82-85]. This effect is expected to take place in our experiment, though its impact on particle breakage is out of scope in this study. It is also expected that particle segregation takes place as a function of size whilst breakage occurs [191], with smaller particles migrating towards the bottom of the bed. With agitation, the location of highest breakage rate changes from the bottom of the bed [16] at the beginning where the load is the highest to the upper region of the bed where the most elongated particles are as they need less force to be broken [191]. Additionally, a greater radial distance increases the breakage rate of particles as they are experiencing a higher strain rate [1, 108].

Finally, the fragmentation is reported as the main breakage mechanism of elongated particles [1, 26] and mainly occurs along the shortest axis of the crystals [52] due to the predominance of geometric effect [27] increasing their bending stress [1]. As breakage occurs, the aspect ratio of particles is reduced which decreases their breakage rate as they need a greater load to be broken [55, 191]. It is confirmed by the results that elongated particles break then more rapidly than shorter ones [8, 9, 53-55] in both cases by fragmentation. The particle breakage is also affected by the presence of moisture content. There is however no consensus in the literature on whether the presence of liquid is promoting [1, 8, 16, 156] or reducing [1, 8, 9] particle breakage in a particle bed. The analysis of PSD data reveals that particle attrition is almost non-existent in the wet bed due to the lubrication effect of the liquid [1]. The weight of the liquid increases the normal stress applied on the particles which facilitates their breakage by fragmentation. The present work shows an enhanced breakage phenomenon in a dry system compared to wet. The effect of different moisture contents is not investigated here, however it can be anticipated that an equilibrium point exists where the particle breakage is minimised by reducing the liquid volume, and hence the normal stress, whilst maintaining the lubrication effect. The reduction of moisture content would also decrease the number and strength of liquid bridges [102], reducing the cohesive forces between particles and affecting the behaviour of the particulate system [113, 120-125, 156].

3.4 Conclusion

The impact of agitation on the breakage of β -LGA crystals is investigated for both dry and wet conditions.

The particles break mainly by fragmentation in the wet case and from both fragmentation and attrition in the dry case. The dry environment promotes attrition and the production of fines, which is attributed to the increased friction between particles compared to the wet case. Indeed, the moisture content creates liquid bridges at inter-particle contacts and has a lubrication effect reducing the extent of attrition. The increased weight of the wet particle bed due to moisture content is expected to have augmented the normal stress on particles and quantifying this effect would require an inductive study varying the liquid volume in the bed.

The quantification of breakage in situ allows the validation of the predictive breakage model presented in Chapter 8.

4 The Breakage Strength of Elongated Organic Crystals

4.1 Introduction

The work initiated by Hallac in his Master's report [295] on the breakage of elongated crystals is continued. In the MSc degree part of the integrated PhD program, Hallac introduced a novel 2-point method to assess the yield strength of β -LGA crystals using Atomic Force Microscopy (AFM).

In this chapter, further crystal breakage are performed and the measurement of crystals dimensions on microscopy images performed during the MSc is refined. Overall, 52 crystals are broken for the present analysis and are listed in Appendix 5: crystals no 1 to 50 have been broken during the MSc, and crystals no 51 to 52 are broken during the PhD component of the integrated program. A completely new data analysis has been performed with the new dataset and a study of the crystals Young's modulus has been added. Among the figures in this chapter, only Figure 4.3.2 is also present in the Master's report, and metric indications have been added to it.

The study presented in this chapter has been published [18] and beam bending simulations in Chapter 4.3.4 were performed by the co-author Dr. Fragkopoulos.

An assessment of the breakage strength and the Young's modulus of a sample of β -LGA crystals is performed in this chapter. The crystals are produced following the same crystallisation method as for the lab-scale AFD experiments in Chapter 3, giving consistency for the further cross-validation of results in the following chapters.

4.2 Background Context

The majority of pharmaceutical and fine chemical active ingredients consist of high aspect ratio particles such as needles and plates. Such highly elongated materials are significantly prone to undesired breakage during manufacturing processes such as filtration [26] and drying [26, 296] where crystals are subjected to significant forces by the processing equipment. Changes in particle size distribution can significantly affect downstream processing characteristics of active pharmaceutical ingredients (APIs)

[126], and can unintentionally alter critical quality attributes, affecting patients [297]. For instance, in an agitated pressure filter dryer, high aspect ratio crystals form an open structure in which crystals are deposited on top of each other. In such structure, forces applied by pressurising the equipment or rotation of the agitator are conveyed via the contact points between two crystals touching each other. High aspect ratio particles have multiple contact points along their long axis which leads to crystal bending. Undesired breakage occurs when the incurred internal stress is higher than the critical strength of a crystal [298].

The fundamental mechanical properties data to underpin a mechanistic postulate such as the one described above is largely missing for organic crystalline materials. Yet, mechanical properties such as Young's modulus E , tensile strength σ_c and the critical stress factor K_{IC} are fundamental to linking the impact of forces at macro or process scale to the behaviour of crystals at the micro scale. This is highly relevant for processes such as crystallisation, filtration, drying, granulation, milling and compaction as crystals are exposed to significant force.

Organic crystals are usually formed by solvent crystallisation as small crystals, typically with high aspect ratios (e.g. needles, plates). As these materials are not typically used for construction, measurement data has lagged behind compared to inorganic materials and polymers.

Table 4.2.1: Literature values of mechanical properties for organic materials.

Material	E (GPa)	σ_B (MPa)	K_{IC} (MPa m ^{0.5})	l_c (μm)	Method [ref]
phenylbutazone	3.33	6.8	0.14	424	PE [34, 126]
ibuprofen	5.02	7.71	0.104	182	PE [34, 126]
sulfadiazine	7.70	8.04	0.148	339	PE [34, 126]
tolbutamide	5.22	9.6	0.113	139	PE [34, 126]
caffeine (anhydrous)	8.73	9.93	0.261	691	PE [34, 126]
aspirin	7.45	11.89	0.156	172	PE [34, 126]
theophylline (anhydrous)	12.93	13.33	0.264	392	PE [34, 126]
paracetamol		13.38	0.115	74	PE [34, 126]
α -lactose monohydrate	24.06	18.33	0.345	354	PE [34, 126]
sildenafil citrate	13.9 \pm 1.5		0.02 \pm 0.01		NI [299]

Chapter 4: The Breakage Strength of Elongated Organic Crystals

pharma compound c	14.9 ± 1.3		0.05 ± 0.01		NI [299]
pharma compound b	7.6 ± 0.5		0.04 ± 0.01		NI [299]
pharma compound a	2.9 ± 0.4		0.06 ± 0.00	(15-70)*	NI [299]
voriconazole	3.7 ± 0.4				NI [299]

* range depending on applied load; PE: porosity extrapolation, NI: nano-indentation

Roberts et al. [34, 46] formed macroscopic square bars with varying porosity and, by extrapolating to zero porosity, determined mechanical properties of organic materials, summarised in Table 4.2.1. The observed breakage strengths varied between $\sigma_B = 4$ to 25 MPa and the Young's modulus between 3 and 24 GPa . They also measured the critical stress index, an important measure to describe the breakage of crystals under high impact [300], and reported $K_{IC} = 0.1$ to $0.35 \text{ MPa} \cdot \text{m}^{1/2}$. Under the assumption that the surface energy is significantly less than the energy required to plastically deform the material near the tip of a crack (J_{IC} , the toughness), the breakage strength σ_c and K_{IC} are correlated by:

$$\sigma_B = \frac{K_{IC}}{\sqrt{l_c}} = \sqrt{\frac{E J_{IC}}{l_c}} \quad 4.2.1$$

Where l_c is the average flaw length (or crack length). Table 4.2.1 gives the crack lengths for the materials they studied, interestingly, the crack lengths are similar to typical width and/or thickness of crystals found after crystallisation ($5 - 400 \mu\text{m}$).

Ast et al [301] reviewed the experimental approaches to measure fracture toughness and identifies three key methods: (i) Nano indentation, (ii) micro pillar splitting (not discussed in this paper) and (iii) micro cantilever testing. Nano-indentation is widely used to assess mechanical properties, typically K_{IC} , E , and hardness. Nano indentation assesses these properties on, and close to, the surface of the solid. An indenter, the apex of a small pyramidal shape, is used to penetrate the crystalline material leading to the formation and propagation of cracks. The observed crack length and propagation can consequently be employed to determine the fracture toughness K_{IC} , and Young's modulus E , but not the breakage strength of APIs. Very detailed work on Sucrose [302] shows that the elasticity is dependent on the phase of the crystal investigated as may be expected from crystallographic considerations. This method gives similar values for the Young's modulus of organic molecules [299] to those

obtained by extrapolation of porosity and excipients (see Table 4.2.1). The values of the critical stress index are however an order of magnitude lower when measured by nano-indentation compared to porosity extrapolation. Nano-indentation experiments have also been performed using the tip of the Atomic Force Microscope's cantilever (AFM) [303]. Relevant results are $E \approx 2.5\text{GPa}$ for polymer films [304] and the hardness of a number of organic materials [305].

The micro cantilever method requires the construction of the pillar/beam using lithographic or micro machining methods. In 2000, Namazu et al. described a three point bending test using AFM to determine tensile (breaking) strength and elastic modulus of Si [49]. This work showed both elasticity and breakage strength could be measured for well-defined lithographically engineered silicon structures.

Nano-indentation systems have also been used to conduct 3-point bending experiments of Schiff bases [306]. These materials have a very low Young's modulus, ($E = 0.190$ to 0.880GPa) which was attributed to the presence of weak hydrogen-halogen and halogen-halogen interactions which are easily broken and reformed, thus allowing the molecules to easily slip over each other. Plastic deformation is however prevented by interlocking of crystallographic planes so as to hinder long range molecular movement.

In this study, we present an alternative *single crystal* cantilever method to measure micro-mechanical properties of single organic materials, which are often unstable at their melting point, making it difficult to prepare the homogeneous large-scale samples used in mechanical property testing (e.g. beams, dumbbells), nor are they easily manipulated using lithographic methods commonly used on inorganic substances.

4.3 Materials and Methods

4.3.1 Materials

4.3.1.1 Organic Crystals

The needle-shaped beta polymorph of glutamic acid was the selected organic material. A 99% purity glutamic acid powder provided by Sigma-Aldrich was re-crystallised following the methodology described in Shier's paper [293]. The glutamic

acid powder was dissolved in deionised water and heated up to 70°C . The solution was cooled down to 60°C and previously crushed β -LGA seed material was added to the solution. The solution was held for 2 hours and then slowly cooled down to 20°C at approximately $3.5^{\circ}\text{C}/\text{h}$ allowing the crystals time to grow. The β -LGA crystals produced have of a length in the order of 0.1 to 1 mm (see Figure 4.3.1).



Figure 4.3.1: Light microscope image of the re-crystallised β -LGA crystals.

4.3.1.2 Metallic Support

A 303 stainless steel metallic piece of $5 \times 5 \times 2 \text{ mm}$, small enough to fit in the AFM stub, was milled using a DMG 40evo machine with a milling cutter of 0.8 mm diameter to give three corridors (1 mm width each and with 0.5 mm distance between each other) in both sides of the piece (see Figure 4.3.2). Each corridor was milled at different depth (0.3 mm , 0.6 mm and 0.9 mm) allowing the measurement of the dimensions (height, length, and width) of three crystals per face – 6 crystals in total (see Figure 4.3.3) –

with lateral and top-down microscopy. The rectangular corners of the corridors ensured about 90° ($\pm 10\%$) angle between the crystal (cantilever) and the steel support. The steel's hardness guarantees that the crystals' breakage strength is not affected by movement of the support.

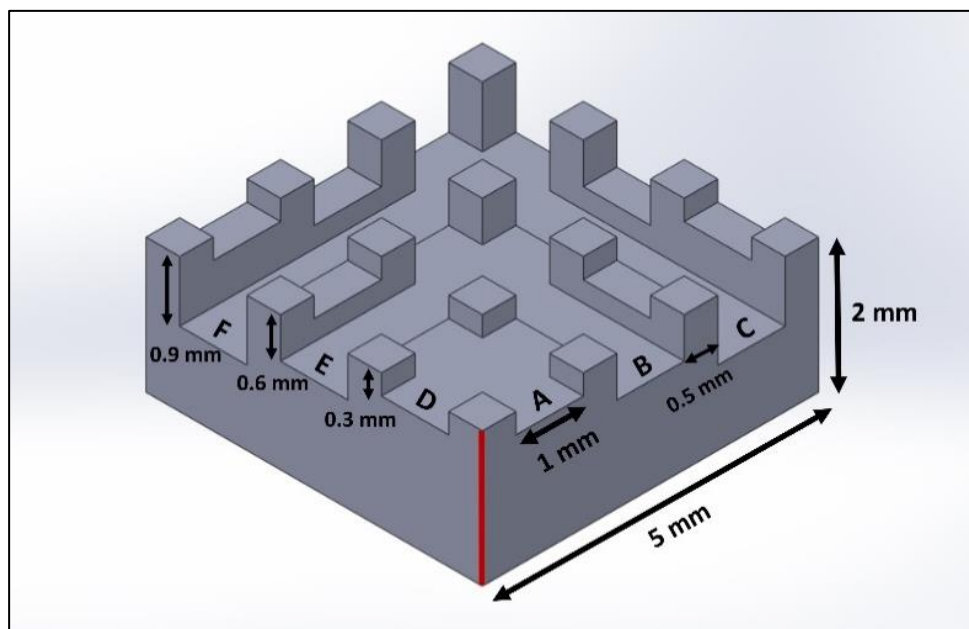


Figure 4.3.2: Metallic support: the red corner is placed at the centre of the AFM stub. 6 crystals can be mounted as cantilevers on positions A to F.

4.3.1.3 Glue

Industrial superglue (Everbuild products industrial super glue gp CYN50) composed of ethyl-2-cyanoacrylate was mixed with acetone in a 1:5 (glue:acetone) volume ratio, providing sufficient bonding strength and not affecting the physical and chemical properties of the β -LGA crystals [307, 308]. The two liquids are miscible with each other, and the reduced viscosity of the resulting glue mixture allows an easier application onto crystals.

4.3.2 Preparation

4.3.2.1 Crystal Mounting

The designed metallic piece was glued on the AFM magnetic stub in such a way so that the corner with the highest corridor height was placed at the centre of the stub (see Figure 4.3.3). Beta-LGA crystals were carefully dropped on the metallic piece to minimise potential fragmentation. The higher elongated and better-shaped crystals were manoeuvred with fine tweezers within each corridor towards its edge as cantilevers. Over the 52 crystals studied, 3 were lying on their sides (crystals no 26, 32 and 47 in Appendix 5): their measured height is greater than their width.

About $1\mu\text{L}$ glue mixture was dispersed on each corridor using an Acura 825 micro-dispenser with $0.1\text{--}1\mu\text{L}$ micropipette tip. The glue spreading was carefully controlled to avoid any movement of the crystals due to capillary flow, and to prevent the spreading of the glue past the metallic support edge and the subsequent coating of the cantilever part of the crystal.

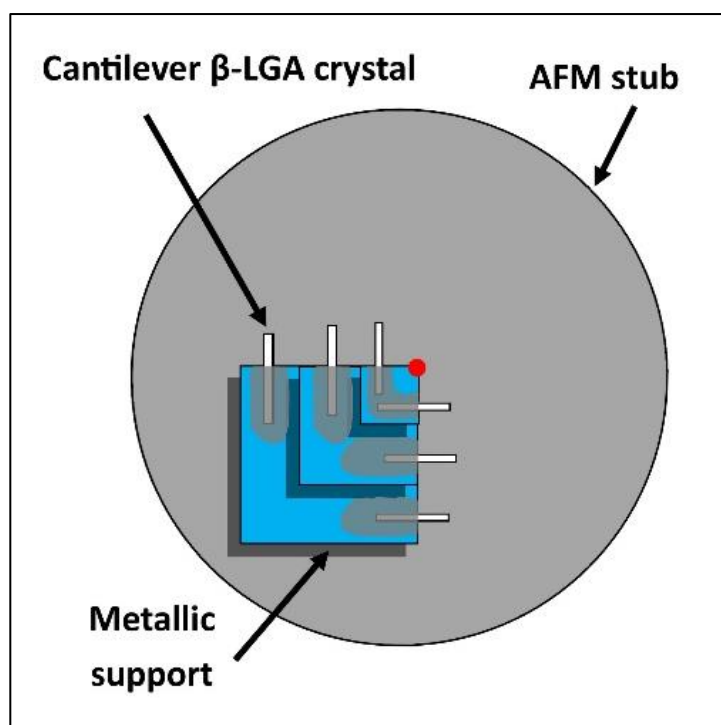


Figure 4.3.3: AFM magnetic stub. The corner of the metallic support highlighted in red is positioned at the centre of the AFM stub.

4.3.2.2 AFM Calibration

A Bruker Multimode 8 atomic force microscope using the stiffest Bruker RTESP-525 AFM probe model was used to enable force application onto the organic beta-LGA crystal cantilever. A Bruker Sapphire-12M sample was used for the AFM probe calibration; the deflection error sensitivity of the laser sensors was estimated to be equal to $45\text{nm}/V$ ($\pm 50\%$) using the gradient of a ramp curve (small deflection) on the sapphire's hard surface (see Figure 4.3.4) [309]. The probe's spring constant k_p was taken to be the manufacturer's value of $200\text{N}/\text{m}$.

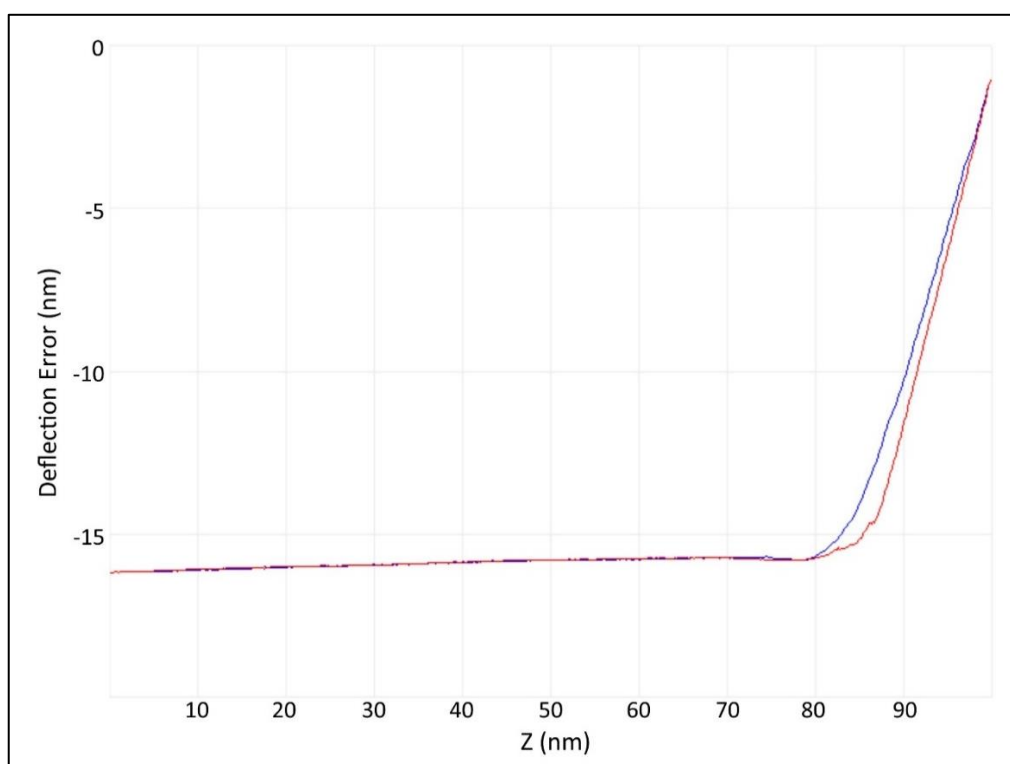


Figure 4.3.4: Ramp curve on Bruker Sapphire-12M used for the AFM probe calibration.

4.3.2.3 Sample Cleaning

After each breakage experiment, the metallic piece was washed in an acetone bath followed by a 30min ultrasonic bath wash (James SONIC 3MX) to remove the glue mixture and the crystals.

4.3.3 Measurements

4.3.3.1 Crystal Dimensions

The macro-system light microscope Motic SMZ-168 with a built-in AxioCam camera (ERc5s) was used here for the observation of the crystals. The cantilevers' dimensions (length, width and height) were measured using the AxioVision 7 software (see Figure 4.3.5). The crystals were considered as cuboids.

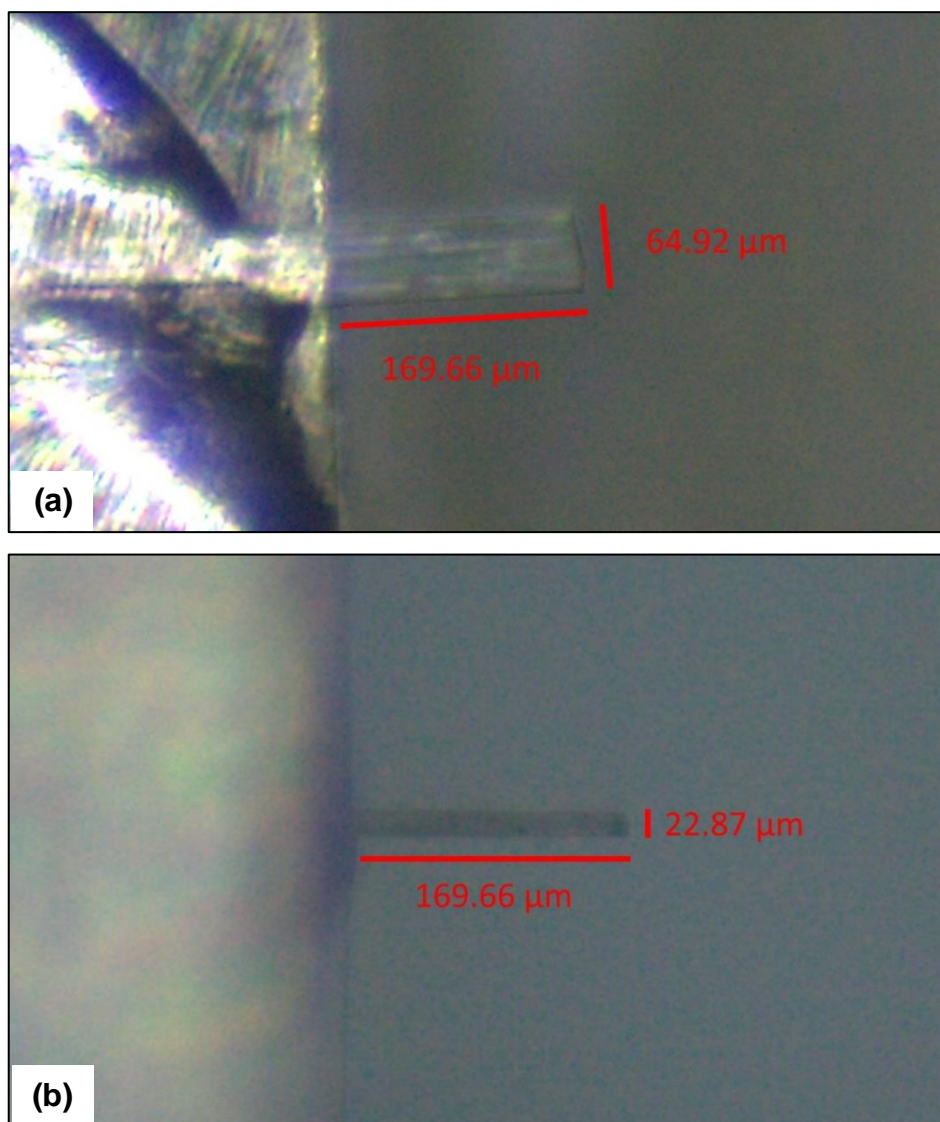


Figure 4.3.5: (a) Top and (b) lateral views of a mounted crystal (see No 38 in Appendix 5). The image was produced using a light microscope at $\times 5$ magnification.

4.3.3.2 Force Calculation

With the prepared stub in the AFM, the AFM probe was engaged at the edge of the crystal cantilever (see Figure 4.3.6).

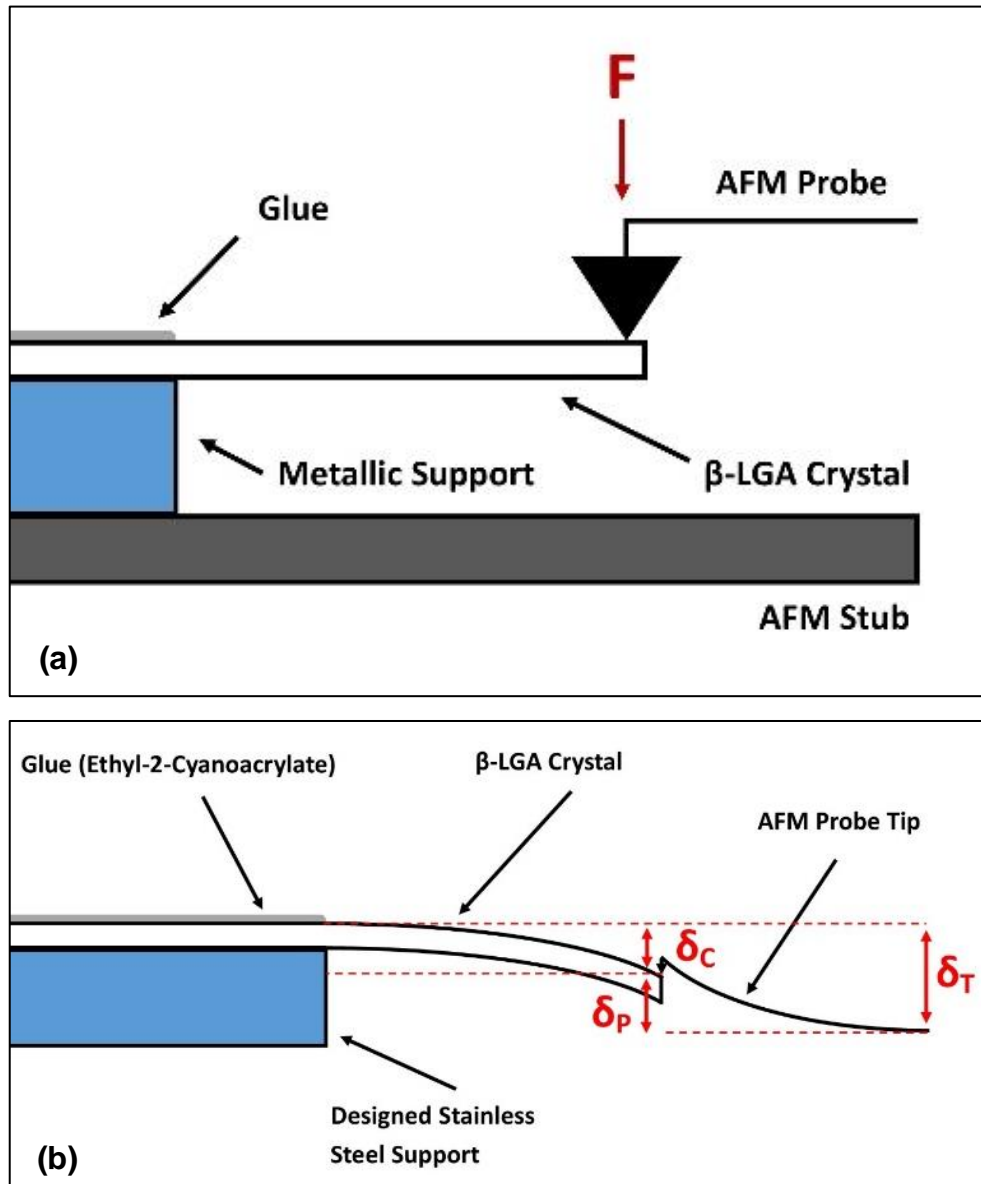


Figure 4.3.6: Schematic representation of (a) the force application on the β -LGA cantilever and (b) the AFM probe and β -LGA cantilever deflections.

A ramp curve was performed on the cantilever's edge to determine the system (probe & crystal) spring, k_T ; the system spring was equal to the gradient of the loading curve (see Figure 4.3.7).

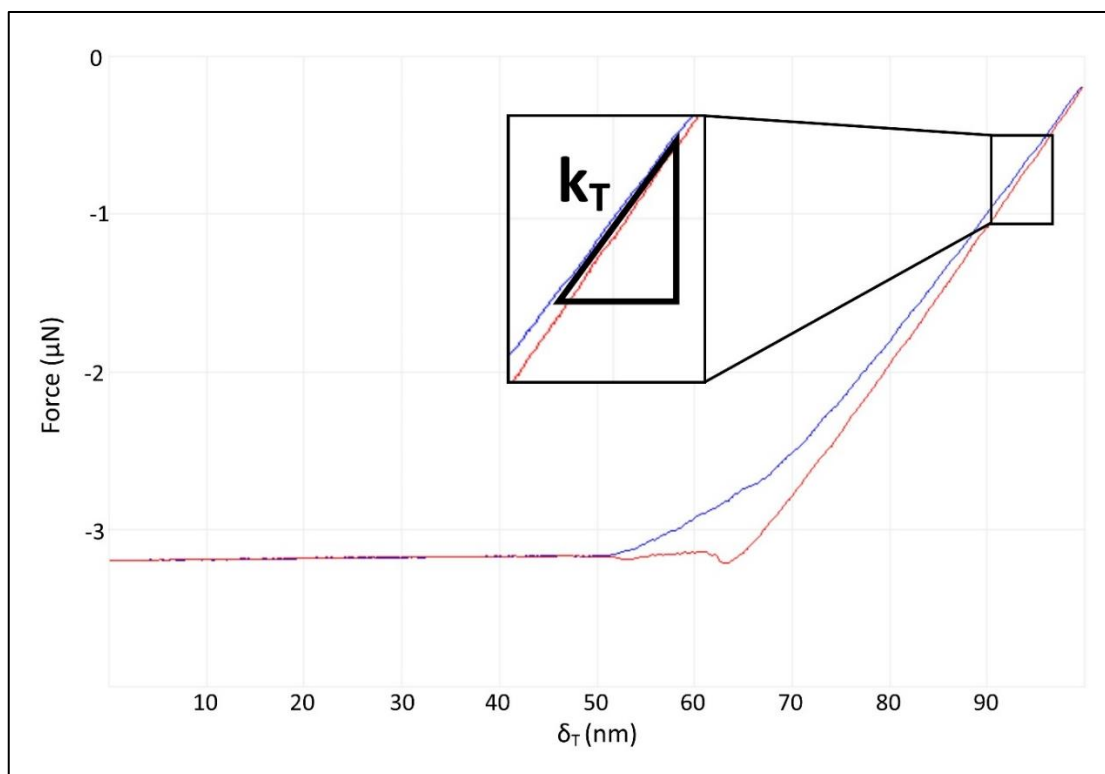


Figure 4.3.7: Ramp loading (blue)/unloading (red) curve of a Bruker RTESP-525 AFM probe engaged on the beta-LGA cantilever. The system spring, k_T , is equal to the gradient of the loading curve ($k_T = \text{Force}/\delta_T$).

The AFM step motor was then used to apply a load at the crystal's edge by lowering the AFM probe step-by-step in a quasi-static way until crystal breakage occurred (see Figure 4.3.8). No significant indentation of the AFM tip into the glutamic acid crystal has been observed, and it is therefore assumed the error due to deformation at the AFM tip is negligible.

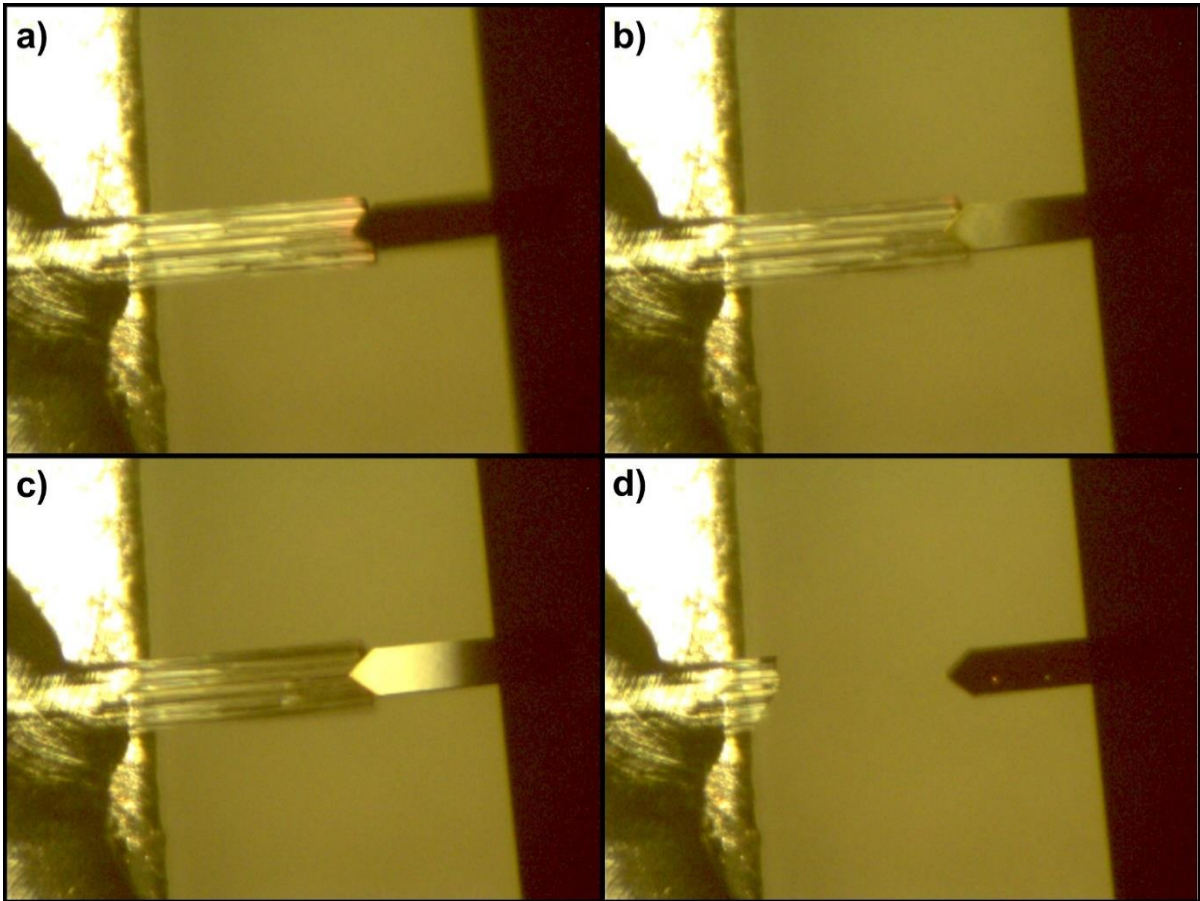


Figure 4.3.8: Top view of the AFM probe engagement at the tip of the glued crystal at different step motor deflections: a) 0 steps, b) 40 steps, c) 60 steps and d) 63 steps (when crystal breakage occurred).

β -LGA was considered here as linear-elastic material (based on the elastic nature of similar organic materials [306]) and consequently, the β -LGA crystal cantilever was considered to have a linear spring. The applied force was obtained using Hooke's law [310]:

$$F = k_c \cdot \delta_c \quad 4.3.1$$

where F is the applied force (in m), k_c the crystal spring (in $N \cdot m^{-1}$) and δ_c the deflection of the crystal (in m). The crystal spring was calculated by (see derivation in Appendix 20):

$$k_c = \frac{k_p \cdot k_T}{k_p - k_T} \quad 4.3.2$$

here k_T is the system spring (in $N.m^{-1}$) and k_P the probe's spring constant. The deflection of the crystal, δ_C , was expressed as (see derivation in Appendix 21):

$$\delta_C = \delta_T \cdot \frac{k_P}{k_P + k_C} \quad 4.3.3$$

With δ_T is the step motor deflection (in m) given by:

$$\delta_T = n_{steps} \cdot S_m \quad 4.3.4$$

n_{steps} is the number of the step motor steps and S_m is the deflection per step. The deflection for 9 motor steps was measured to be $4.2\mu m$ making $S_m = 0.466 \mu m/step$.

4.3.3.3 Broken Crystal Measurement

The beta-LGA organic crystals were not identical and the position at which crystal breakage occurred was different for each crystal. The length of each crystal's broken part, L_B , was calculated by (see Figure 4.3.9):

$$L_B = L - L_A \quad 4.3.5$$

where L is the total crystal cantilever length (in m) and L_A the length of the crystal's remaining part (in m), which was measured using the light microscope after each breakage event (see Figure 4.3.10).

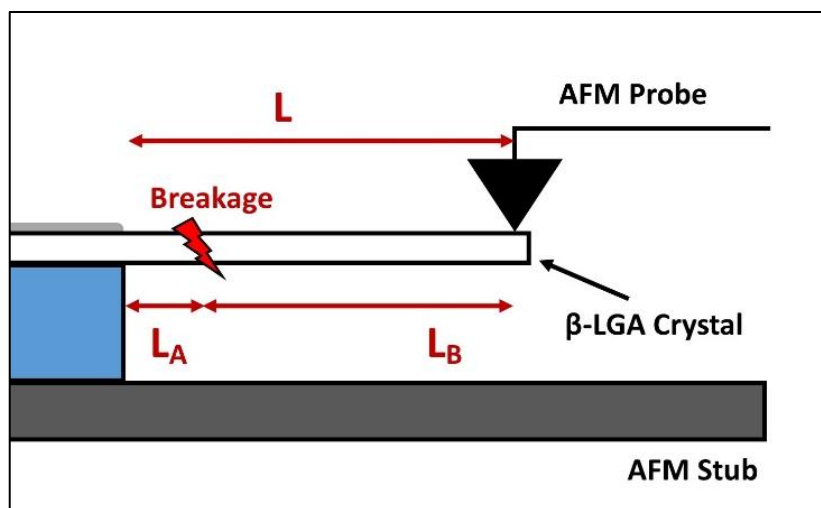


Figure 4.3.9: Schematic representation of the crystal length before and after breakage.

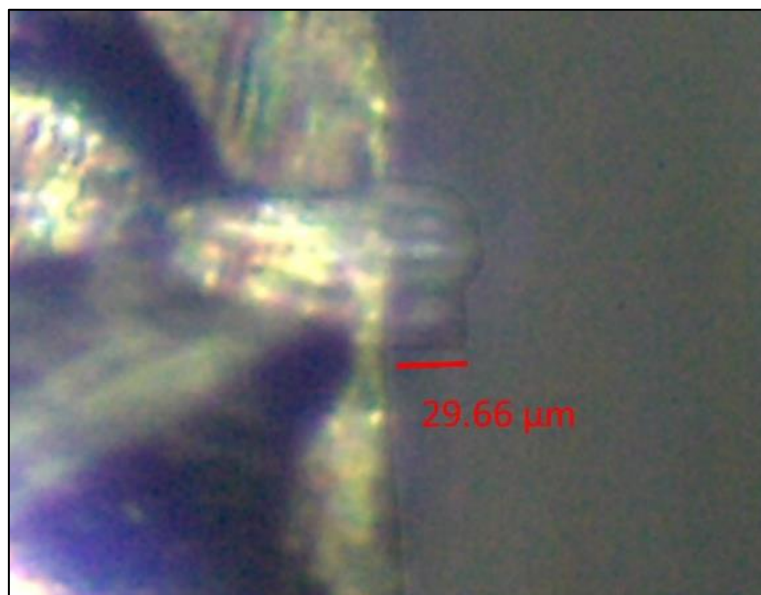


Figure 4.3.10: Top view of the crystal after breakage. The image was produced using a light microscope at $\times 5$ magnification.

4.3.3.4 Mechanical Properties

Having the individual beta-LGA crystal dimensions at hand, one can calculate the Young's modulus, E , using [311]:

$$E = \frac{4 k_c L^3}{w h^3} \quad 4.3.6$$

w is the crystal's width (in m) and h the crystal's height (in m). Note that E is based on forces applied by the AFM directly and k_c results from the measured force ramp (see Figure 4.3.4 and Equation 4.3.2).

The breakage strength, σ_B , was estimated using a derivative from the Euler-Bernoulli beam theory [26, 38]. For a rectangular beam:

$$\sigma_B = F_B \frac{6 L_B}{w h^2} = \frac{n_{steps} S_m k_p}{\left(1 + \frac{k_T}{k_P - k_T}\right) \left(\frac{k_p}{k_T} - 1\right)} \frac{6 L_B}{w h^2} \quad 4.3.7$$

where F_B is the applied force that leads to crystal breakage (in N). The breakage force was calculated using Equations 4.3.1 to 4.3.4 and the total number of motor steps that led to crystal breakage. The length of each crystal's broken part, L_B , was used here to calculate the stress on the breakage site of the crystal.

4.3.4 Beam Bending Simulations

The linear elastic material solid mechanics model, available in COMSOL structural mechanics suite, was used here for crystal bending simulations. The model was tested against literature data of bending of crystal silicon [49], and then applied to cuboid crystals of high aspect ratio, fixed at the bottom face (see Figure 4.3.11).

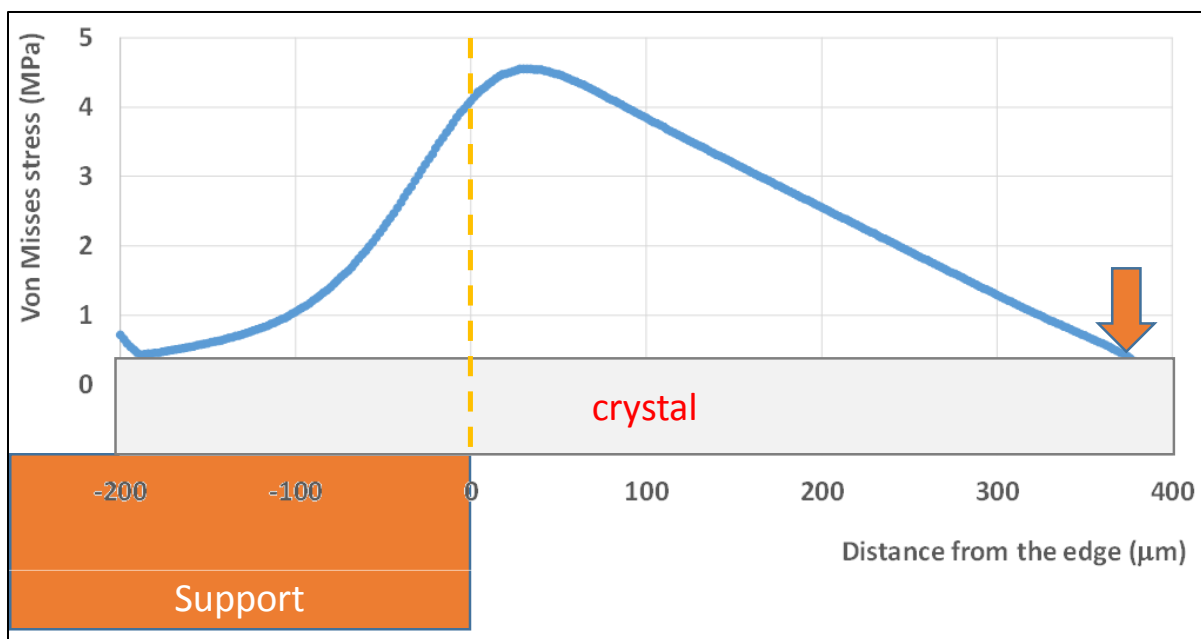


Figure 4.3.11: Predicted von Mises stress along the crystal arc length. The crystal is fixed on a support and the force applied $\sim 375\mu\text{m}$ from the edge of the support.

4.4 Results and Discussion

4.4.1 Preliminary Observations

In this study, 52 crystals were broken. More than 50% of the crystals were found to break close to the fixed point (within a distance equal to 10% of their length). The crystals tend to break some distance from the support and the glue, which indicates that the gluing process has not affected the strength of the crystals. Simulation of the crystal bending stress across a line boundary at the top of the beam (see Figure 4.3.11) was found to reach its maximum value at 8% of the distance between the edge of the support and the location where the force is applied.

The descriptive statistics of the obtained breakage strength and Young's Modulus values are summarised in Appendix 6 (Appendix 5 gives the values for each crystal). The mean value of Young's modulus equals 3.08GPa , which compares well to the Young's modulus predicted for organic molecules using a crystal modelling program [312]. Namazu et al. [49] use a three-point bending test on Si beams using AFM to apply the force and found a consistent value for the Young's Modulus across different

size beams (169.9GPa , inorganic materials have typically much higher Young's modulus than organic crystals). Taylor et al. [299] observed a standard deviation of 14% in the Young's modulus from nano-indentation for pharmaceutical materials. Our study finds the Young's modulus varies randomly from crystal to crystal with a wide variation of 85% i.e. $0.163 - 12.4\text{GPa}$ (see Appendix 6).

Comparing the data from different AFM tips shows that different crystals behave differently on the same tip, and the crystal-to-crystal variation appears randomly spread over the tips, eliminating tip fatigue or tip to tip performance variations as a cause of the distribution (see Figure 4.4.1).

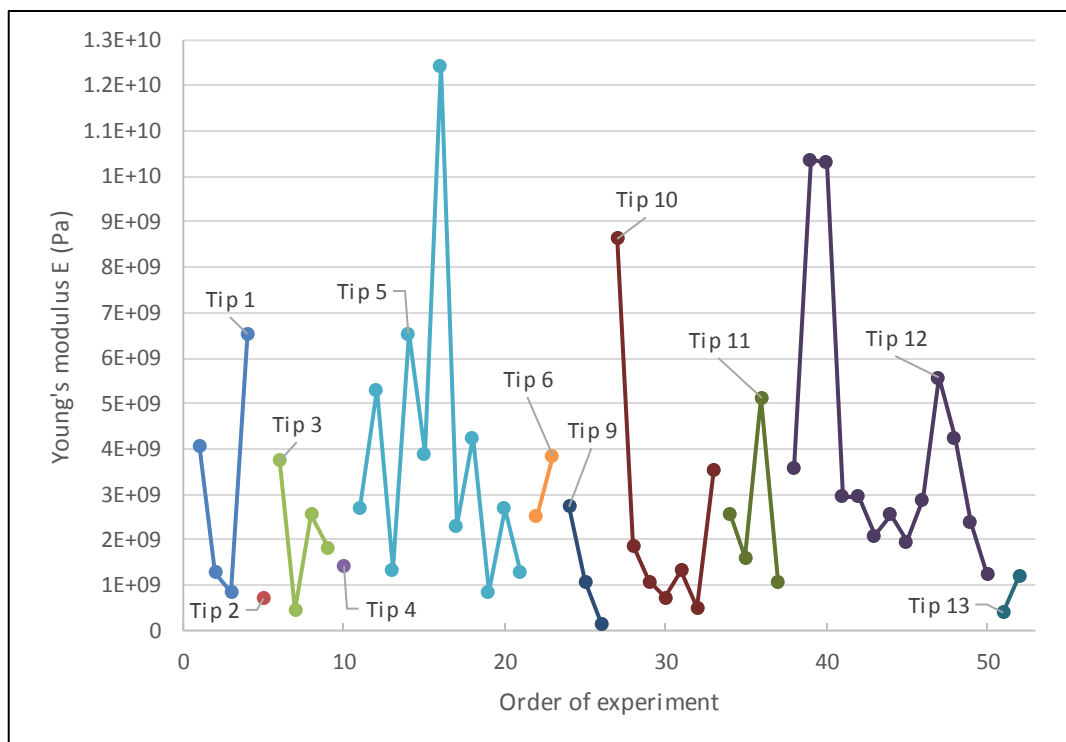


Figure 4.4.1: Crystals Young's Modulus E values against the associated probe and order of usage (individual data can be found in Appendix 5).

The quality of the glue joint that fixes the crystal on the support is a second cause of variability. Elasticity measurements on crystals in runs where crystals were bent and then returned to the rest position showed the spring constant and thus the Young's modulus varied less than 10% (10 tests on the same crystal with increasing extend of bending). This is indicative of a good joint but does not exclude the fact that the observed elasticity could be the result of the combined glue and crystal elasticity. However, it is interesting that Roberts et al. [46] observed the average crack length to

be of the same order of magnitude as our crystals (see Table 4.2.1), indicating that our assumption that a crystal is a solid beam consisting of a single continuous lattice with few faults may not be correct.

The presence of defects of a size equivalent to the crystal width and height, would result in significant deviation from the ideal cantilever assumptions. In addition, it is worth noting that Matoy et al [313] using silicon oxide, oxinitride and nitride beams observed the analytical solution (see Equation 4.3.6) to underestimate the Young's modulus by 30%, because additional shear stresses in short and thick cantilevers, and a systematic error of the length of the cantilever beams, which has a cubic influence on the Young's modulus (see Equation 4.3.6).

In any case, for each crystal the spring constant k_c remains constant during the experiment, and thus allows accurate estimation of the force. The calculated breakage force (see Equation 4.3.7) is thus not impacted by “give” in the glue, or unexpected changes in E from crystal to crystal due to lattice defects. The observed breakage strength also varies strongly, between 5.27MPa and 81.1MPa . This is however more in line with expected behaviour as it's well known that the breakage property is not just a physical material property, but rather dependent on cracks in the surface and crystal lattice that vary from crystal to crystal [314-316]. The position of crystal imperfections is critical: a small crack in the region of maximal stress could initiate the breakage process, reducing the breakage strength of the crystal with respect to another crystal with fewer defects in the high stress zone.

4.4.2 Model Fitting

Tensile strength distributions are usually captured with the Weibull probability distribution function:

$$f(x, k, \lambda) = 1 - e^{-\left(\frac{x}{\lambda}\right)^k} \quad 4.4.1$$

where k and λ are the Weibull repartition function shape and scale parameters respectively, and x corresponds to the distributed property values. Such distribution is more suitable for mechanical properties data than the Normal distribution [48, 317]. The utility of a distribution lies in its direct implementation in numerical investigations,

e.g. Discrete Element Method (DEM), as it represents the probability of breakage for a given exerted stress [48], and helps predict breakage due to forces applied on crystals in processing equipment [16, 168, 192, 194].

The Weibull repartition function was fitted to the cumulative distribution values obtained by evenly distributing the logarithmic values of breakage strength and Young's modulus over 8 and 9 bins respectively (see Figure 4.4.2 and Figure 4.4.3).

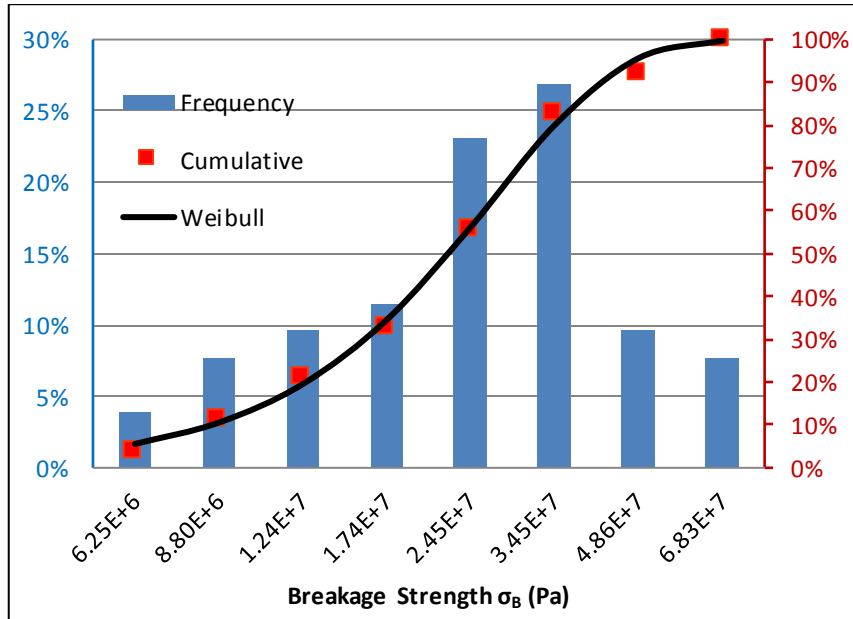


Figure 4.4.2: Distribution of breakage strength σ_B (see data in Appendix 7)

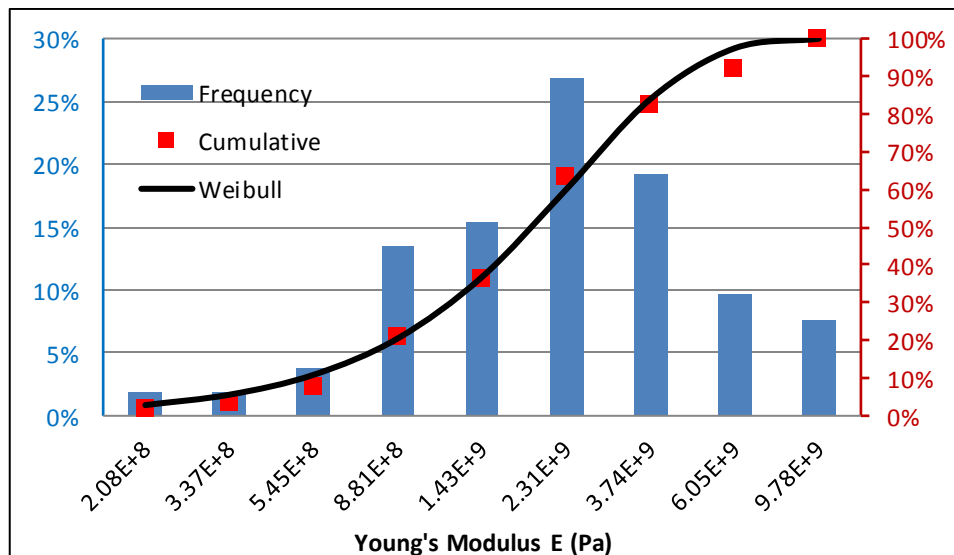


Figure 4.4.3: Distribution of Young's modulus E (see data in Appendix 8).

The estimated Weibull parameters along with the Weibull average and median values of both distributions are tabulated in Table 4.4.1, and show 50% of the crystals experience breakage at $22.4MPa$ which is in good agreement with estimates of the glutamic acid breakage strength by MacLeod and Muller, who found that for 300 – 600 μm long beta glutamic acid crystals σ_B was 13 – 17MPa [26].

Table 4.4.1: Weibull fitting parameters of breakage strength distribution of the β -LGA crystals.

Weibull	Breakage Strength, σ_B	Young's Modulus, E
Nbr of bins	8	9
Shape parameter k	1.95274	1.43674
Scale parameter λ (Pa)	2.70E+07	2.45E+09
Median (Pa)	2.24E+07	1.90E+09
Average (Pa)	2.40E+07	2.23E+09
R^2	0.99670	0.99509

4.4.3 Correlations

In order to gain a better understanding of the significance of each crystal dimension on the distribution of the mechanical property estimates, the monotonicity between these variables was assessed using the Spearman correlation, a rank-based statistical analysis method, which is ideal for small samples and is insensitive to extreme values.

The results of the Spearman analysis, using interval of confidence of 95% and a significance level, of 0.05, are tabulated in Table 4.4.2. The coefficient of correlation takes a value between -1 (for a strictly inverse proportionality) and $+1$ (for a strictly

positive proportionality). A coefficient of 0 shows a non-monotonic relationship between the variables [318].

Table 4.4.2: Spearman correlation analysis. The shaded columns have p-values larger than the significance limit $\alpha = 0.05$.

Spearman Correlation ($N = 52, \alpha = 0.05$)		L_B , crystal broken length	L , crystal length	w , width	h , height	σ_B , breakage strength
σ_B , breakage strength	Corr.	0.259	0.131	0.0444	-0.419	-
	P-value	0.0637	0.356	0.755	0.00201	-
E , Young's modulus	Corr.	0.215	0.254	0.206	-0.290	0.544
	P-value	0.126	0.0691	0.142	0.0370	3.07E-05

The correlation coefficient between the Young's modulus and the breakage strength is 0.544 with a p-value well below the significance level ($p_{corr} = 3.07 \times 10^{-5}$): the stronger the crystal the higher its Young's modulus and vice versa. The Spearman coefficient was found equal to -0.419 with a p-value of 2.01×10^{-3} between crystal height and breakage strength, and -0.290 with a p-value of 3.70×10^{-2} for Young's Modulus. Thus, the thicker crystals seem to have a lower breakage strength (and Young's modulus). This is consistent with Equation 4.2.1 if the crack length is proportional to the height of the crystals:

$$\frac{E}{\sigma_b^2 h} = 0.04 \text{ to } 0.26 \sim \frac{1}{J_{ic}} \frac{\lambda}{h} \quad 4.4.2$$

For the data set measured, the left term in Equation 4.4.2 is 10% on average, but in a wide range of 0.04 to 0.26, suggesting that the carefully crystallised crystals (seeded cooling crystallisation) have a wide range of initial crack lengths.

4.4.4 Potential Improvements and Future Work

A penetration phenomenon may have occurred during our experiments and a fraction of the force applied might have this way been absorbed. Even if the absorbed force is expected to be marginal, the idea of using another shape of AFM probe can be considered in the future. Swadener et al. [319] have shown that a spherical tip does not affect the hardness of the tested materials. Furthermore, Perkins et al. [320] found that such an operation should distribute the applied force over a larger area.

Crystals are by nature symmetrical arrangements of molecules in a solid form. It has been observed that the atomic bonds play a crucial role in the mechanical response of nano-indented crystals, not only because of their strength but also due to their spatial distribution [321]. As a forward look, it would thus be interesting to consider the energetic characteristics of the miller plane at which the breakage occurs and attempt to find a correlation between the energy of the breakage plane and the mechanical properties of the crystal alongside this plane.

4.5 Conclusions

An innovative method to measure breakage strength and elastic modulus from single crystal cantilevers using Atomic Force Microscopy is presented in this study. Crystals break at $\sim 10\%$ of the distance between where forces are applied and the edge the cantilever hangs over, in line with prediction of 8% for linear elastic materials.

The Euler-Bernoulli beam theory was used to calculate the breakage strength and Young's modulus of 52 β -LGA crystals. The mechanical properties data were fitted into a Weibull distribution model which defines that 50% of the crystals break at 22.4MPa and have Young's modulus below 1.90GPa . Spearman analysis demonstrated that (i) stronger crystals have a higher Young's modulus and vice versa, and (ii) thicker crystals have lower breakage stress and Young's modulus and vice versa, which corresponds with the established fracture mechanics theory.

The data generated using the single crystal cantilever method provides the fundamental material properties essential for understanding of undesirable crystal fracture in manufacturing processes such as crystallisation, filtration and drying of chemical ingredients but the broad range of E and σ_b values reported suggests a

Chapter 4: The Breakage Strength of Elongated Organic Crystals

significant extend of crystal imperfections, even though the crystals where carefully crystallised using a seeded cooling crystallisation.

The Young's modulus and crystals dimensions obtained for the β -LGA sample in this study will be used to design particles for the DEM shear cell simulations in Chapter 5 and 6, whilst their breakage strength will be used the create the probabilistic breakage kernel in Chapter 8.

5 Optimisation of Simulation Setup and Methods

5.1 Introduction

In this chapter, particles are sheared in a shear cell created using distinct element modelling (DEM) and their behaviour is examined for different stress conditions.

The particles populating the shear cell are modelled after the samples of β -LGA crystals with their mechanical and physical properties assessed in both Chapter 3 and Chapter 4. The movement of the parallel walls exerts compressive and shear stress on the particles, imitating the mechanical environment experienced by a particle bed in an agitated filter dryer (see Figure 5.1.1): strain applied, normal and shear stresses.

After preliminary observations, the shear cell parameters are optimised to be representative of the quasi-static flow regime in industrial dryers and to minimise the computational resources needed for the completion of the simulations.

Finally, the relevance of different methods for the calculation of the particle internal stress on the studied system is investigated and the most suitable one is chosen for the further analysis.

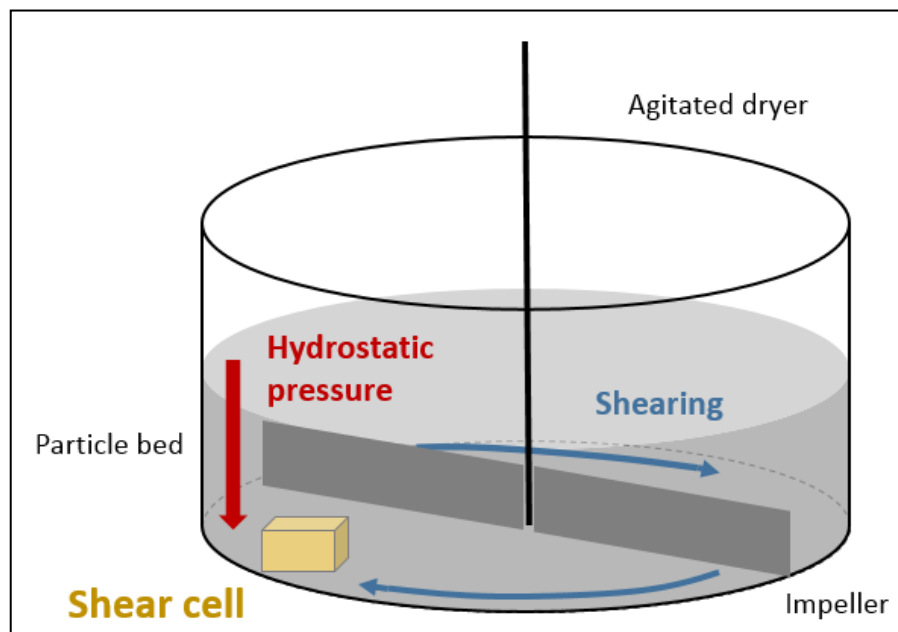


Figure 5.1.1: Stress conditions within a particle bed sheared in an agitated filter dryer.

5.2 Initial Simulation Setup

The simulations are performed using DEM, a computational modelling method introduced in 1971 [22] which models particles using discrete elements. Simulations are run with EDEM software supplied by Altair Engineering with spheres as DEM elements.

5.2.1 Particles

5.2.1.1 Physical Properties

DEM elements can be assembled to create particles with the desired shape [24]. In this study, elongated particles are created using multi-element model composed of overlapped soft spheres. High aspect ratio particles are generally created using spheres overlapped along an axis [192-197]. 11 identical spheres are then aligned with the same overlapping distance to create a particle (see Figure 5.2.1). The spheres are clumped together making the particles rigid: the internal contacts between the spherical elements are ignored in the contact model calculations and internal contacts don't break [195, 212-215]. An overlap distance of one sphere radius (i.e. overlap ratio [149] of 1) is selected as compromise between a too low overlap distance requiring more element spheres and computational power, and a too high overlap distance which would induce an additional particle roughness promoting interlocking and generating a higher shear stress [149, 228, 260]. Indeed, the clumped sphere approach creates artificially rough surfaces [199-203] which is often considered more similar to actual granular materials compared to particles with smooth surfaces [205].

Moreover, it is reported that a minimum Young's modulus of 100MPa for particles is necessary to observe the same bulk mechanical behaviour of the bed compared than for rigid particles [228]. Therefore, the use of flexible particle models [192, 226-228] is unnecessary for the particles in this study as the experimentally assessed elastic modulus of the β -LGA crystals is at the scale of GPa (see Chapter 4).

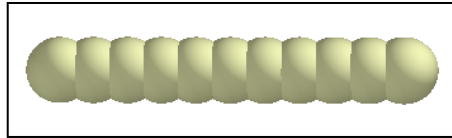


Figure 5.2.1: Elongated particle modelled in EDEM

The particles are sized following the observation of the sample of β -LGA crystals used in Chapter 4 (see Figure 5.2.2) [18]. The sphere diameter is set at $50\mu m$, which corresponds approximately to the average of the experimental mean crystal width (see Appendix 6). The mean length of the simulated particles equals $300\mu m$ which corresponds to an aspect ratio [119, 208, 209] of 6. This length is selected to also consider the non-cantilever part of the crystals mounted in the AFM experiments.

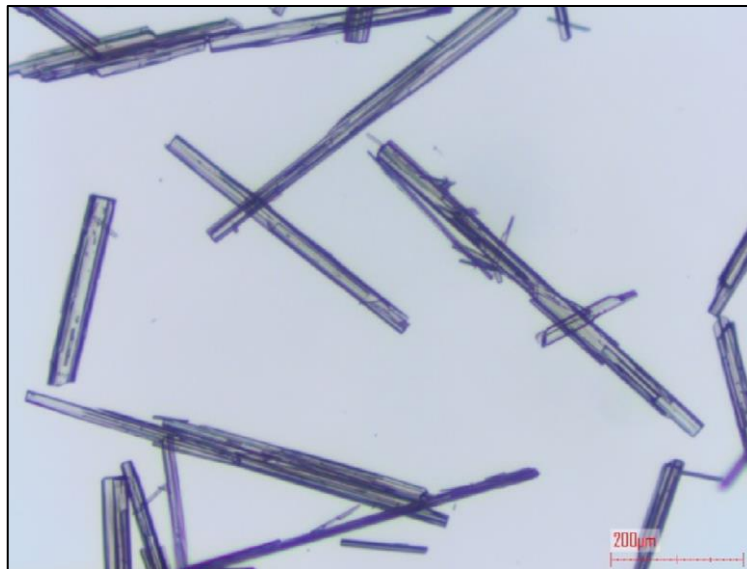


Figure 5.2.2: Light microscope image of β -LGA crystals.

5.2.1.2 Mechanical Properties

The mechanical properties are representative of β -LGA crystals for the particles and stainless steel for the walls (see Table 5.2.1). The Young's modulus of the particles is determined experimentally in Chapter 4 [18].

Table 5.2.1: Mechanical properties of simulation objects

Object	Particle	Wall
Material	β -LGA	Steel
Poisson's ratio ν	0.25 [196]	0.3 [322]
Solid density ρ ($kg \cdot m^{-3}$)	1460 [323]	8000 [324]
Young's modulus E (GPa)	1.9 [18]	200 [325]

5.2.1.3 Interactions

In DEM simulations, the motion of each particle is determined discretely by solving Newton's second law of motion [210, 216] (see Equations 2.4.1 and 2.4.2). Simulations of particle shearing are generally operated using Hertzian models [55, 190, 218].

5.2.1.3.1 Contact Model

The contact model used in this study for particle-particle and particle-wall contacts is called "Hertz-Mindlin (No Slip)" [217], with the normal force component based on Hertzian contact theory [219] and the tangential force model based on Mindlin-Deresiewicz work [220, 326]. The damping components of the normal and tangential forces are calculated using a damping coefficient related to the coefficient of restitution as presented in Tsuji et al. [218]. The tangential friction force is calculated following the Coulomb law of friction model as in Cundall et al. [327]. The rolling friction is implemented as the contact-independent directional constant torque model as in Sakaguchi et al. [328].

At a particular contact, the normal force F_n is given as a function of normal overlap δ_n :

$$F_n = \frac{4}{3} E^* \sqrt{R^*} \cdot \delta_n^{3/2} \quad 5.2.1$$

Where the equivalent Young's Modulus E^* and the equivalent radius R^* are defined as follows:

$$\frac{1}{E^*} = \frac{(1 - \nu_i^2)}{E_i} + \frac{(1 - \nu_j^2)}{E_j} \quad 5.2.2$$

$$\frac{1}{R^*} = \frac{1}{R_i} + \frac{1}{R_j} \quad 5.2.3$$

With E_i , ν_i , R_i , and E_j , ν_j , R_j being the Young's Modulus, Poisson ratio and radius of each sphere in contact. Additionally there is a damping force F_n^d given by:

$$F_n^d = -2 \sqrt{\frac{5}{6}} \beta \sqrt{S_n m^*} \cdot v_n^{\overline{rel}} \quad 5.2.4$$

With $m^* = \left(\frac{1}{m_1} + \frac{1}{m_2}\right)^{-1}$ the equivalent mass, $v_n^{\overline{rel}}$ is the normal component of the relative velocity, β and the normal stiffness S_n are given by:

$$\beta = \frac{\ln(e)}{\sqrt{\ln^2(e) + \pi^2}} \quad 5.2.5$$

$$S_n = 2E^* \sqrt{R^* \delta_n} \quad 5.2.6$$

With e the coefficient of restitution. The tangential force F_t depends on the tangential overlap δ_t and the tangential stiffness S_t :

$$F_t = -S_t \delta_t \quad 5.2.7$$

With

$$S_t = 8G^* \sqrt{R^* \delta_n} \quad 5.2.8$$

Here G^* is the equivalent shear modulus (see Equation 5.2.13). Additionally, tangential damping is given by:

$$F_t^d = -2 \sqrt{\frac{5}{6}} \beta \sqrt{S_t m^*} \cdot v_t^{\overline{rel}} \quad 5.2.9$$

Where $v_t^{\overline{rel}}$ is the relative tangential velocity. The tangential force is limited by Coulomb friction $\mu_s F_n$ where μ_s is the coefficient of static friction.

For simulations in which rolling friction is important, this is accounted for by applying a torque to the contacting surfaces.

$$\tau_i = -\mu_r F_n R_i \omega_i \quad 5.2.10$$

With μ_r the coefficient of rolling friction, R_i the distance of the contact point from the centre of mass, and ω_i the unit angular velocity vector of the object at the contact point.

5.2.1.3.2 Model Parameters

The coefficient of static friction between particles and walls is increased to 10 to ensure an effective grip and force propagation to the particle bed during the shearing phase (see Table 5.2.2). Indeed, the roughness of the walls is needed to avoid slipping at the particle-wall interface: the particles in contact with the walls are then dragged efficiently to prevent strain localisation at the boundaries [13, 23, 242, 243]

Table 5.2.2: Interaction properties of simulation objects

Contact type	Particle-Particle	Particle-Wall
Contact model	Hertz-Midlin (no-slip)	Hertz-Midlin (no-slip)
Coefficient of restitution e	0.3 [329]	0.4 [196]

Coefficient of static friction μ_s	0.3 [196]	10
Coefficient of rolling friction μ_r	0.05 [196]	0.05 [196]

5.2.2 Shear Cell

A shear cell is built in DEM to mimic the mechanical environment experienced by particles within an agitated dryer.

5.2.2.1 Domain

A minimum number of particles in the shear cell is essential to have a representative and homogeneous [191] mechanical behaviour of the bed, as the mechanical properties of assemblies vary with sample size [247, 248]. It has been demonstrated that the mechanical behaviour for cell size of about $15 \times 15 \times 7.5 dv$ (dv : diameter of sphere with equivalent volume of a particle [119, 154]) with 2000 elongated particles having an aspect ratio of 6 is comparable to a $20 \times 20 \times 11 dv$ domain with 4000 particles in terms of normal stress, shear stress, kinetic and collisional components [203]. The smaller domain size and number of particles are then chosen to reduce the time cost of the simulations [228]. Therefore, the shear cell width and length measure $1.5mm$. It corresponds to $\times 5$ the particle length ($300\mu m$) which is reported as the minimum ratio for the recommended specimen size [246].

Moreover, periodic boundaries are used on the length \vec{x} and width \vec{y} axis to create an infinite shear band (see Figure 5.2.3). The distance between the two walls defines the depth of the shear band i.e. the volume of the bed that experiences deformation [239, 240]. This method has become a standard in DEM simulations [21, 244] and reduces wall effects. Lees-Edwards boundaries [245], i.e. periodic boundaries on the three axes, are not considered in this study as the shear cell is designed to allow the variation of cell volume and keep the normal stress applied constant.

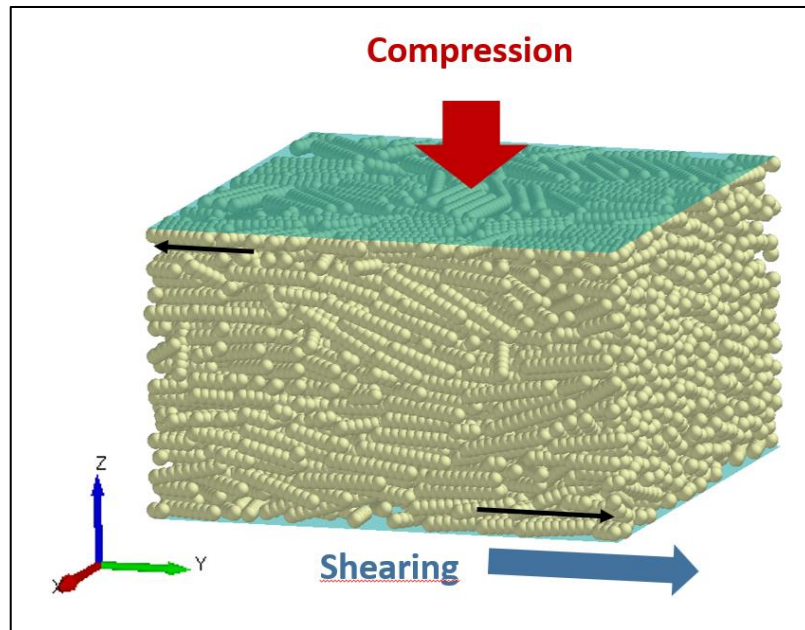


Figure 5.2.3: Shear cell designed in EDEM. Both normal and shear stress are applied on particle bed

There is no gravity applied to the particles. Indeed, it is likely that gravity would not generate an important disparity in the results since the hydrostatic pressure applied is at least $\times 100$ superior (magnitude of kPa) to the pressure induced by the weight of particle at the scale of the shear cell. The absence of gravity also creates an homogeneous stress field within the particle bed [13], an isotropic dense assembly [205], and is generally chosen for the observation of small-scale phenomenon [203, 228, 241, 261].

5.2.2.2 Bed Filling

The 2000 particles are generated within a space of $1.5 \times 1.5 \times 1.6 \text{ mm}$ ($\vec{x}, \vec{y}, \vec{z}$), between the two parallel walls, at random initial position and orientation, with no initial translational and angular velocity. This method is widely used to populate a shear cell in DEM to obtain an inert, homogeneous and randomly packed bed [55, 191]. The embedded solver within EDEM software ensures that particles do not enter in contact when generated. The two walls are $200\mu\text{m}$ distant from the bed filling space, greater than half particle length to ensure no particle touches the walls when generated. The particles are identical which produces a monodisperse particle bed.

Bed filling methods exist to generate isotropic dense assemblies, such as setting to zero the gravitational acceleration and friction coefficients of particle-particle and particle-wall interactions [205]. The use of this method results in the densest granular assemblies [282, 283]. These methods are avoided here to allow the analysis of the impact of particle alignment on the bed mechanical behaviour. Indeed, the particle bed is randomly packed at the start of shearing phase, where its alignment is minimal, and is expected to increase its ordering with strain applied [188].

5.2.2.3 Compression and Shearing

Once the particle bed is generated, a force controller is assigned to the upper wall in the $-\vec{z}$ direction and is compressing the bed (see Figure 5.2.3). The target value of the force controller $\vec{F}_{w,control}$ is determined from the selected compressive stress $\vec{\sigma}$:

$$\vec{F}_{w,control} = A_{wall} \cdot \vec{\sigma} \quad 5.2.11$$

With A_w the area of the wall. The lower wall remains static in the \vec{z} direction.

Then, the upper wall lowers down and compresses the particle bed. Once the upper wall's compressive force reaches a steady state at the targeted value, the two walls move in opposite directions at $1\text{mm} \cdot \text{s}^{-1}$ on the \vec{y} axis. This wall movement strains the bed and generates a shear stress on the particle due to their ability to transfer stresses from normal to shear direction [151], creating a Couette flow [13, 21, 23, 24, 241, 242]. The motion of the upper wall in the \vec{z} axis is allowed to enable the variation of the bed volume during the shearing phase and keep the compressive stress constant [13, 21, 23, 24, 195].

This shear cell setup reproduces the mechanical environment experienced by a particle bed in an agitated filter dryer where the normal stress is the compression induced by the bed mass, the shear stress resulting from frictional contacts between particles and the strain generated from the movement of the impeller during its rotation.

The stress environment is generally defined with the components of the stress tensor [13, 254, 255]. Therefore, the normal and shear stress on the particle bed is calculated as a function of the normal and tangential forces of particle-wall contacts (see Equations 2.4.8 and 2.4.9).

5.2.3 Simulator Settings

5.2.3.1 Time Step

The simulation consists of a Euler time integration [330, 331] calculating the contact force between particles at time t_n based on their position at t_{n-1} using a contact model. The force calculated will then be used to determine the new particle position. The chosen time step between two calculations corresponds to 20% of the Rayleigh time step T_R , which is typically used for quasi-static packed particle bed with high coordination number (≥ 4) [332]:

$$T_R = \frac{\pi \cdot r_{min} (\rho/G)^{1/2}}{0.1631\nu + 0.8766} \quad 5.2.12$$

With r_{min} the radius of the smallest sphere element radius, ρ the material's density, G the shear modulus and ν the Poisson's ratio of the particle.

The shear modulus G is related to the Young's modulus E with the following equation [333]:

$$E = 2G(1 + \nu) \quad 5.2.13$$

5.2.3.2 Simulator Grid

The domain is divided into grid cells and the simulator calculates contact forces within cells containing 2 element spheres or more. This method reduces processing time without affecting the simulation results. The value of the cell size is optimised within EDEM and set at $2.5R_{min}$, with R_{min} the smallest element sphere radius.

5.3 Preliminary Observations

5.3.1 Velocity Profile

When performing a shearing simulation on a particle bed, it is crucial to ensure that the strain is effective on the whole bed, especially in the present case where no speed controller is applied to particles [203] and strain is promoted by sliding parallel walls. The velocity profile along the shear cell height [242] is a common way to confirm the absence of strain localisation in the particle bed. Moreover, the coefficient of static friction has been increased to 10 to ensure an effective particle-wall grip (see Table 5.2.2), which can be quantified by the grip factor [155] (see Equation 2.4.5).

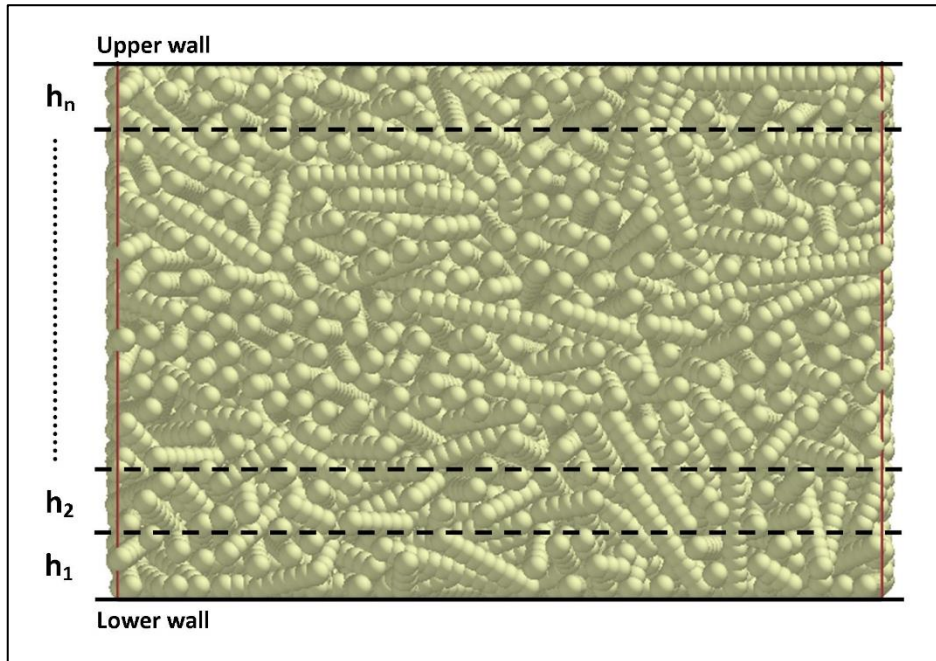


Figure 5.3.1: Division of the particle bed within a shear cell along its height.

The particle bed is divided along its height into zones of equal volume (see Figure 5.3.1) and the mean particle speed within each zone is calculated as:

$$\bar{v}_i = \frac{1}{m} \sum_{p=1}^m \vec{v}_p \cdot \vec{y} \quad 5.3.1$$

With i the index of the zone, m the number of particles p in this zone and \vec{y} the direction of shearing. A particle belongs to a zone when its centre of gravity is in the corresponding range of bed height.

The average velocity profile along the simulation is close to linear (see Figure 5.3.2) with a coefficient of determination $R^2 = 0.966$. The tested linear function crosses the velocity of walls at their position. It demonstrates that the modified particle-wall coefficient of static friction is sufficient to stick the particles to the walls, with a grip factor estimated at 1, and that the strain application is uniform throughout the bed [13].

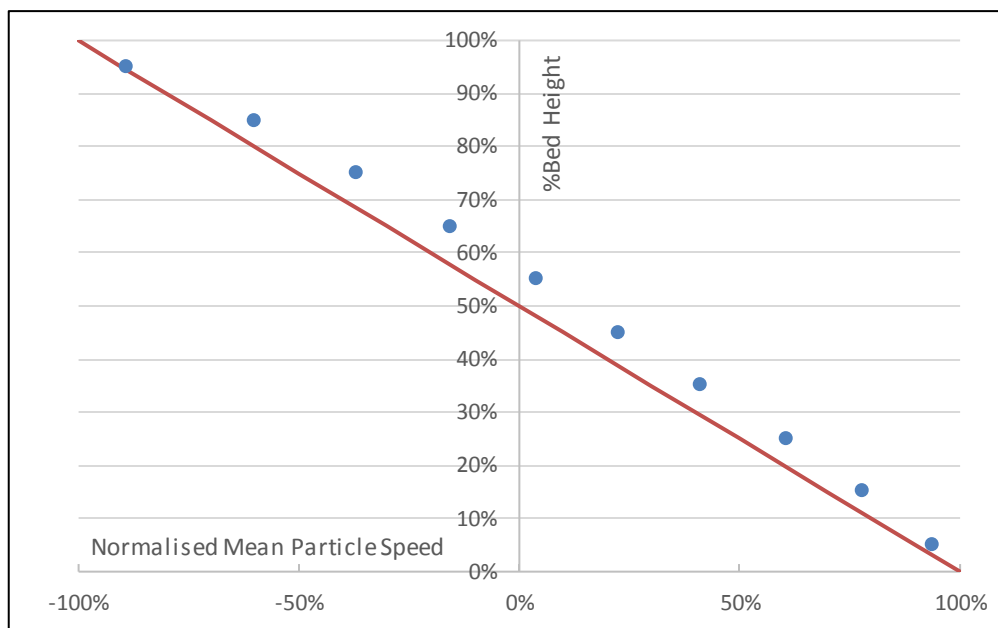


Figure 5.3.2: Mean velocity profile of a simulation with 10 bed divisions height-wise. The speed values are normalised over the module of wall speed. The case of a linear velocity profile is shown by the red line.

The bed is composed of elongated particles, and the slight dissymmetry in the average velocity profile is assumed to be an artefact of the simulation due to the random packing of particles. Also, the upper wall enters in contact with particles and pushes the particles downwards to the lower wall during the compression phase, which can be responsible of this dissymmetry. Moreover, particles are rearranging throughout the shearing phase, and this non-uniform phenomenon creates a discontinuity of particles speed within the different zones of the bed (see Figure 5.3.3).

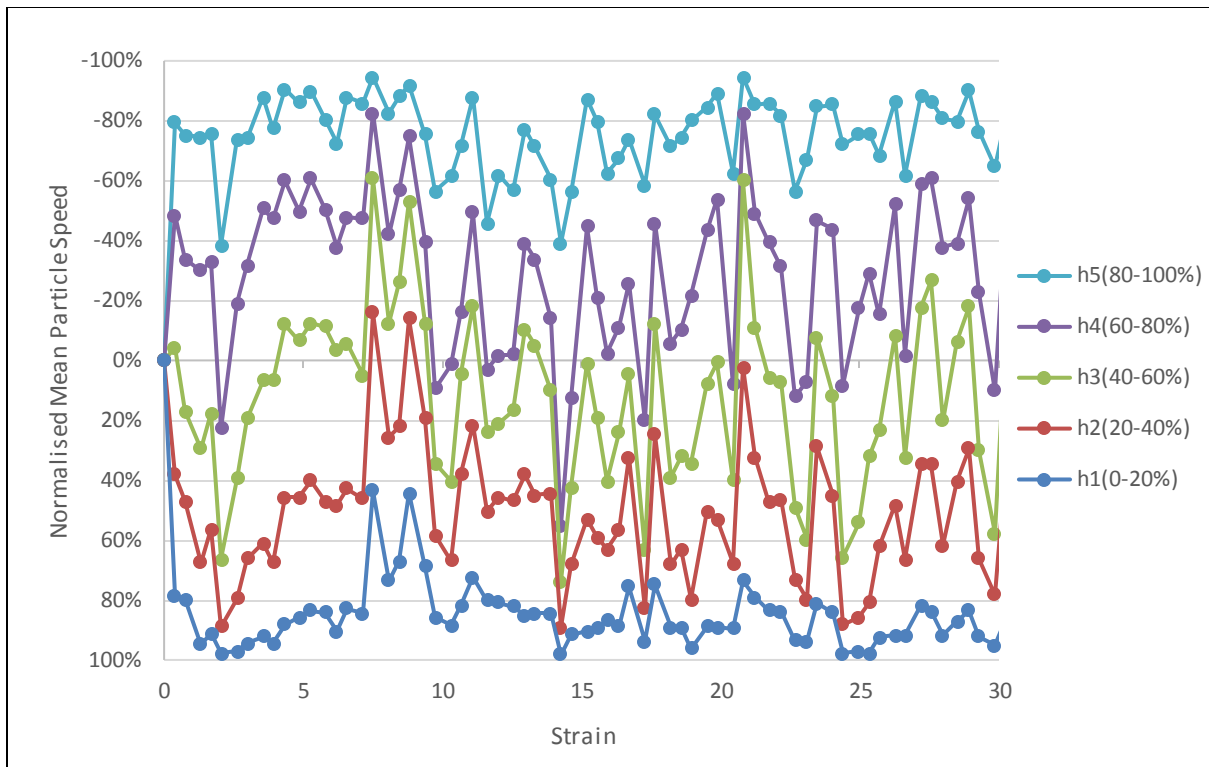


Figure 5.3.3: Mean particle speed during bed shearing simulation for 5 zones of the particle bed divided along the height. The speed values are normalised over the module of wall speed.

5.3.2 Particle Alignment

5.3.2.1 Calculation Method

Elongated particles have the ability to align along the flow stream in sheared systems [188] and the order parameter S , originally used to determine molecular ordering of liquid crystals [280], quantifies the uniformity of their ordering in the same direction [205, 279, 280]: the order director.

5.3.2.1.1 Order Tensor

Each particle p has a unit vector \vec{u}_p directed along its neutral axis (see Figure 5.3.4).

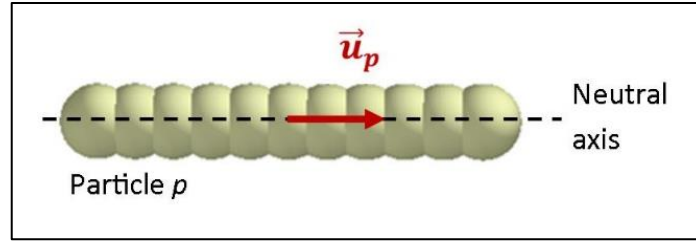


Figure 5.3.4: Clumped sphere particle with its neutral axis and unit vector \vec{u}_p .

The order tensor Q of a group of N particles is obtained from their unit vector using the following equation [205, 279, 280]:

$$Q_{\alpha,\beta} = \frac{3}{2N} \sum_{p=1}^N (u_{p,\alpha}u_{p,\beta} - I_{\alpha,\beta}) \quad 5.3.2$$

With α and β cartesian axes among (x, y, z) and I the identity matrix. Here, the biaxiality of particles have no effect on the order tensor calculation i.e. either \vec{u}_p or $-\vec{u}_p$ can be used.

The order tensor is symmetrical:

$$Q_{\alpha,\beta} = Q_{\beta,\alpha} \quad 5.3.3$$

And as \vec{u}_p is a unit vector, the order tensor is traceless:

$$Q_{xx} + Q_{yy} + Q_{zz} = 0 \quad 5.3.4$$

The 2nd order tensor Q has 3 eigenvalues λ_1 , λ_2 and λ_3 corresponding to 3 eigenvectors \vec{v}_1 , \vec{v}_2 and \vec{v}_3 . The calculation of eigenvalues is performed with a diagonalization of Q :

$$Q = PDP^T \quad 5.3.5$$

With D the diagonalized matrix, P the system of eigenvectors and P^T the transpose of P :

$$D = \begin{bmatrix} \lambda_1 & 0 & 0 \\ 0 & \lambda_2 & 0 \\ 0 & 0 & \lambda_3 \end{bmatrix} \quad P = \begin{bmatrix} \vdots & \vdots & \vdots \\ v_1 & v_2 & v_3 \\ \vdots & \vdots & \vdots \end{bmatrix} \quad P^T = \begin{bmatrix} \dots & v_1 & \dots \\ \dots & v_2 & \dots \\ \dots & v_3 & \dots \end{bmatrix}$$

P^T is here used instead of P^{-1} as the eigenvectors are orthogonal.

As the eigenvectors are unit vectors, D is traceless:

$$\lambda_1 + \lambda_2 + \lambda_3 = 0 \quad 5.3.6$$

5.3.2.1.2 Eigenvalues and Order Parameter

Using the method of the determinant, the eigenvalues are the solutions of λ for which:

$$\det(Q - \lambda I) = 0 \quad 5.3.7$$

With Q the order tensor and I the identity matrix.

After developing the determinant, the characteristic polynomial is then obtained:

$$a\lambda^3 + b\lambda^2 + c\lambda + d = 0 \quad 5.3.8$$

With:

$$a = 1 \quad b = Q_{xx} + Q_{yy} + Q_{zz} = 0$$

$$c = Q_{xx}Q_{yy} + Q_{xx}Q_{zz} + Q_{yy}Q_{zz} - Q_{xy}^2 - Q_{xz}^2 - Q_{yz}^2$$

$$d = Q_{xx}Q_{yz}^2 + Q_{yy}Q_{xz}^2 + Q_{zz}Q_{xy}^2 - Q_{xx}Q_{yy}Q_{zz} - 2Q_{xy}Q_{xz}Q_{yz}$$

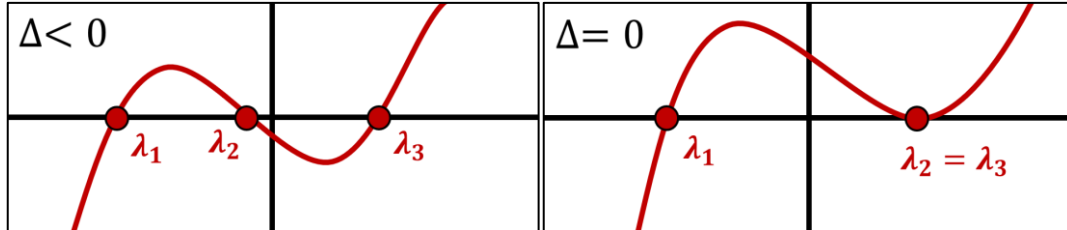
The characteristic polynomial can then be written as followed:

$$\lambda^3 + c\lambda + d = 0 \quad 5.3.9$$

The method of Cardano-Tartaglia [334] is used to solve this 3rd order polynomial with the discriminant Δ is expressed as:

$$\Delta = 4c^3 + 27d^2 \leq 0 \quad 5.3.10$$

Δ is negative as there are at least two real roots to the polynomial.



The three solutions of λ are:

$$\lambda_1 = 2\mu \cos\left(\frac{t_0}{3}\right) \quad \lambda_2 = 2\mu \cos\left(\frac{t_0+2\pi}{3}\right) \quad \lambda_3 = 2\mu \cos\left(\frac{t_0+4\pi}{3}\right)$$

With:

$$\mu = \sqrt{-\frac{c}{3}} \quad t_0 = \cos^{-1}\left(-\frac{d}{2\mu^3}\right)$$

The maximum of the absolute values of the eigenvalues is the order parameter S of the system i.e. the measure of its alignment:

$$S = \text{Max}(\text{Abs}(\lambda_1), \text{Abs}(\lambda_2), \text{Abs}(\lambda_3)) \quad 5.3.11$$

Normally, the order parameter scales from $-1/2$ where all unit vectors are normal to each other, to $+1$ for a perfect alignment ($S = 0$ during the isotropic phase). The standard approach is to take the absolute value as a basis to compare the ordering of different particle beds.

5.3.2.1.3 Eigenvectors and Order Director

The eigenvectors \vec{v} are determined using the calculated eigenvalues in the following equation:

$$(Q - \lambda I)\vec{v} = 0 \quad 5.3.12$$

$$\vec{v} = \begin{bmatrix} X \\ Y \\ Z \end{bmatrix} \neq \begin{bmatrix} 0 \\ 0 \\ 0 \end{bmatrix} \quad 5.3.13$$

A system of three equations is obtained:

$$L_1: (Q_{xx} - \lambda)X + Q_{xy}Y + Q_{xz}Z = 0$$

$$L_2: Q_{xy}X + (Q_{yy} - \lambda)Y + Q_{yz}Z = 0$$

$$L_3: Q_{xz}X + Q_{yz}Y + (Q_{zz} - \lambda)Z = 0$$

The method of Gauss is used on two of these equations to calculate two eigenvectors:

$$X = \frac{\alpha}{M} \quad Y = \frac{\beta}{M} \quad Z = \frac{\gamma}{M}$$

With:

$$M = \sqrt{\alpha^2 + \beta^2 + \gamma^2}$$

With α, β, γ values obtained by solving a system of two equations among L_1, L_2 and L_3 :

	$L_1 \ \& \ L_2$	$L_1 \ \& \ L_3$	$L_2 \ \& \ L_3$
α	$Q_{xz}(Q_{yy} - \lambda) - Q_{xy}Q_{yz}$	$Q_{xy}(Q_{zz} - \lambda) - Q_{xz}Q_{yz}$	$Q_{yz}^2 - (Q_{yy} - \lambda)(Q_{zz} - \lambda)$
β	$Q_{yz}(Q_{xx} - \lambda) - Q_{xy}Q_{xz}$	$Q_{xz}^2 - (Q_{xx} - \lambda)(Q_{zz} - \lambda)$	$Q_{xy}(Q_{zz} - \lambda) - Q_{xz}Q_{yz}$
γ	$Q_{xy}^2 - (Q_{xx} - \lambda)(Q_{yy} - \lambda)$	$Q_{yz}(Q_{xx} - \lambda) - Q_{xy}Q_{xz}$	$Q_{xz}(Q_{yy} - \lambda) - Q_{xy}Q_{yz}$

This method offers 3 systems of equations, which allows the calculation of eigenvectors coordinates even when $\alpha = \beta = \gamma = 0$ (i.e. calculation impossible) for one of the systems. If the calculation is impossible for the 3 systems, a cross product can be performed on two eigenvectors to obtain the third one:

$$\vec{v}_3 = \vec{v}_1 \times \vec{v}_2 \quad 5.3.14$$

The eigenvector corresponding to the eigenvalue selected as order parameter is the order director i.e. the direction along which the particles are the most aligned to.

5.3.2.2 Order Parameter

The order parameter is a dimensionless number quantifying the level of alignment of a particle bed, and the order director is the vector along which the particles are the best aligned to.

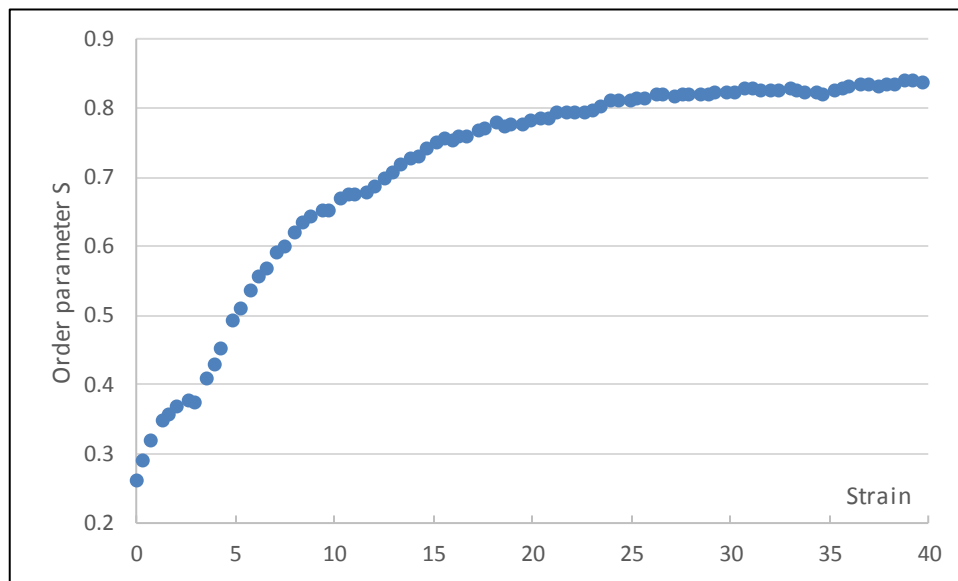


Figure 5.3.5: Order parameter of a particle bed along simulation of shear cell.

Mechanical shearing promotes the alignment of elongated particles in a bed [14, 188]. Indeed, the order parameter starts at $S = 0.26$ on the beginning of the shearing phase and increases monotonically until reaching a plateau at $S = 0.82$ after an applied strain of $\gamma = 30$ (see Figure 5.3.5). The steady state value obtained corresponds to the value reported in DEM shear cell for particles with an aspect ratio of 6 [14].

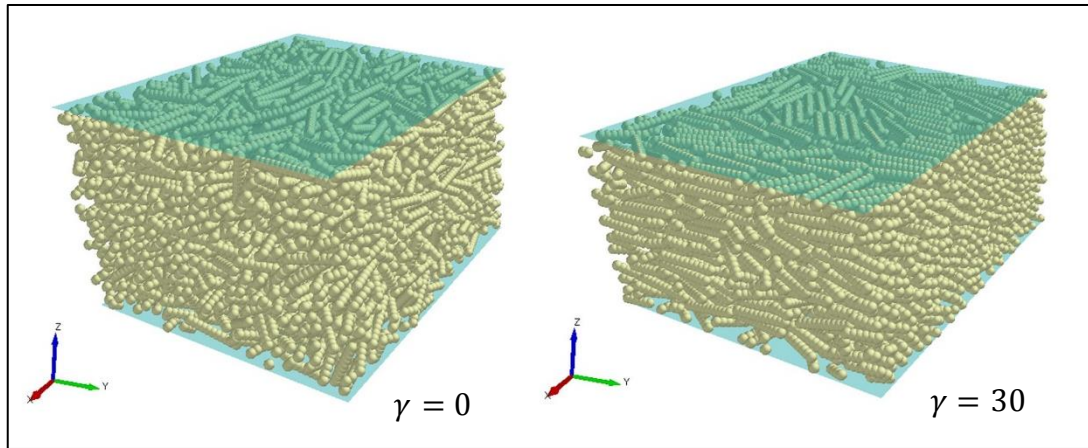


Figure 5.3.6: Particle bed within the shear cell at a strain applied of $\gamma = 0$ and $\gamma = 30$.

The particles align along the direction of shearing $\vec{\gamma}$ (see Figure 5.3.6) as demonstrated by the predominance of the y component in the order director after only $\gamma = 4$ applied strain (see Figure 5.3.7). The y and z components switch values when the theoretical order parameter switches sign at a strain of $\gamma = 4$. In the present study, only the absolute value of order parameter is studied.

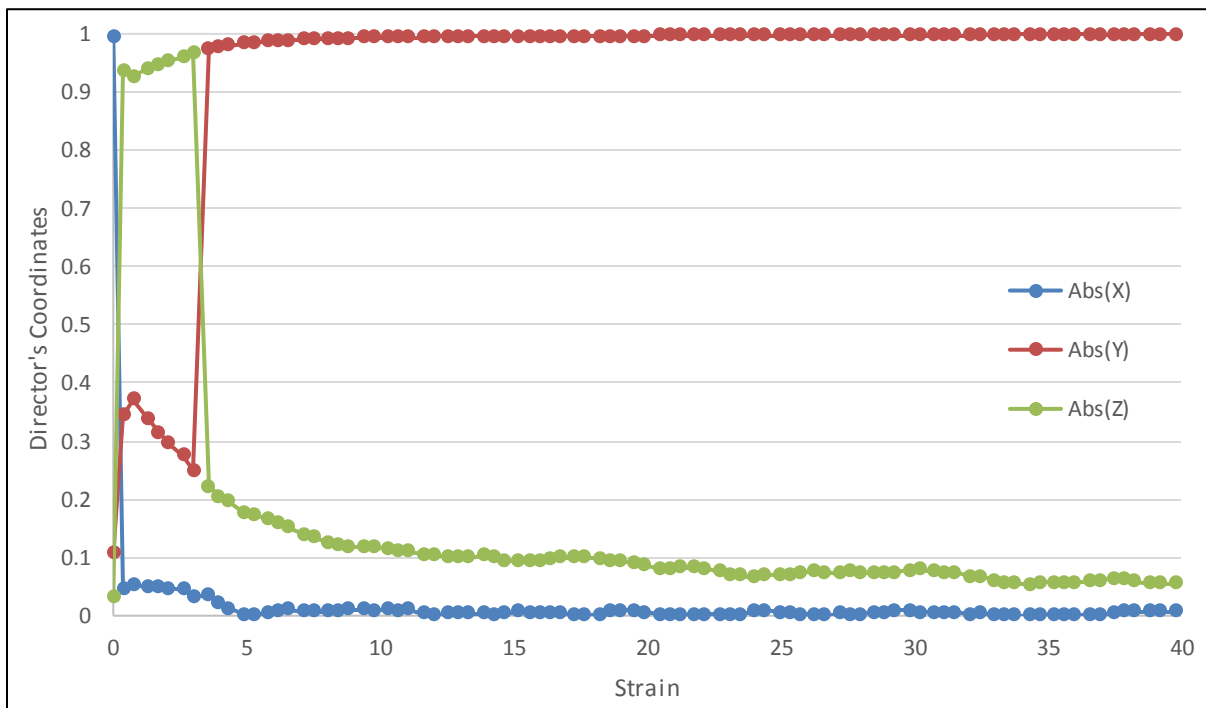


Figure 5.3.7: Absolute value of order director's coordinates of a particle bed along simulation of shear cell.

5.3.3 Bed Densification

As the particle bed is sheared, the bed changes conformation from its initial random packing and elongated particles align, which densifies the bed [188]. The closer packing of the bed increases its volume solid fraction until reaching a steady state (see Figure 5.3.8). The steady state value is reached after a strain applied of $\gamma = 30$, which corresponds to the steady state of particle alignment (see Figure 5.3.5).

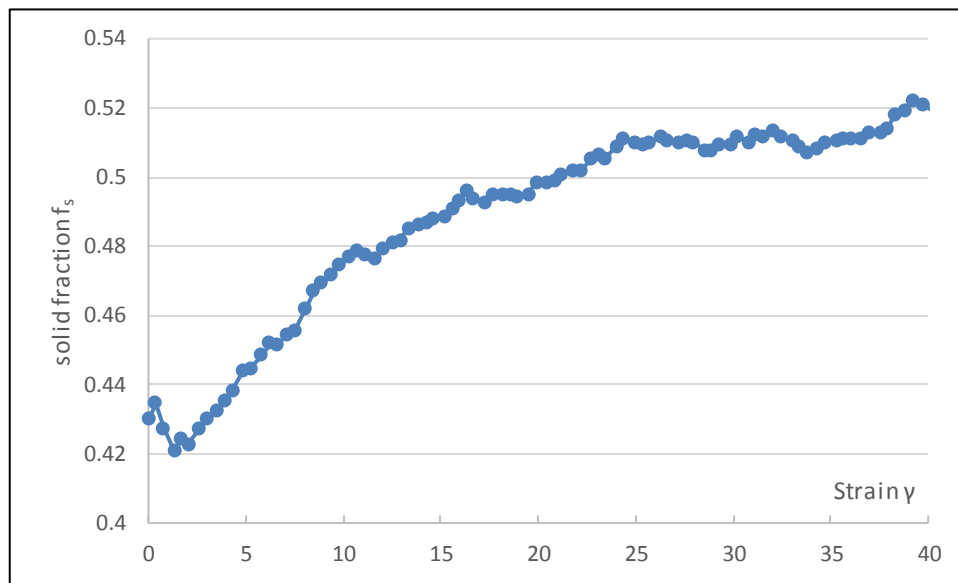


Figure 5.3.8: Solid fraction f_s during the shearing phase for a normal stress applied $\sigma = 6.5kPa$ and an aspect ratio $\alpha_p = 6$.

A slight decrease of f_s is observed after inducing the shearing phase and reaches a minimum after a strain applied at $\gamma = 2$. Here, the bed dilates due to particle interlocking [21] where contacts are stable and require more energy to be broken: this phenomenon is called Reynold's dilatancy [250, 251]. This higher energy is provided to the bed via an initial peak of shear stress (see Chapter 5.5.2) to overcome the yield strength of the particle bed.

5.4 Particles Internal Stress

Two methods for the calculation of the particle internal stress are examined: the Simple Beam Bending [59] and the Euler Equation of Motion [55]. The applicability of these two methods to the designed system in this study is assessed and the most suitable one is identified for further analysis. In both methods, the maximum internal stress value obtained for a particle is defined as its proper internal stress experienced.

5.4.1 Calculation Methods

5.4.1.1 Analytical Solving of Simple Beam Bending

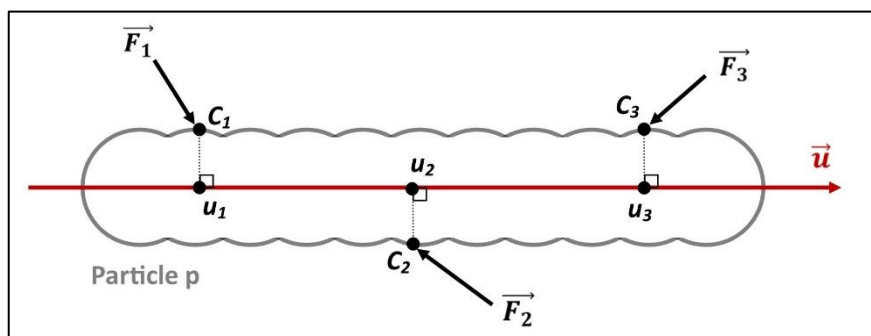
This bending stress calculation method is widely used in mechanical engineering for its simplicity [335]. It requires a force equilibrium on the studied system i.e. static condition.

Applying this bending stress method to calculate particle internal stress implies that the bending stress is considered acting predominantly on particles internal stress.

The bending stress of the particle is calculated from the component of the contact forces \vec{F}_i directed normally to its neutral axis \vec{u} . A cross product is performed to obtain the bending moment \vec{M}_n at contact index n :

$$\vec{M}_n = \sum_{i=1}^n \vec{F}_i \times (\vec{u}_n - \vec{u}_i) \quad 5.4.1$$

With the contact index i sorted by increasing u_i .



The maximum bending moment of a particle is here expected to be located at the position u_n of a contact point rather than in between contacts. Moreover, the bending moment at the first and last contacts are null (see Figure 5.4.1).

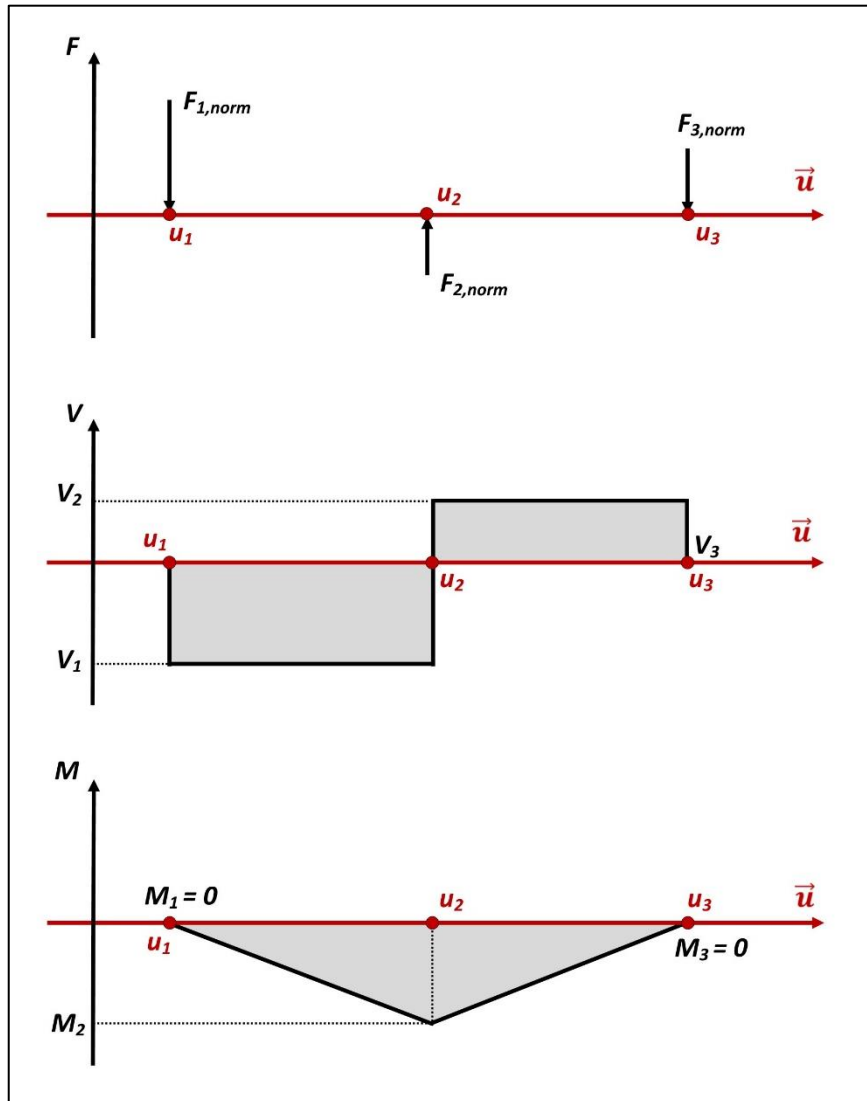


Figure 5.4.1: Typical case of force application on a particle represented by its neutral axis \vec{u} . The shear force V and the bending moment M are calculated based on the magnitude of the normal component of the forces $F_{X,norm}$ and their application point

$$u_x \text{ with } \sum F_{X,norm} = 0.$$

Two-dimensionally, the bending moment at contact n is expressed as:

$$M_n = \sum_{i=1}^n F_{i,norm} (u_n - u_i) \quad 5.4.2$$

Where $F_{i,norm}$ is the normal component of \vec{F}_i .

The shear force V_n at contact index n is expressed as:

$$V_n = \sum_{i=1}^n F_{i,norm} \quad 5.4.3$$

With:

$$M_n = \int_{u_1}^{u_n} V_n du \quad 5.4.4$$

Three-dimensionally, at each contact a plan (P) including \vec{u} exists for which the projections of force vectors \vec{F}_i produce the maximum value of bending moment using Equation 5.4.2. The projection $F_{i,proj}$ of $F_{i,norm}$ on plan (P) is expressed as:

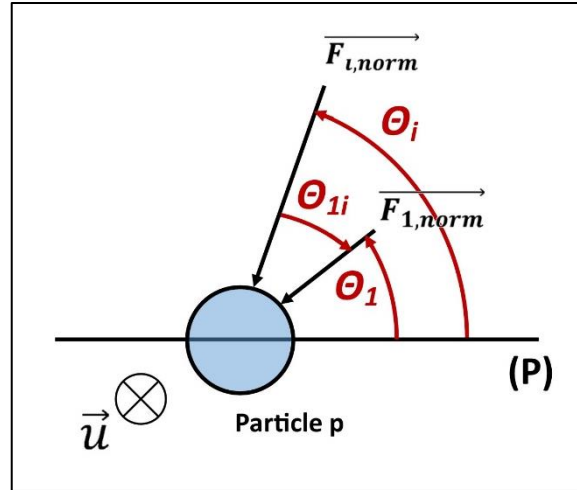
$$F_{i,proj} = F_{i,norm} \cos \theta_i \quad 5.4.5$$

With θ_i the angle from plan (P) to $\vec{F}_{i,norm}$.

To minimise the number of unknown variables, all force projections are expressed as a function of θ_1 :

$$F_{i,proj} = F_{i,norm} \cos(\theta_1 - \theta_{1i}) \quad 5.4.6$$

With $\theta_{1,i}$ the angle from $\vec{F}_{i,norm}$ to $\vec{F}_{1,norm}$ ($\theta_{1i} \in [0; \pi]$).



Signs of angles are here important for the analytical solving and are determined by the direction of $\vec{F}_{i,norm} \times \vec{F}_{1,norm}$: if the cross-product is in the same direction than \vec{u} then θ_{1i} is positive, else θ_{1i} is negative (see Figure 5.4.2).

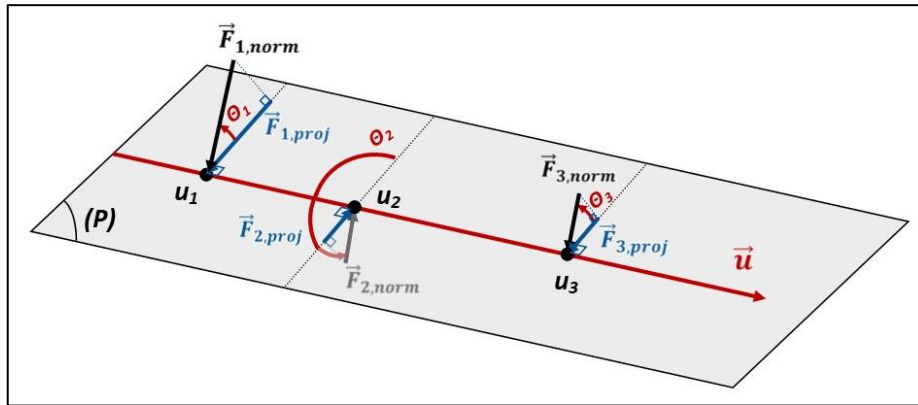


Figure 5.4.2: Projection $\vec{F}_{x,proj}$ of the normal component $\vec{F}_{x,norm}$ of contact force on a defined plane (P) and θ_x the angle between these two vectors.

$$\theta_{1,i} = \text{Sign}(\theta_{1,i}) \cdot \text{Abs}(\theta_{1,i}) \quad 5.4.7$$

$$\theta_{1i} = \frac{(\vec{F}_{i,norm} \times \vec{F}_{1,norm}) \cdot \vec{u}}{\|\vec{F}_{i,norm} \times \vec{F}_{1,norm}\|} \cdot \cos^{-1} \left(\frac{\vec{F}_{i,norm} \cdot \vec{F}_{1,norm}}{\|\vec{F}_{i,norm}\| \cdot \|\vec{F}_{1,norm}\|} \right) \quad 5.4.8$$

The bending moment of the particle at contact index n for a selected plan (P) is then expressed as:

$$M_{n,(P)} = \sum_{i=1}^n F_{i,norm} \cos(\theta_1 - \theta_{1i}) (u_n - u_i) \quad 5.4.9$$

The minimum and maximum bending moment are found when:

$$M'_{n,(P)} = \frac{dM_{n,(P)}}{d\theta_1} = 0 \quad 5.4.10$$

The derivative of $M_{n,(P)}$ is developed:

$$M_{n,(P)} = \sum_{i=1}^n F_{i,norm} (\cos \theta_1 \cos \theta_{1i} + \sin \theta_1 \sin \theta_{1i}) (u_n - u_i) \quad 5.4.11$$

With $\cos(a + b) = \cos a \cos b + \sin a \sin b$

$$M'_{n,(P)} = \sum_{i=1}^n F_{i,norm} (\cos \theta_1 \sin \theta_{1i} - \sin \theta_1 \cos \theta_{1i}) (u_n - u_i) \quad 5.4.12$$

$$M'_{n,(P)} = \sum_{i=1}^n F_{i,norm} \left(\frac{1-t^2}{1+t^2} \sin \theta_{1i} - \frac{2t}{1+t^2} \cos \theta_{1i} \right) (u_n - u_i) \quad 5.4.13$$

With $t = \tan(\theta_1/2)$ and $\theta_1 \in [0; \pi]$.

$$M'_{n,(P)} = 0 \quad 5.4.14$$

$$\sum_{i=1}^n F_{i,norm} (t^2 \sin \theta_{1i} + 2t \cos \theta_{1i} - \sin \theta_{1i}) (u_n - u_i) = 0 \quad 5.4.15$$

The 2nd degree polynomial of t is solved ($at^2 + bt + c = 0$):

$$a = \sum_{i=1}^n F_{i,norm} \sin \theta_{1i} (u_n - u_i) \quad 5.4.16$$

$$b = 2 \sum_{i=1}^n F_{i,norm} \cos \theta_{1i} (u_n - u_i) \quad 5.4.17$$

$$c = - \sum_{i=1}^n F_{i,norm} \sin \theta_{1i} (u_n - u_i) \quad 5.4.18$$

The two real roots of θ_1 are:

$$\theta_{1,1} = 2 \tan^{-1} \left(\frac{-b - \sqrt{\Delta}}{2a} \right) \quad 5.4.19$$

$$\theta_{1,2} = 2 \tan^{-1} \left(\frac{-b + \sqrt{\Delta}}{2a} \right) \quad 5.4.20$$

With $\Delta = b^2 - 4ac$.

The maximum absolute bending moment is selected as bending moment at contact index n :

$$M_n = \text{Max} \left(\text{Abs} \left(M_n(\theta_{1,1}) \right), \text{Abs} \left(M_n(\theta_{1,2}) \right) \right) \quad 5.4.21$$

Once the bending moment is calculated for all contacts N on particle p , the maximum value is selected as bending moment M_p of the particle:

$$M_p = \text{Max}(M_1, \dots, M_N) \quad 5.4.22$$

The bending stress σ_p of particle p is then obtained with the simple beam bending stress formula:

$$\sigma_p = \frac{M_p \cdot y}{I_u} \quad 5.4.23$$

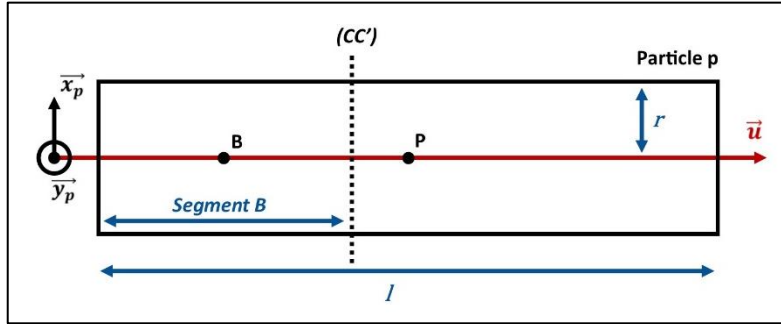
With y the perpendicular distance to neutral axis \vec{u} and I_u the second moment of area of neutral axis.

A cylindrical shape of the particles is assumed, therefore $y = r$ the radius of an element sphere and:

$$I_u = \frac{\pi r^4}{4} \quad 5.4.24$$

5.4.1.2 Euler Equation of Motion

The following methodology is used to calculate discretely the internal stress of the particles [55] from its contact forces. Further calculations are performed integrally in the particle's referential $(\vec{x}_p, \vec{y}_p, \vec{u})$.



A cross-section (CC') of the particle, normal to its neutral axis \vec{u} , splits the particle into two segments, one of them designated as *Segment B*. The internal normal force $\vec{N} = (0, 0, N)$ and shear force $\vec{V} = (V_x, V_y, 0)$ on (CC') are given by the following equation:

$$\vec{N} + \vec{V} + \sum \overrightarrow{F_{l,segB}} + \overrightarrow{G_B} = m_B \cdot \overrightarrow{a_B} \quad 5.4.25$$

Where $\overrightarrow{F_{l,segB}}$ are the contact forces on *Segment B*, $\overrightarrow{G_B}$ the gravity force of *Segment B* and m_B the mass of *Segment B*.

The translational acceleration of point B (centre of gravity of *Segment B*) $\overrightarrow{a_B}$ is calculated as follows:

$$\overrightarrow{a_B} = \overrightarrow{a_P} + \overrightarrow{\omega_P} \times (\overrightarrow{\omega_P} \times \overrightarrow{PB}) + \overrightarrow{\omega_P} \times \overrightarrow{PB} \quad 5.4.26$$

With P the centre of gravity of the particle, \vec{a}_p the translational acceleration of the particle, $\vec{\omega}_p$ its rotational velocity and $\vec{\dot{\omega}}_p$ its rotational acceleration given by:

$$\vec{\dot{\omega}}_p = I_p^{-1} \cdot \vec{M}_p \quad 5.4.27$$

\vec{M}_p is the moment of forces on P and I_p the principal moment of inertia of the particle, here assumed having a cylindrical shape:

$$I_p = \begin{bmatrix} \frac{m_p l^2}{12} + \frac{m_p r^2}{4} & 0 & 0 \\ 0 & \frac{m_p l^2}{12} + \frac{m_p r^2}{4} & 0 \\ 0 & 0 & \frac{m_p r^2}{2} \end{bmatrix} \quad 5.4.28$$

With r the radius of the element sphere, m_p the mass of the particle and l its length.

The bending moment $\vec{M} = (M_x, M_y, 0)$ and twisting moment $\vec{T} = (0, 0, T)$ on (CC') are given by:

$$I_B \cdot \vec{\dot{\omega}}_B + \vec{\omega}_B \times (I_B \cdot \vec{\omega}_B) = \sum \vec{BC}_i \times \vec{F}_{i,segB} + \vec{M} + \vec{T} + \vec{B}(CC') \times \vec{V} \quad 5.4.29$$

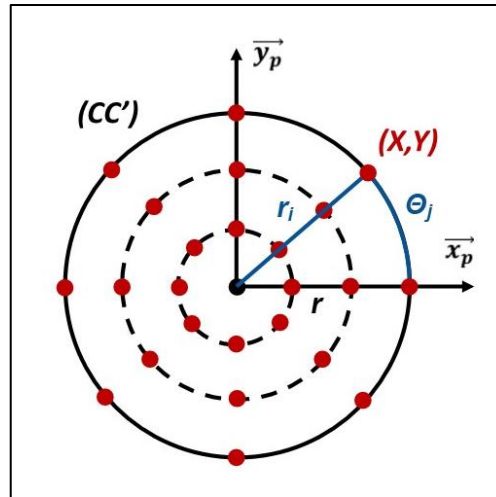
With I_B the second moment of inertia of *Segment B*, C_i the contact point for contact index i , and:

$$\vec{\omega}_B = \vec{\omega}_p \quad \vec{\dot{\omega}}_B = \vec{\dot{\omega}}_p$$

Then, the stress tensor $\sigma(X, Y)$ at coordinates (X, Y) within (CC') is calculated as followed:

$$\sigma(X, Y) = \begin{bmatrix} 0 & 0 & \frac{4V_x(r^2 - X^2) - 6TY}{3\pi r^4} \\ 0 & 0 & \frac{4V_y(r^2 - Y^2) + 6TX}{3\pi r^4} \\ \frac{4V_x(r^2 - X^2) - 6TY}{3\pi r^4} & \frac{4V_y(r^2 - Y^2) + 6TX}{3\pi r^4} & \frac{Nr^2 + 4M_x Y - 4M_y X}{\pi r^4} \end{bmatrix} \quad 5.4.30$$

The stress tensor is diagonalised and the maximum absolute eigenvalue is retained as the internal stress of the particle at that location.



The internal stress is calculated at different locations using discretisation of cylindrical coordinates of the particle (r_i, θ_j, l_k) with $i \in [1, N_r]$, $j \in [1, N_\theta]$ and $k \in [1, N_l]$:

$$X = r_i \cos \theta_j \quad Y = r_i \sin \theta_j$$

The maximum internal stress value found from these (i, j, k) combinations is selected as particle internal stress. Here, the higher the N values, the more accurate the estimation of the maximum internal stress value for the particle.

5.4.2 Discretisation of Location for Euler Equation of Motion Method

Euler Equation of Motion method is used to calculate the particles internal stress at different location within them. The location is determined using a discretisation of cylindrical coordinates: radius, angle and length (see Chapter 5.4.1.2).

5.4.2.1 Radius

It has been demonstrated that the maximum internal stress is located at the particle's surface [55]. Indeed, the bending component of the stress tensor will promote breakage at the surface due to the tensile stress induced. This crack nucleation then propagates within the particles through a preferred cleavage plane following Kendall's theory of breakage [106].

Thus, the particles internal stress is only calculated at the surface of particles.

5.4.2.2 Length

An observation of the particles internal stress calculated along the length shows that the maximum stress is likely to be located at the projection of a particle contact onto the particle neutral axis (see Figure 5.4.3). Indeed, the contact force is suddenly added to the internal force on the cross section (CC') when it reaches the contact location. It explains why there is a sudden change in the particle's internal stress at the location of a contact.

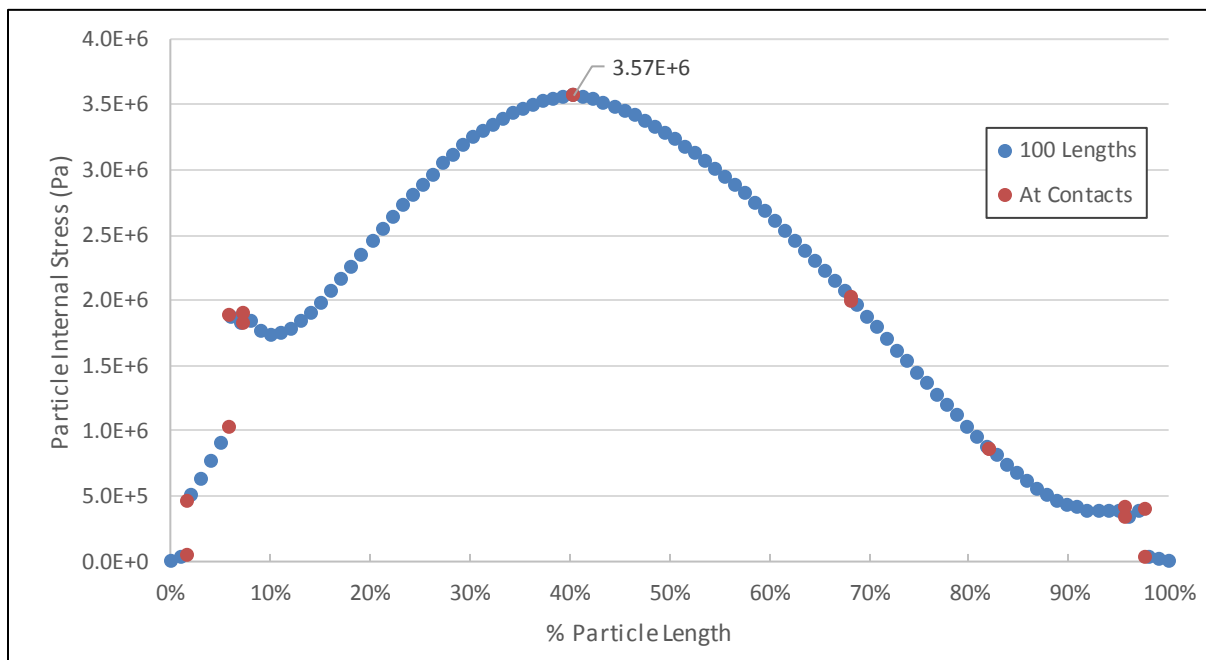


Figure 5.4.3: Internal stress of a particle calculated with Euler Equation of Motion at different length positions: for the particle length discretised at 100 locations and at the location of contacts.

The mean particles internal stress, i.e. the mean value of the individual maximum particle internal stress, is calculated among the particle bed for different length discretisation numbers (see Figure 5.4.4). The higher the discretisation number the closer the calculated mean particles internal stress is to the real maximum value. The plot is fitted using the following equation reaching coefficient of determination $R^2 = 0.99996$:

$$y = y_0 + A_1(1 - e^{-x/t_1}) + A_2(1 - e^{-x/t_2}) \quad 5.4.31$$

$$\lim_{x \rightarrow +\infty} y = y_0 + A_1 + A_2 \quad 5.4.32$$

With $y_0 = 369146$, $A_1 = 16742$, $t_1 = 98.6$, $A_2 = 94831$ and $t_2 = 11.77$.

The real mean particles internal stress is the predicted limit of the fitted curve which is $480720Pa$.

The calculation at the location of contacts has an error of 1.22%, and is in average $5x$ faster than a discretisation number of 100 for the same accuracy. Thus, the calculation at contacts appears as an excellent comprise.

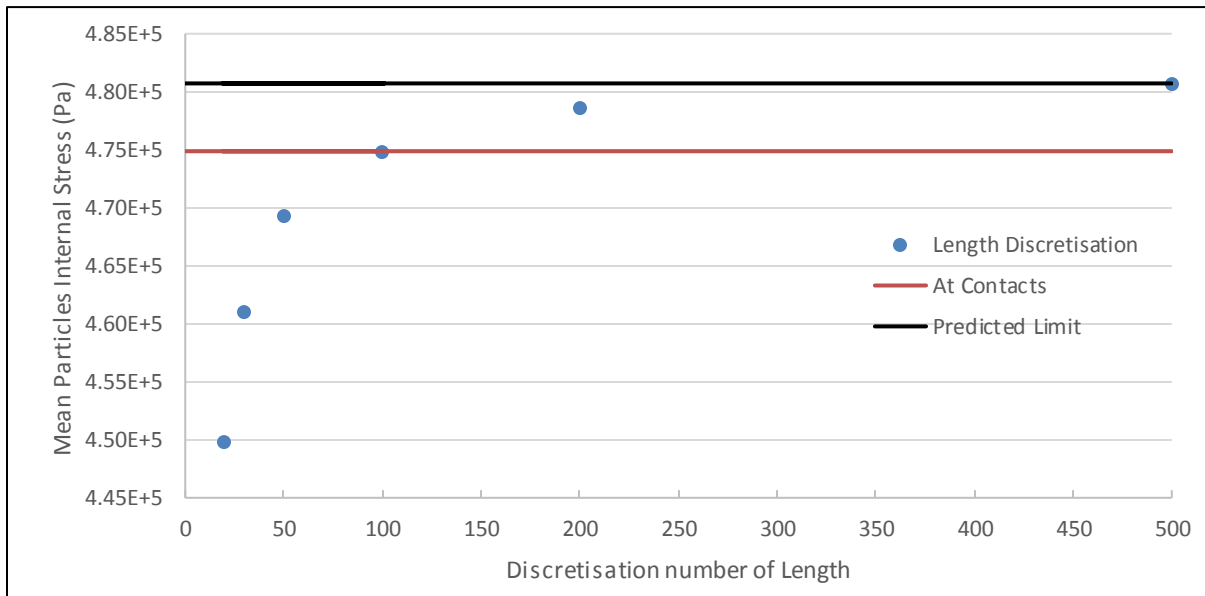


Figure 5.4.4: Mean particles internal stress calculated for different length discretisation numbers and at location of contacts.

5.4.2.3 Angle

The mean particles internal stress is calculated with different discretisation numbers (see Figure 5.4.5). The plot is fitted using the same method as in Chapter 5.4.2.2 reaching coefficient of determination $R^2 = 0.9998$ with $y_0 = 214372$, $A_1 = 8047.7$, $t_1 = 12.82$, $A_2 = 253174$ and $t_2 = 2.372$.

The real mean particles internal stress is the predicted limit of the fitted curve which is $475604Pa$.

An angle discretisation number of 30 is a good compromise between computational resources and accuracy, with an error of 0.15%.

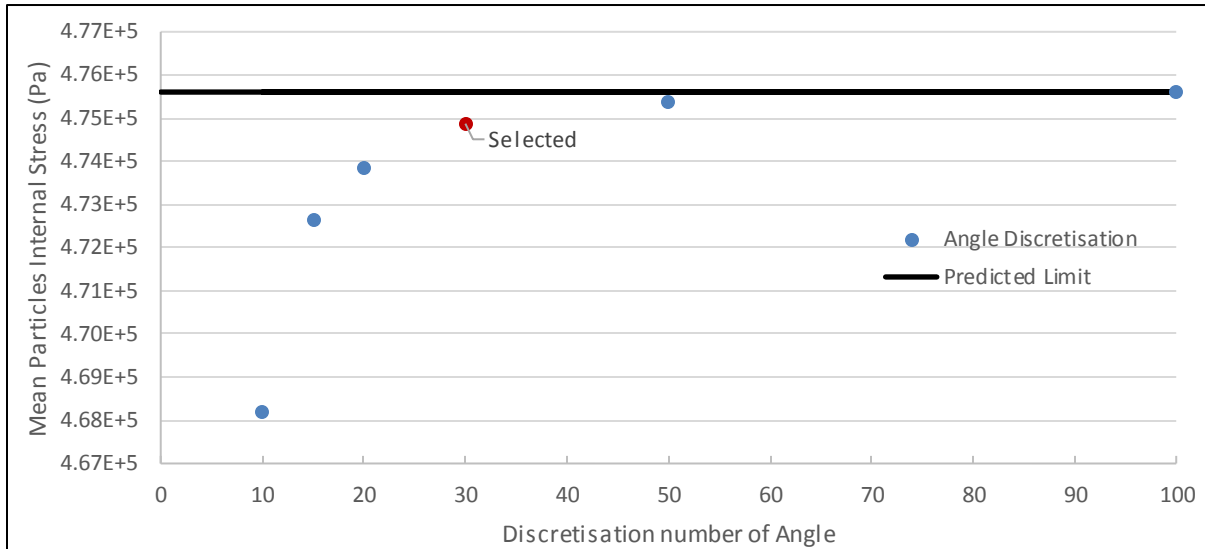


Figure 5.4.5: Mean particles internal stress calculated for different angle discretisation numbers.

5.4.2.4 Concluding Remarks

Euler Equation of Motion is a discretised calculation method, and a selection of discretisation numbers is made with a consideration for the computational resources to accuracy ratio. The found comprise is a calculation of the particle's internal stress at its surface, for a length corresponding to the location of its contacts, and at 30 different angles. The error associated with this selection of discretisation parameters is 1.37%.

5.4.3 Comparison of Methods

A comparison of the Simple Beam Bending (SBB) and Euler Equation of Motion (EEM) methods for particles internal stress calculation is performed to select the most adequate.

SBB (see Chapter 5.4.1.1) is solved analytically to find the maximum bending stress within a particle and has the advantage to be calculated faster. It requires the assumptions that the particle is in quasi-static state and that bending stress is the dominant component of the particles internal stress. EEM (see Chapter 5.4.1.2) is a discrete calculation and requires more time and computational resources to solve. This method can be used for all flow regimes and considers all types of internal stress within particles.

EEM results are considered as reference values to evaluate if the faster and easier SBB method can be used for the performed simulations.

The mean particles internal stress is overestimated using SBB (see Figure 5.4.6) showing that at least one of the assumptions for the use of this method is not valid.

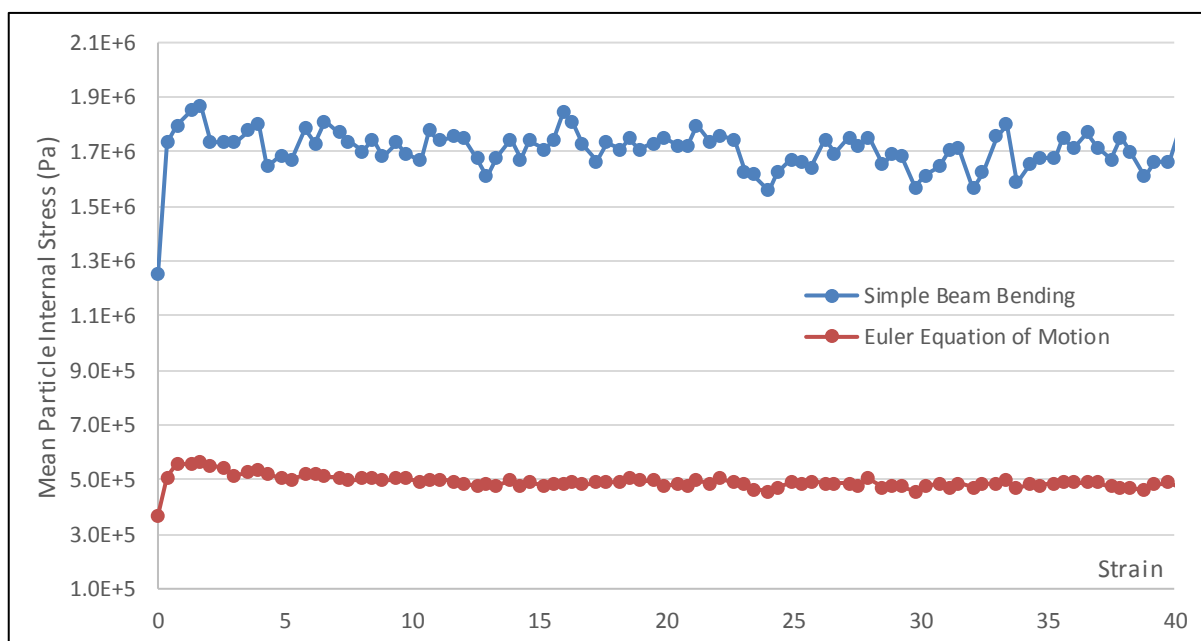


Figure 5.4.6: Mean particle internal stress calculated with Simple Beam Bending and Euler Equation of Motion methods.

Having a closer look at the internal stress of a single particle along its length (see Figure 5.4.7), the stress doesn't reach zero at the last contact for SBB method as it is supposed to in quasi-static case. It means that the forces on the particle system are not balanced enough for SBB to be used for the performed simulations.

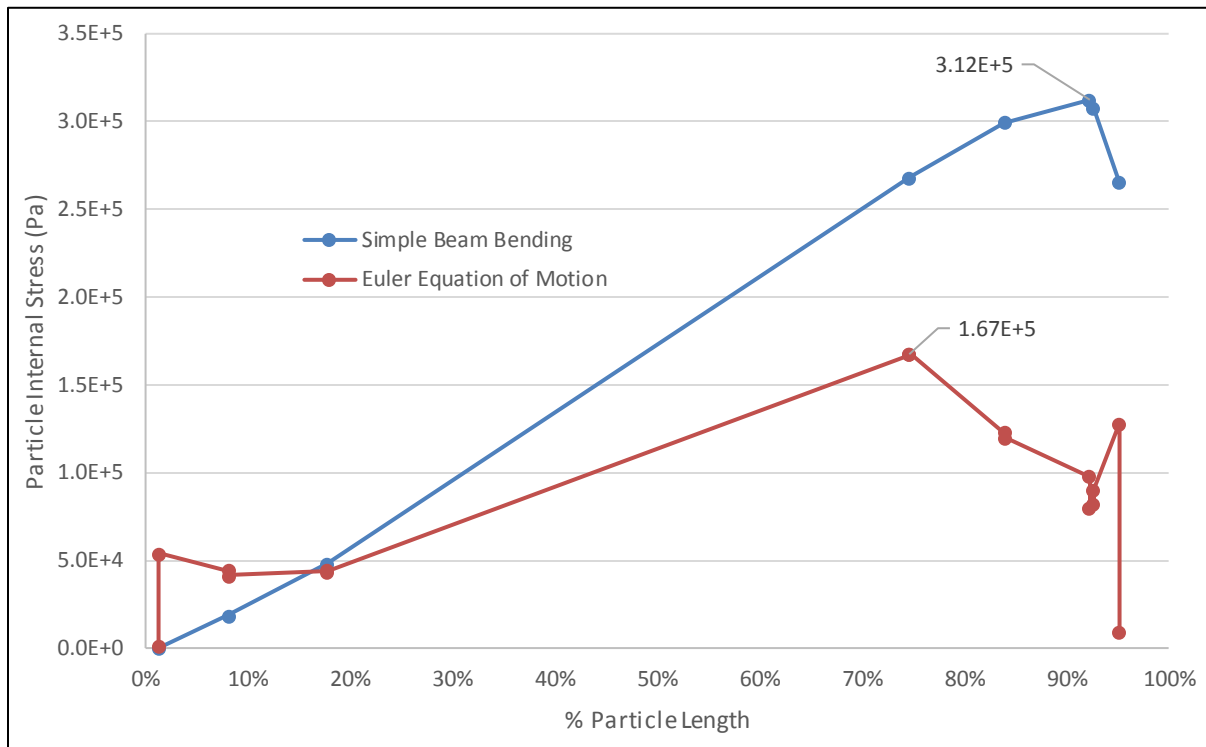


Figure 5.4.7: Internal stress of a particle along its length, calculated with Simple Beam Bending and Euler Equation of Motion methods

Thus, the EEM method is used for the calculation of particles internal stress in all further analysis.

5.5 Optimisation of Parameters

5.5.1 Wall Mass

The normal stress applied on the particle bed is desired to be constant throughout the shearing phase. Indeed, the normal stress is reported being the major parameter affecting particles internal stress [156], therefore a constant normal stress allows a

finer analysis of correlations for the other variables involved (e.g. particles alignment) by reducing the number of degrees of freedom.

At first, the upper wall mass is calculated as follows:

$$Mass_{wall_original} = F_{w,control} \times g \quad 5.5.1$$

With $F_{w,control}$ the normal force set to the upper wall (see Chapter 5.2.2.3) and $g = 9.81m.s^{-2}$ the gravitational acceleration on Earth. Here, the upper wall behaves like a weight where the normal force corresponds to its gravitational force on Earth. The lower wall position is fixed, so the value of its mass does not affect the simulations.

The normal stress measured on the upper wall exhibits non-negligible variations. Indeed, the wall acceleration is insufficient to adjust its position during the rearrangement of the particle bed in the shearing phase. Here, the normalised standard deviation of normal stress equals 9.4%.

As given by Newton's second law of motion (see Equations 2.4.1 and 2.4.2), the wall acceleration is inversely proportional to the wall mass for a given normal force. Therefore, the wall mass is reduced to increase wall acceleration. The wall mass is decreased from its original value using a multiplier:

$$Mass_{wall_adjusted} = Mass_{wall_original} \times Multiplier \quad 5.5.2$$

An inductive study is performed to find the multiplier for which minimum normal stress variations are observed (see Figure 5.5.1).

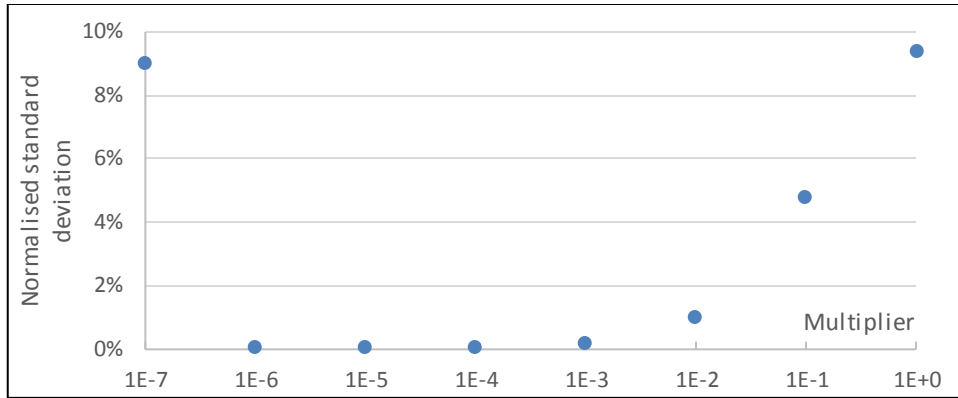


Figure 5.5.1: Normalised standard deviation of normal stress for different wall mass multipliers.

It must be noted that if the wall acceleration is too high, the wall over-reacts to the rearrangement of the particle bed and jump out of the simulation environment: this is happening for $Multiplier = 10^{-8}$. The safe option of $Multiplier = 10^{-5}$ is selected which corresponds to a normalised standard deviation of 0.1%: the normal stress can here be considered as constant (see Figure 5.5.2).

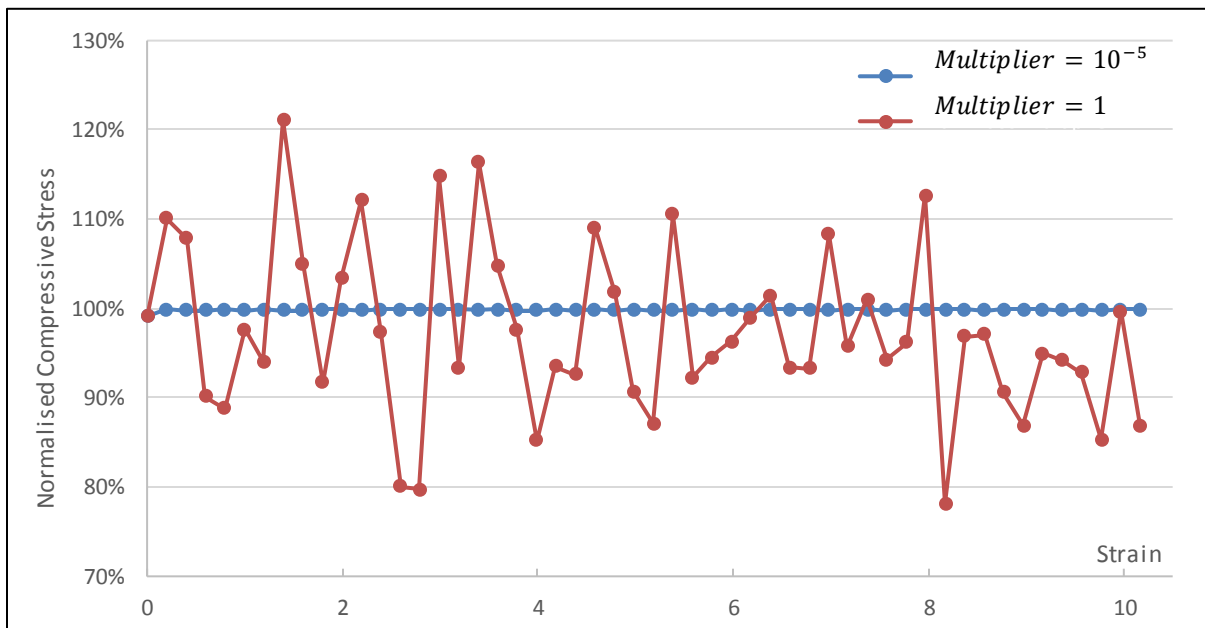


Figure 5.5.2: Compressive stress during shear phase for wall mass multiplied by 1 and 10^{-5} . The stress values are normalised over the target value.

5.5.2 Strain Rate and Flow Regime

The selection of strain rate (see Equation 2.4.4) applied to the particle bed impacts its flow regime in the shearing phase. Indeed, the type of inter-particulate contact is mostly determined by their relative speed, the frictional part of contact forces and interlocking [252, 253].

The flow regime of a granular assembly is determined by the effect of the imposed strain rate on the stress ratio (see Equation 2.4.6) in the steady state. A particle bed in an AFD typically experiences a quasi-static flow regime [1, 8, 9, 108, 156, 191, 235] where the momentum transfer is governed by frictional forces between particles [112, 114] and is independent of the shear rate [115]. Indeed, most of the energy is dissipated by frictional contact rather than inter-particulate damping [24] and the kinetic energy can be considered negligible [205]. Therefore, a quasi-static flow regime of the particle bed is desired in this study to be representative of the mechanical behaviour of a particle bed in an AFD. In quasi-static flow of non-cohesive assembly, the stress ratio (and shear stress) is constant [112, 191, 235], independent of the strain rate [115, 116], and scales with the angle of internal friction by the Coulomb's law of static friction [1, 152-154] (see Equation 2.3.3).

It has been demonstrated that a strain rate varying in the range of 0 to $5s^{-1}$ doesn't impact the amount of attrition of low aspect ratio particles for the same applied strain in DEM simulation of particle agitation [108], demonstrating a quasi-static flow regime for this range of strain rate.

A range of strain rates are applied to the particle bed within the shear cell and the stress ratio is calculated throughout the shearing phase (see Figure 5.5.3). As expected, the stress ratio increases to a peak during the transitional state [13] at the beginning of the shearing phase before reaching a steady state [258] after a strain applied of about 3. It is noted that the initial value of shear cell height is taken for the calculation of the dimensionless strain (see Equation 2.4.4 and 2.4.5). The average value of stress ratio in steady state is considered as a characteristic value for the mechanical behaviour of the particle bed [13, 21, 149]. It is assumed that the possible initial shock disturbance due to the sudden acceleration of the walls [24] disappears when entering the steady state of stress ratio. Small variations of stress ratio still occur

in the steady state due to the “slip-and-stick” behaviour of particles in this flow regime [1, 116]. It is observed that a strain rate of $200s^{-1}$ increases the value of stress ratio, whilst it remains similar for $2s^{-1}$ and $20s^{-1}$. Indeed, the angle of internal friction in steady state for $2s^{-1}$, $20s^{-1}$ and $200s^{-1}$ are respectively 24° , 24.5° and 27.4° .

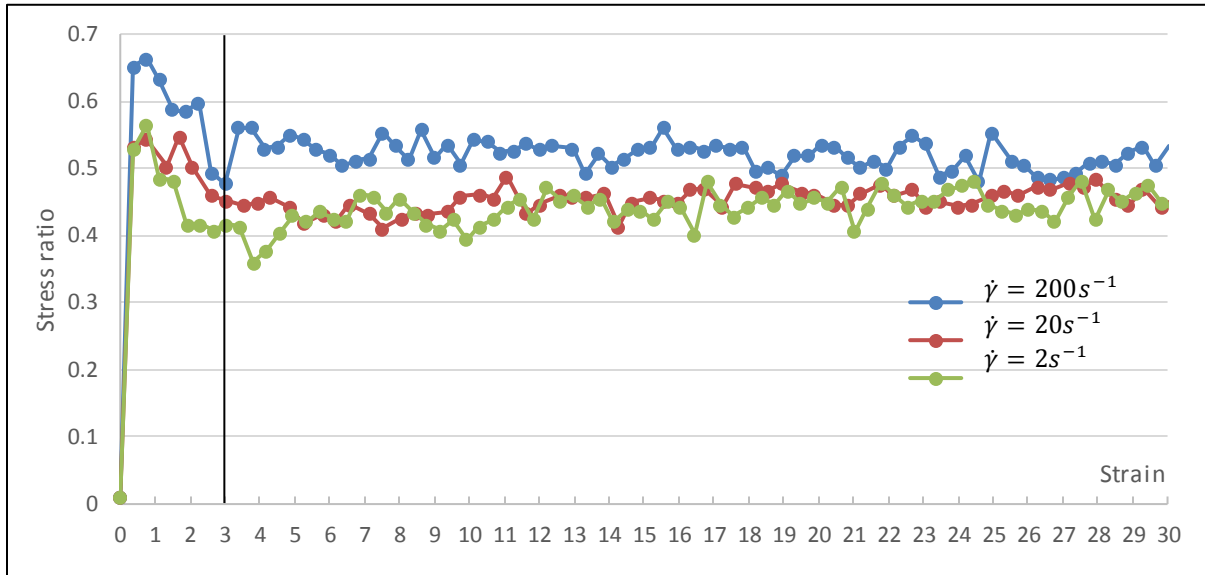


Figure 5.5.3: Stress ratio during the shearing phase for a strain rate of 2, 20 and $200s^{-1}$

The maximum strain rate conserving the mechanical behaviour of the particle bed is selected for further simulations to decrease the simulation time, here $20s^{-1}$.

5.5.3 Young’s Modulus

The median Young’s modulus of β -LGA has been determined experimentally [18] in Chapter 4 and equals $1.9GPa$.

It is common practice in DEM simulations to scale down the Young’s modulus to increase the Rayleigh time step (see Chapter 5.2.3.1), which reduces the computational cost and time required to perform the simulations. The elastic modulus is generally scaled down by several orders of magnitude [55].

Simulations are performed to determine if scaling down the Young’s modulus from its reported value modifies the mechanical behaviour of the particle bed. It is observed

that scaling the Young's modulus down to 19MPa (i.e. by a factor of 100) results in an instability of the particle bed where particles are penetrating the walls (see Figure 5.5.4). Here, particles are too soft and penetrate their respective overlap volume of their clumped element spheres (see Chapter 5.2.1.1) during contact. It creates an artefact of calculation where the same contact force is calculated multiple times.

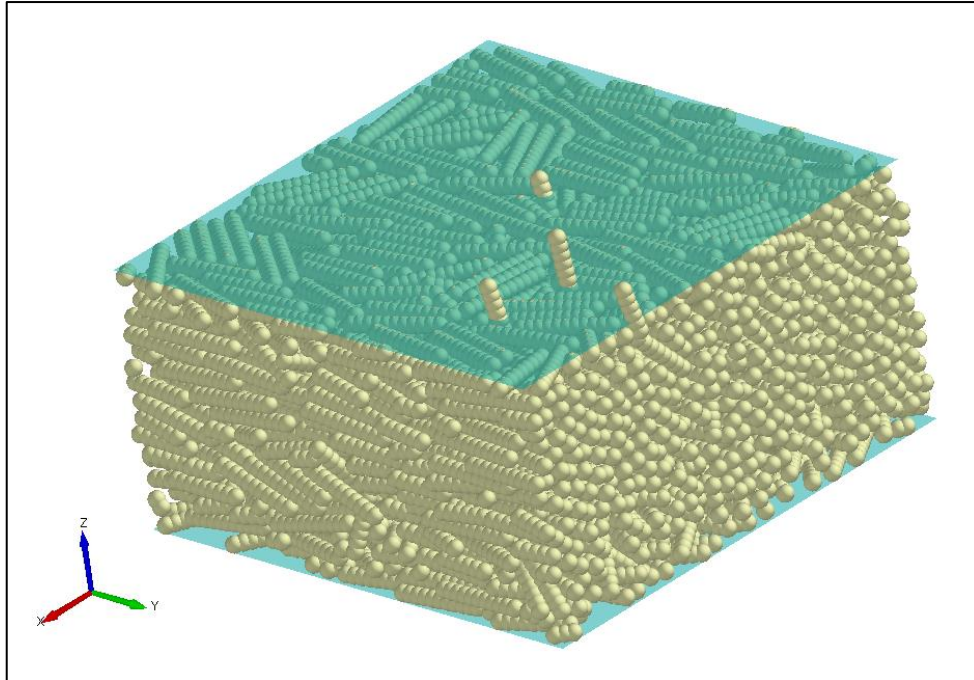


Figure 5.5.4: Shear cell at $\gamma = 40$ with particles at $E = 19\text{MPa}$. A few particles have penetrated the upper wall.

$E = 19\text{MPa}$ being out of scope, simulations are performed for $E = 190\text{MPa}$ and the reported value $E = 1.9\text{GPa}$. The stress ratio is lower for $E = 190\text{MPa}$ (see Figure 5.5.5) with a sensible difference in the angle of internal friction in the steady state (i.e. strain $\gamma > 3$): 23.1° with $E = 190\text{MPa}$ instead of 24.5° with $E = 1.9\text{GPa}$.

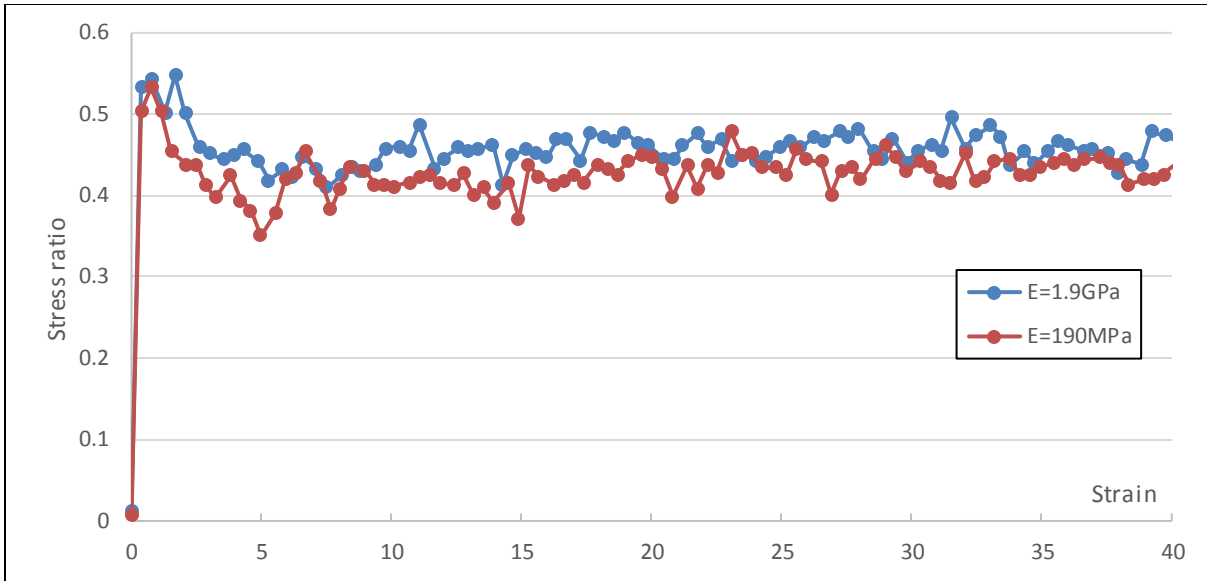


Figure 5.5.5: Stress ratio during in shearing phase for particles Young's modulus of 1.9GPa and 190MPa.

This phenomenon is attributed to the reduction of particles single contact force resulting from 23% to 39% more particle contacts in the bed with the lower Young's modulus (see Figure 5.5.6). Moreover, the strength of particle-particle interlocking, intrinsic phenomenon due to their clumped-spheres morphology [149, 228, 260], is decreases with softer particles.

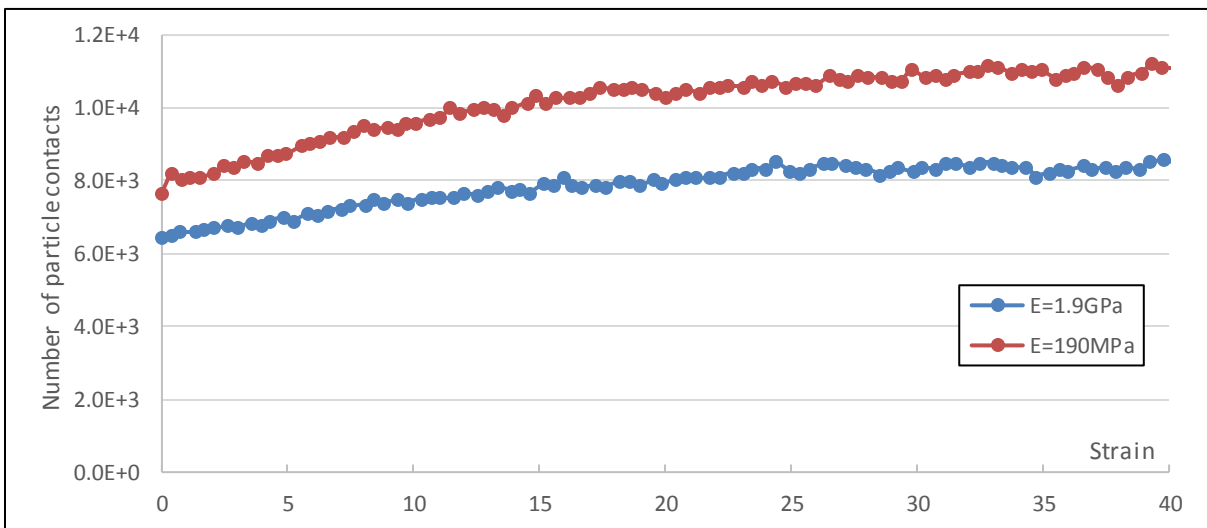


Figure 5.5.6: Number of particle contacts during the shearing phase for particles Young's modulus of 1.9GPa and 190MPa.

Also, the particles internal stress is different for the two Young's modulus. The mean value is in average 6.8% lower for $E = 190\text{MPa}$ (with $\gamma > 3$) (see Figure 5.5.7).

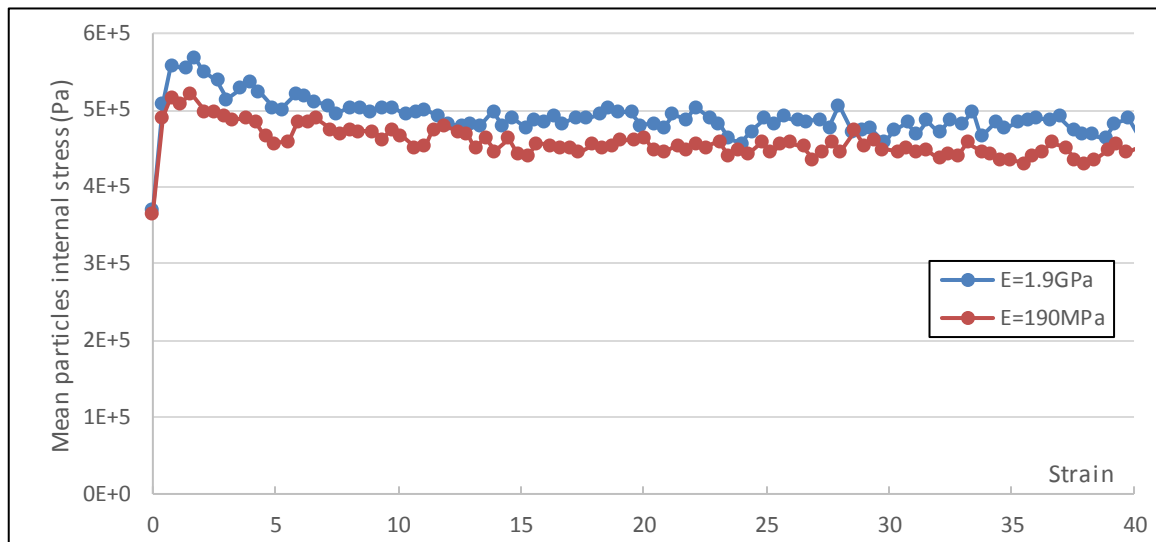


Figure 5.5.7: Mean particles internal stress during the shearing phase for particles Young's modulus of 1.9GPa and 190MPa.

Scaling down particles Young's modulus is found to have an important effect on the mechanical behaviour of the bed and internal stress experienced by particles. This observation is confirmed by comparisons performed between DEM and experimental agitation in vertical axis mixer where the use of realistic elastic modulus produces a similar torque as experimentally observed [188]. Thus, the experimental Young's modulus of β -LGA is selected for all performed simulations.

5.6 Wall Effect

The flat surfaces of the walls may have an impact on particles mechanical behaviour along the simulation. Indeed, the raised coefficient of static friction for particle-wall contacts restrains the ability of particles to rearrange freely when touching the walls. The wall effect is then investigated and the data of affected particles will be removed from further analysis to obtain universal model.

5.6.1 First Layer

To evaluate the importance of the wall effect, two groups of particles are studied: categorised as “wall particles” when they are touching one of the two walls, and “core particles” the remaining ones (see Figure 5.6.1).

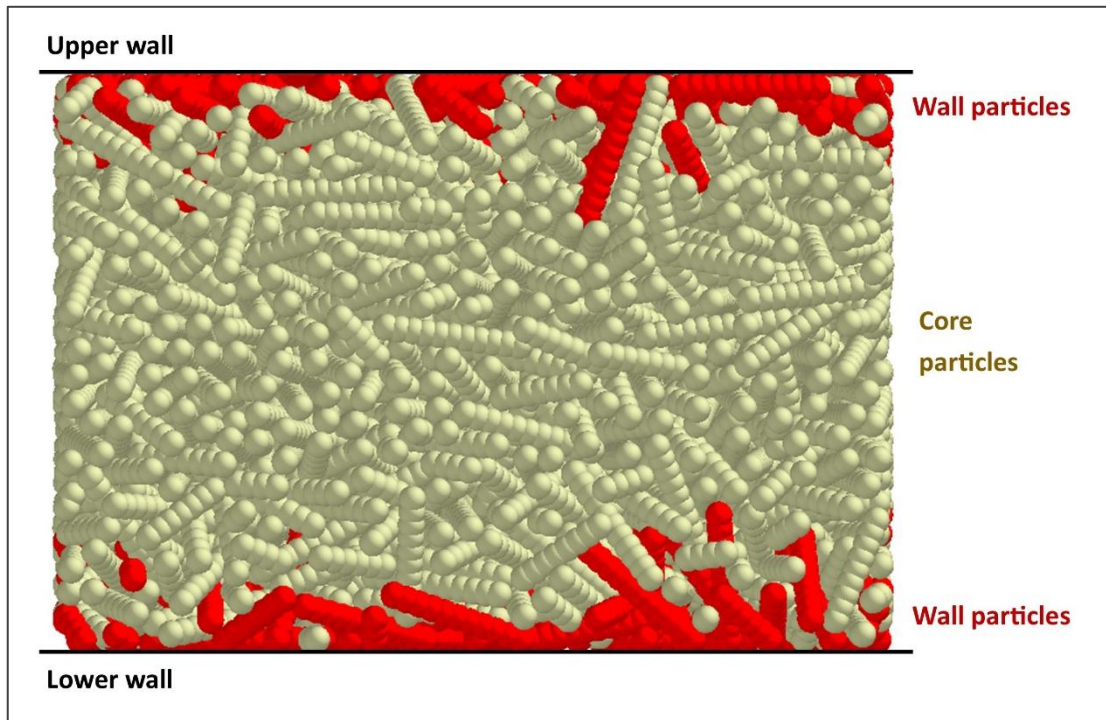


Figure 5.6.1: Side view of particle bed in the shear cell. Wall particles are in contact with one of the two walls.

A quick observation of box plots of particles internal stress for the two groups of particles at $\gamma = 3$ (see Figure 5.6.2) supports the hypothesis that being in contact with a wall affects the internal stress experienced by particles.

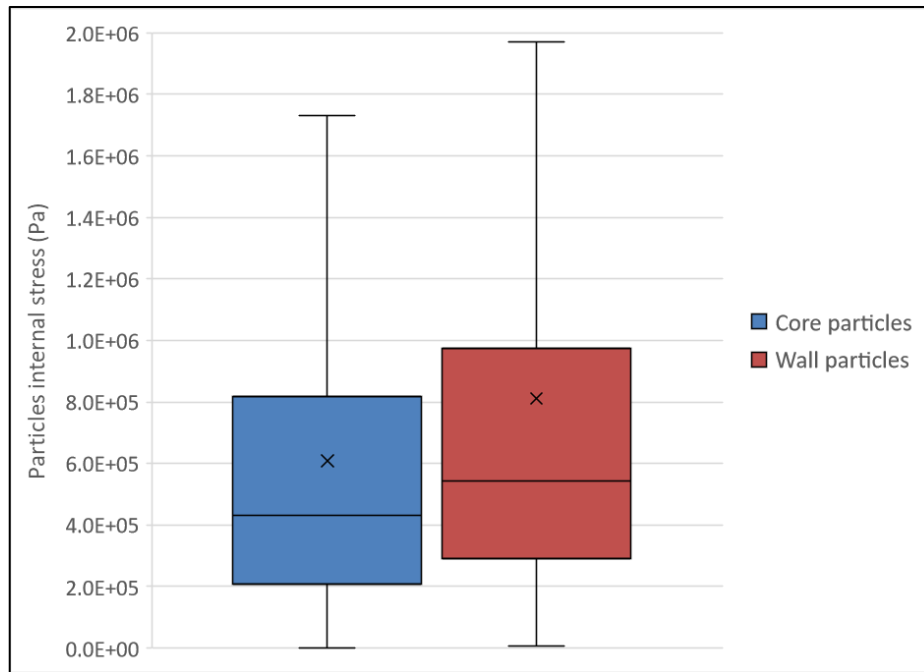


Figure 5.6.2: Box plots of particles internal stress for wall particles and core particles at $\gamma = 3$. The crosses indicate the mean values for the two groups of particles and the horizontal bars are (from bottom to top) the lower boundary, first quartile, median, third quartile and upper boundary. The boundaries of the whiskers is based on the $1.5 \times$ interquartile range value.

Here, wall particles have a higher internal stress. The mean value (see Figure 5.6.3) and standard deviation (see Figure 5.6.4) are also higher for wall particles during the shearing phase.

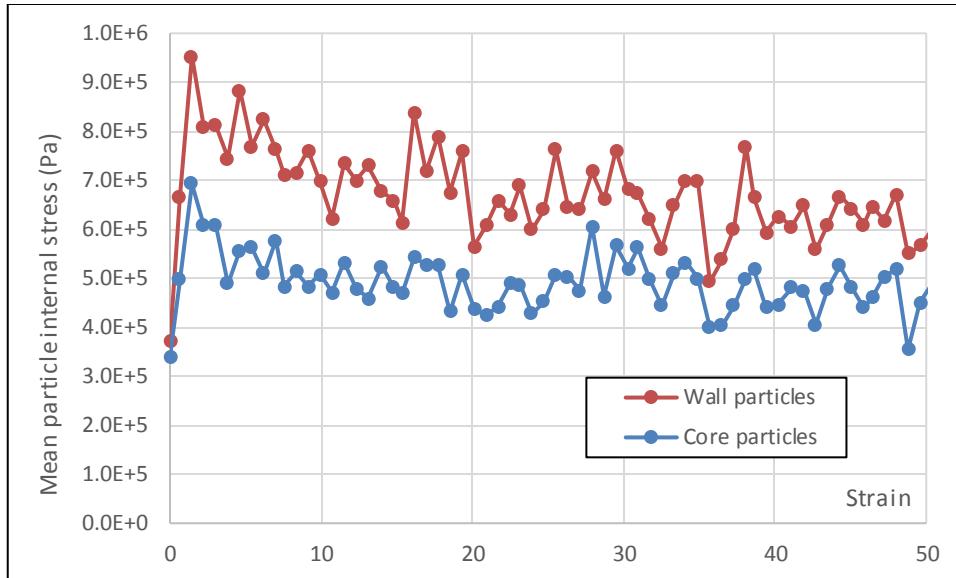


Figure 5.6.3: Mean particle internal stress of wall particles and core particles in the shearing phase.

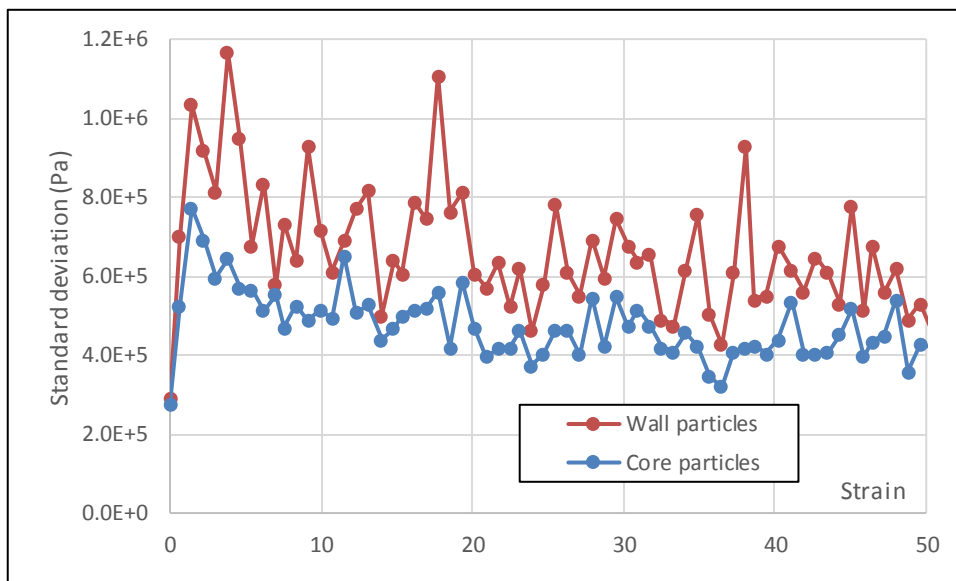


Figure 5.6.4: Theoretical standard deviation of particles internal stress for wall particles and core particles in the shearing phase.

To statute on whether these two groups of particles belong to the same population, a parametric test is performed on the entire particle population at each time recorded with the categorical variable being “in contact with walls”: True or False.

The high number of particles in each group, i.e. around 200 wall particles and 1800 core particles, allows the assumption that the distribution of values for the observed variable follows a normal distribution according to the *Central Limit Theorem* [318].

The particles touching walls represent 8.2 to 12.5% of the total particle population in the bed, which creates unbalanced group sizes and prevents the realisation of variances comparison tests: the hypothesis of homoscedasticity cannot be supported.

Under these conditions, the most robust parametric test for comparison of means, the Welch's T-test [336], is chosen to conduct this analysis. The test of hypothesis is expressed as:

$$H_0: \mu_{walls} = \mu_{core} \quad 5.6.1$$

$$H_1: \mu_{walls} \neq \mu_{core} \quad 5.6.2$$

With μ_{walls} and μ_{core} being respectively the mean particle internal stress for wall and core particles.

The statistic T and the critical threshold $t_{0.975}(\nu)$ for the two-tailed Student law with 5% risk are calculated. When the calculated number of degrees of freedom is a decimal figure, a linear interpolation of the critical threshold is used to obtain the exact critical value.

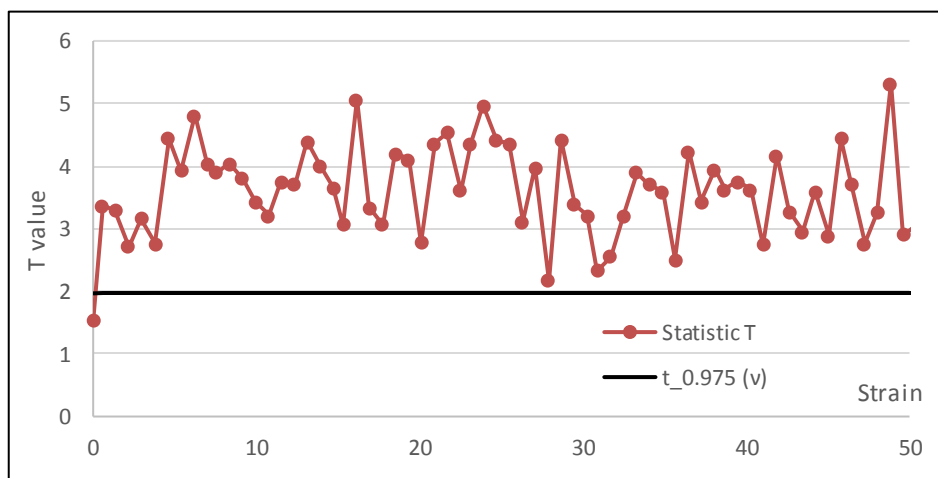


Figure 5.6.5: T value and critical $t_{0.975}(\nu)$ of null hypothesis H_0 during the shearing phase.

The statistic T value is higher than the critical $t_{0.975}(\nu)$ when $\gamma > 3$ (i.e. steady state of stress ratio). The null hypothesis H_0 is therefore rejected, meaning that wall particles and core particles belong to different population.

Thus, wall particles won't be included in further analysis.

5.6.2 Second Layer

It is questioned whether the observed wall effect spreads to the 2nd layer of particles i.e. particles in contact with wall particles.

First observation of box plots of particles internal stress at $\gamma = 3$ (see Figure 5.6.6) shows that the descriptive statistics of particles internal stress are similar for the 2nd layer particles and new core particles (i.e. all particles excepting wall particles and 2nd layer particles).

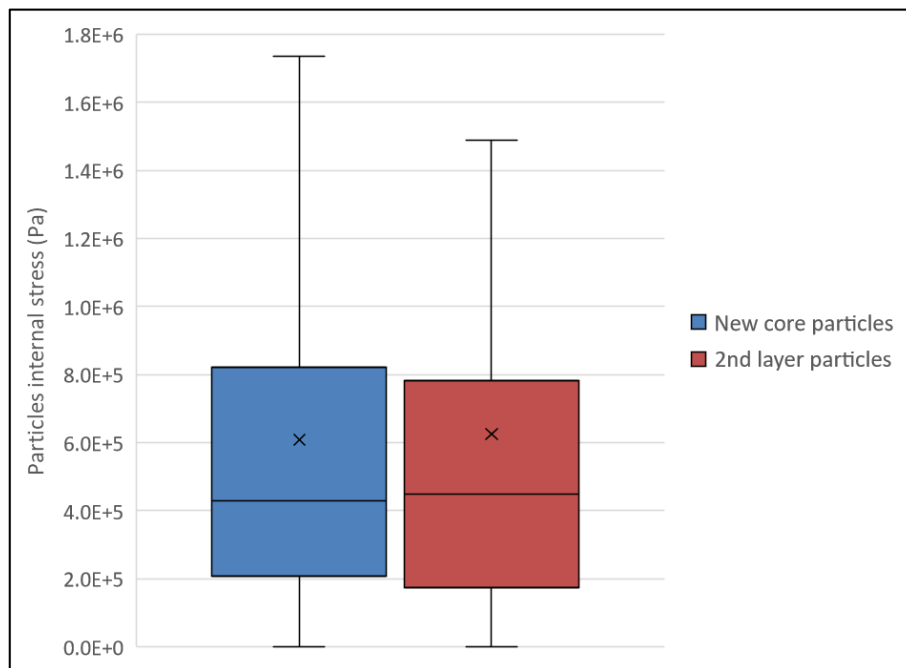


Figure 5.6.6: Box plots of particles internal stress for 2nd layer particles and new core particles at $\gamma = 3$. The crosses indicate the mean values for the two groups of particles and the horizontal bars are (from bottom to top) the lower boundary, first quartile, median, third quartile and upper boundary. The boundaries of the whiskers is based on the $1.5 \times$ interquartile range value.

The mean value (see Figure 5.6.7) and standard deviation (see Figure 5.6.8) of particles internal stress are comparable during the shearing phase. The variations are more significant for the 2nd layer particles, which is attributed to their reduced number i.e. around 70 compared to 1700 new core particles.

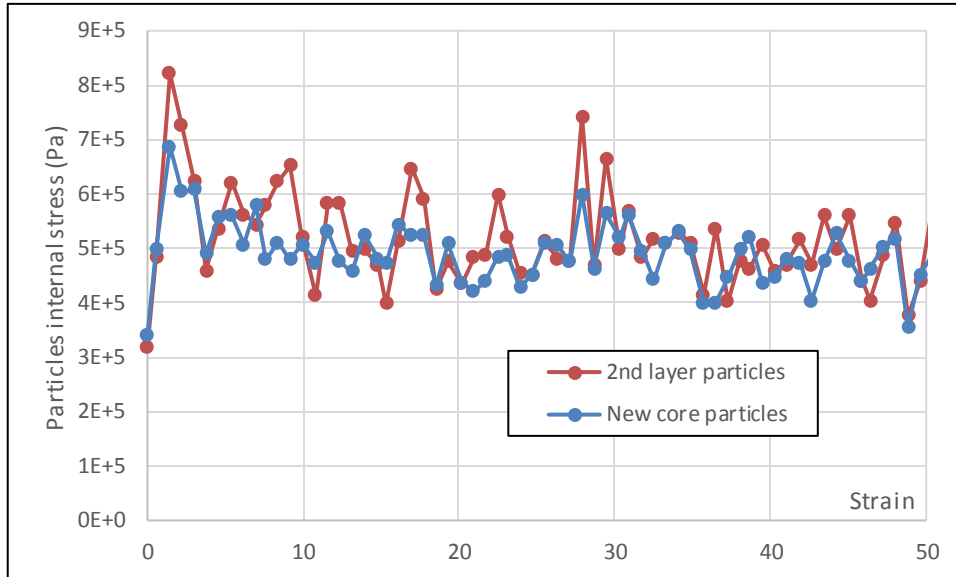


Figure 5.6.7: Mean particle internal stress of 2nd layer particles and new core particles in the shearing phase.

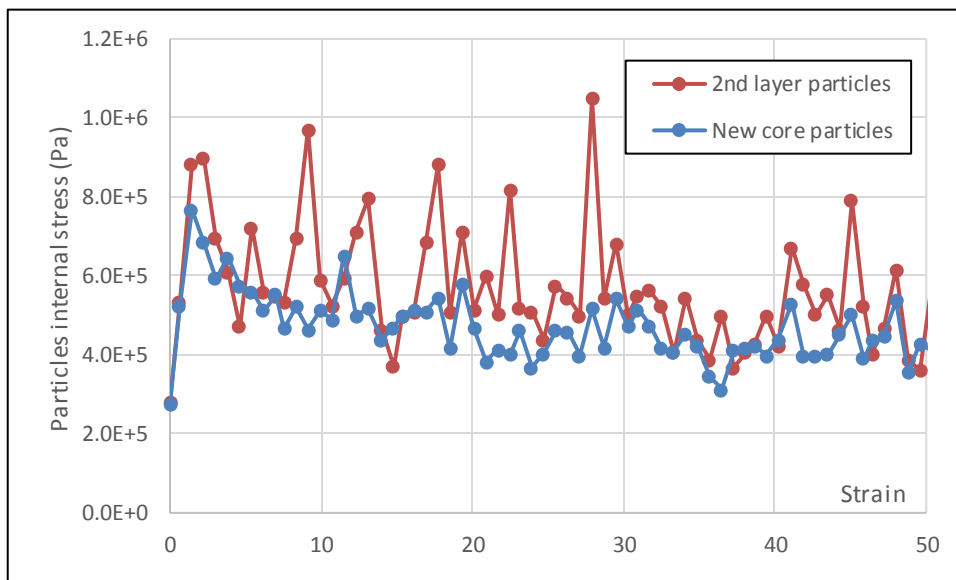


Figure 5.6.8: Theoretical standard deviation of particles internal stress of 2nd layer particles and new core particles in the shearing phase.

The similar values obtained for the two groups of particles supports the hypothesis that the wall effect is limited to the only wall particles and is inexistent or negligible for the 2nd layer particles.

Same as for previous case (see Chapter 5.6.1), the number of particles in the two groups allows the assumption that the *Central Limit Theorem* is respected.

Also, since 2nd layer particles represent 2.4 to 7.4% of the total particle population in the bed, the hypothesis of homoscedasticity cannot be supported.

To confirm the assumption that 2nd layer and new core particles belong to the same population, a Welch's T-test is performed with 5% risk. The test of hypothesis is then expressed as:

$$H_0: \mu_{2nd\ layer} = \mu_{new\ core} \quad 5.6.3$$

$$H_1: \mu_{2nd\ layer} \neq \mu_{new\ core} \quad 5.6.4$$

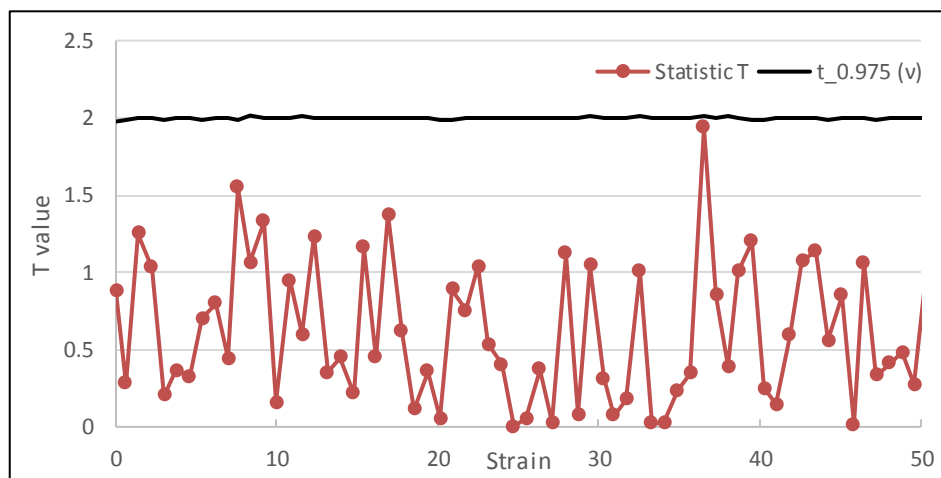


Figure 5.6.9: *T* value and critical $t_{0.975}(v)$ of null hypothesis H_0 during the shearing phase.

The statistic T value is found to be lower than the critical $t_{0.975}(v)$ when $\gamma > 3$ (see Figure 5.6.9). The null hypothesis is therefore accepted, meaning that 2nd layer and new core particles belong to the same population.

Thus, only the core particles population will be considered in further analysis.

5.7 Conclusions

The initial simulation setup is optimised and validated through a series of inductive studies. The velocity profile is close to linear, meaning that the strain is homogeneously effective along the bed height. A strain rate of $20s^{-1}$ is selected as it is the maximum order of magnitude allowing conservation of mechanical behaviour of the particle bed. The wall mass is reduced from its theoretical value – calculated from the force controller value – by a factor of 10^{-5} to ensure a constant compressive stress on the particle bed using the force controller. The Young's modulus couldn't be scaled down to reduce simulation time as it has a significant impact on particles mechanical behaviour, including their internal stress. The internal stress of particles is calculated using the Euler equation of motion method as the simple beam bending method is too sensitive to the absence of force equilibrium on single particle system. Finally, the particles touching the walls are excluded from further analysis as their internal stress is shown to be significantly impacted by their contacts with walls.

This optimised simulation setup is used for the further analysis in Chapter 6 where the correlations between key parameters in the particle bed are assessed from the results of an inductive study with the variation of particle aspect ratio, normal stress and particle ordering.

6 Particles Internal Stress for Agitated Drying Conditions

6.1 Introduction

When processed in agitated dryers, the particles experience mechanical stress which promotes breakage. Understanding how the drying conditions impact the particles internal stress is the key for the selection of drying equipment and parameters to reduce particle breakage.

The objective of this chapter is to correlate the particles internal stress to the mechanistic environment and physical properties of particles, giving insights for the prediction of particle breakage.

A series of simulations are performed for different particle shapes, bed conformations and mechanistic environments for both shearing phase and uniaxial compression to isolate the effect of the shear stress in data analysis. The simulation setup is designed based on the optimisations and parameters selection performed in Chapter 5. In this chapter, the existing correlations between key variables are highlighted and are the basis of further creation of mathematical models for the prediction of the particles internal stress (see Chapter 7).

6.2 Modelling of Distributions

The population of the bed in the performed simulations is composed of approximately 2000 particles. To undertake an effective analysis, the distributions of interest are regressed to models that are well known to fit accurately the studied variables: the particles internal stress and the location of this stress on the particles neutral axis.

6.2.1 Weibull Fitting for Distribution of Particles Internal Stress

The distribution of the particles internal stress is modelled using a cumulative Weibull fit [47, 48]:

$$f(x) = 1 - e^{-(x/\lambda)^k} \quad 6.2.1$$

With λ the scale parameter and k the shape parameter. Here, the greater the k , the narrower the distribution.

Indeed, the Weibull model is known to correctly fit the distribution of particles internal stress and is more appropriate than a normally distributed function [47].

The coefficient of determination R^2 (i.e. method of least residual sum of squares) is selected to assess the quality of the model fitting of the cumulative distribution. Mathematically, this method set the priority on fitting accurately the greatest values, here the data for particles experiencing the highest internal stress i.e. that are the most likely to break.

6.2.2 Gaussian Fitting for Distribution of Maximum Stress Location

The distribution of location of the maximum stress on the particles neutral axis is modelled using a Gaussian fit [318]:

$$f(x) = \frac{1}{\sigma_{dev}\sqrt{2\pi}} e^{-\frac{1}{2}\left(\frac{x-\bar{x}}{\sigma_{dev}}\right)^2} \quad 6.2.2$$

With \bar{x} the mean value of x , σ_{dev} the standard deviation of x , and $x \in (0; L_p)$ with L_p the particle length (see Figure 6.2.1).

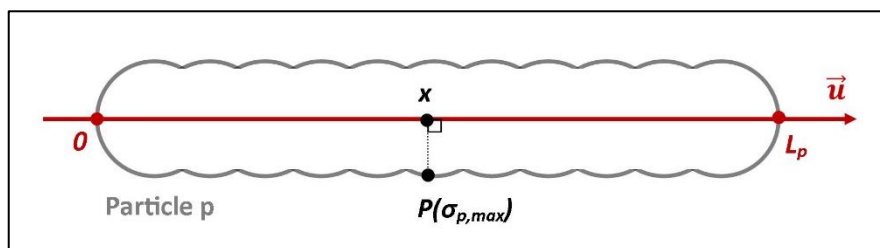


Figure 6.2.1: Position P of maximum particle internal stress and x its projection on the particle neutral axis \vec{u} .

Indeed, it is reported that elongated particles preferably break at their centre and the distribution of breakage location along the particle neutral axis follows a Gaussian model in both attrition cell [191] and compaction simulations [194].

6.3 Simulation Setups

The simulation setup has been optimised in Chapter 5. Particle and geometry properties are listed in Table 5.2.1. The interaction properties are listed in Table 5.2.2. As of conclusion of simulation setup optimisation (see Chapter 5.7), the chosen strain rate is $\dot{\gamma} = 20s^{-1}$ and the wall mass is scaled down by 10^{-5} from its theoretical value.

The varying parameters in this chapter are presented in the following sub-sections.

6.3.1 Particles and Domain Size

The particle bed is monodispersed and the shearing simulations are performed for 5 different aspect ratios $\alpha_p \in [2;6]$. The elongation of particles is varied by changing the number of element spheres n_s composing the particles such as $n_s = 2\alpha_p - 1$, preserving an overlap ratio of 1 (see Figure 6.3.1).

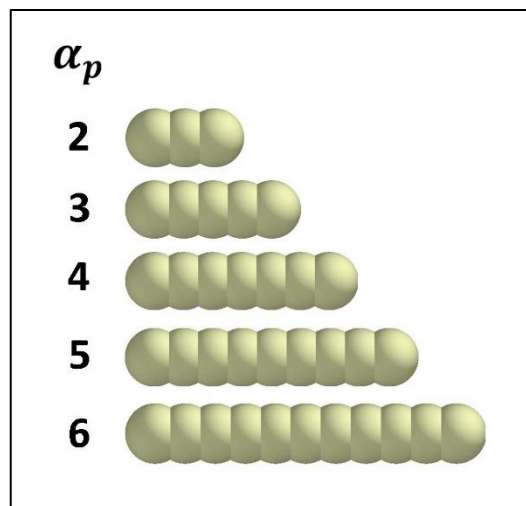


Figure 6.3.1: Particles shape for the different aspect ratio α_p .

The shear cell dimensions are modified so that its height remains unchanged for the different aspect ratios and a 2000 particles bed (see Table 6.3.1). This ensures that the strain rate remains the same without the need to change the walls speed.

Table 6.3.1: Number of element spheres composing the different aspect ratio particles and their corresponding shear cell width.

Aspect ratio	Number of elements	Shear cell width (mm)
2	3	0.7
3	5	1
4	7	1.3
5	9	1.4
6	11	1.5

6.3.2 Stress Environment

6.3.2.1 Shearing Phase

The normal stress is reported as the predominant factor impacting particle breakage in AFD [156]. Therefore, an inductive study is performed on 5 different normal stress values applied by the upper wall on the particle bed whilst being sheared: $\sigma \in [1; 2; 4; 6.5; 10]kPa$. The order of magnitude of the normal stress applied corresponds to the compressive stress experienced by particles in an industrial and pilot scale AFD [1]. The wall mass is scaled down accordingly using the same multiplier 10^{-5} to ensure that the normal stress recorded remains constant (see Chapter 5.5.1). These normal stress values are applied for 5 different aspect ratios, for a total of 25 shearing simulations performed.

6.3.2.2 Uniaxial Compression

The behaviour of the particle bed is analysed on a wider range of normal stress for 10 different values i.e. $\sigma \in [100; 200; 500; 1k; 2k; 5k; 10k; 20k, 50k, 100k]Pa$, with no shear stress involved. This extended range of normal stress applied allows the observation of the effect of the number contact on a wider range. To perform the analysis for different bed conformation (e.g. alignment), the 10 values of compression are applied on a particle bed having experienced different level of strain for the 5 different aspect ratios. To do so, the shearing simulations are stopped when the strain value is reached, then the coefficient of static friction is set to 0 between walls and particles to eliminate the shear stress, and finally the 10 values of normal stress are applied to the particle bed in an ascending order. As the strain required for the bed order parameter to reach steady state increases with aspect ratio, more bed conformations are tested for higher aspect ratio (see Table 6.3.2). In total 250 combinations of aspect ratio, bed conformation and normal stress are analysed in the compression case simulations. For each of these combinations, 5 time recordings of simulation data are performed.

Table 6.3.2: Strain levels applied in compression case simulations for different aspect ratios.

Aspect ratio	Strain applied
2	0; 2; 5; 15
3	0; 2; 5; 10
4	0; 5; 10; 20
5	0; 5; 10; 15; 20
6	0; 3; 5; 10; 15; 20; 25; 30

6.3.3 Data Recording

A total of 50 simulations are performed: 25 in uniaxial compression and 25 in shearing phase. Around 100 data points are conserved for each shearing simulation, and around 50 for each compression simulation (i.e. 5 data points for each of the 10 normal stresses applied). It represents overall 2510 data points for the shearing phase (see Appendix 11) and 1174 for uniaxial compression (see Appendix 12).

6.4 Shearing Phase

The analysis performed for the shearing phase distinguish the transitional phase from the steady state for most of the variables studied. Defining the steady state is a visual exercise made from the observation of corresponding graphs.

6.4.1 Number of Core Particles

As observed in Chapter 5.6, the presence of flat walls and absence of periodic boundary on the \vec{z} axis (i.e. direction of normal stress) have an impact on the internal stress experienced by particles. It has been demonstrated that this “wall effect” is limited to the particles in contact with the walls. Therefore, all analysis are performed on the “core particles” only, i.e. those not in contact with the walls.

The number of core particles can vary slightly throughout the shearing phase but remains relevant for statistical analysis with a minimum population of 1758 (see Figure 6.4.1).

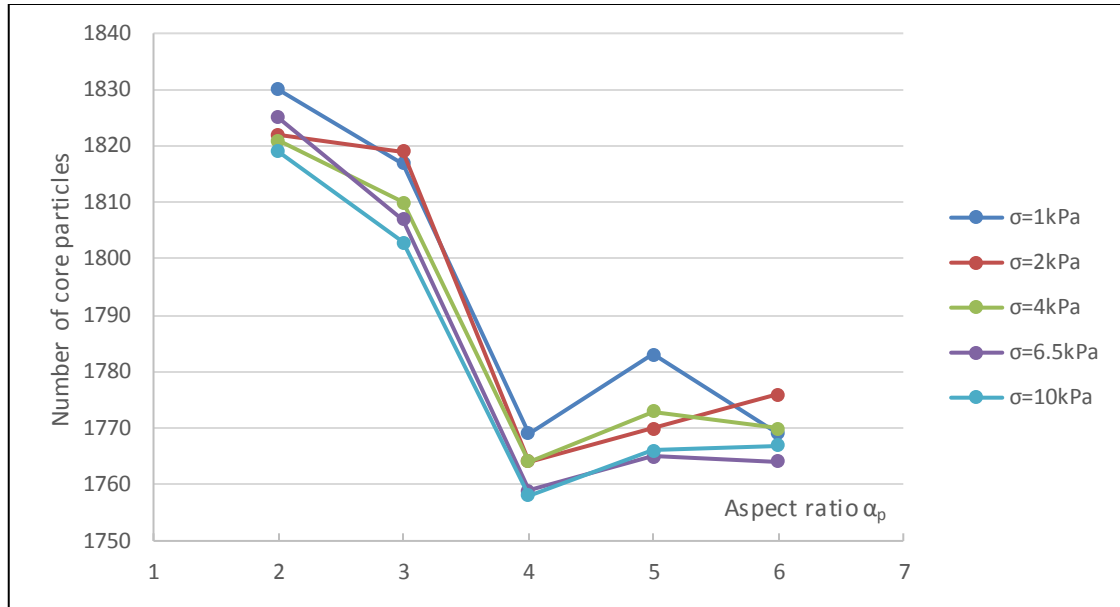


Figure 6.4.1: Minimum number of core particles in shearing simulations for the different aspect ratios α_p and normal stresses σ .

6.4.2 Bed Conformation

6.4.2.1 Particle Alignment

Elongated particles are known to align when mechanical strain is applied on a particle bed [14]. They align in the direction of shearing [188] and their level of ordering is quantified by the order parameter S [205, 279, 280] (see Chapter 5.3.2.1.2). At the beginning of the shearing phase, the bed is at its maximum level of disorder due to the initial random packing. So, S has a minimum value at the beginning of the shearing phase and then increases until reaching a steady state (see Figure 6.4.2).

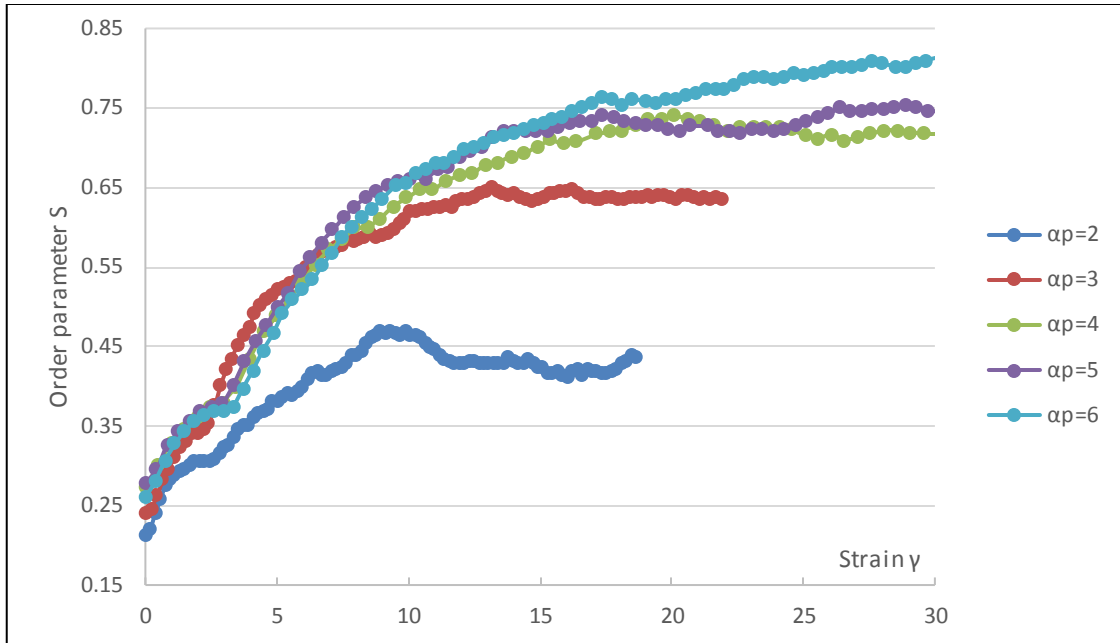


Figure 6.4.2: Order parameter S during the shearing phase for the different aspect ratios α_p and a normal stress at $\sigma = 4kPa$.

The strain required to reach the steady state value of S increases with the particle's aspect ratio (see Figure 6.4.3), meaning that more elongated particles need greater mechanical strain to reach their maximum level of alignment. The normal stress σ applied has no impact for the tested range of values, i.e. $\sigma \in [1; 2; 4; 6.5; 10]kPa$.

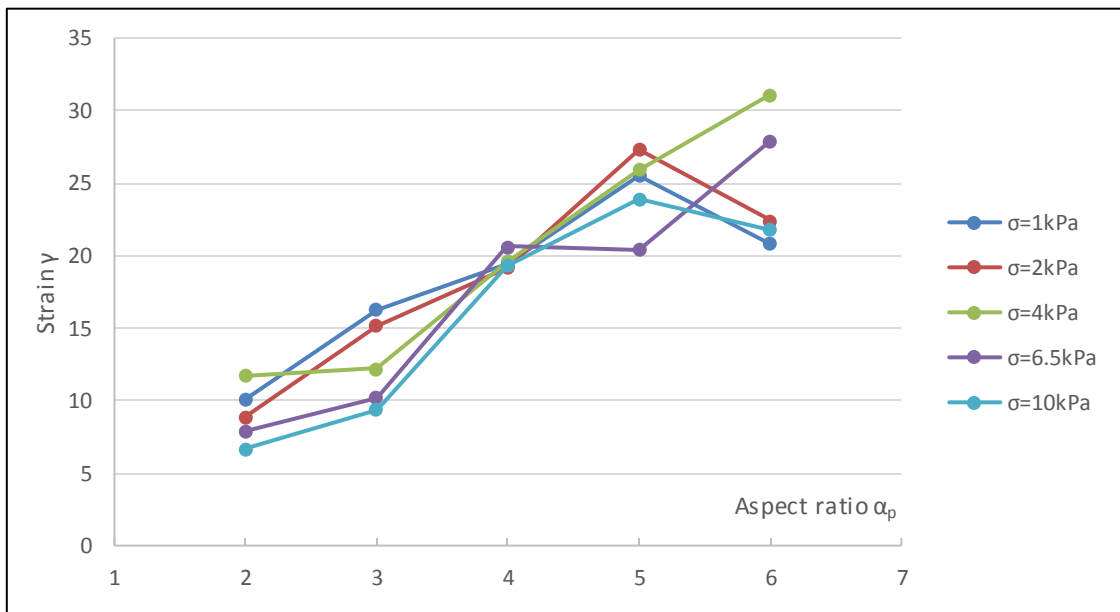


Figure 6.4.3: Strain γ required to reach steady state of order parameter S for the different aspect ratios α_p and normal stresses σ .

The mean value of order parameter in steady state, \bar{S} , increases with the aspect ratio (see Figure 6.4.4). Again, no impact of the normal stress is observed with a very low Spearman coefficient at 0.05. It shows that the more elongated the particles, the better they align in their steady state. Indeed, shorter particles will be more prone to rotate on a direction normal to their neutral axis due to their reduced mass moment of inertia [205], and the variation of particles angular rotation is reported to decrease with increasing aspect ratio [149].

This phenomenon is also observed in DEM shear cell involving cylindrical particles [14]. The values obtained corresponds to the reported order parameter for aspect ratio 6 with 0.8 in this study and 0.85 in Guo et al. [14], and aspect ratio 4 with 0.72 in this study compared to 0.76. However, the values for aspect ratio 2 are higher in this study, 0.45 compared to 0.25, which is attributed to the higher solid fraction in this study with 0.57 (see Chapter 6.4.2.2) compared to 0.5 in Guo et al.

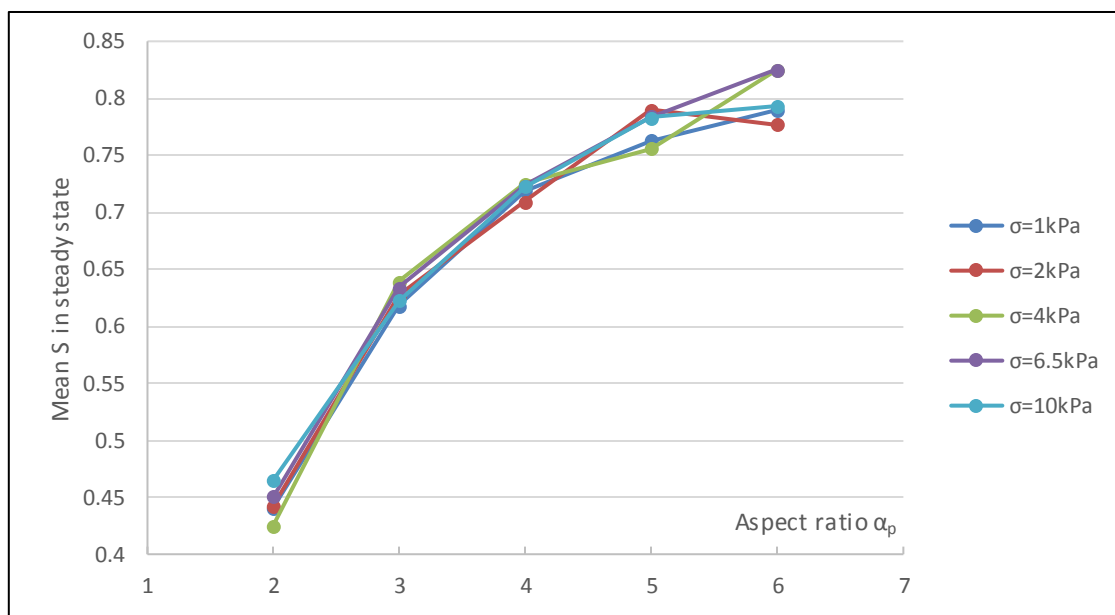


Figure 6.4.4: Mean value of order parameter \bar{S} in steady state for the different aspect ratios α_p and normal stress σ .

Elongated particles then naturally align in a sheared bed. A certain level of compaction is needed to hold particles together and promotes the ordering of the bed with increasing strain applied. In an AFD, variations of compaction and solid density can produce disorder within the particle bed e.g. when particles are avalanching behind the blade after its passage [118].

6.4.2.2 Bed Densification

The particle bed densifies as particles align [188] from their initial random packing state at the beginning of the shearing phase to their steady state of ordering (see Chapter 6.4.2.1). As observed in Chapter 5.3.3, the volume solid fraction f_s in the bed first decreases at the beginning of the shearing phase as the bed expands (see Figure 6.4.5). This bed dilatation, called Reynold's dilatancy [250, 251], is due to the interlocking between particles and rearrangement of particles [21]. The solid fraction then increases to reach a steady state when the maximum level of alignment is obtained.

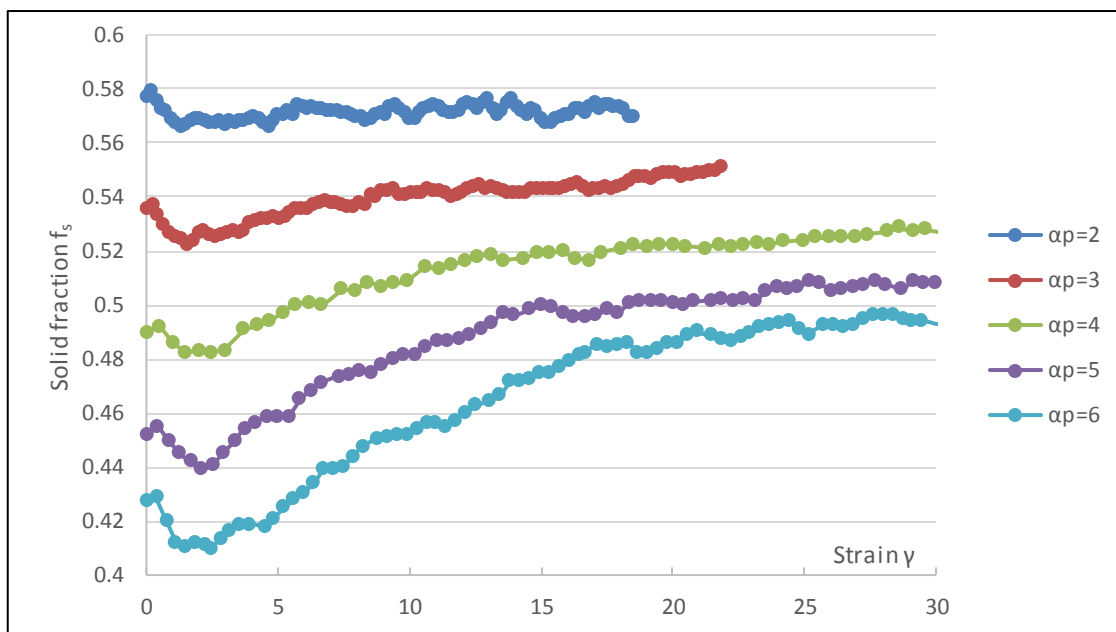


Figure 6.4.5: Solid fraction f_s of particle bed in shearing phase for the different aspect ratios and a normal stress at $\sigma = 1kPa$.

The mean solid fraction in steady state, \bar{f}_s , decreases with higher particle aspect ratio as they have a lower ability to closely pack [188] (see Figure 6.4.6). The observation is confirmed by the reported increase of the void ratio of a bed with elongation of ellipsoids having an aspect ratio greater than 1.5 [119, 205]. The same observation is made for sphero-cylinders in DEM monodisperse system with periodic boundaries [273-276].

The normal stress has a moderate impact on \bar{f}_s , nevertheless they are positively correlated [205]. Here, the normal stress promotes a closer packing of particles, even when conserving the same bed conformation, as no effect of normal stress is observed on the steady state value of order parameter (see Chapter 6.4.2.1).

It is noted that the overlap distance between the constitutive sphere elements of a particle affects the packing properties of an assembly: the void ratio is observed to be larger for rough particles compared to smooth [272, 277]. Also, high aspect ratio particles may decrease the solid fraction uniformity within the bed and can affect the particle velocity [188]. The impact of this phenomenon on the key variables analysed in this study is assumed marginal.

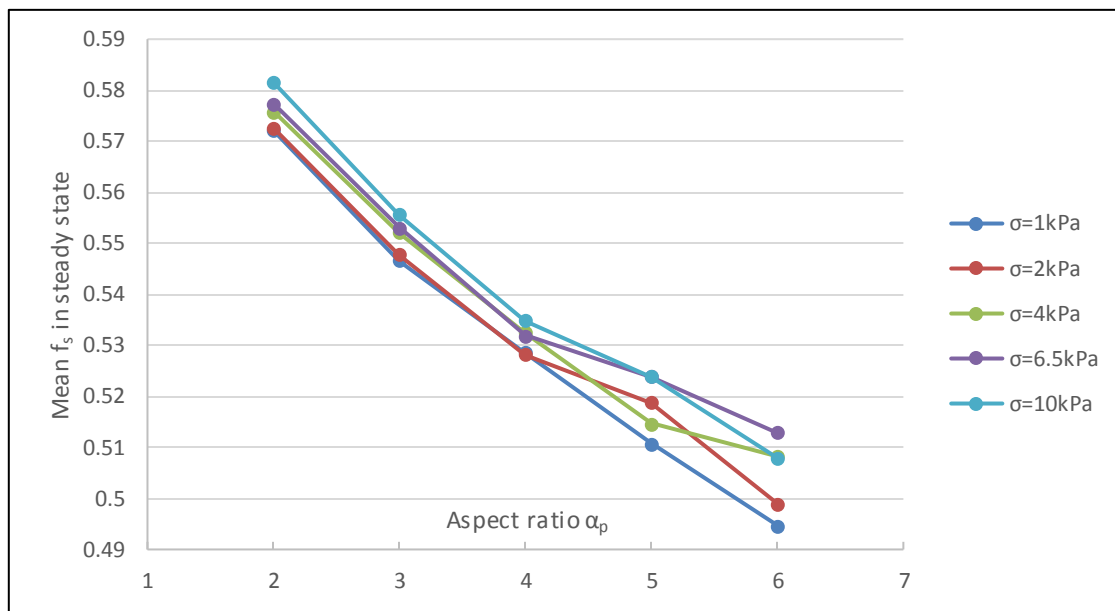


Figure 6.4.6: Mean solid fraction in steady state of shearing phase, \bar{f}_s , for the different aspect ratios α_p and normal stresses σ .

The overlap between touching particles due to the soft-sphere approach of the used contact model (see Chapter 5.2.1.3) is expected to play a minor role in the bed density value since the material's Young's modulus is not scaled down and is at the order of magnitude of the *GPa* (see Chapter 5.5.3).

6.4.2.3 Particle Contacts

The mean number of contacts on a particle, $\bar{N}_{c,p}$, increases from a minimum value at the beginning of the shearing phase and reaches a steady state value (see Figure 6.4.7). $\bar{N}_{c,p}$ increases throughout the shearing phase as the particles align (see Chapter 6.4.2.1) and the bed densifies (see Chapter 6.4.2.2). The number of contacts on a particle is different to the coordination number [270] (number of particles in contact with the studied one) as there can be here more than one contact between two particles. The choice of modelling the particles with clumped spheres (see Chapter 5.2.1.1) decreases their coordination number but increases the total number of contacts compared to smooth shapes [249, 258, 266, 272, 278], up to twice as high for rough particles [228].

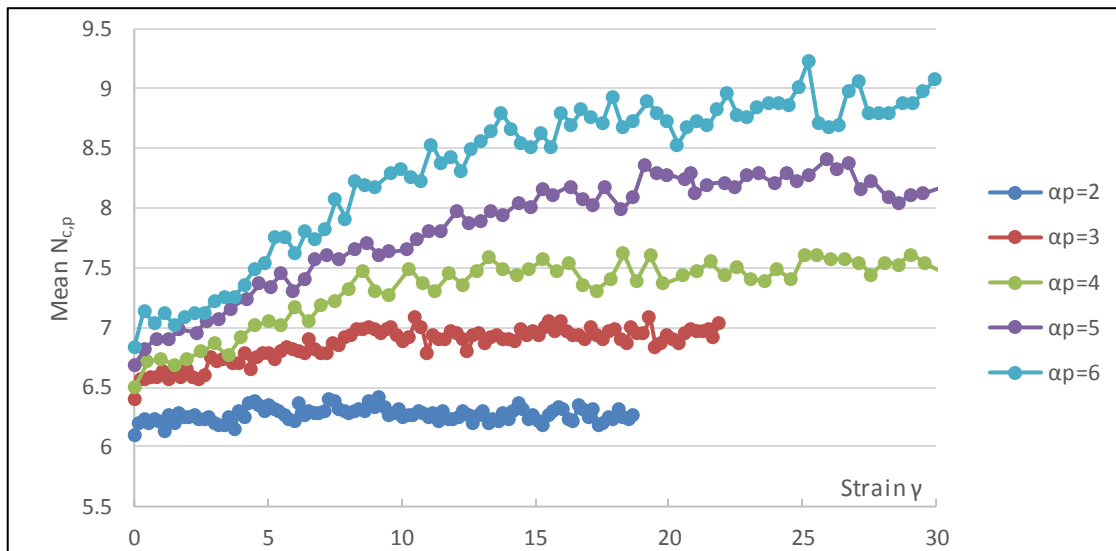


Figure 6.4.7: Mean number of contacts on particle, $\bar{N}_{c,p}$, in shearing phase for the different aspect ratios α_p and a normal stress at $\sigma = 10kPa$.

The mean value of $\bar{N}_{c,p}$ in steady state increases with both aspect ratio and normal stress applied (see Figure 6.4.8). Indeed, elongated particles have a greater available surface for contact creation and a higher compression augments the coordination number [205].

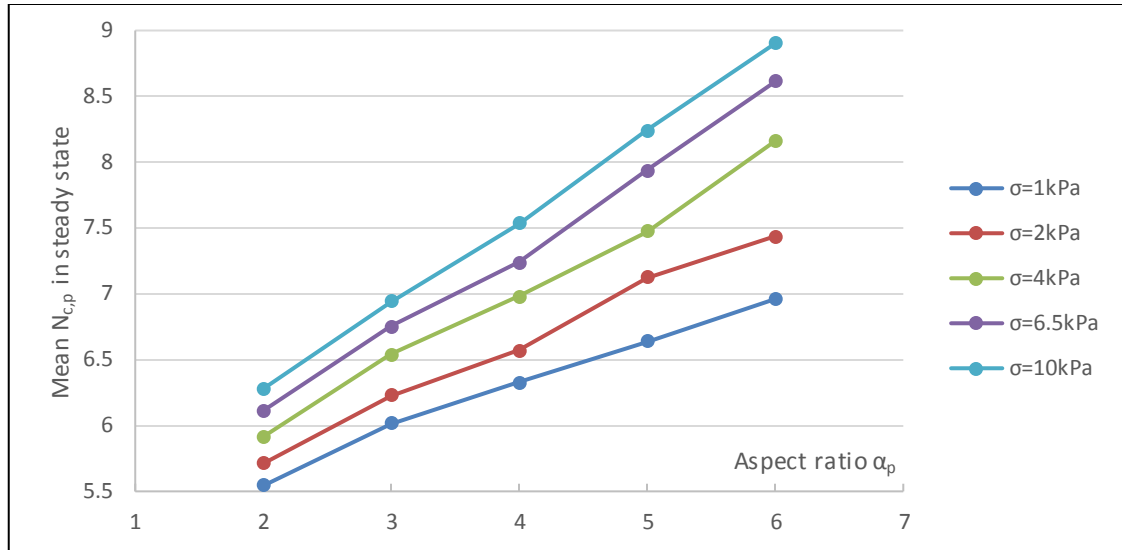


Figure 6.4.8: Mean number of contacts on particle, $\bar{N}_{c,p}$, in steady state of shearing phase for the different aspect ratios α_p and normal stresses σ .

The influence of the normal stress σ on $\bar{N}_{c,p}$ is partially due to the increase of solid fraction with higher σ [270] (see Chapter 6.4.2.2). Indeed, $\bar{N}_{c,p}$ appears as quasi-linearly correlated with the solid fraction f_s for a fixed aspect ratio and normal stress applied (see Figure 6.4.9).

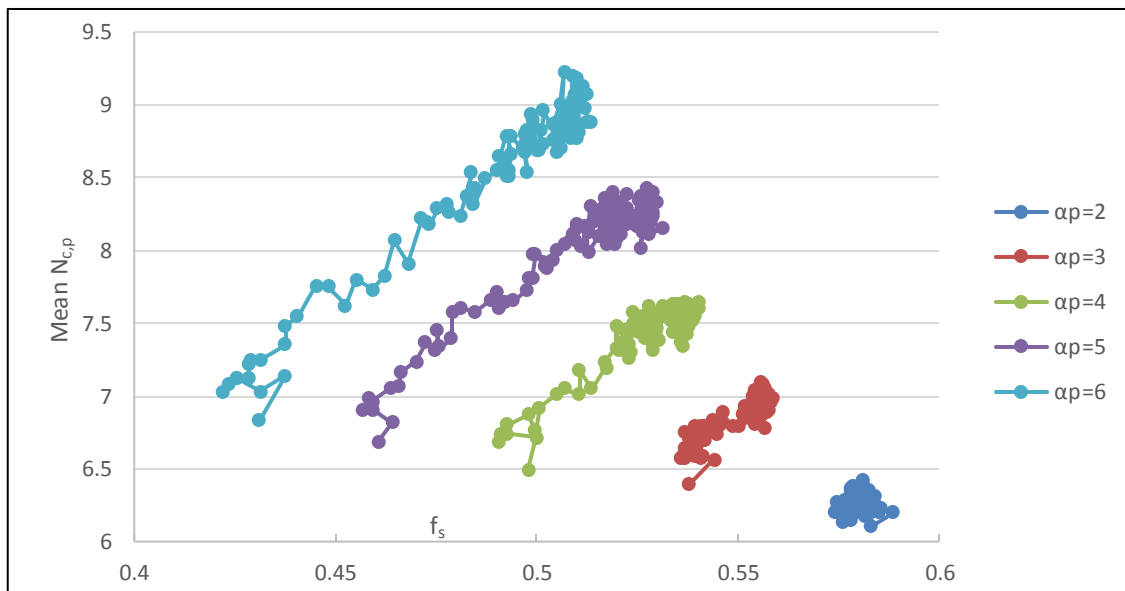


Figure 6.4.9: Mean number of contacts on particle, $\bar{N}_{c,p}$, in the shearing phase given by the solid fraction f_s for the different aspect ratios α_p and a normal stress applied at $\sigma = 10\text{kPa}$.

The correlation between f_s and $\bar{N}_{c,p}$ remains linear and shifted for the different normal stresses applied (see Figure 6.4.10), meaning that the effect of σ on $\bar{N}_{c,p}$ is not entirely due to the increase of bed density. Indeed, there is a phenomenon of forced stacking between particles when a greater normal stress is applied, which increases their number of contacts.

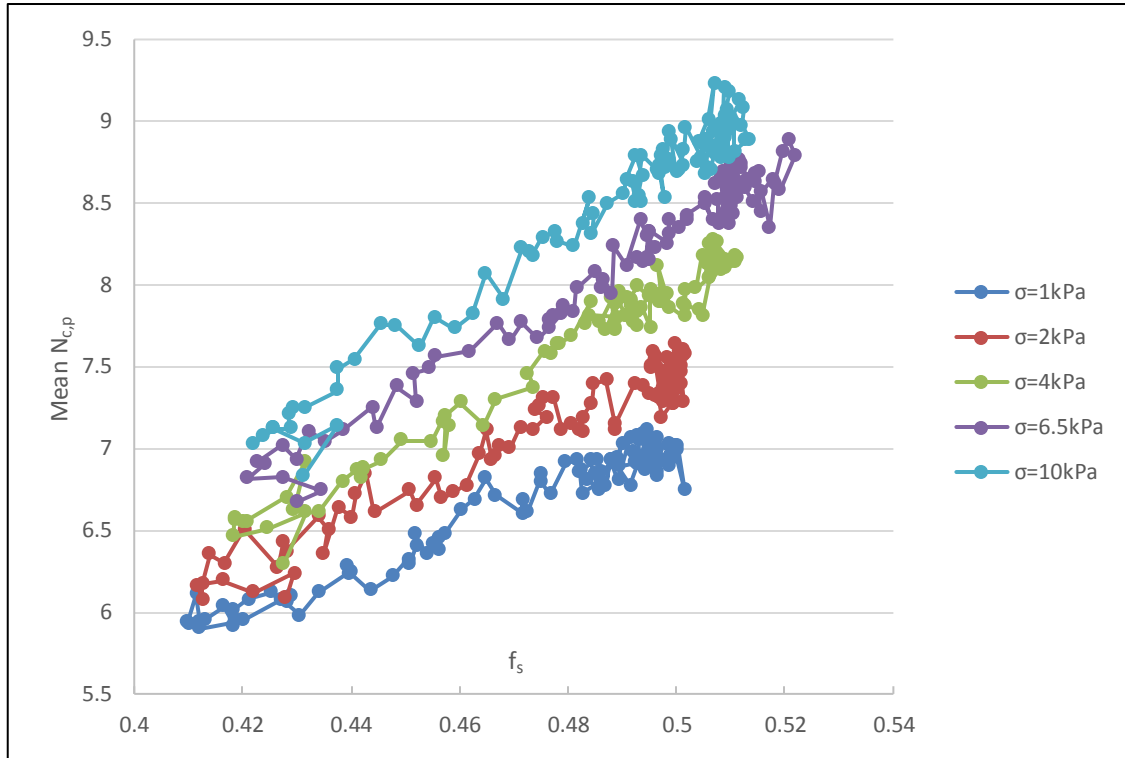


Figure 6.4.10: Mean number of contacts on particle $\bar{N}_{c,p}$, given by the solid fraction f_s for the different normal stresses σ and an aspect ratio at $\alpha_p = 6$.

It is expected that the available surface for contact increases with particle aspect ratio, explaining why $\bar{N}_{c,p}$ is positively correlated to particle elongation for the same solid fraction. The clumped-sphere modelling of the particles also influences the number of contacts, especially when elongated particles align and experience stacking. Indeed, it is likely that two particles enter in contact on multiple locations due to their asperity, which is confirmed by the increase of the mean number of contacts between two interacting particles, $\bar{N}_{c,2p}$, with the order parameter S during the shearing phase (see Figure 6.4.11). Here, $\bar{N}_{c,2p}$ increases with aspect ratio as more elongated particles are made of more clumped spheres, which offers a higher number of possible contact locations.

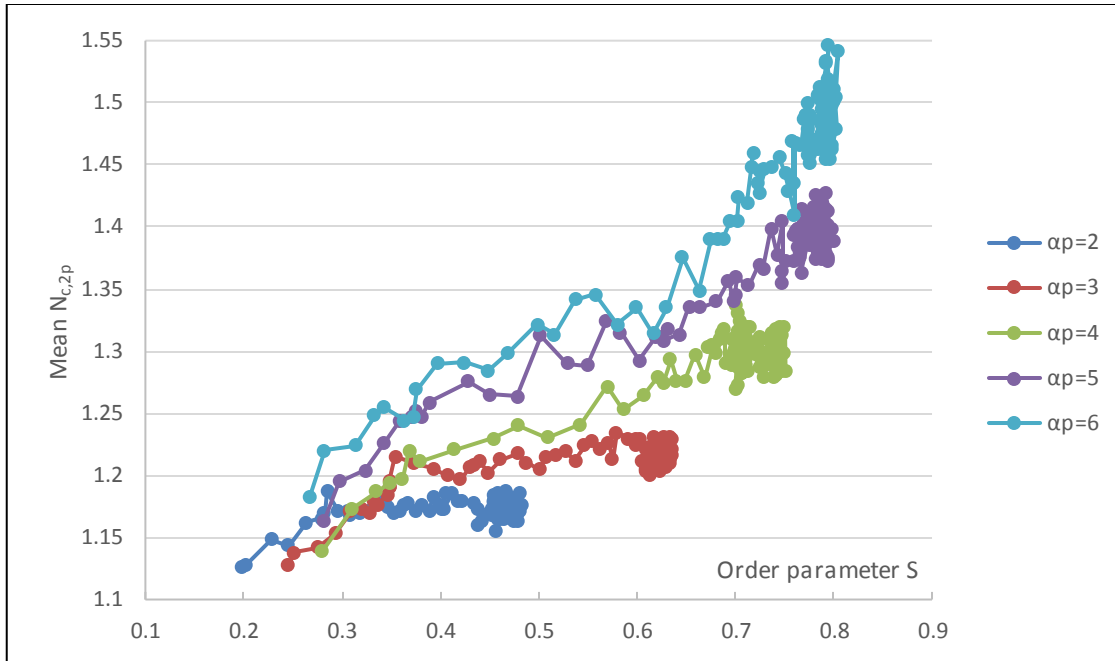


Figure 6.4.11: Mean number on contacts between two interacting particles, $\bar{N}_{c,2p}$, given by the order parameter S during shearing phase for the different aspect ratios α_p and a normal stress at $\sigma = 10kPa$.

6.4.3 Stress Ratio

The stress ratio φ (see Equation 2.4.6) is the main dimensionless number for the characterisation of the mechanical behaviour of a particle bed [13, 21] and is given as the shear stress τ divided by the normal stress σ applied on the particle bed by the translating walls (see Chapter 5.2.2.3).

At the very beginning of the shearing phase, the walls have not started straining the bed (i.e. strain applied $\gamma = 0$), hence a quasi-absence of shear stress with the stress ratio $\varphi \approx 0$ (see Figure 6.4.12). The stress ratio then increases to a peak in the transitional state [13] before decreasing to reach a steady state [258]. Indeed, the quasi-static flow regime with optimised simulation setup has been demonstrated in Chapter 5.5.2, where the shear stress scales linearly with the normal stress [152-154] (see Equation 2.3.3) in this non-cohesive particle assembly. The stress ratio varies in the steady state due to the “slip-and-stick” behaviour of the particles flow [1, 116].

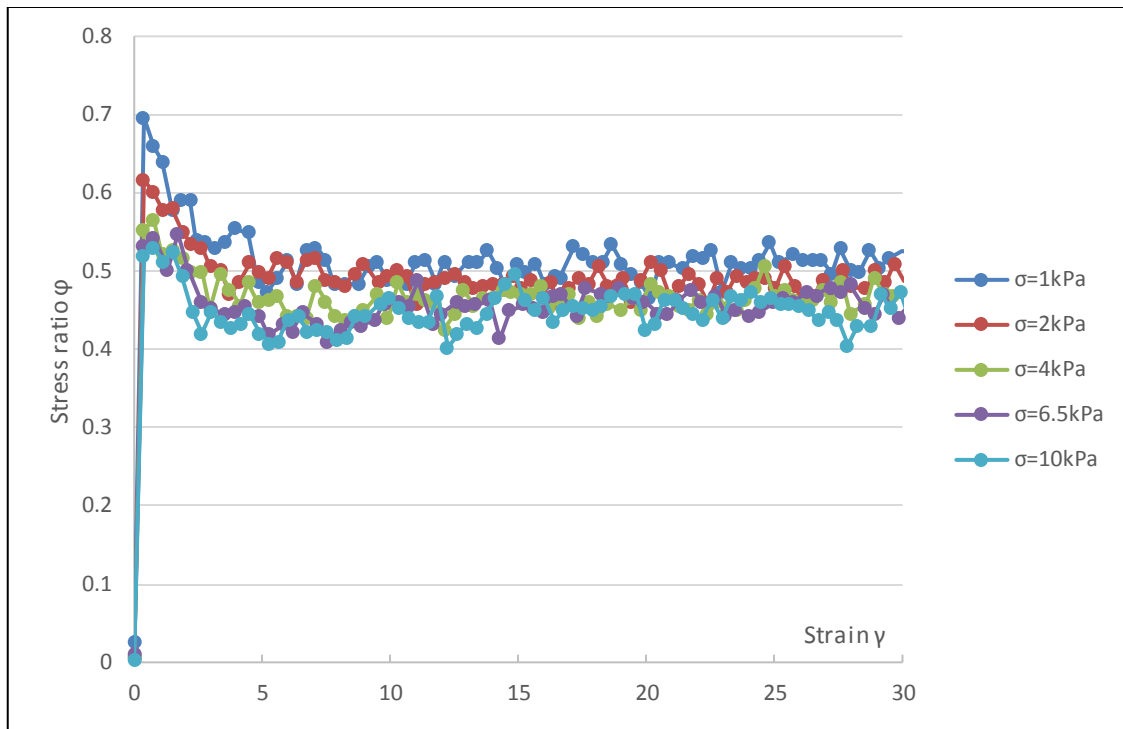


Figure 6.4.12: Stress ratio in the shearing phase, φ , for the different normal stresses σ and an aspect ratio $\alpha_p = 6$.

The strain required to reach the steady state of stress ratio tends to increase with the particles aspect ratio, and decrease with a higher normal stress applied (see Figure 6.4.13). The proportionality with aspect ratio was observed in triaxial compression where the strain required to reach a plateau of effective stress ratio increases with aspect ratio of ellipsoids [205]. The same observation is made for clumped-sphere particles in direct shear test [195]. On the contrary, the normal stress applied isn't reported to impact the strain needed to reach a steady state of stress ratio for the wide range of $50k - 2MPa$ [195].

The strain required to reach the steady state is around 0.5 for aspect ratio 2, which is typically the order of magnitude reported in a 3D conventional shear cell with particles aspect ratio between 1 and 2.5 [149] and in direct shear test of clumped-sphere particles for the same range of aspect ratio [195]. A strain of 2.5 is reported for platy particles in a shear cell [13], which corresponds to the order of magnitude for more elongated particles in this study.

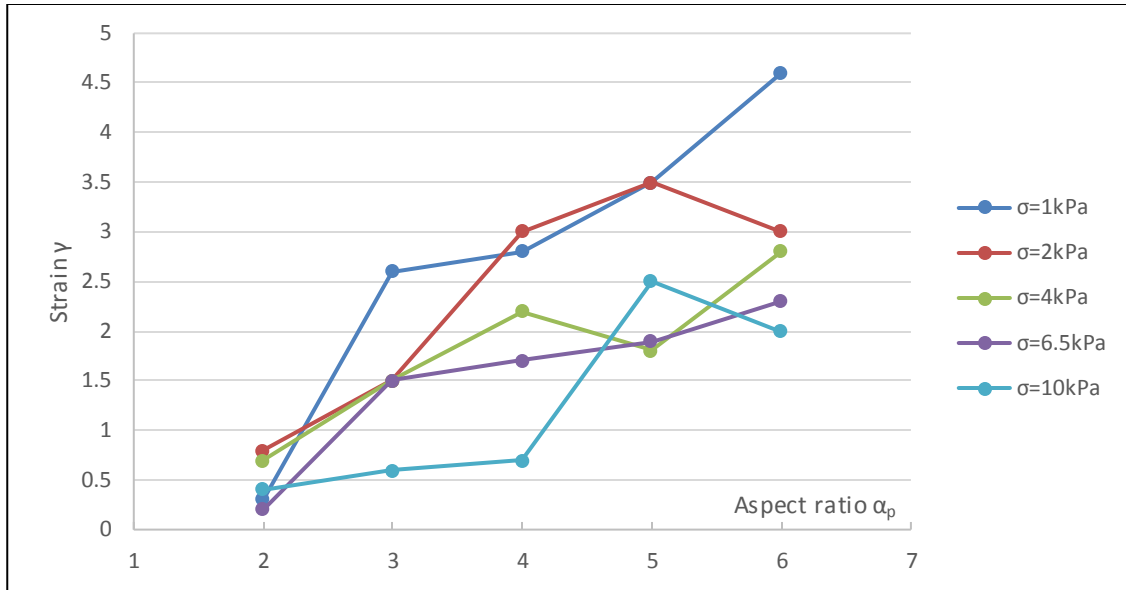


Figure 6.4.13: Strain required to reach steady state value of stress ratio ϕ for the different particles aspect ratio α_p and normal stresses σ .

The peak value reached by the stress ratio in the transitional state is inversely proportional to the normal stress applied (see Figure 6.4.14) and no monotonic relation is found with the aspect ratio. Both observations are also reported in direct shear test of clumped-sphere particle with an aspect ratio > 1.2 [195].

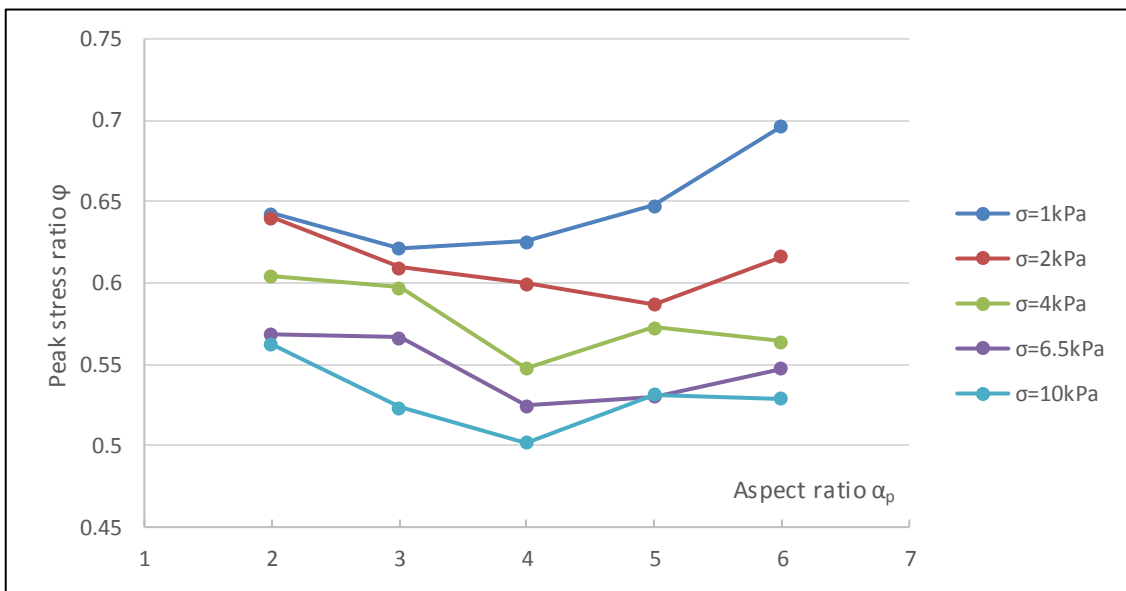


Figure 6.4.14: Peak value of stress ratio ϕ during transitional state for the different aspect ratio α_p and normal stresses σ .

The mean stress ratio in the steady state, $\bar{\varphi}$, is taken as a characteristic value for the analysis of the mechanical behaviour of the bed [149]. It is primarily correlated to the mean number of contacts on particle, $\bar{N}_{c,p}$, with a Spearman correlation coefficient of -0.74 : $\bar{\varphi}$ is inversely proportional to $\bar{N}_{c,p}$. Indeed, when $\bar{N}_{c,p}$ increases, the mean contact force \bar{F}_c decreases (see Chapter 6.4.4) which reduces the tangential contact force required to break the contact by sliding, itself linearly proportional to \bar{F}_c by the coefficient of static friction between particles (see Chapter 5.2.1.3.1). This lowers the resistance of the particle bed to shear, decreasing the shear stress and thus the stress ratio.

$\bar{N}_{c,p}$ being correlated to the particle aspect ratio (see Chapter 6.4.2.3), $\bar{\varphi}$ is then also inversely proportional to the aspect ratio. Indeed, the aspect ratio of elongated particles is also known to influence the bed flow of in shear tests [264] and affects the shear stress [203]. The stress ratio is reported to decrease with higher particle elongation when the aspect ratio is greater than 1.5 in shear cells [149, 228]. Moreover, the angle of friction, proportional to the stress ratio by Coulomb's law of static friction [152-154] (see Equation 2.3.3), for ellipsoids is shown to slightly decrease with increasing aspect ratio [258]. This phenomenon may be attributed to particles alignment reducing the resistance of particles to shear and make them slide easier [149]. However, different observation have also been reported regarding the correlation between the stress ratio and aspect ratio. It is positive for clumped-sphere particle with aspect ratio from 1 to 2 in 3D shear cell [154]. Also, the critical direct shear angle of friction increases with particle elongation for aspect ratio ranging from 1.2 to 2.2 in direct shear test [195]. Same correlation in 2D simulations using clumped spheres for aspect ratio ranging from 1 to 3.3 [259]. In AFD simulations, the impeller torque, proportional to the shear stress using Darelus equation [152] (see Equation 2.3.4), scales with particle elongation up to an aspect ratio of 5 [119]. The increase of torque with non-spherical particles made of clumped spheres is confirmed in DEM Freeman powder rheometer [193]. These studies tend to demonstrate that the flowability of powder is reduced with particle elongation [126-129].

The normal stress σ has an additional impact on $\bar{\varphi}$, with $\bar{\varphi}$ increasing when σ decreases (see Figure 6.4.15). Indeed, the solid fraction scales with normal stress applied (see Chapter 6.4.2.2), and the proportionality between normalised shear

stress and volume solid fraction is also reported in shear cell for aspect ratio 6 [228]. Likewise, the densification of the bed in AFD experiment increases the measured torque [1], and therefore augments the shear stress [152] (see Equation 2.3.4). This effect is more important for lower aspect ratio α_p . This phenomenon is attributed to the difficulty of elongated particles to rotate around an axis normal to its neutral axis due to their higher mass moment of inertia [205], which forces more elongated particles to slide in the shearing direction rather than rotate as the bed is strained. This is confirmed by the reported decreases of variation of particles angular rotation with increasing aspect ratio [149]. The lower value of order parameter for reduced aspect ratio (see Chapter 6.4.2.1) confirms the greater ability of shorter particles to rotate easier this way. Such particle rotation is rendered more difficult as the normal stress on the bed increases. Thus, particle rotation is easier for lower aspect ratio and normal stress, which reduces contact slipping and increases the resistance of the particle bed to shearing. The mechanical behaviour of the bed is then governed to a greater extent by particle rearrangement due to interlocking rather than by the release frictional contacts. This observation confirms the importance of the particle shape in the mechanical response of a bed to straining.

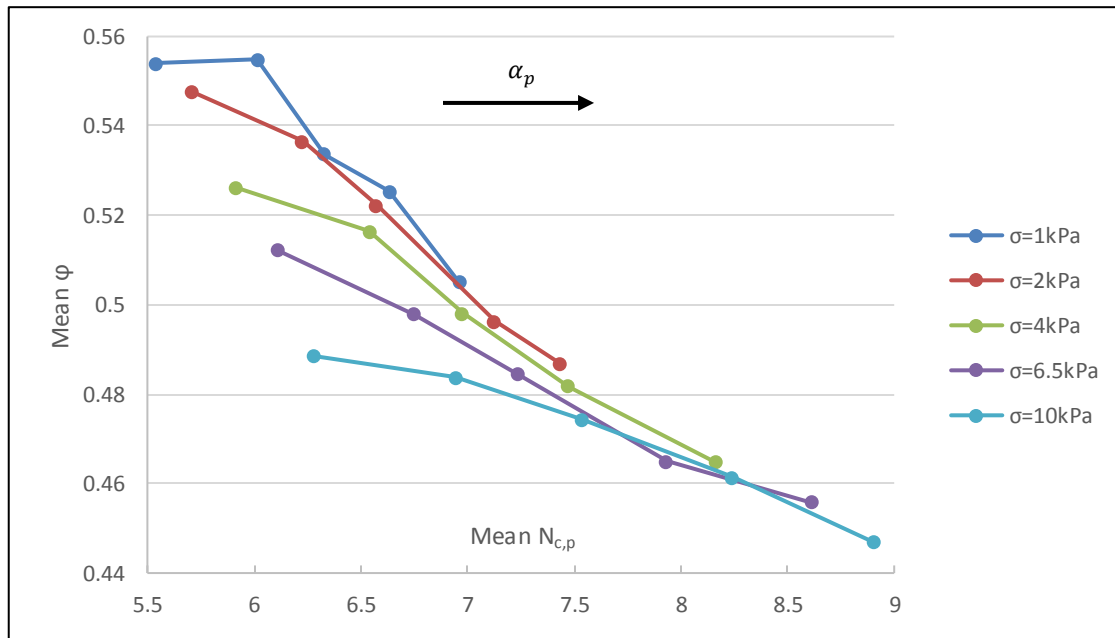


Figure 6.4.15: Mean stress ratio in steady state, $\bar{\phi}$, given by the mean number of contacts on particle $\bar{N}_{c,p}$ for the different normal stresses σ . Within each σ series, $\bar{N}_{c,p}$ increases with the particle aspect ratio α_p set at [2; 3; 4; 5; 6].

It is noted that the particle bed is here monodisperse and as the shear stress depends on the number of frictional contacts on particles, the difference between the size of a given particle and the size of its neighbours (i.e. size ratio) is expected to affect the stress experienced by this particle [155]. Thus, introducing polydispersity in the simulations would alter the stress ratio.

6.4.4 Contact Force

At the beginning of the shearing phase, the mean contact force \bar{F}_c increases from its initial value to reach a peak before decreasing to a plateau (see Figure 6.4.16). This phenomenon recalls the behaviour of the stress ratio in these transitional and steady states (see Chapter 6.4.3), especially since the contact force results mechanically from the normal and shear stresses applied to the bed. Here, a higher force is needed to overcome the yield strength of the bed and initiate the flow [112].

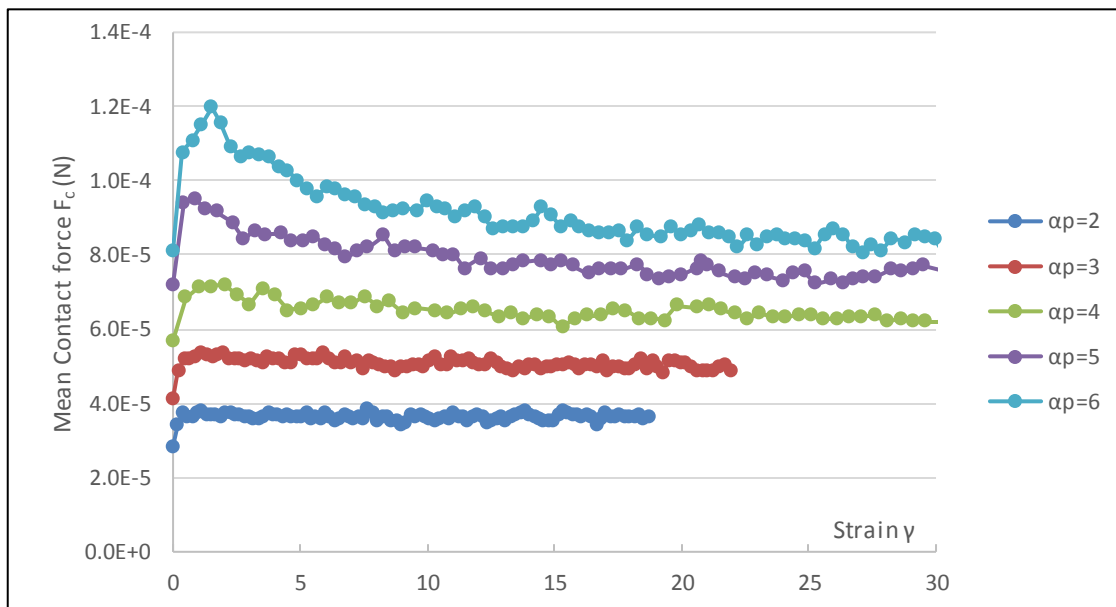


Figure 6.4.16: Mean contact force, \bar{F}_c , in the shearing phase for the different aspect ratios α_p and a normal stress at $\sigma = 10kPa$.

When the normal stress increases, a combination of two mechanisms occurs. The first one is the linear increase of the mean contact force \bar{F}_c as the load on the bed is amplified. The second one is the multiplication of contacts, due to a closer packing of particles (see Chapter 6.4.2.2), which spreads the load on the bed over more

supporting points. This second phenomenon creates more and weaker force chains for the same normal stress applied, confirmed by the negative correlation between \bar{F}_c and the mean number of contacts on particle $\bar{N}_{c,p}$ (see Figure 6.4.17). A heterogeneity of contact force is also expected within the contact network composed of weak and strong subnetworks [195, 285-287]. The strongest contacts then support a greater portion of the stress applied on the bed and form the strongest force chains. The weak contacts are called sliding contacts as they need less force to be broken during straining [205, 285, 288]. They behave like interstitial liquid providing stability for the force propagation along the strong contacts [205, 285]. The ratio between sliding and strong contacts is expected to remain unchanged for the different aspect ratios [205].

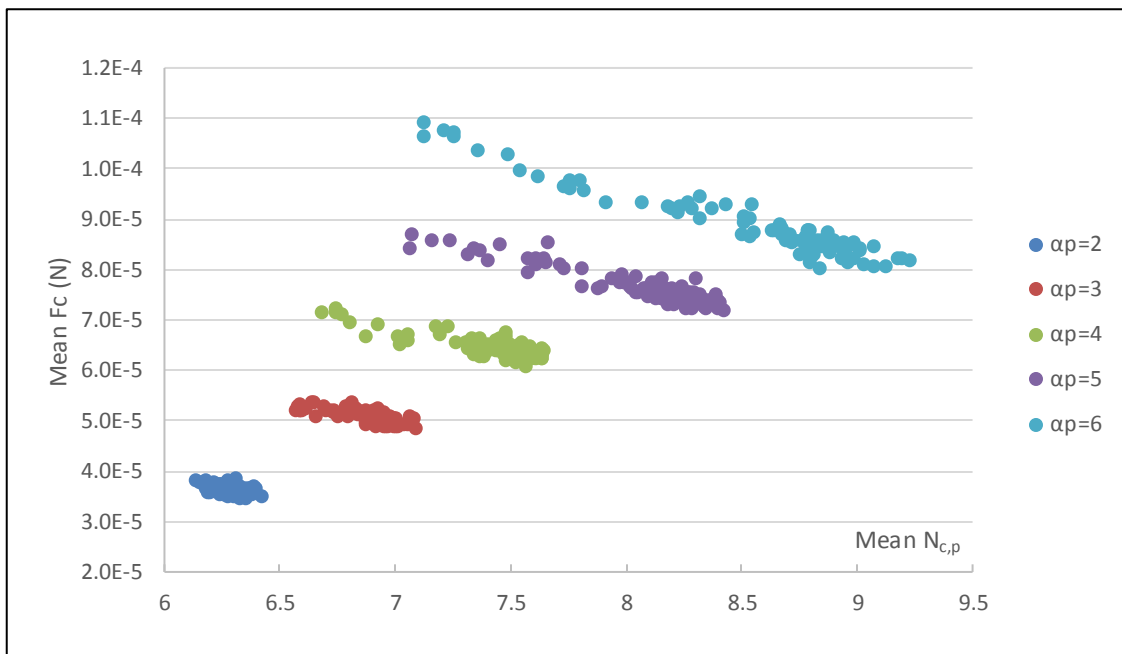


Figure 6.4.17: Mean contact force \bar{F}_c given by the mean number of contacts on particle $\bar{N}_{c,p}$ for the different aspect ratios α_p and a normal stress applied at $\sigma = 10 \text{ kPa}$. The values are given in the steady state of stress ratio.

Clearly, the first mechanism is dominating as the mean value of \bar{F}_c in the steady state scales with the normal stress applied σ (see Figure 6.4.18). The effect of the second mechanism prevents the perfect linearity of this correlation with a Pearson coefficient at 0.87.

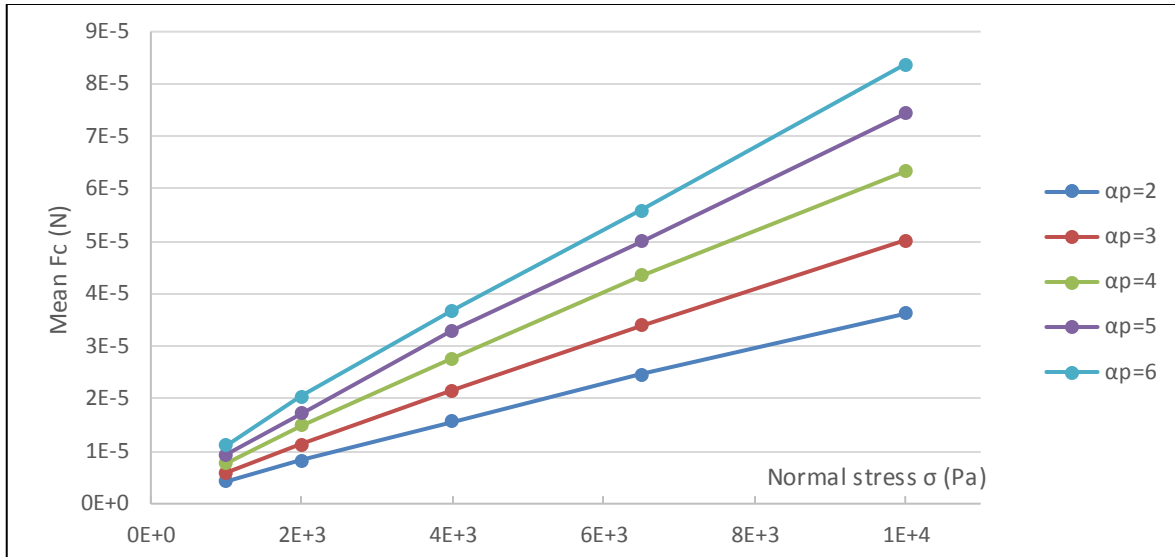


Figure 6.4.18: Mean contact force in steady state of shearing phase, \bar{F}_c , for the different aspect ratios α_p and normal stresses σ .

\bar{F}_c also correlates with α_p . Indeed, elongated particles don't pack as efficiently as shorter ones (see Chapter 6.4.2.2), which decreases the cross-sectional concentration of contacts $c_{c,area}$ (see Figure 6.4.19) estimated from the volume concentration of contacts $c_{c,vol}$ and assuming an isotropic distribution of contacts:

$$c_{c,area} = c_{c,vol}^{2/3} \quad 6.4.1$$

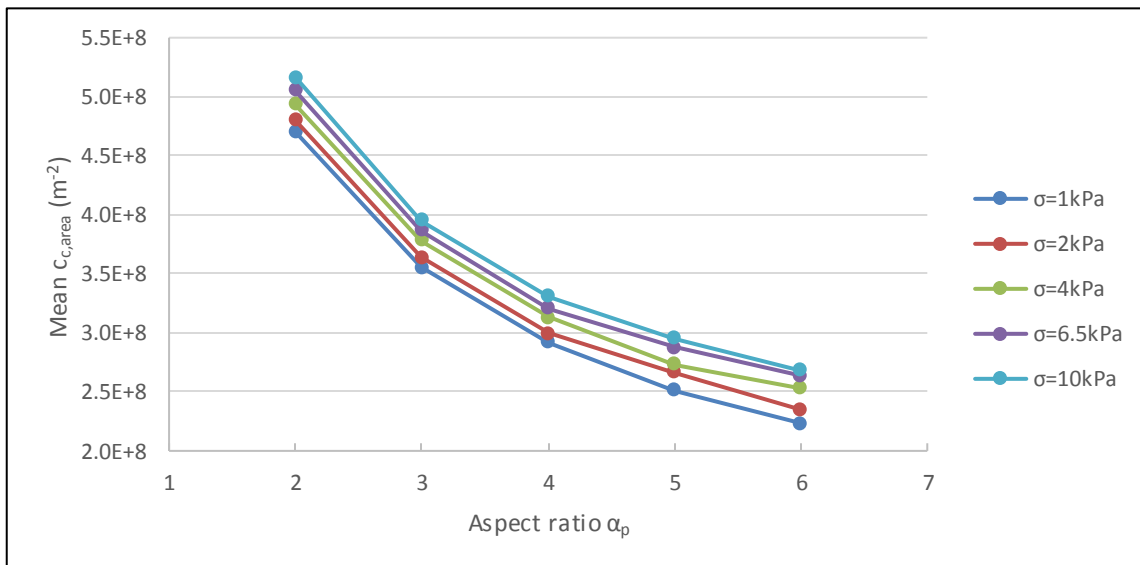


Figure 6.4.19: Mean surface concentration of contacts in steady state, $\bar{c}_{c,area}$, for the different aspect ratios α_p and normal stresses σ .

The surface concentration of contacts appears as a key variable and is inversely proportional to \bar{F}_c for the same normal stress applied (see Figure 6.4.20). Here, a higher $c_{c,area}$ increases the number of force chains, and thus decreases the mean contact force.

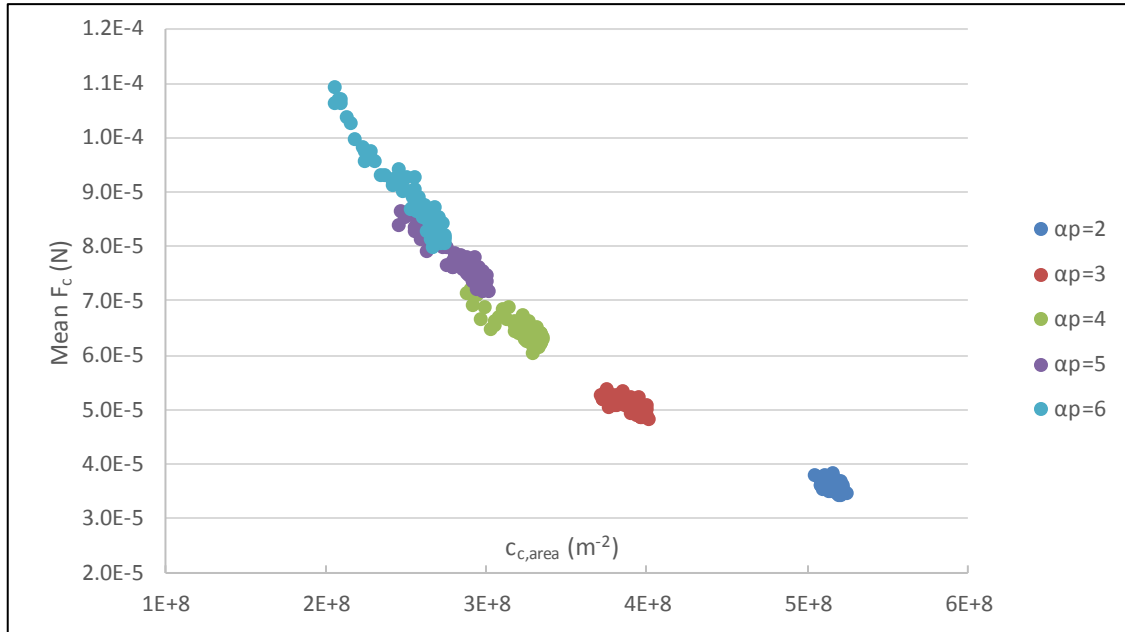


Figure 6.4.20: Mean contact force \bar{F}_c given by the surface concentration of contacts $c_{c,area}$ for the different aspect ratios α_p and a normal stress at $\sigma = 10kPa$. The data are given in the steady state of stress ratio.

6.4.5 Inter-Contact Distance on Particle

The mean distance between contacts on a particle's neutral axis, $\bar{\Delta L}$, is calculated from the particle aspect ratio α_p and number of contacts on particle:

$$\bar{\Delta L} = \frac{L_p}{\bar{N}_{c,p} + 1} \quad 6.4.2$$

During the shearing phase, $\bar{\Delta L}$ starts from a maximum value and reaches a steady state (see Figure 6.4.21) when the number of contacts has reached a plateau (see Chapter 6.4.2.3).

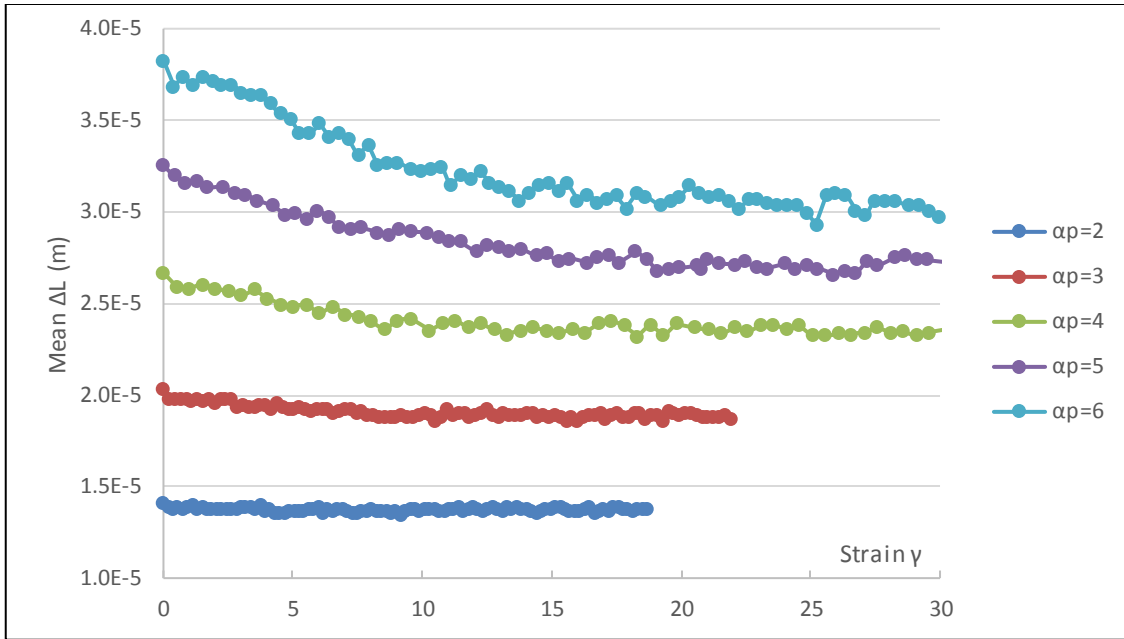


Figure 6.4.21: Mean inter-contact distance on particle, $\overline{\Delta L}$, during the shearing phase for the different aspect ratios α_p and a normal stress applied at $\sigma = 10kPa$.

$\overline{\Delta L}$ correlates with the normal stress applied σ , as a higher σ increases the mean number of contacts on particle $\overline{N}_{c,p}$ (see Chapter 6.4.2.3). By definition, $\overline{\Delta L}$ correlates directly with α_p and is inversely proportional to $\overline{N}_{c,p}$ (see Figure 6.4.22).

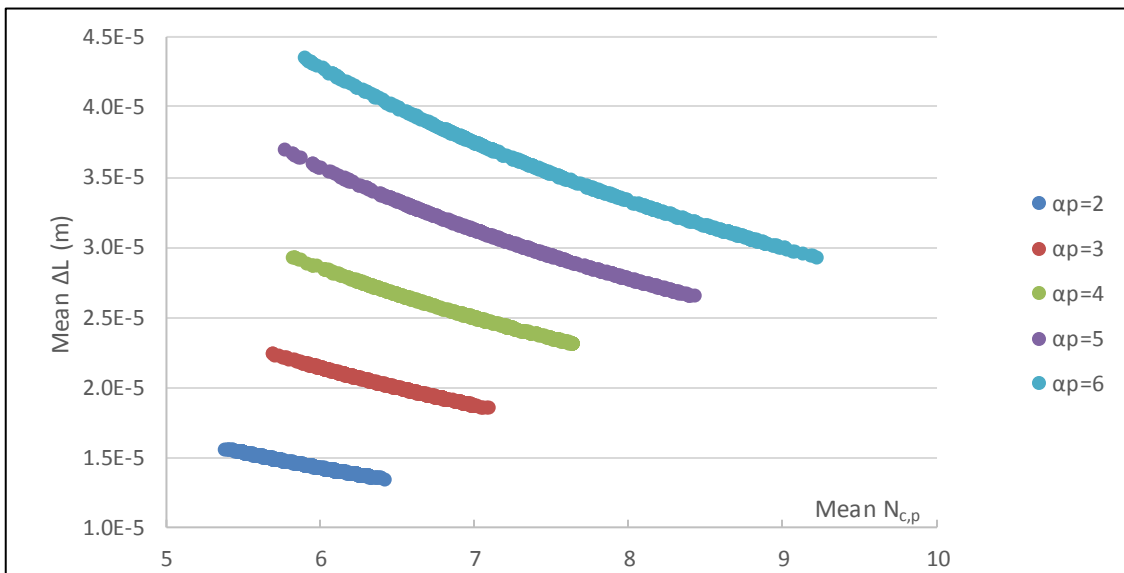


Figure 6.4.22: Mean inter-contact distance on particle, $\overline{\Delta L}$, in shearing phase given by the mean number of contacts on particle $\overline{N}_{c,p}$ for the different aspect ratios α_p .

6.4.6 Particles Internal Stress

6.4.6.1 Predominance of Bending Stress Component

The particle internal stress is determined by diagonalisation of the stress tensor (see Chapter 5.4.1.2). To assess the importance of the bending stress component with the stress tensor, i.e. component (Z,Z) involving the bending moment (see Equation 5.4.30), its absolute value is divided by the particle internal stress σ_p to obtain the bending stress ratio $\alpha_{\sigma,ZZ}$:

$$\alpha_{\sigma,ZZ} = \frac{|\sigma_{Z,Z}|}{\sigma_p} \quad 6.4.3$$

The mean bending stress ratio, $\bar{\alpha}_{\sigma,ZZ}$, experiences a slight decrease at the beginning of the shearing phase before increasing to reach a steady state. The phenomenon is more pronounced for lower aspect ratios (see Figure 6.4.23).

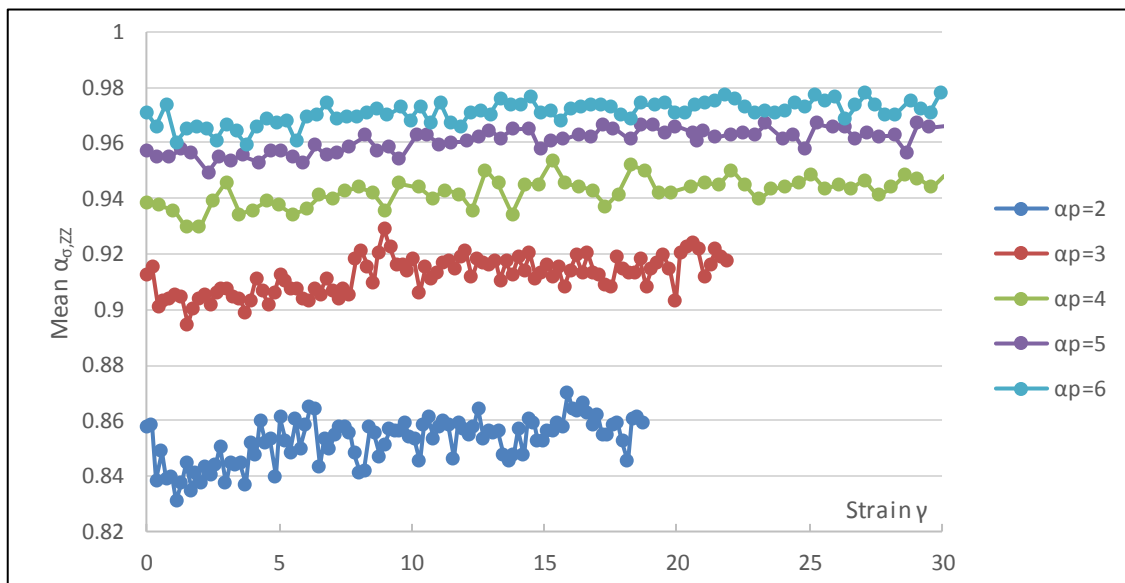


Figure 6.4.23: Mean bending stress ratio, $\bar{\alpha}_{\sigma,ZZ}$, for the different aspect ratios α_p and a normal stress at $\sigma = 10kPa$.

As expected, the mean $\bar{\alpha}_{\sigma,ZZ}$ in steady state scales with the particles aspect ratio α_p with a Spearman coefficient at 0.97. Indeed, the bending stress is reported as the main cause of breakage for elongated particles [1]: the higher the aspect ratio of a particle, the more rapidly it breaks [53-55], as it increases its bending stress and therefore the

predominance of the bending stress in the particle internal stress. For high aspect ratios, $\bar{\alpha}_{\sigma,ZZ}$ slightly increases with the normal stress σ (see Figure 6.4.24). This proportionality isn't observed for lower α_p . This positive correlation between $\bar{\alpha}_{\sigma,ZZ}$ and σ seem counter-intuitive since it is demonstrated that the mean number of contacts on particle $\bar{N}_{c,p}$ increases with higher normal stress (see Chapter 6.4.2.3), which decreases the inter-contact distance (see Chapter 6.4.5) and then bending moment. In addition, a greater normal stress increases the mean contact force \bar{F}_c (see Chapter 6.4.4), and therefore the compressive internal stress in particles. The combination of these two aspects should produce an inverse correlation between $\bar{\alpha}_{\sigma,ZZ}$ and σ .

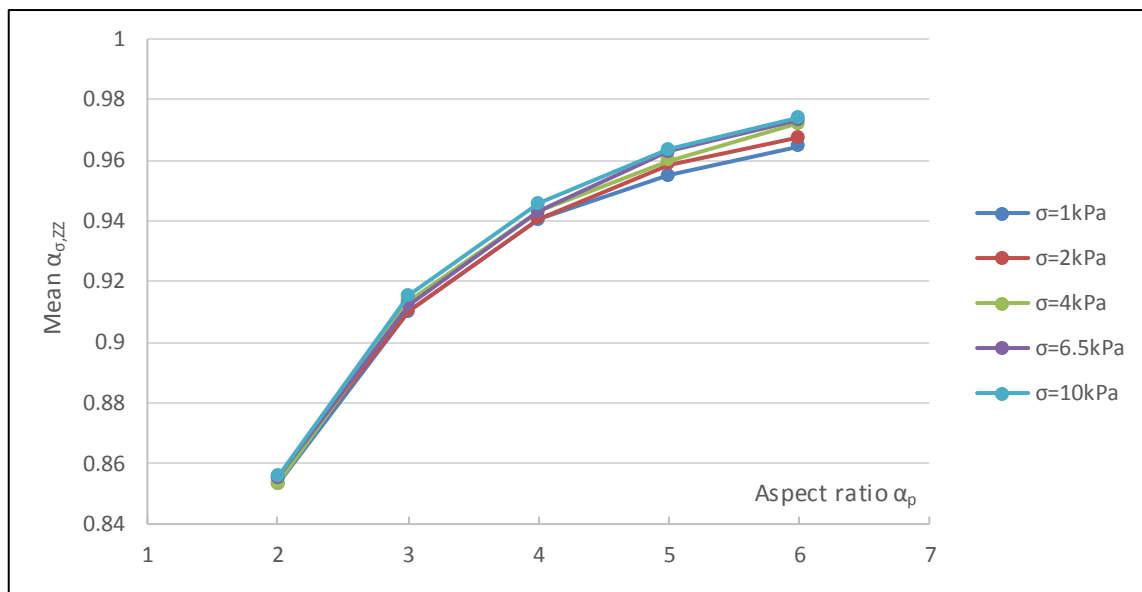


Figure 6.4.24: Mean bending stress ratio in steady state, $\bar{\alpha}_{\sigma}$, for the different aspect ratios α_p and normal stresses σ .

The explanation resides in the presence of particles experiencing a low number of contacts. Indeed, the probability for a particle to experience bending is related to the conformation of its contacts. The higher the number of contacts, the more likely the conditions for an effective bending are being met as the particle gains stability (see Chapter 6.5.4). It is observed that, for aspect ratio $\alpha_p = 6$, $\bar{\alpha}_{\sigma,ZZ}$ decreases significantly for a number of contacts $N_{c,p} \leq 5$ (see Figure 6.4.25).

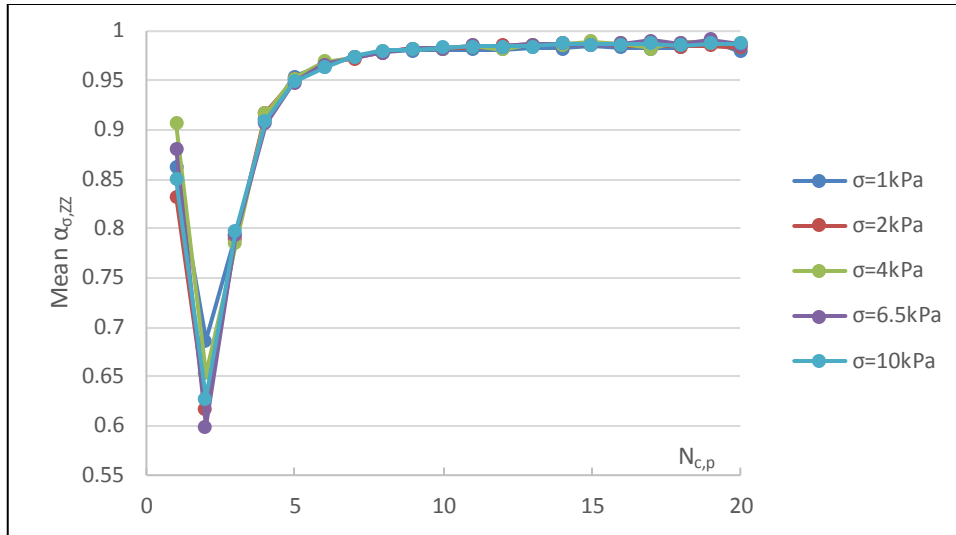


Figure 6.4.25: Mean bending stress ratio in the steady state, $\bar{\alpha}_{\sigma,ZZ}$, given by the number of contacts on particle $N_{c,p}$ for the different normal stresses σ and a particle aspect ratio of $\alpha_p = 6$.

As demonstrated in Chapter 6.4.2.3, a higher normal stress increases the $N_{c,p}$ (see Figure 6.4.8), and thus contributes to the reduction of the particles having a low $\bar{\alpha}_{\sigma,ZZ}$. In fact, the proportion of particles with aspect ratio $\alpha_p = 6$ experiencing a number of contacts below 5 decreases from 26% at normal stress $\sigma = 1kPa$ to 11.2% at $\sigma = 10kPa$ (see Figure 6.4.26).

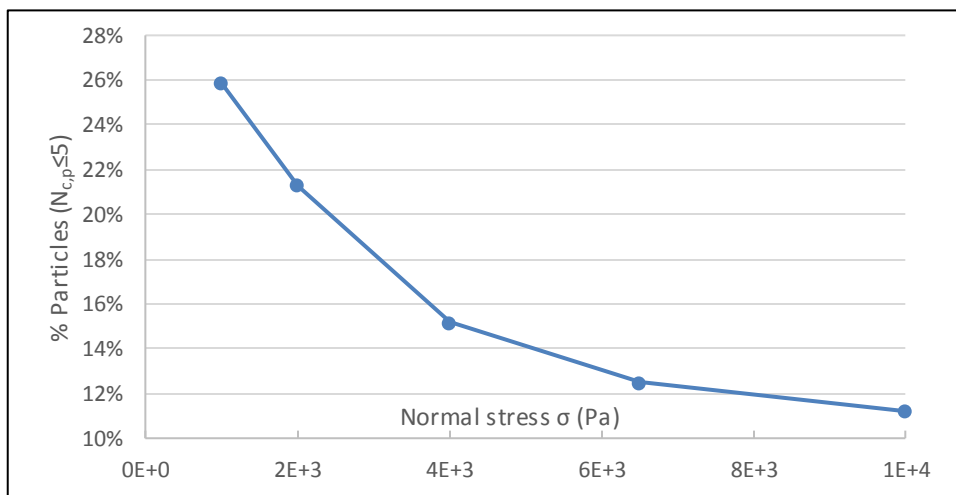


Figure 6.4.26: Proportion of particles experiencing a number of contacts $N_{c,p} \leq 5$, given by the different normal stresses σ and for a particle aspect ratio at $\alpha_p = 6$.

6.4.6.2 Weibull Fit Parameters

The Weibull cumulative distribution function is fitted on the particle internal stress distribution, calculated using Euler equation of motion with discretisation parameters optimised in Chapter 5.4.2, to obtain two key variables for analysis: the scale and shape parameters, respectively λ and k (see Chapter 6.2.1).

6.4.6.2.1 Scale Parameter

The Weibull scale parameter λ (see Chapter 6.2.1) has an initial value lower than during the rest the shearing phase (see Figure 6.4.27). λ increases then to a peak before reaching a steady state value, recalling the behaviour of the stress ratio φ in these shearing simulations (see Chapter 6.4.3).

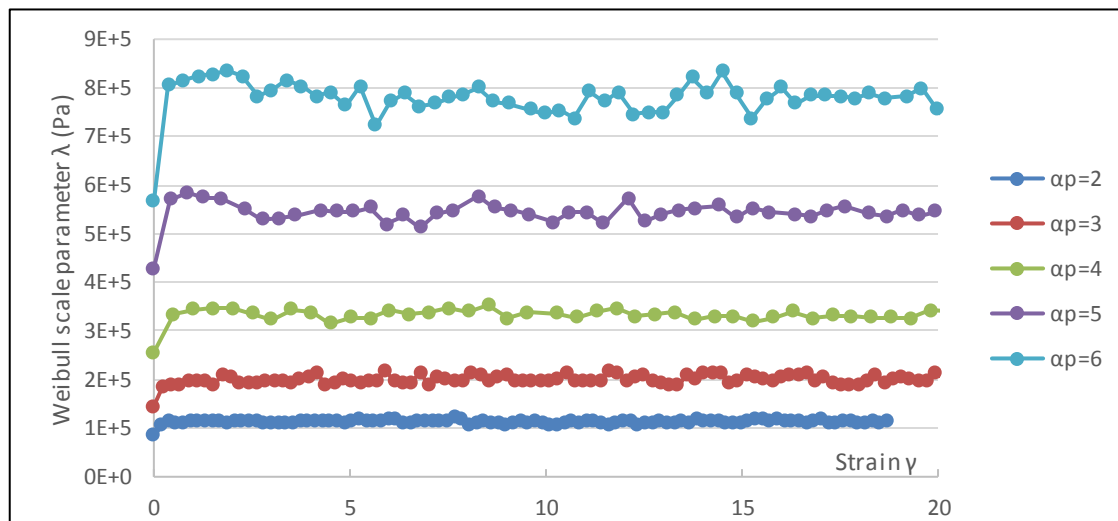


Figure 6.4.27: Weibull scale parameter λ during the shearing phase for the different aspect ratios α_p and a normal stress applied at $\sigma = 10kP$.

As expected, the mean Weibull scale parameter in the steady state, $\bar{\lambda}$, scales with both the particles aspect ratio α_p and the normal stress applied σ (see Figure 6.4.28).

The sensitivity of a particle to mechanical stress scales with its elongation [8, 9], explaining why elongated particles break easier than shorter ones in the same conditions [1], as shorter particles need a greater load to be broken [55, 191]. Indeed, particle elongation promotes the inter-contact distance on a particle (see Chapter

6.4.5), which increases the bending moment and thus the bending stress of particles (see Chapter 5.4.1.1). Considering that the bending stress component contributes predominantly to the particles internal stress (see Chapter 6.4.6.1), it explains the strong correlation between parameter $\bar{\lambda}$ and the aspect ratio.

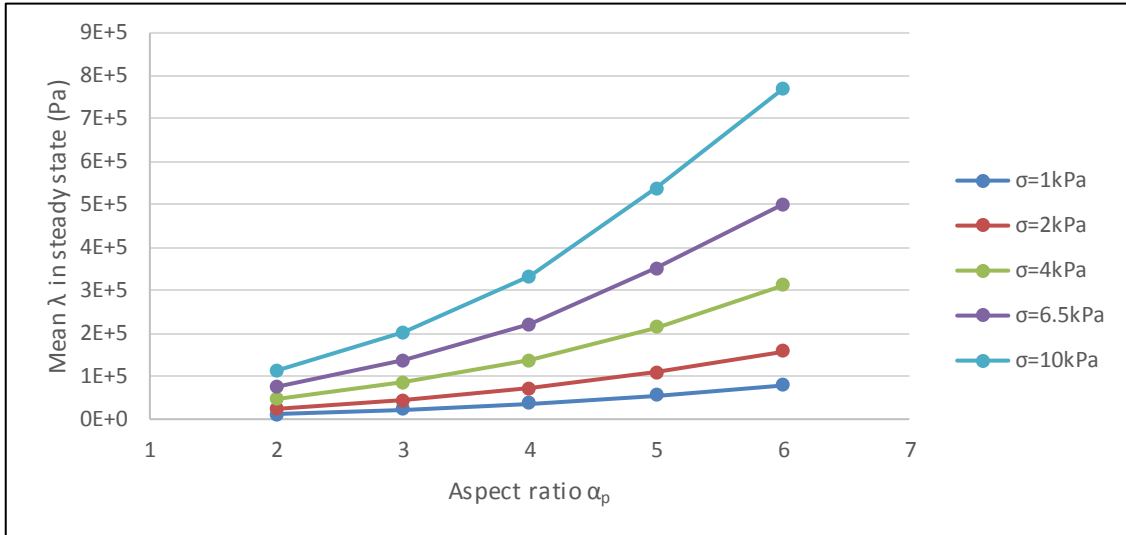


Figure 6.4.28: Mean Weibull scale parameter in steady state, $\bar{\lambda}$, for the different aspect ratios α_p and normal stresses σ .

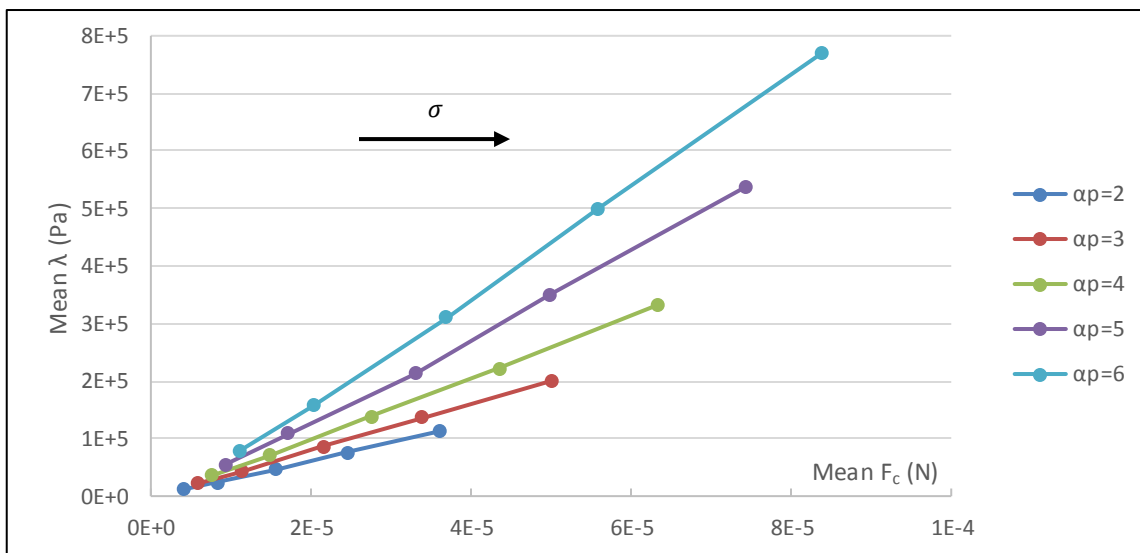


Figure 6.4.29: Mean Weibull scale parameter in the steady state, $\bar{\lambda}$, given by the mean contact force \bar{F}_c for the different aspect ratios α_p . Within each α_p series, \bar{F}_c increases with the normal stress applied σ set at [1; 2; 4; 6.5; 10]kPa.

A greater normal stress applied increases the mean contact force \bar{F}_c (see Chapter 6.4.4), and the linear correlation between $\bar{\lambda}$ and \bar{F}_c (see Figure 6.4.29) is in good agreement with the equation of bending stress calculation (see Chapter 5.4.1.1), with a Pearson coefficient of 0.94, confirming that \bar{F}_c is a key parameter for the estimation of $\bar{\lambda}$.

6.4.6.2.2 Shape Parameter

The value of Weibull shape parameter k increases at the beginning of the shearing phase to reach a steady state (see Figure 6.4.30).

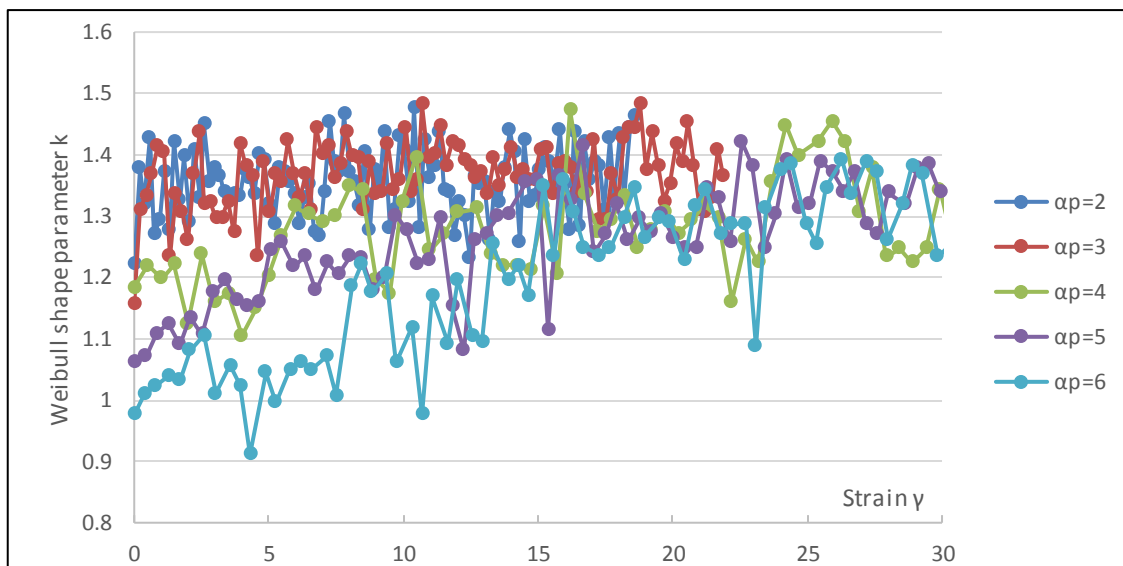


Figure 6.4.30: Weibull shape parameter k in the shearing phase for the different aspect ratios and a normal stress at $\sigma = 6.5 \text{ kPa}$.

The strain required to reach the steady state of k increases with the particles aspect ratio and is not dependant on the normal stress applied (see Figure 6.4.31).

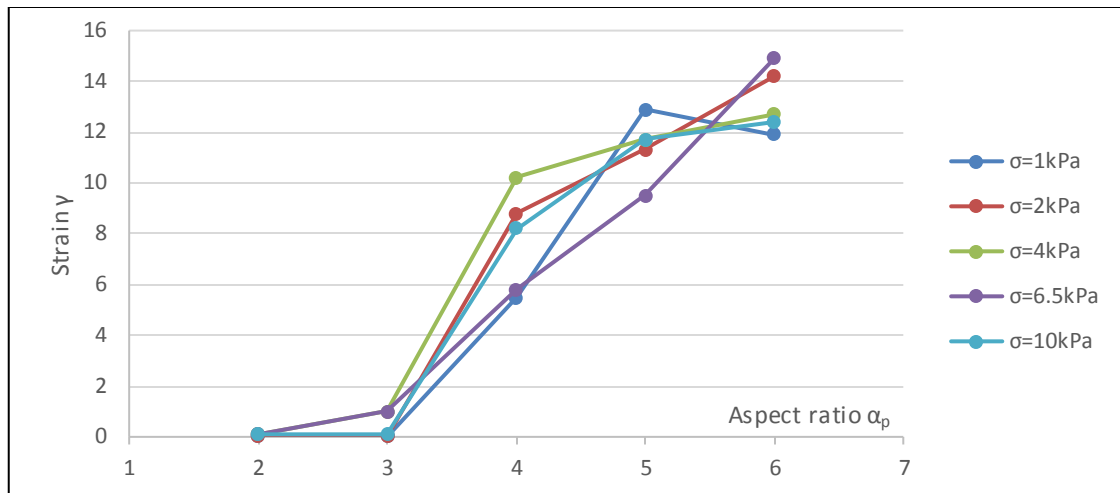


Figure 6.4.31: Strain γ required to reach steady state value of Weibull shape parameter k for the different aspect ratios α_p and normal stresses σ .

The shape parameter k is associated to the standard deviation of the distribution of particles internal stress in an inversely proportional fashion: the greater the shape parameter, the narrower the distribution.

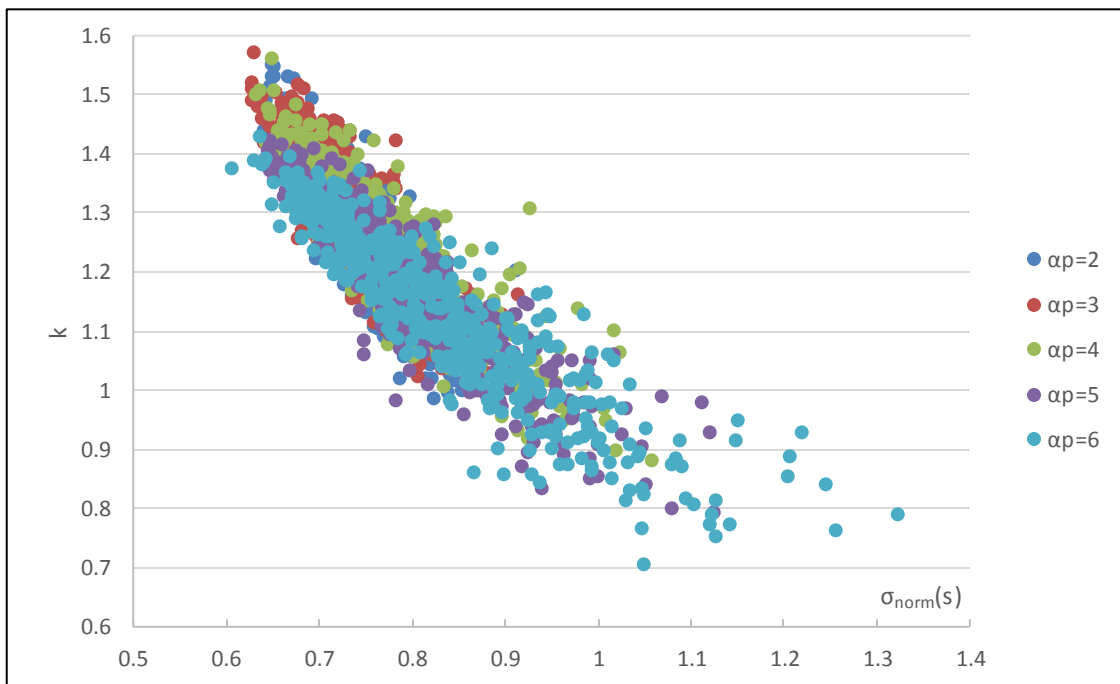


Figure 6.4.32: Weibull shape parameter k in the steady state, given by the normalised standard deviation of the sum of absolute forces on particle $\sigma_{norm}(s)$ for the different aspect ratios α_p .

The strongest correlation found involving k is with the normalised standard deviation of the sum of absolute forces on particle $\sigma_{norm}(s)$ (see Equation 6.5.1) with a Spearman coefficient at -0.9 in the shearing simulations. Interestingly, this correlation is stronger than between the shape parameter and the normalised standard deviation of the particle internal stress with a Spearman coefficient at -0.81 . k is then inversely proportional to $\sigma_{norm}(s)$ in the same fashion for all normal stresses and aspect ratios studied (see Figure 6.4.32).

The mean value of shape parameter during the steady state also increases with the normal stress applied and tends to an inverse proportionality with the particle aspect ratio (see Figure 6.4.33).

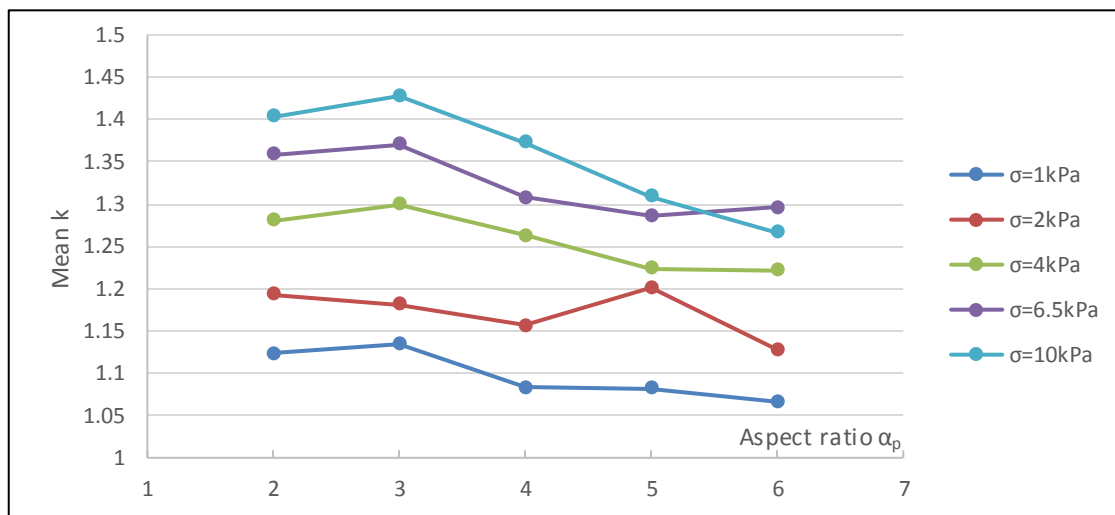


Figure 6.4.33: Mean Weibull shape parameter in steady state, \bar{k} , for the different aspect ratios α_p and normal stresses σ .

6.4.6.2.3 Coefficient of Determination

The coefficient of determination R^2 of Weibull model fitting increases at the beginning of the shearing phase before reaching a steady state (see Figure 6.4.34). The strain required to reach the steady state of R^2 is identical to the values reported for the steady state of Weibull shape parameter k (see Figure 6.4.31).

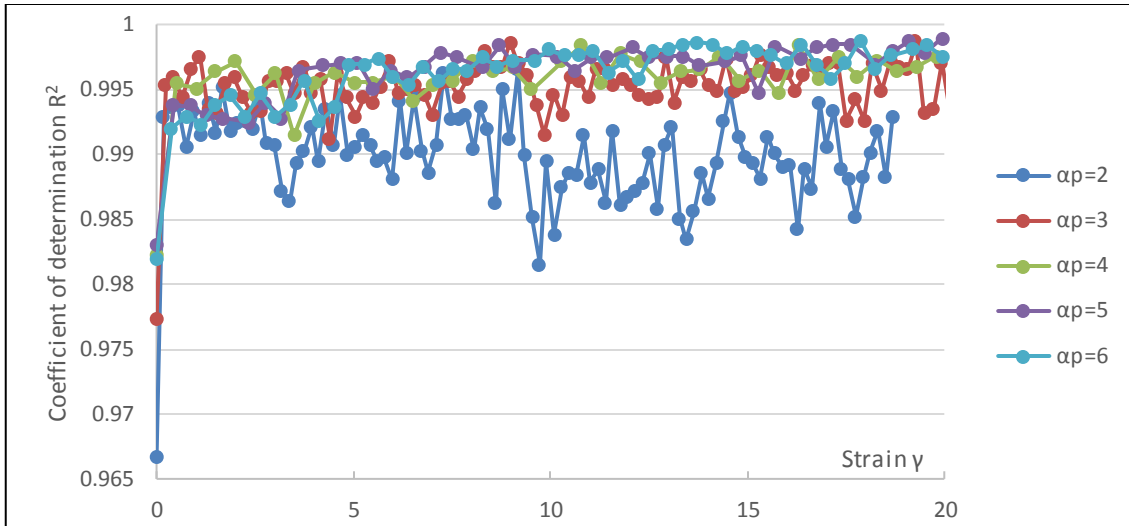


Figure 6.4.34: Coefficient of determination R^2 of Weibull model fitting in the shearing phase for the different aspect ratios α_p and a normal stress at $\sigma = 10\text{kPa}$.

The mean coefficient of determination in the steady state, $\overline{R^2}$, is above 0.97 in all shearing simulations, which indicates an excellent precision of Weibull model fitting (see Figure 6.4.35). $\overline{R^2}$ scales predominantly with the mean number of contacts on particle $\overline{N}_{c,p}$ in the same fashion for all values of aspect ratio α_p and normal stress σ studied.

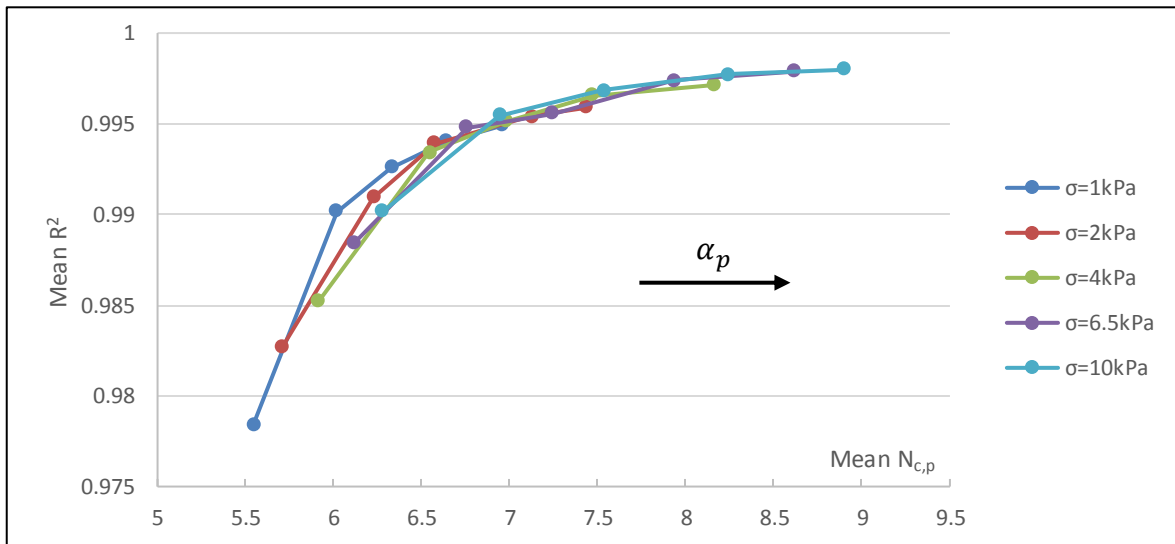


Figure 6.4.35: Mean coefficient of determination $\overline{R^2}$ of Weibull model fitting in the steady state, given by the mean number of contacts on particle $\overline{N}_{c,p}$ for the different normal stresses σ . Within each σ series, $\overline{N}_{c,p}$ scales with the aspect ratio α_p set at [2; 3; 4; 5; 6].

Moreover, the predominance of bending stress in the particle internal stress increases with higher aspect ratio (see Chapter 6.4.6.1), which is in good agreement with the known excellent accuracy of the Weibull model for the fitting of bending stress distributions [47].

Also, the quality of model fitting is more stable during the steady state for higher normal stress and aspect ratio, as R^2 exhibits a lower normalised standard deviation in its steady state (see Figure 6.4.36). Overall, the quality of model fitting is extremely stable with a normalised standard deviation of R^2 below 0.8% in steady state in all shearing simulations.

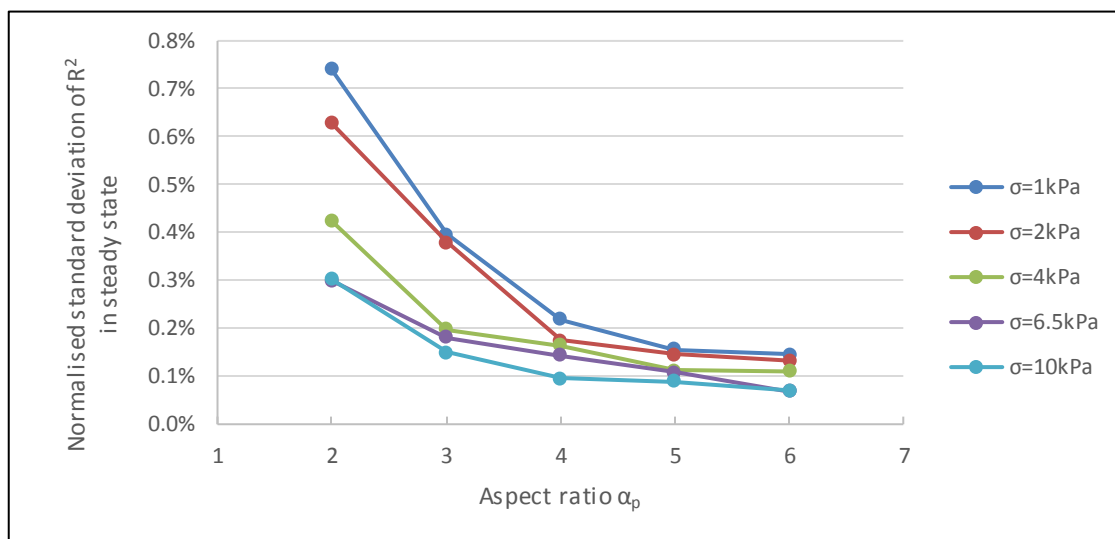


Figure 6.4.36: Normalised standard deviation of the coefficient of determination R^2 in steady state for the different aspect ratios α_p and normal stresses σ .

6.4.6.3 Location of Maximum Stress on Particles

A Gaussian (normal) model is fitted on the distribution of location of maximum stress on particles neutral axis, and the two fitting parameters are obtained i.e. the mean value and the standard deviation σ_{dev} (see Chapter 6.2.2).

The mean value is on the middle, i.e. 50%, of the particle length for all aspect ratios and normal stress applied. This value is confirmed in several DEM simulations involving elongated particles [55, 191, 192, 194, 235].

The standard deviation σ_{dev} is stable during the shearing phase (see Figure 6.4.37).

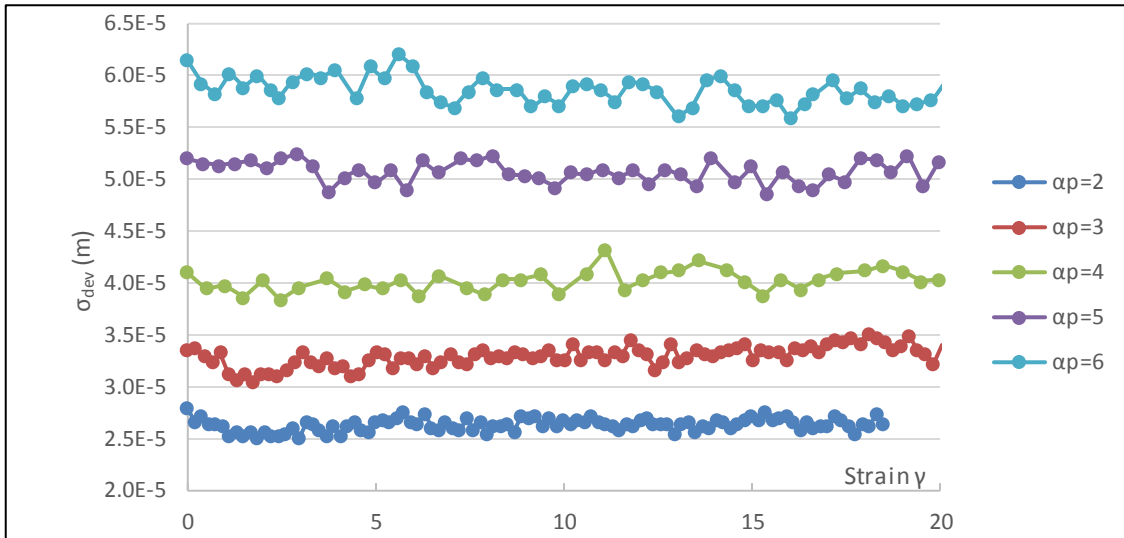


Figure 6.4.37: Standard deviation σ_{dev} of Gaussian fitting of distribution of maximum stress location in the shearing phase for the different aspect ratios α_p and a normal stress at $\sigma = 1kPa$.

$\bar{\sigma}_{dev}$, the mean of σ_{dev} , scales linearly with the aspect ratio α_p (see Figure 6.4.38). Indeed, an increased particle elongation offers a wider range of distance and more possible locations on the particle length, which logically skews the distribution of location of maximum stress.

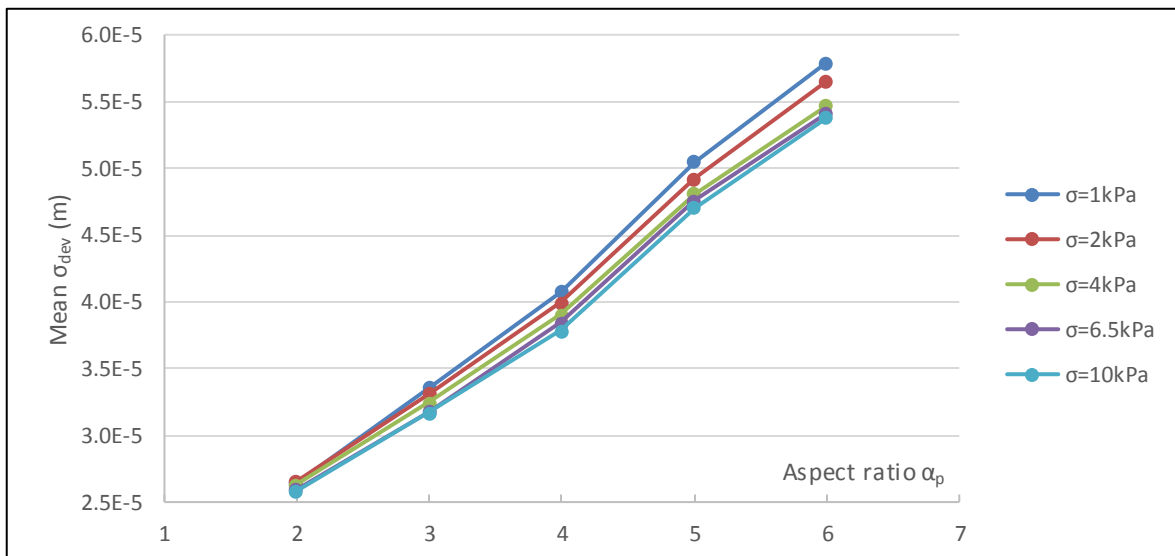


Figure 6.4.38: Mean standard deviation $\bar{\sigma}_{dev}$ of Gaussian fitting of distribution of maximum stress location for the different aspect ratios α_p and normal stresses σ .

The influence of normal stress on $\bar{\sigma}_{dev}$ is due to the number of contacts it produces. Indeed, a higher mean number of contacts on particle $\bar{N}_{c,p}$ decreases $\bar{\sigma}_{dev}$, although with a moderate effect compared to the influence of the aspect ratio (see Figure 6.4.39).

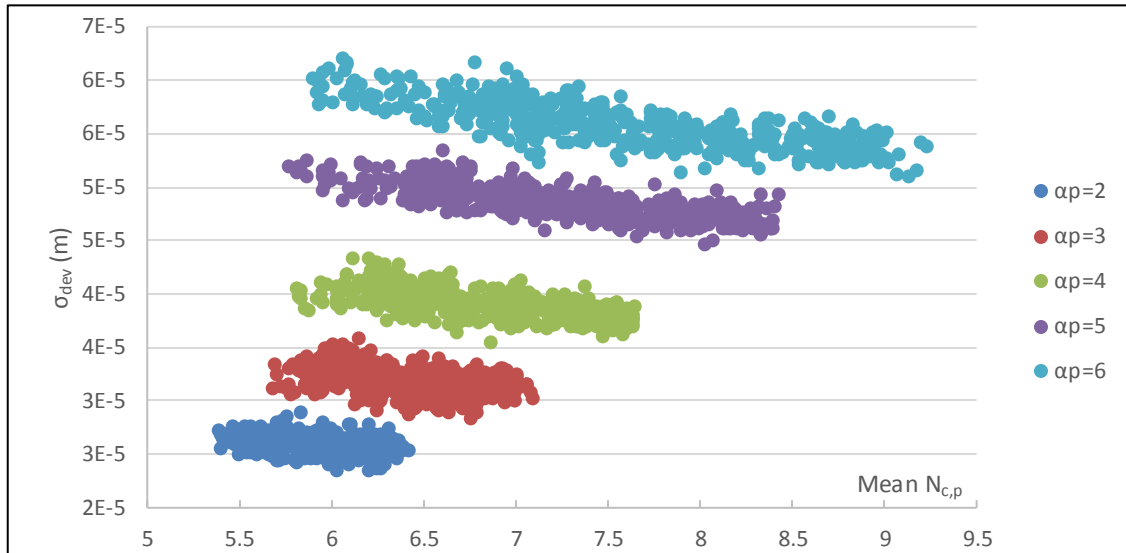


Figure 6.4.39: Standard deviation σ_{dev} of Gaussian fitting of the distribution of maximum stress location in the shearing phase, given by the mean number of contacts on particle $\bar{N}_{c,p}$ for the different aspect ratios α_p .

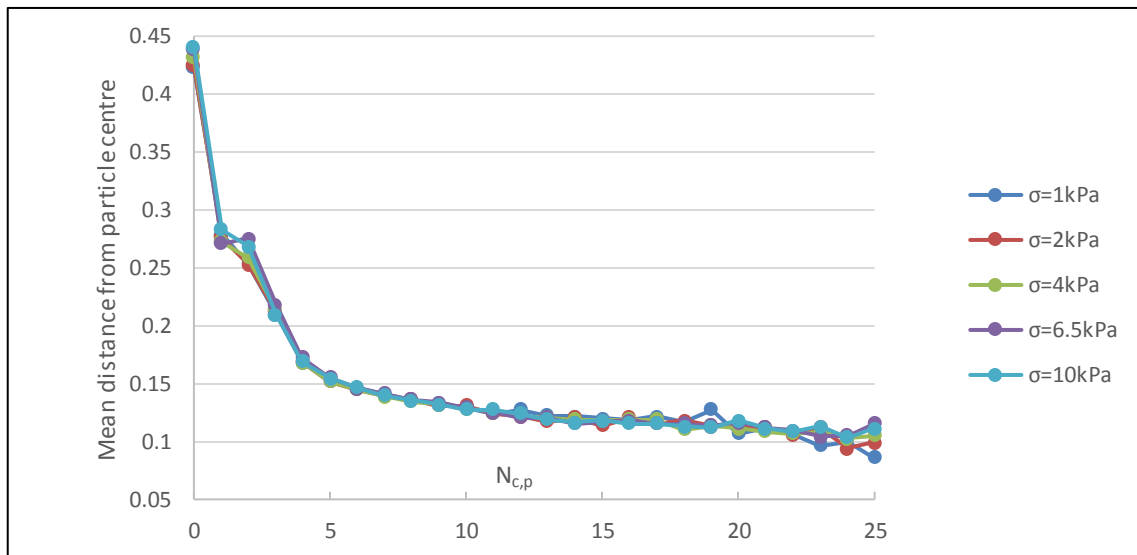


Figure 6.4.40: Mean distance from particle centre of location of maximum stress in the shearing phase, given by the number of contacts on particle $N_{c,p}$ for the different normal stresses σ and an aspect ratio at $\alpha_p = 6$.

The correlation between σ_{dev} and $\bar{N}_{c,p}$ appears linear in the range of data studied, however an observation of this relationship for all the values of $N_{c,p}$ present on an individual particle level shows an inverse function with an important increase of the mean distance of max stress location from particle centre for low $N_{c,p}$ (see Figure 6.4.40). The steady state of this distance for high $N_{c,p}$ is around 10%, which corresponds to the reported normalised standard deviation at 11% of the particle length [191].

6.5 Uniaxial Compression

All variables analysed in this section are averaged over the 5 time recordings for each combination of particle aspect ratio, normal stress and state of alignment.

6.5.1 Number of Core Particles

The number of core particles, determined following the method described in Chapter 5.6, decreases with increasing normal stress in the uniaxial compression (see Figure 6.5.1).

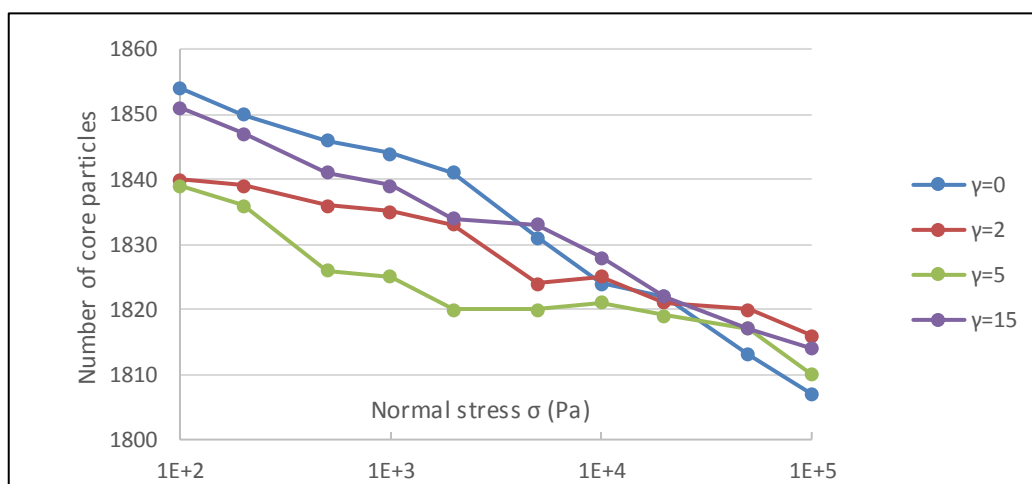


Figure 6.5.1: Minimum number of core particles in uniaxial compression for the different strains γ performed in the shearing phase, normal stresses applied σ , and an aspect ratio of $\alpha_p = 2$.

This indicates a rearrangement of the particles within the bed when a higher pressure is applied, due to the release of contact frictional energy between particles. The coefficient of static friction between walls and particles set at zero might also have facilitated the rearrangements of the particles touching the walls.

The number of core particles in all uniaxial compression simulations remains relevant for statistical analysis with an overall minimum population of 1705 (see Figure 6.5.2).

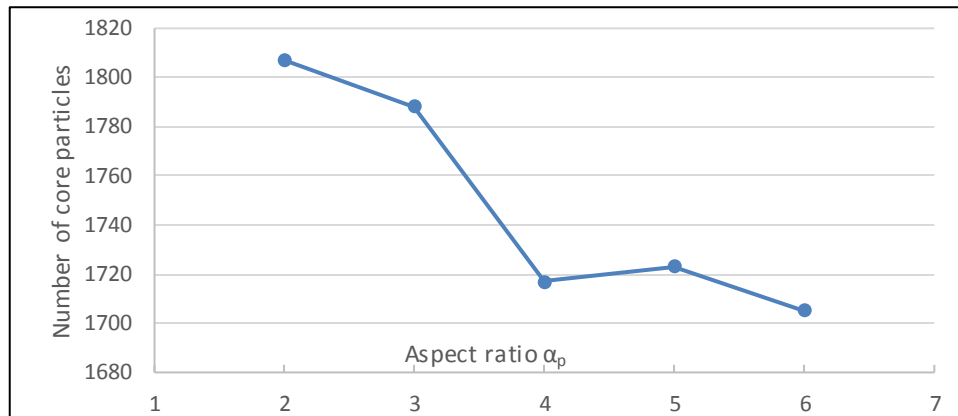


Figure 6.5.2: Minimum number of core particles in all uniaxial compression simulations for different aspect ratios α_p .

6.5.2 Bed Conformation

6.5.2.1 Particle Alignment

The order parameter S quantifies the level of alignment of an elongated particle bed (see Chapter 5.3.2.1). As the normal stress increases in uniaxial compression, the particle bed rearranges which promotes the increase of particle alignment (see Figure 6.5.3).

The variation of S for the different normal stresses applied σ remains low for all performed simulations as it ranges from 1% to 3.1% of initial value i.e. $\sigma = 100Pa$ (see Figure 6.5.4).

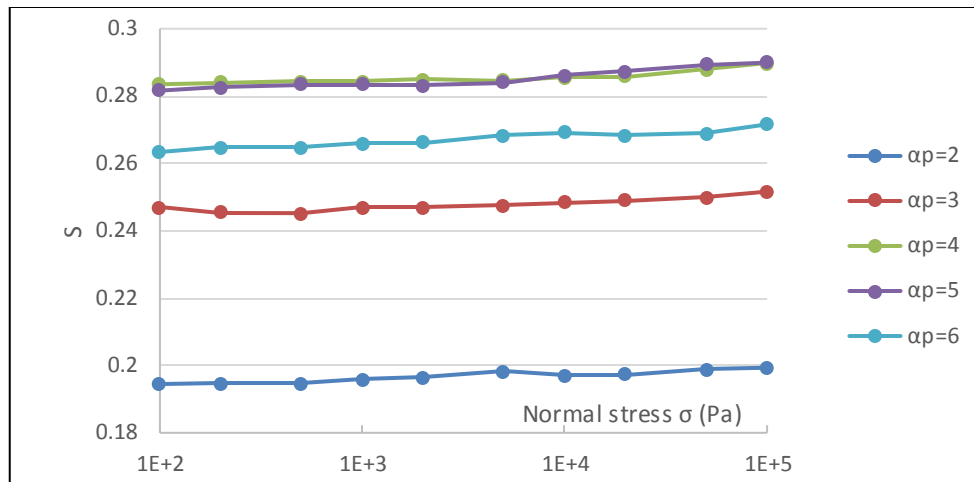


Figure 6.5.3: Order parameter S in uniaxial compression performed at the beginning of shearing phase (i.e. strain applied $\gamma = 0$), for different normal stresses applied σ and aspect ratios α_p .

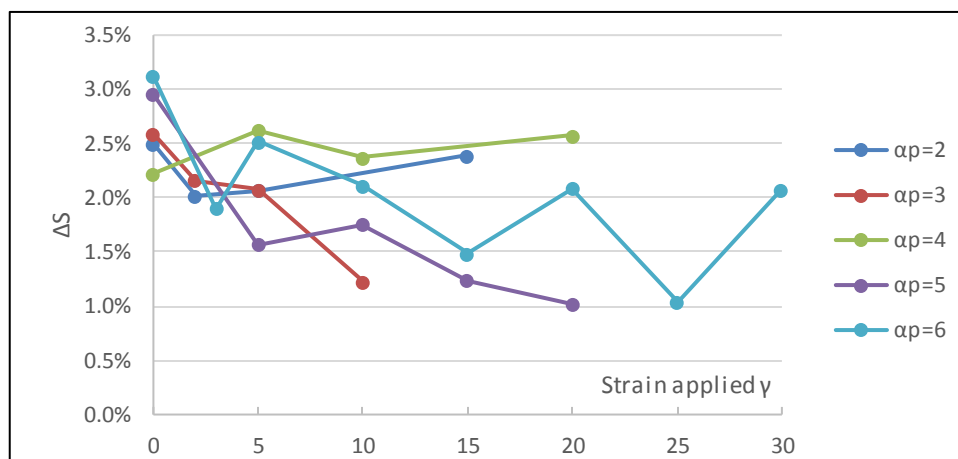


Figure 6.5.4: Maximum variation of order parameter ΔS in uniaxial compression for different aspect ratios α_p and strain applied γ .

6.5.2.2 Bed Densification

As the normal stress applied increases, the bed densifies and the solid fraction augments (see Figure 6.5.5). As observed in Chapter 6.5.2.1, the particle bed rearranges slightly in these uniaxial compression simulations and explains the densification of the bed.

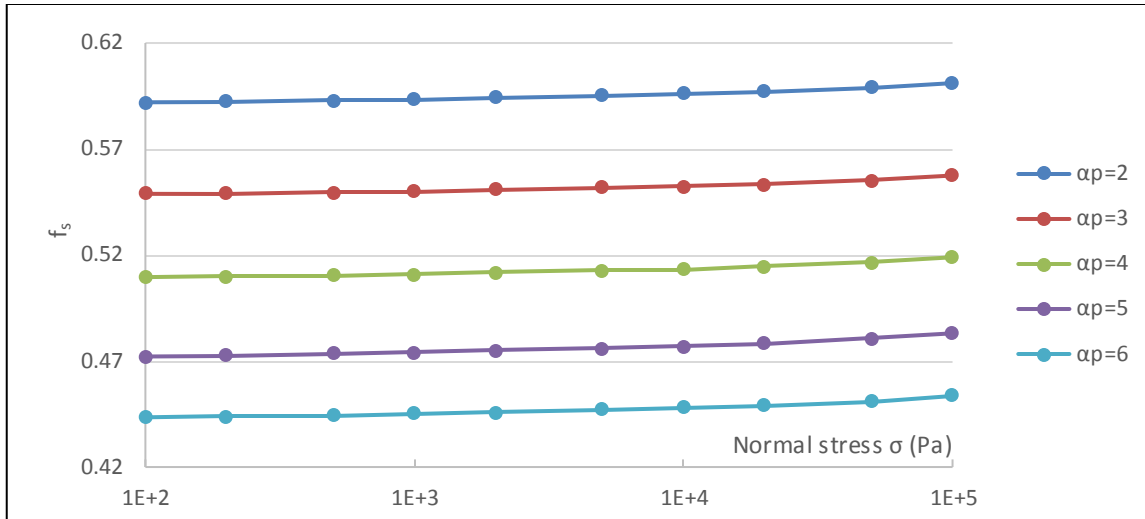


Figure 6.5.5: Solid fraction f_s in uniaxial compression simulations, performed at the beginning of shearing phase ($\gamma = 0$), for different normal stresses applied σ and aspect ratios α_p .

Indeed, the maximum variation of solid fraction Δf_s ranges between 1.5% and 3.1%, which corresponds to the variation observed for the order parameter (see Figure 6.5.6). Δf_s increases with the aspect ratio, whilst the order parameter of the bed doesn't have a particular effect on it.

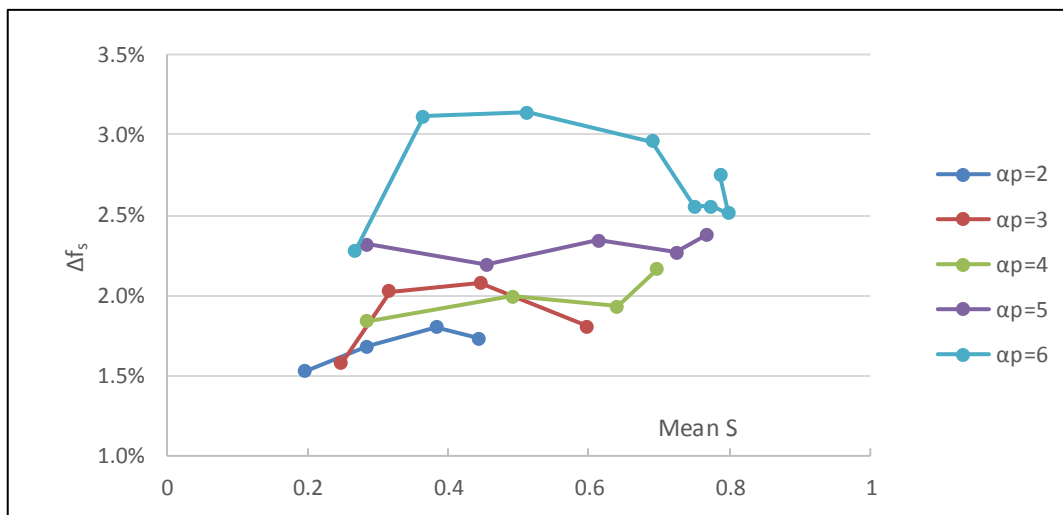


Figure 6.5.6: Maximum variation of solid fraction Δf_s from initial value (i.e. at normal stress applied $\sigma = 100Pa$) in uniaxial compression simulations for different aspect ratios α_p and mean order parameter \bar{S} of the bed.

6.5.2.3 Particle Contacts

The mean number of contacts on particle, $\bar{N}_{c,p}$, increases significantly with the normal stress in uniaxial compression (see Figure 6.5.7).

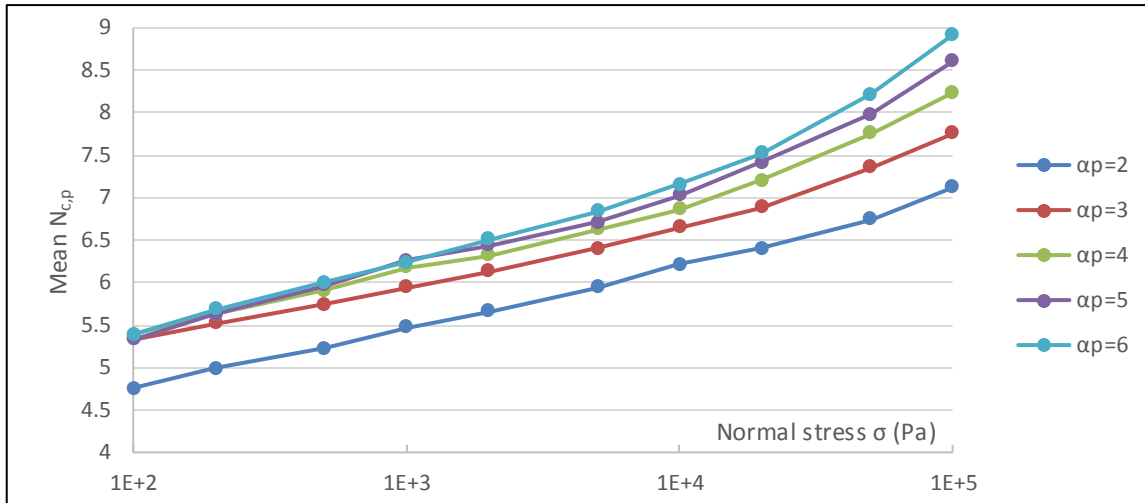


Figure 6.5.7: Mean number of contacts on particle $\bar{N}_{c,p}$ in uniaxial compression simulations, performed at the beginning of shearing phase (i.e. strain applied $\gamma = 0$), for different normal stress applied σ and aspect ratios α_p .

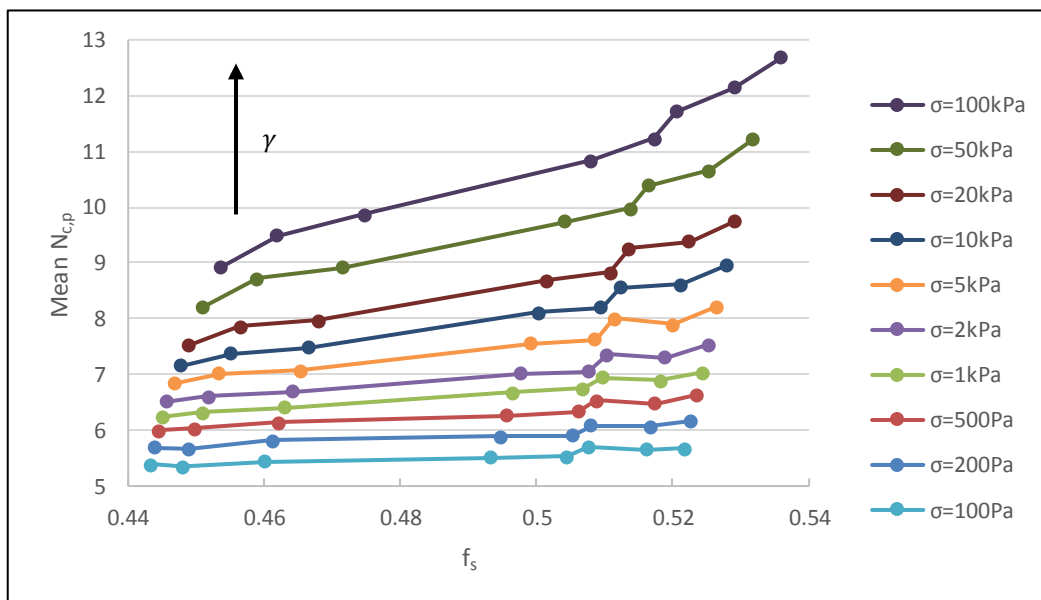


Figure 6.5.8: Mean number of contacts on particles, $\bar{N}_{c,p}$, in uniaxial compression, given by the solid fraction f_s for the different normal stresses σ and an aspect ratio at $\alpha_p = 6$. Within each σ series, $\bar{N}_{c,p}$ scales with the strain applied γ set at [0; 3; 5; 10; 15; 20; 25; 30].

$\bar{N}_{c,p}$ is linearly correlated with the solid fraction f_s due to a denser bed packing (see Figure 6.5.8). The normal stress applied σ affects the ramp between $\bar{N}_{c,p}$ and f_s , where $\bar{N}_{c,p}$ increases with σ for the same f_s . Therefore, in addition to a denser packing related to the increase of particle alignment (see Chapter 6.5.2.2), a greater normal stress also induces forced stacking between particles.

The shape of the particles also has an impact on $\bar{N}_{c,p}$. Indeed, a greater aspect ratio α_p increases the available surface on particles creating more contact points (see Figure 6.5.9). The clumped sphere model used for particle design increases the asperity at the surface of the particles which increases the number of contacts, especially when elongated particles align and experience stacking. In those cases, two particles can enter in contacts on multiple location (see Chapter 6.4.2.3).

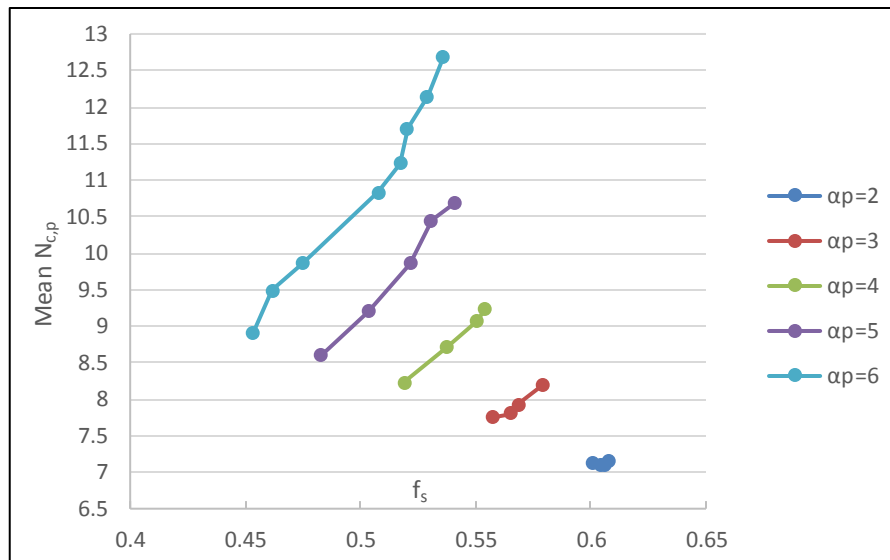


Figure 6.5.9: Mean number of contacts on particles, $\bar{N}_{c,p}$, in uniaxial compression, given by the solid fraction f_s for the different aspect ratios α_p and a normal stress at $\sigma = 100kPa$.

6.5.3 Contact Force

The contact force between particles is dependent on two main factors: the load on the particle bed and its concentration of contacts (see Chapter 6.4.4). The mean contact force \bar{F}_c increases with the aspect ratio α_p as elongated particles pack less efficiently

(see Chapter 6.5.2.2) which decreases the concentration of contacts in the bed. Indeed, this concentration determines the number of force chains supporting the load applied on the bed. Therefore, for a given normal stress applied σ , \bar{F}_c is inversely proportional to the cross-sectional concentration of contacts in the bed (see Figure 6.5.10).

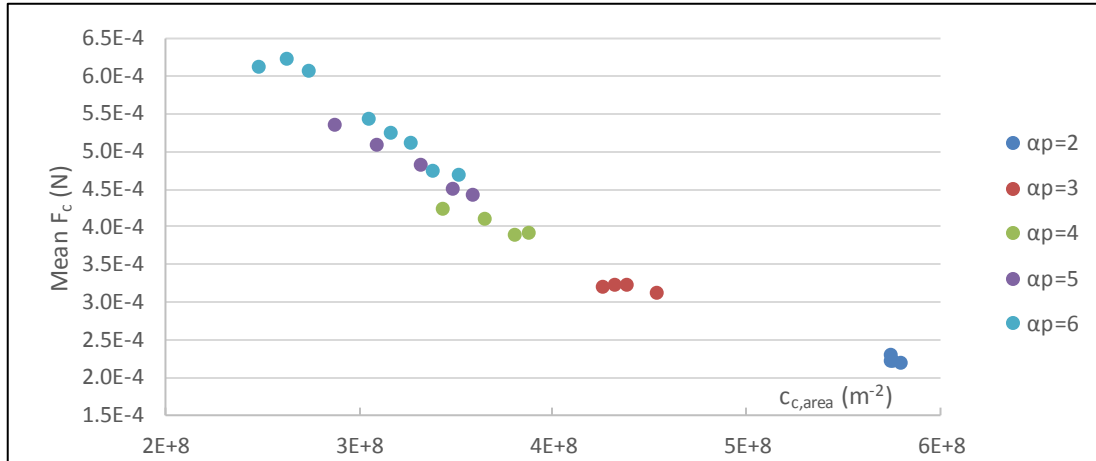


Figure 6.5.10: Mean contact force \bar{F}_c in uniaxial compression, given by the cross-sectional concentration of contacts $c_{c,area}$ for the different aspect ratios α_p and a normal stress at $\sigma = 100kPa$. Each data point corresponds to the different strain value tested.

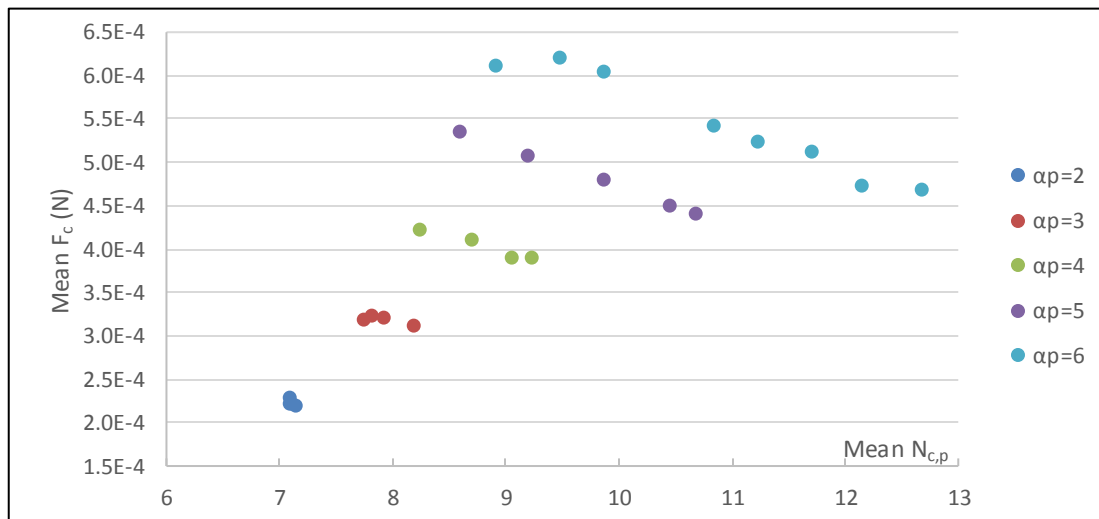


Figure 6.5.11: Mean contact force \bar{F}_c in uniaxial compression, given by the mean number of contacts on particle $\bar{N}_{c,p}$ for the different aspect ratios α_p and a normal stress at $\sigma = 100kPa$. Each data point corresponds to the different strain value tested.

As the bed densifies, the mean number of contacts on particle $\bar{N}_{c,p}$ increases which reduces the magnitude of \bar{F}_c for a given aspect ratio and normal stress (see Figure 6.5.11).

As expected, \bar{F}_c scales with the normal stress applied (see Figure 6.5.12). Nevertheless, this correlation is not perfectly linear as a higher normal stress increases the bed density spreading the load onto additional force chains (see Figure 6.5.9).

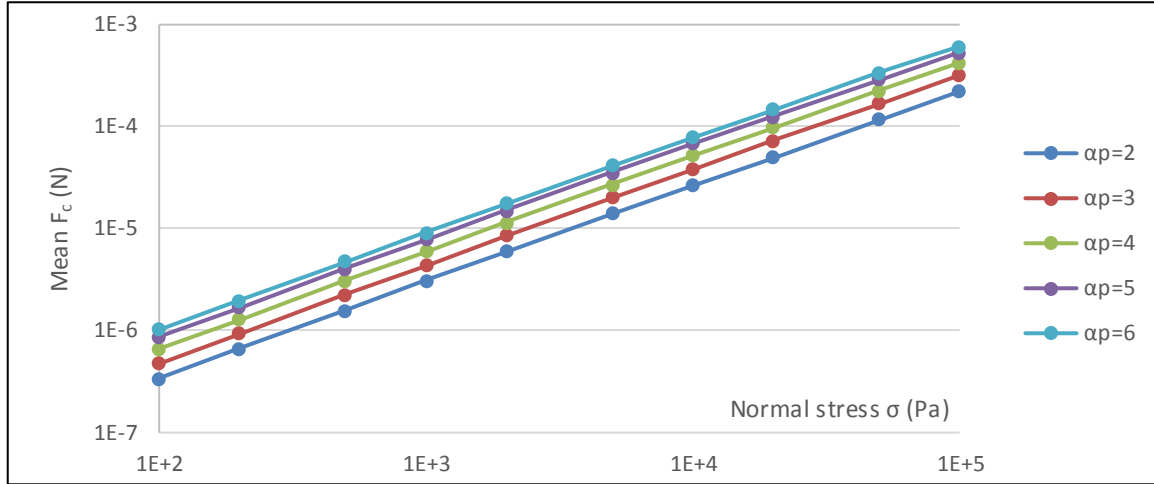


Figure 6.5.12: Mean contact force \bar{F}_c in uniaxial compression, performed at the beginning of the shearing phase (i.e. strain applied $\gamma = 0$), for the different aspect ratios α_p and normal stresses applied σ .

6.5.4 Particles Stability

The mean sum of absolute forces on particle \bar{s} is calculated using the following equation:

$$\bar{s} = \frac{1}{N_p} \sum_{i=1}^{N_p} \sum_{j=1}^{N_{c,i}} |\vec{F}_{j,i}| \quad 6.5.1$$

With N_p number of particles, $N_{c,i}$ number of contacts on particle i and \vec{F} the contact force.

\bar{s} increases with the number of contacts on particle $N_{c,p}$ until it reaches a steady state, at $N_{c,p} \approx 15$ for aspect ratio 6 (see Figure 6.5.13). On an individual particle level, this means that forces are added up to the total force system of the particle with increasing $N_{c,p}$ until enough contacts are made for the particle to reach stability i.e. when \bar{s} reaches a plateau. When a particle is stabilised, new contacts are not adding forces to the force system of the particle, but spread the total load on the particle onto additional supports. This phenomenon is related to the structural stability of granular assembly [271]. As an example, a coordination number greater than 4 is reported necessary to consider stable an assembly of polydisperse spheres [270].

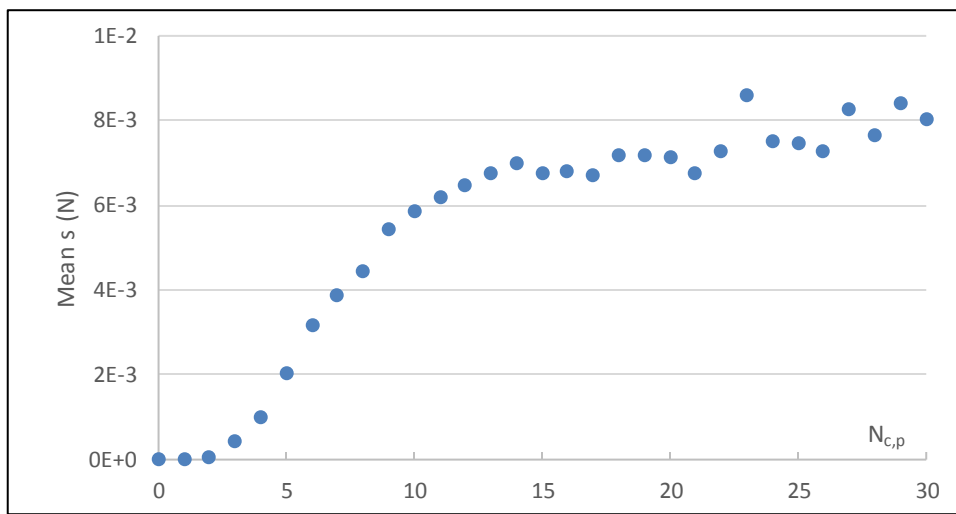


Figure 6.5.13: Mean sum of absolute forces on particle \bar{s} given by the number of contacts on particle $N_{c,p}$ for a strain applied $\gamma = 30$, an aspect ratio $\alpha_p = 6$ and a normal stress $\sigma = 100kPa$.

The shape of the curve can be interpreted as a cumulative density function giving the probability of particles to be stable, and experience the highest force system, for the number of contacts they encounter.

6.5.5 Inter-Contact Distance on Particle

The mean inter-contact distance on particle's neutral axis $\overline{\Delta L}$ is, by definition (see Equation 6.4.2), inversely proportional to the mean number of contacts on particle $\overline{N}_{c,p}$.

As elongated particles have a greater length, this correlation is shifted where $\overline{\Delta L}$ scales with the particles aspect ratio α_p (see Figure 6.5.14).

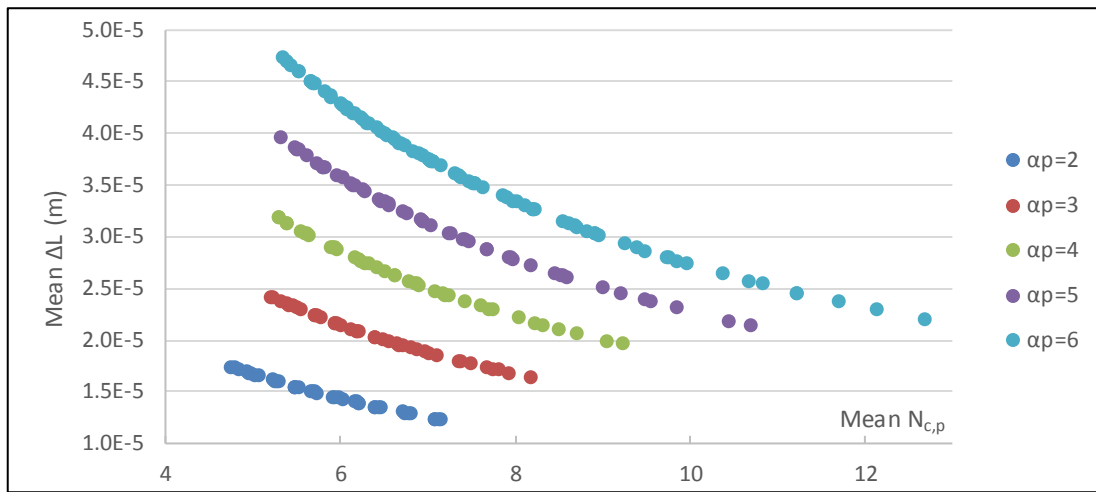


Figure 6.5.14: Mean inter-contact distance on particle $\overline{\Delta L}$ in uniaxial compression, given by the mean number of contacts on particle $\overline{N}_{c,p}$ for different aspect ratios α_p .

$\overline{\Delta L}$ decreases with a greater normal stress applied (see Figure 6.5.15) as it promotes the number of contacts in the bed (see Chapter 6.5.2.3). Even if elongated particles have a higher $\overline{N}_{c,p}$ due to the increased available surface for contacts, their greater length bestows them a higher $\overline{\Delta L}$ for the same normal stress applied (see Figure 6.5.15).

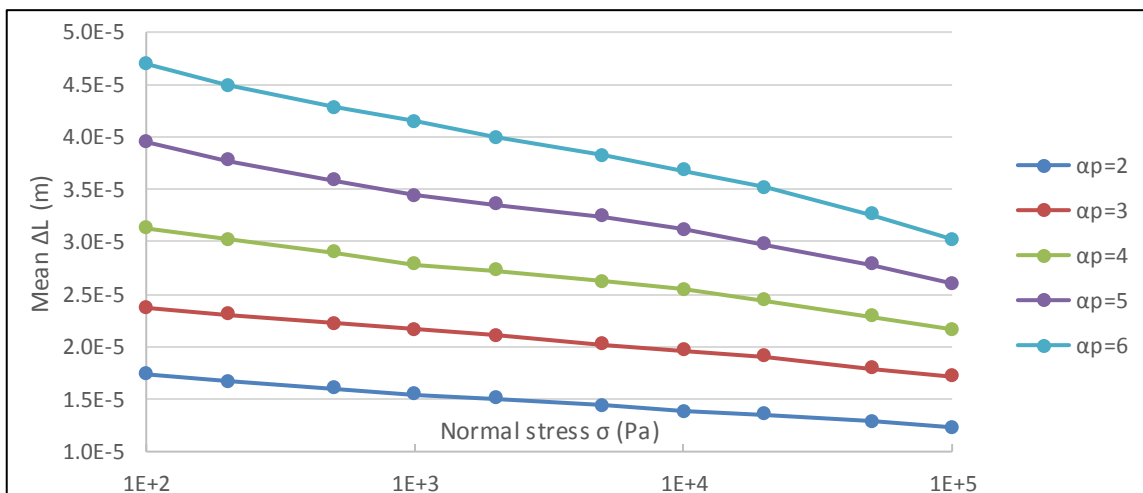


Figure 6.5.15: Mean inter-contact distance on particle $\overline{\Delta L}$ in uniaxial compression, performed at the beginning of the shearing phase (i.e. strain applied $\gamma = 0$), for the different aspect ratios α_p and normal stresses σ .

6.5.6 Particles Internal Stress

6.5.6.1 Predominance of Bending Stress Component

The importance of the bending stress component in the particles internal stress is determined using the bending stress ratio (see Equation 6.4.3). The mean bending stress ratio $\bar{\alpha}_{\sigma,ZZ}$ is above 0.84 in the uniaxial compression simulations which denotes a predominance of the bending stress in the particles internal stress. $\bar{\alpha}_{\sigma,ZZ}$ scales with the particles aspect ratio α_p (see Figure 6.5.16) which confirms the consensus on the fact that bending stress is main breakage mechanism of elongated particles [1].

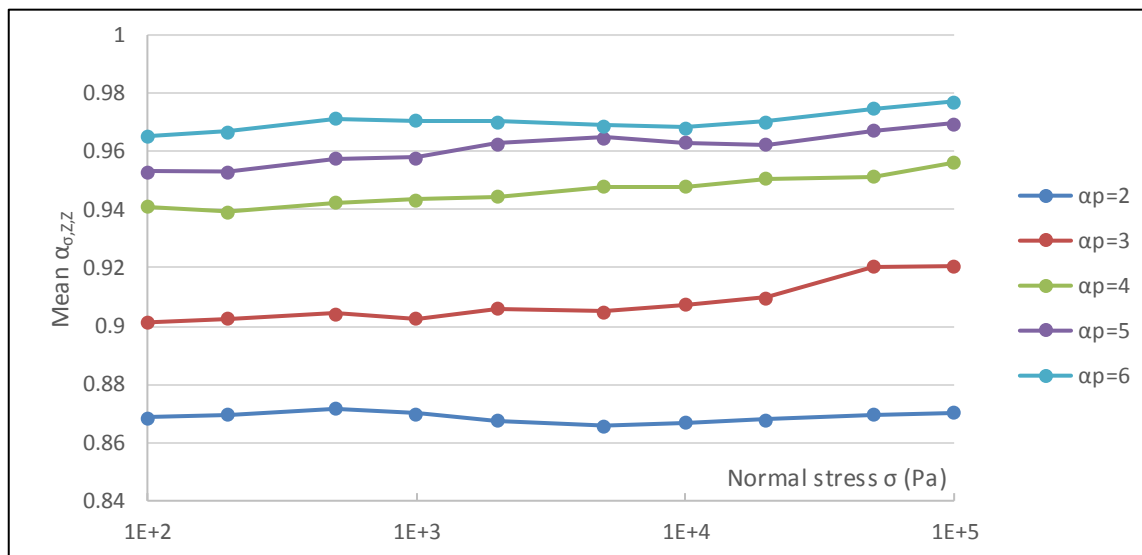


Figure 6.5.16: Mean bending stress ratio $\bar{\alpha}_{\sigma,ZZ}$ in uniaxial compression, performed at the beginning of the shearing phase (i.e. strain applied $\gamma = 0$), for the different aspect ratios α_p and normal stresses σ .

6.5.6.2 Weibull Fit Parameters

The Weibull cumulative distribution function is fitted on the particle internal stress distribution to obtain two key variables for analysis: the scale and shape parameters, respectively λ and k (see Chapter 6.2.1).

6.5.6.2.1 Scale Parameter

As expected, the internal stress experienced by particles, represented by the Weibull scale parameter λ , scales with the normal stress applied onto the bed σ (see Figure 6.5.17) as it increases the mean contact force \bar{F}_c (see Chapter 6.5.3). Also, λ increases with the aspect ratio α_p as it increases the mean inter-contact distance on particle $\bar{\Delta L}$ (see Chapter 6.5.5) and thus the bending stress dominating the particles internal stress (see Chapter 6.5.6.1).

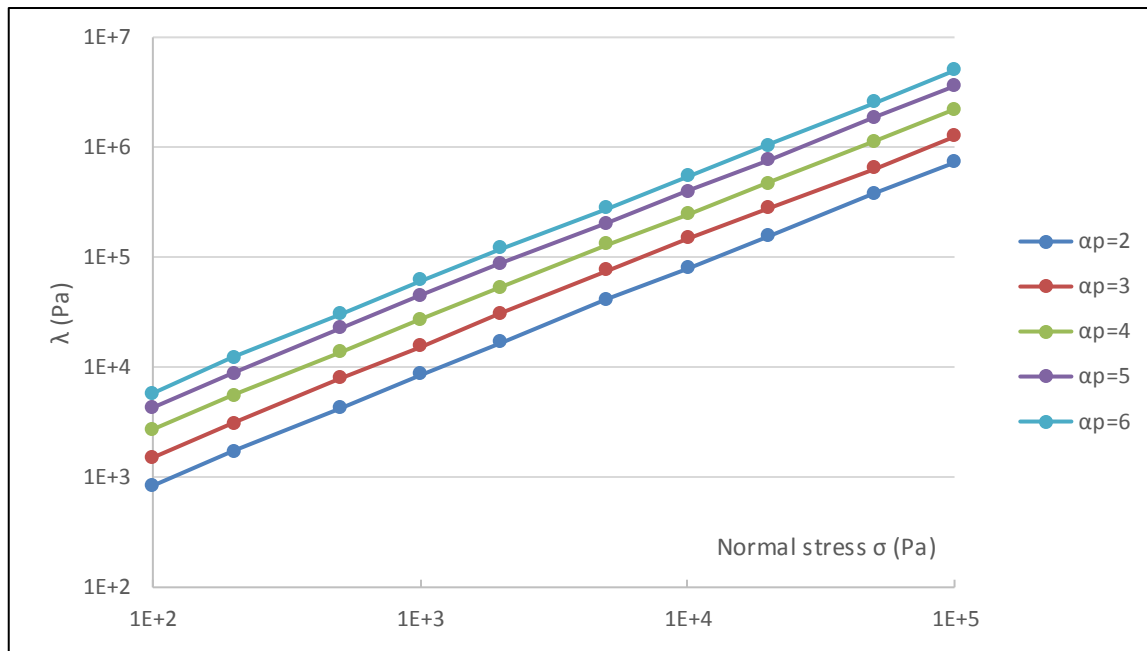


Figure 6.5.17: Weibull scale parameter λ in uniaxial compression simulations, performed at the beginning of shearing phase ($\gamma = 0$), for different normal stress applied σ and aspect ratios α_p .

Surprisingly, a greater ordering of the bed (i.e. strain applied γ) increases λ for the same \bar{F}_c (see Figure 6.5.18). Indeed, the mean number of contacts on particle $\bar{N}_{c,p}$ increases with γ (see Chapter 6.4.2.3) which decreases \bar{F}_c (see Chapter 6.5.3) and $\bar{\Delta L}$ (see Chapter 6.5.5), both by definition positively correlated to λ due to the predominance of the bending stress component (see Chapter 6.5.6.1). This phenomenon is not observable in the range of normal stress applied in the shearing simulations (see Chapter 6.4.6.2.1).

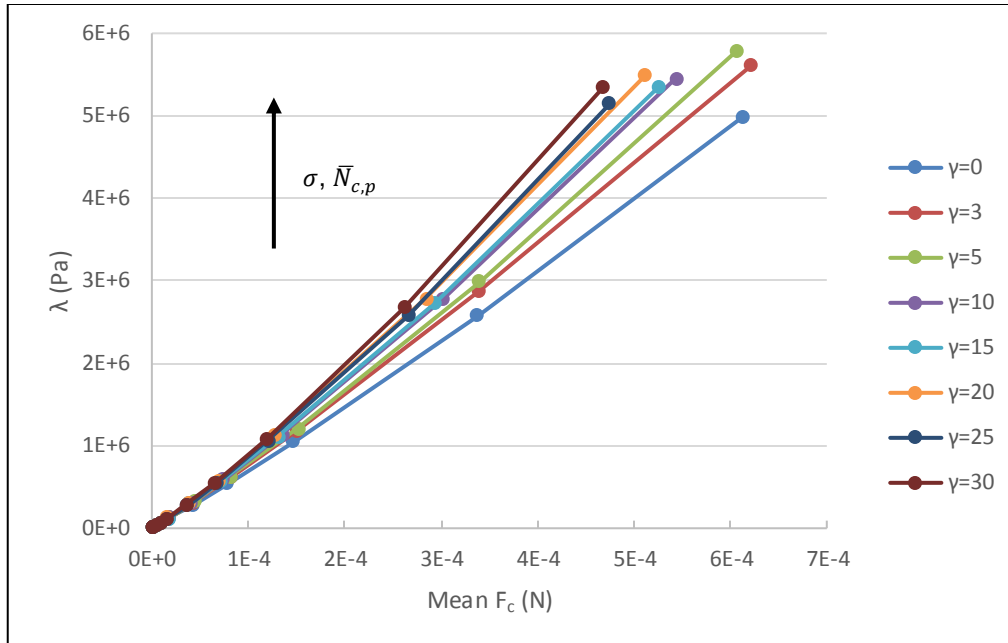


Figure 6.5.18: Weibull scale parameter λ in uniaxial compression, given by the mean contact force \bar{F}_c for the different strain applied γ and an aspect ratio at $\alpha_p = 6$. Within each γ series, λ scales with the normal stress applied σ and the mean number of contacts on particle $\bar{N}_{c,p}$.

The explanation resides in the correlation between λ and the mean sum of absolute forces on particle, \bar{s} , in uniaxial compression simulations being one of the strongest with a Spearman coefficient at 0.99. Indeed, \bar{s} increases with the number of contacts and the particles stability (see Chapter 6.5.4), explaining the positive correlation between λ and $\bar{N}_{c,p}$.

6.5.6.2.2 Shape Parameter

The strongest correlation associated to the Weibull shape parameter k is with the normalised standard deviation of the sum of absolute forces on particle $\sigma_{norm}(s)$ (see Equation 6.5.1) with a Spearman coefficient at -0.96 in uniaxial compression. This correlation is stronger than between k and the normalised standard deviation of the particles internal stress with a Spearman coefficient at -0.88 , which is surprising as k describes the narrowness of the particle internal stress distribution. Here, k is inversely

proportional to $\sigma_{norm}(s)$ in the same fashion for all aspect ratios and normal stresses studied (see Figure 6.5.19).

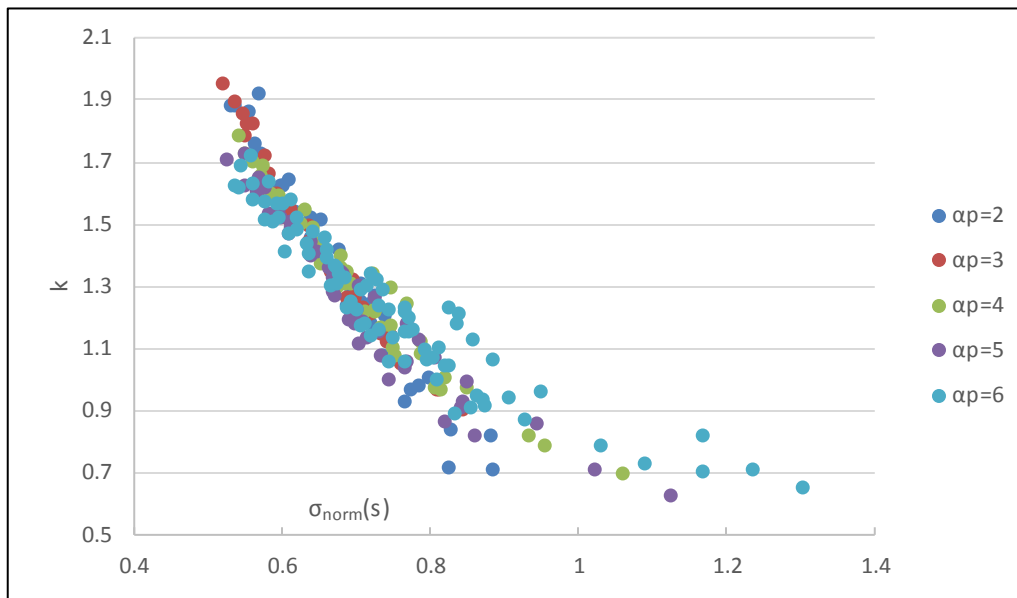


Figure 6.5.19: Weibull shape parameter k in uniaxial compression, given by the normalised standard deviation of the sum of absolute forces on particle $\sigma_{norm}(s)$ for the different aspect ratios α_p .

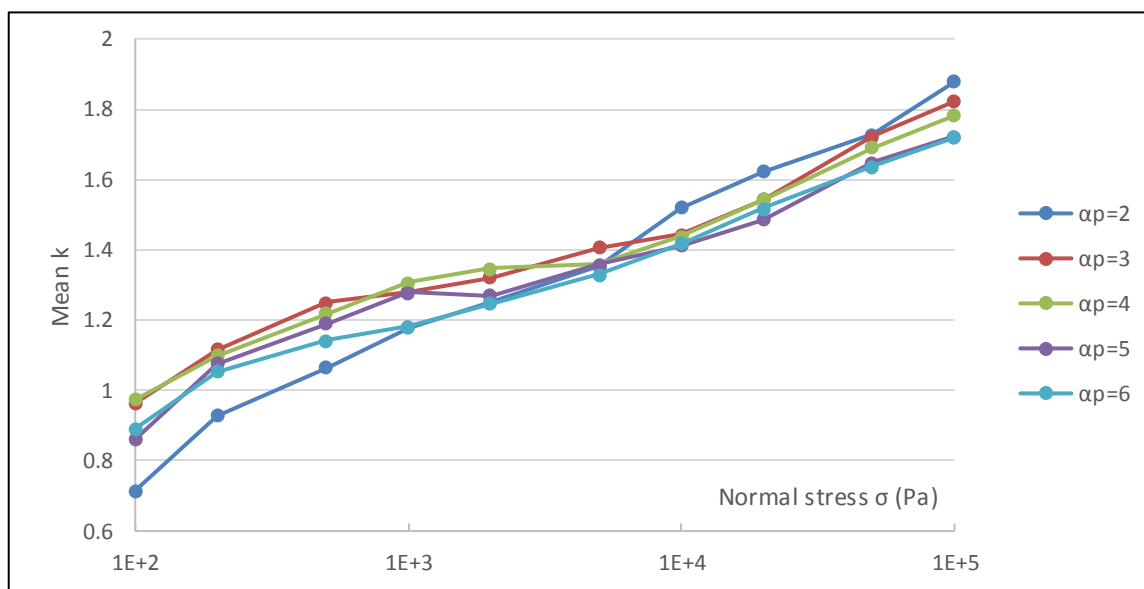


Figure 6.5.20: Mean Weibull shape parameter k in uniaxial compression simulations, performed at the beginning of shearing phase ($\gamma = 0$), for different normal stress applied σ and aspect ratios α_p .

The shape parameter is also strongly correlated with the normal stress applied σ on the bed (see Figure 6.5.20) with a Spearman correlation coefficient of 0.94. Here, the higher the normal stress, the narrower the particle internal stress distribution.

The mean number of contacts on particles $\bar{N}_{c,p}$ doesn't have a particular effect on the shape parameter for a fixed normal stress and aspect ratio (see Figure 6.5.21). This means that the homogenisation of the bed related to a greater k is not due to the increase of number of contacts, but rather due to an overall augmentation of the total force systems on the particles s along with a diminution of their standard deviation.

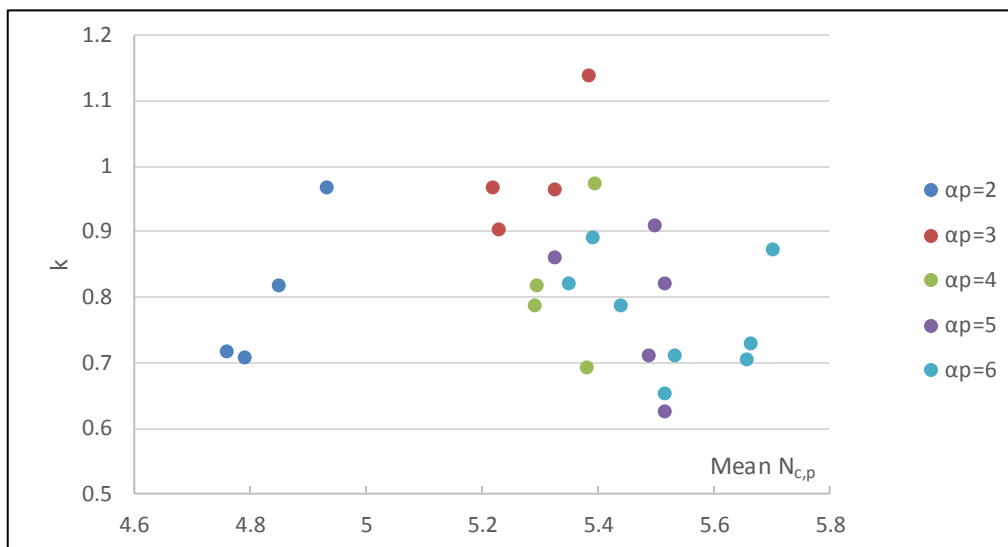


Figure 6.5.21: Weibull shape parameter k given by mean number of contacts on particles $\bar{N}_{c,p}$ in uniaxial compression with a normal stress applied of $\sigma = 100Pa$, for different aspect ratios α_p and bed ordering.

6.5.6.2.3 Coefficient of Determination

The quality of the Weibull fitting of particle internal stress distribution is assessed by calculating the coefficient of determination R^2 . This coefficient is strongly correlated with the mean number of contacts on particle $\bar{N}_{c,p}$ (see Figure 6.5.22) with a Spearman correlation coefficient of 0.92. Indeed, a greater $\bar{N}_{c,p}$ reduces the number of unstable particles with a low number of contacts (see Chapter 6.5.4) and participates to the homogenisation of the bed, promoting a better Weibull distribution fitting.

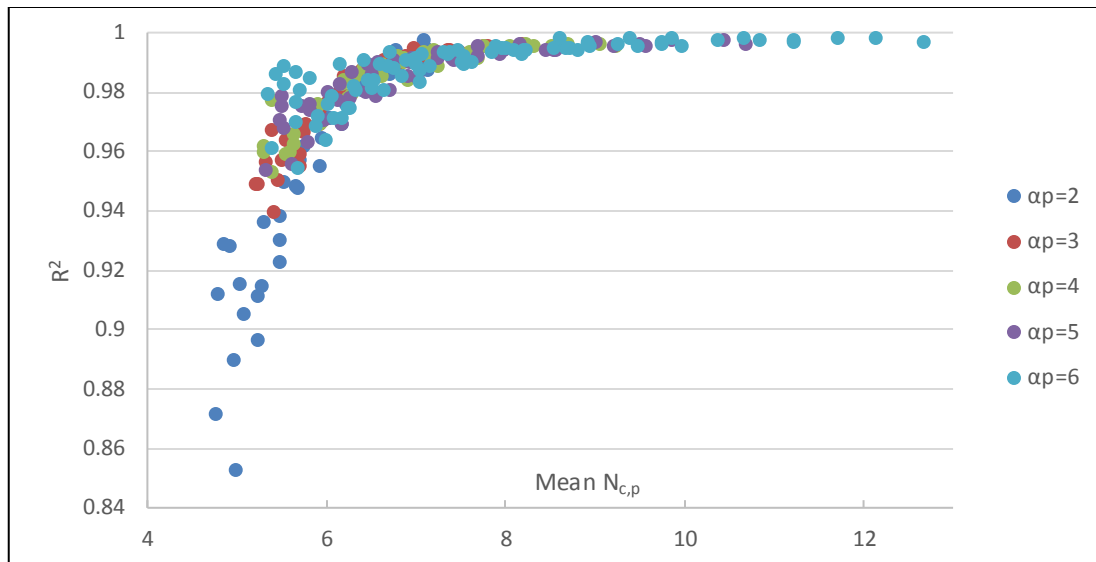


Figure 6.5.22: Coefficient of determination R^2 of Weibull fitting, given by mean number of contacts on particle $\bar{N}_{c,p}$ in uniaxial compression for the different aspect ratios α_p .

Both the aspect ratio α_p and normal stress σ promote $\bar{N}_{c,p}$ (see Chapter 6.5.2.3), explaining their indirect positive correlation with R^2 .

6.5.6.3 Location of Maximum Stress on Particles

A Gaussian cumulative density function is fitted onto the distribution of location of maximum internal stress on particles with two parameters: the mean, which always equals to 50% of the particle length, and the standard deviation σ_{dev} (see Chapter 6.2.2).

σ_{dev} is inversely proportional to the mean number of contacts on particle $\bar{N}_{c,p}$ (see Figure 6.5.23) with a Spearman correlation coefficient of -0.82 . Therefore, the higher the number of contacts, the closer to the centre of the particle the maximum stress is likely to be (see Chapter 6.4.6.3).

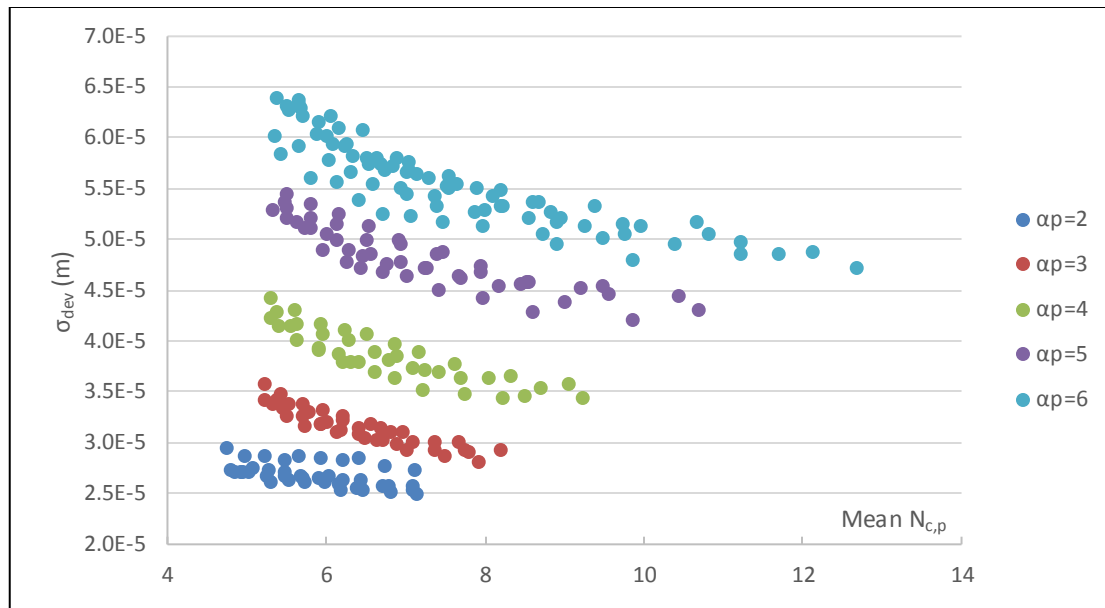


Figure 6.5.23: Standard deviation σ_{dev} of Gaussian fitting of distribution of maximum stress location in uniaxial compression, given by the mean number of contacts on particle $\bar{N}_{c,p}$ for the different aspect ratios α_p .

σ_{dev} is also proportional to the aspect ratio α_p as longer particles offer more possible location for contacts, which inevitably skews the distribution of maximum stress location.

6.6 Conclusions

The behaviour of the particle bed under both shearing and uniaxial compression conditions is analysed and correlations between the main variables characterising the particle bed are evaluated (see Figure 6.6.1).

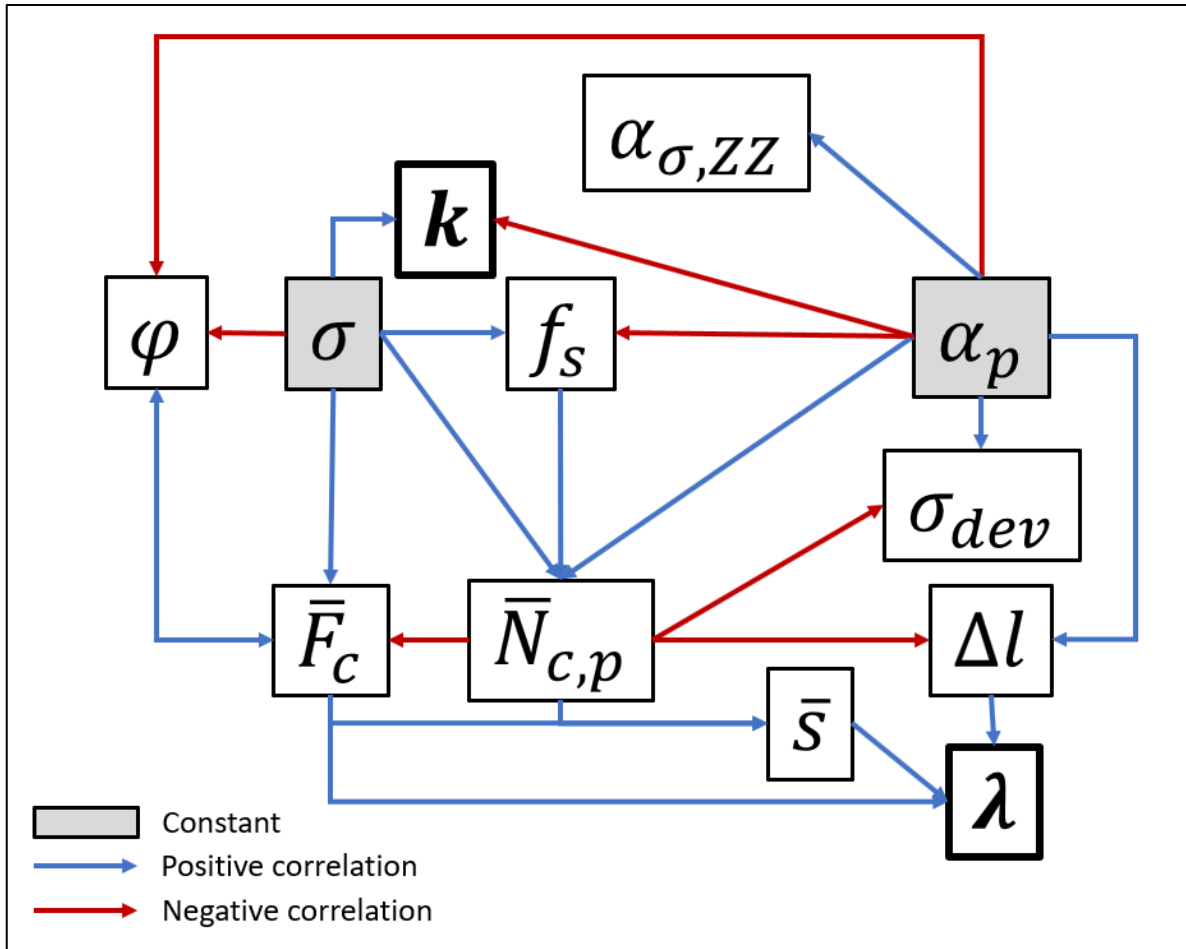


Figure 6.6.1: Direct correlations between main variables characterising the particle bed in the simulations. The description of the variables is listed in Chapter Nomenclature.

The particle aspect ratio α_p and the normal stress applied on the bed σ are the two input variables and remain constant during the shearing phase.

It is found that two variables have a direct impact on the Weibull scale parameter λ of particle internal stress distribution: the mean contact force \bar{F}_c and the mean inter-contact distance on particles $\bar{\Delta l}$. This is in good agreement with the fact that the bending stress is predominant in the particle internal stress, especially for more elongated particles. Additionally, the probability of the particle's stability, represented by the sum of absolute forces on a particle s , appears as a key factor for the evaluation of λ . This probability is dependent on the number of contacts on a particle $N_{c,p}$.

The Weibull shape parameter k is conditioned by the particles aspect ratio α_p and the normal stress applied on the bed σ . Here, shorter particles and a higher bed compression promote a narrower distribution of the particles internal stress.

The Gaussian standard deviation of the maximum internal stress location on the particle neutral axis, σ_{dev} , scales with particle length and aspect ratio. A higher number of contact on particle $N_{c,p}$ decreases σ_{dev} , meaning that the maximum particle internal stress is more likely to be located towards the middle of the particle.

Finally, it is mentioned that the implementation, testing and running of the complex Euler Equation of Motion for the calculation of particles internal stress has requested a non-negligible amount of time and computational power. Thus, the use of this technique would difficultly be viable for a higher population of particles considering its resource-consuming trait. The correlations found in this chapter will be used in Chapter 7 for the creation of mathematical models for the prediction both Weibull scale parameter λ , Weibull shape parameter k , and the Gaussian parameter σ_{dev} . This model building will allow to avoid the use of the resource-consuming use of Euler Equation of Motion.

7 Prediction of Particles Internal Stress for Agitated Drying Conditions

7.1 Introduction

The analysis of the behaviour of a particle bed in DEM shear cell simulations in Chapter 6, on both uniaxial compression and shearing phase, has given insights on the existing mechanical phenomena and direct correlations between characteristic variables. The provided explanation and quantification of these inter-connections between variables allows the creation of predictive models for the estimation of key factors impacting particle breakage in agitated drying conditions.

In this chapter, models are built from both physical theory and empirical regressions to predict the particle internal stress, the Weibull parameters λ and k of the particle internal stress distribution (see Chapter 6.2.1), and the standard deviation of the maximum stress location on particles σ_{dev} (see Chapter 6.2.2) using the identified correlations summarised in Chapter 6.6. These models are calibrated to fit the simulation data and values of particles internal stress calculated using the Euler Equation of Motion (see Chapter 5.4.1.2).

Different models are created to allow the estimation of these key variables from either simulation data or bulk parameters, allowing process designers to avoid the use of simulations. All the models are created in the objective to bypass the resource-consuming implementation, testing and running of the complex Euler Equation of Motion (see Chapter 5.4.1.2).

7.2 Theoretical Model for Prediction of Particle Internal Stress

The analysis of the simulations performed has given insights on the behaviour of an elongated particle bed when submitted to compression and shearing (see Chapter 6). The different phenomena and correlations detected are corroborated by the physical theory and are the basis of the creation of a theoretical model to predict the particles internal stress.

It has been demonstrated that the bending stress is the predominant component of the particle internal stress (see Chapters 6.4.6.1 and 6.5.6.1), and it is reported as the main cause of breakage of elongated particles [1]. The following model is then built accordingly and the predictions are compared with the simulation data to assess the accuracy of the model. A calibration of the model is applied to account for the first approximation approach, the different decided assumptions and the possible phenomena that haven't been considered during the creation of the model.

7.2.1 Mean Contact Force

7.2.1.1 In Uniaxial Compression

In a particle bed, the forces are transmitted via particle-particle contacts creating force chains [195, 285-287]. The compressive force applied to the particle bed within the shear cell is distributed over $N_{c,A}$ number of contacts present on a cross-section (A) parallel to the walls (see Figure 7.2.1). It is noted that a heterogeneity of contact force value is expected creating weak and strong force chains [205, 285, 288].

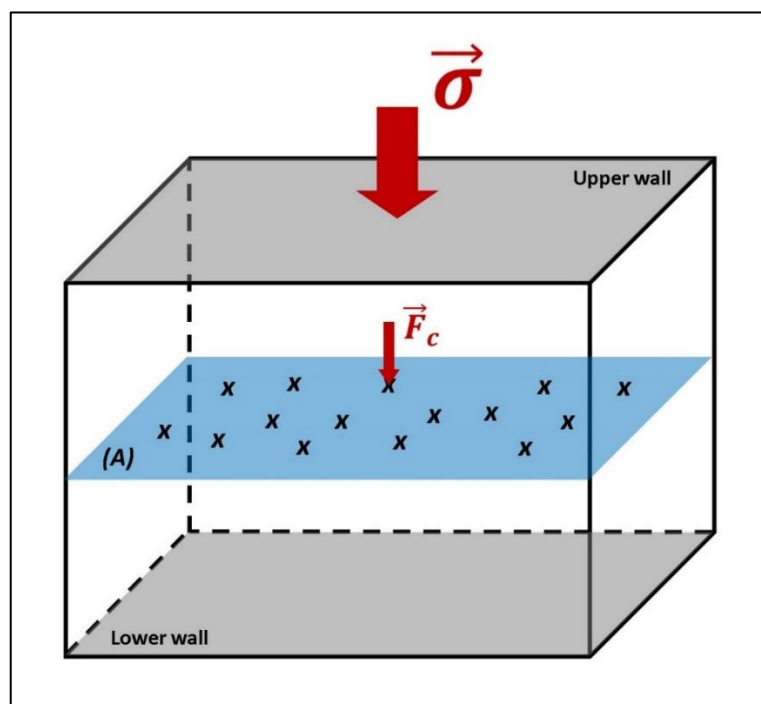


Figure 7.2.1: Compressive stress $\vec{\sigma}$ distributed over contacts (black crosses) on cross-section (A) with contact forces \vec{F}_c

$N_{c,A}$ is expressed as:

$$f(x) = \frac{1}{\sigma_{dev}\sqrt{2\pi}} e^{-\frac{1}{2}\left(\frac{x-\bar{x}}{\sigma_{dev}}\right)^2} \quad 7.2.1$$

$$N_{c,A} = A \cdot c_{c,area}$$

With A the area of the cross-section (A) and $c_{c,area}$ the cross-sectional concentration of contacts which can be estimated from the volume concentration of contacts $c_{c,vol}$ in the shear cell, assuming an isotropic distribution of contacts (see Equation 6.4.1).

The mean contact force \bar{F}_c is then obtained from the normal stress σ :

$$f(x) = \frac{1}{\sigma_{dev}\sqrt{2\pi}} e^{-\frac{1}{2}\left(\frac{x-\bar{x}}{\sigma_{dev}}\right)^2} \quad 7.2.2$$

$$\bar{F}_c = \frac{\sigma}{c_{c,vol}^{2/3}}$$

Indeed, the analysis of correlations in Chapter 6.5.3 demonstrate the linear proportionality between \bar{F}_c and σ (see Figure 6.5.12), and the sole and inverse proportionality between \bar{F}_c and $c_{c,area}$ for a fixed normal stress (see Figure 6.5.10).

$c_{c,vol}$ is expressed as a function of the mean number of contacts on particle $\bar{N}_{c,p}$ and the volume concentration of particle $c_{p,vol}$:

$$c_{c,vol} = \frac{\bar{N}_{c,p}}{2} \cdot c_{p,vol} \quad 7.2.3$$

Here, $\bar{N}_{c,p}$ is divided by 2 as each single contact between two particles is considered as two contacts (one by involved particles) in this variable.

Chapter 7: Prediction of Particles Internal Stress for Agitated Drying Conditions

$c_{p,vol}$ is, by definition, the number of particles in the bed $N_{p,bed}$ divided by the volume of the bed V_{bed} , and $N_{p,bed}$ is itself the solid volume in the bed $V_{sol,bed}$ divided by the volume of a particle V_p , such as:

$$c_{p,vol} = \frac{N_{p,vol}}{V_{bed}} = \frac{V_{sol,bed}}{V_{bed} \cdot V_p} = \frac{f_s}{V_p} \quad 7.2.4$$

With f_s the solid fraction in the bed.

Assuming a cylindrical shape of particles, V_p is given as:

$$V_p = 2\pi\alpha_p r_p^3 \quad 7.2.5$$

With r_p the radius of an element sphere and α_p the aspect ratio of particles in the monodisperse bed.

Here:

$$c_{c,vol}^{-2/3} = \left(\frac{4\pi\alpha_p r_p^3}{\bar{N}_{c,p} \cdot f_s} \right)^{2/3} \quad 7.2.6$$

Thus, \bar{F}_c is expressed as:

$$\bar{F}_c = \sigma \cdot \left(\frac{4\pi\alpha_p r_p^3}{\bar{N}_{c,p} \cdot f_s} \right)^{2/3} \quad 7.2.7$$

Indeed, the analysis of simulation data highlights the inverse proportionality between \bar{F}_c and $\bar{N}_{c,p}$ (see Figure 6.5.11), whilst \bar{F}_c increases with the aspect ratio α_p (see Figure 6.5.12). The variation of solid fraction is too small to detect a direct effect on \bar{F}_c , especially with the direct correlation existing between f_s and $\bar{N}_{c,p}$ (see Figure 6.5.9).

Using the values collected from the performed uniaxial compression simulations, it can be observed that the linearity between \bar{F}_c/σ and $c_{c,vol}^{-2/3}$ is respected for all aspect ratios (see Figure 7.2.2). However, these two terms are not equal, especially for higher aspect ratios, and a calibration of the model will be further needed.

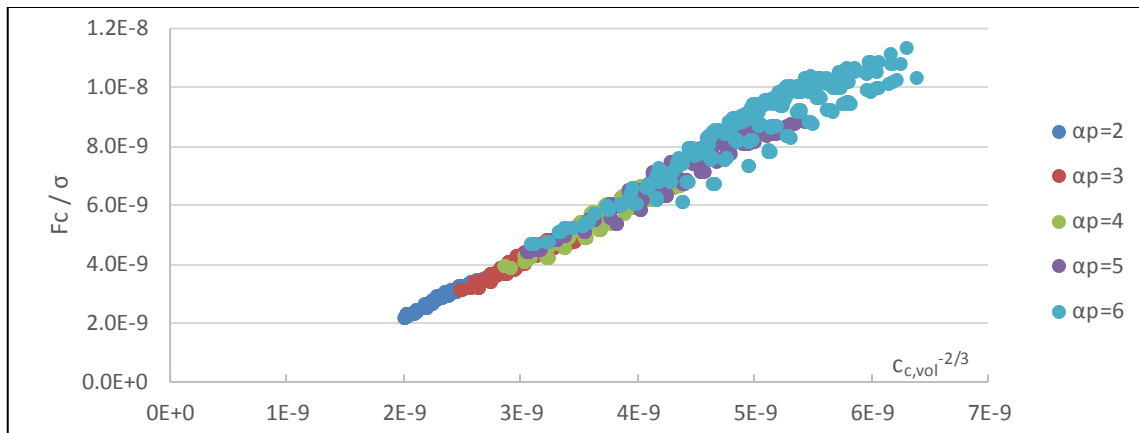


Figure 7.2.2: Linear correlation between \bar{F}_c/σ (in m^{-2}) and $c_{c,vol}^{-2/3}$ (in m^{-2}) for the different aspect ratios α_p in uniaxial compression, as described in Equation 7.2.7.

7.2.1.2 In Shearing Phase

When the walls strain the particle bed, a shear stress τ is induced within the shear cell. For each contact in the bed, a shear component is added to the contact force (see Figure 7.2.3).

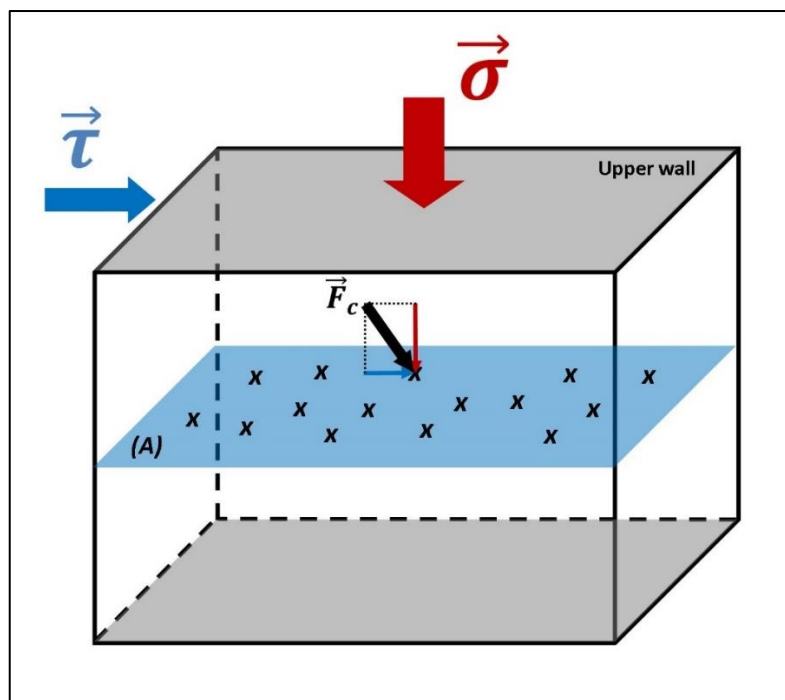


Figure 7.2.3: Compressive stress $\vec{\sigma}$ and shear stress $\vec{\tau}$ distributed over contacts (black crosses) on cross-section (A) with contact forces \vec{F}_c .

Therefore, using Equation 7.2.7 and assuming an isotropy of contact distribution within the particle bed:

$$\bar{F}_c = \sigma \sqrt{1 + \varphi^2} \cdot c_{c,vol}^{-2/3} \quad 7.2.8$$

$$\bar{F}_c = \sigma \sqrt{1 + \varphi^2} \left(\frac{4\pi\alpha_p r_p^3}{\bar{N}_{c,p} \cdot f_s} \right)^{2/3} \quad 7.2.9$$

With φ the stress ratio (see Equation 2.4.6). Here, the shear stress component is included using the Pythagorean theorem.

The analysis of simulation data in Chapter 6.4.4 for the shearing phase highlights the positive correlation between \bar{F}_c and both α_p and σ (see Figure 6.4.18), whilst showing the inverse proportionality between \bar{F}_c and $\bar{N}_{c,p}$ (see Figure 6.4.17). The influence of φ on \bar{F}_c is typically observed at the beginning of the shearing phase where a peak value is detected for both variables (see Figure 6.4.12 & Figure 6.4.16). Similarly to the uniaxial compression data, the small variation of f_s in shearing simulations doesn't allow the observation of its direct correlation with \bar{F}_c , alongside the presence of multiple degrees of freedom.

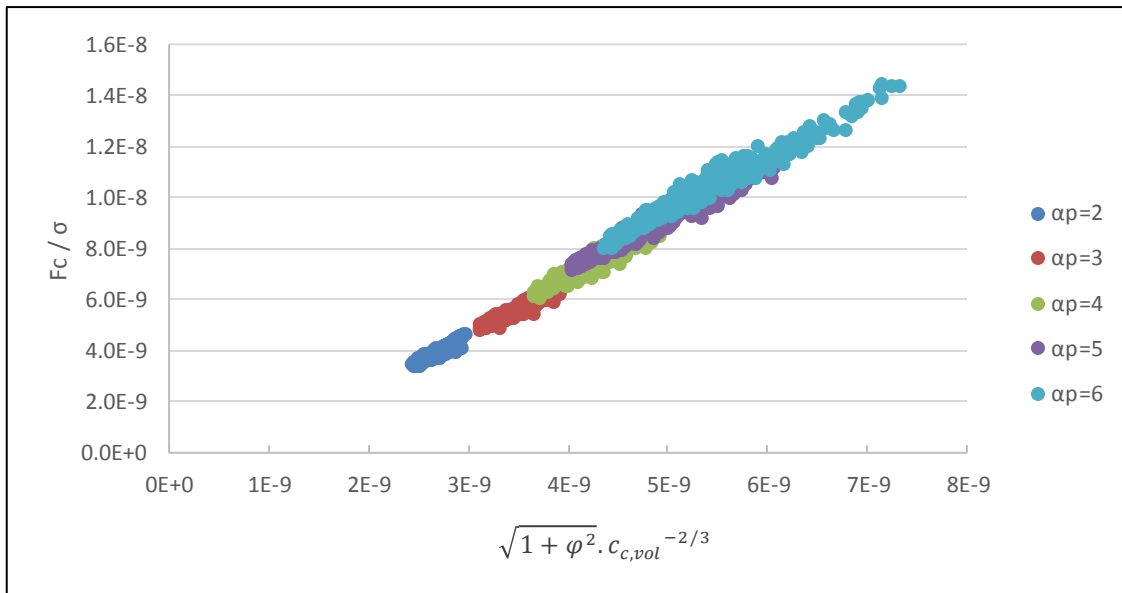


Figure 7.2.4: Linear correlation between \bar{F}_c/σ and $\sqrt{1 + \varphi^2} \cdot c_{c,vol}^{-2/3}$ in the shearing phase for the different aspect ratios α_p as described in Equation 7.2.8.

Using the values collected from the performed shearing simulations, it can be observed that the linearity between \bar{F}_c/σ and $\sqrt{1 + \varphi^2} \cdot c_{c,vol}^{-2/3}$ is respected for all aspect ratios (see Figure 7.2.4). Similarly to the uniaxial compression data, the two terms are not equal (see Figure 7.2.2), especially for higher aspect ratios, and a calibration of the model will be further needed.

7.2.1.3 Model Fitting

A calibration of the model is needed for both uniaxial compression and shearing phase as the equality between \bar{F}_c/σ and $\sqrt{1 + \varphi^2} \cdot c_{c,vol}^{-2/3}$ is not exactly matched (see Figure 7.2.5).

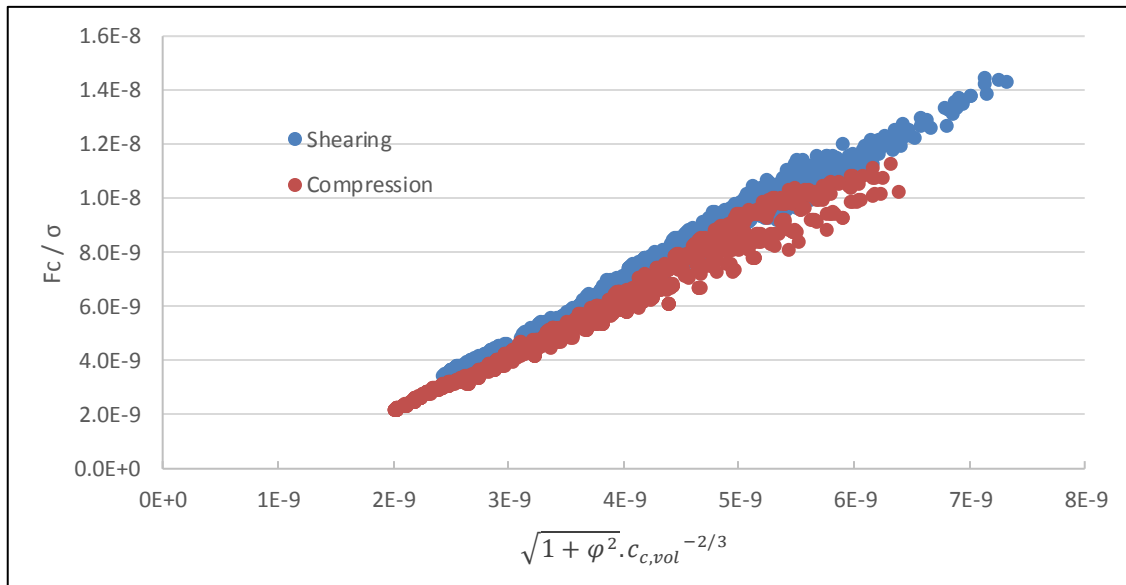


Figure 7.2.5: Linear correlation between \bar{F}_c/σ and $\sqrt{1 + \varphi^2} \cdot c_{c,vol}^{-2/3}$ for all simulation data in uniaxial compression and shearing phase as described in Equation 7.2.8.

The linearity is identical for both uniaxial compression and shearing phase, and the model for the prediction of \bar{F}_c for all simulation data is:

$$\bar{F}_c = \sigma \sqrt{1 + \varphi^2} \cdot (a \cdot c_{c,vol}^{-2/3} + b) \quad 7.2.10$$

With its final expression:

$$\bar{F}_c = \sigma \sqrt{1 + \varphi^2} \left(a \left(\frac{4\pi\alpha_p r_p^3}{N_{c,p} \cdot f_s} \right)^{2/3} + b \right) \quad 7.2.11$$

With parameters a dimensionless and b in m^2 .

This model is fitted on all simulation data and the fitting parameters are given in Table 7.2.1.

Table 7.2.1: Fitting parameters of Equation 7.2.11 on all simulation data.

Parameters	Values	Dimension
a	2.32	\emptyset
b	-2.47E-09	m^2
R^2	0.97	\emptyset

This model has a good accuracy on all stress environments with an overall mean error of 7.41% (see Table 7.2.2). The precision of the model is consistent for all aspect ratios except for $\alpha_p = 2$ where it is more accurate in the uniaxial compression and less accurate in the shearing phase. The higher number of data points in shearing phase (2510) compared to uniaxial compression (1174) (see Chapter 6.3.3) explains that the mean error for all data (last column of Table 7.2.2) is closer to value found for the shearing phase than for uniaxial compression.

Table 7.2.2: Mean error for prediction of \bar{F}_c using Equation 7.2.11 and parameters in Table 7.2.1 for different aspect ratios and stress environments.

Aspect ratio	Compression	Shearing	All
2	2.80%	12.8%	10.1%
3	8.97%	6.12%	6.90%

4	9.17%	6.00%	6.87%
5	7.34%	6.46%	6.73%
6	6.18%	7.09%	6.70%
All	6.79%	7.69%	7.41%

7.2.1.4 Discussion

A mathematical model is built from physical theory and accurately predicts the mean contact force \bar{F}_c from the stress environment in the bed (i.e. normal and shear stress), the particle physical properties, the mean number of contacts on particle and the solid fraction in the bed (see Equation 7.2.11 and Table 7.2.1).

The necessary calibration of this model is due to the first-approximation approach and assumptions. Indeed, the possible anisotropy of contact distribution in the bed, promoted by the particle elongation and alignment, could bias the estimation of the surface concentration of contacts on cross-section (A) (see Figure 7.2.3). Moreover, the distribution of forces on contacts is not homogeneous [205, 285, 288] and the weight of stress components on the contact force might depend on the orientation of the tangential plane to the particle's surface at contact location. The calculation of particle volume based on the assumption of cylindrical shape could also have introduced another error to the prediction.

7.2.2 Particles Bending Stress

According to Simple Beam Bending theory [59] (see Chapter 5.4.1.1), the theoretical bending stress $\sigma_{p,ZZ}$ of particle p – assumed being cylindrically shaped – is calculated as follows:

$$\sigma_{p,ZZ} = \frac{4 \cdot M_p}{\pi r_p^3} \quad 7.2.12$$

With M_p the maximum bending moment on the particle p and r_p the radius of an element sphere (i.e. half the particle width).

The bending moment describes the reaction of an particle to an external force and typically scales with the distance from the position of force application (see Equation 5.4.1). In a particle bed, the mean contact force \bar{F}_c and the mean distance $\bar{\Delta L}$ between two sequenced contacts on a particle length can be used to estimate the mean bending moment \bar{M}_p and mean particle bending stress $\bar{\sigma}_{p,ZZ}$ such as:

$$\bar{M}_p = \bar{F}_c \cdot \bar{\Delta L} \quad 7.2.13$$

$$\bar{\sigma}_{p,ZZ} = \frac{4 \cdot \bar{F}_c \cdot \bar{\Delta L}}{\pi r_p^3} \quad 7.2.14$$

If there is $\bar{N}_{c,p}$ mean number of contacts on particle in the bed, $\bar{\Delta L}$ can be estimated as in Equation 6.4.2 with L_p the particle length:

$$L_p = 2\alpha_p r_p \quad 7.2.15$$

Resulting in:

$$\bar{\sigma}_{p,ZZ} = \frac{8 \cdot \alpha_p \cdot \bar{F}_c}{\pi r_p^2 (\bar{N}_{c,p} + 1)} \quad 7.2.16$$

Thus, using the calibrated model for the estimation of \bar{F}_c (see Equation 7.2.11), the mean particle bending stress $\bar{\sigma}_{p,ZZ}$ can be expressed as:

$$\bar{\sigma}_{p,ZZ} = \frac{8 \cdot \alpha_p \cdot \sigma \sqrt{1 + \varphi^2} \cdot \left(a \left(\frac{4\pi\alpha_p r_p^3}{\bar{N}_{c,p} \cdot f_s} \right)^{2/3} + b \right)}{\pi r_p^2 (\bar{N}_{c,p} + 1)} \quad 7.2.17$$

With parameters a and b given in Table 7.2.1.

7.2.2.1 In Uniaxial Compression

The theoretical value of the mean particles bending stress $\bar{\sigma}_{p,ZZ_{th}}$ is lower than the actual recorded value in simulations $\bar{\sigma}_{p,ZZ_{sim}}$ in uniaxial compression (see Figure 7.2.6). Here, the particles bending stress is under-estimated, and this phenomenon increases with the mean number of contacts on particle $\bar{N}_{c,p}$.

Indeed, it has been observed that the stability of a particle plays an important role in its force system (see Chapter 6.5.4) which is strongly related to the particle internal stress (see Chapter 6.5.6.2.1). The particle stability increases with its number of contacts [270, 271] and this phenomenon hasn't been yet considered in the built ideal model for the prediction of the particles bending stress.

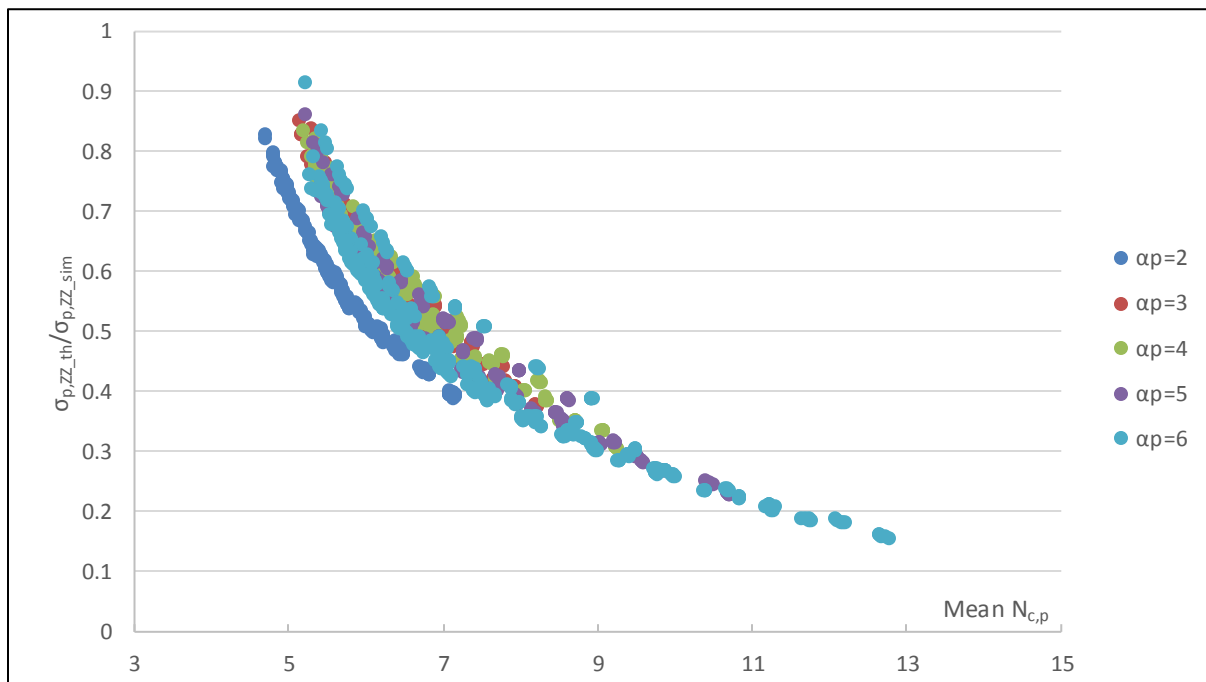


Figure 7.2.6: Ratio between the theoretical and the recorded mean particles bending stress $\bar{\sigma}_{p,ZZ_{th}}/\bar{\sigma}_{p,ZZ_{sim}}$ in uniaxial compression simulations, given by the mean number of contacts on particle $\bar{N}_{c,p}$ for the different aspect ratios α_p .

Also, there is a noticeable offset with the aspect ratio $\alpha_p = 2$ which is probably due to the distinct error in the prediction of the mean contact force for this particle elongation (see Table 7.2.2).

7.2.2.2 In Shearing Phase

Similarly to the uniaxial compression case, the theoretical mean particle bending stress $\bar{\sigma}_{p,ZZ_{th}}$ is under-estimated compared to the recorded $\bar{\sigma}_{p,ZZ_{sim}}$ from simulations, and this phenomenon increases with the mean number of contacts on particle $\bar{N}_{c,p}$ (see Figure 7.2.7).

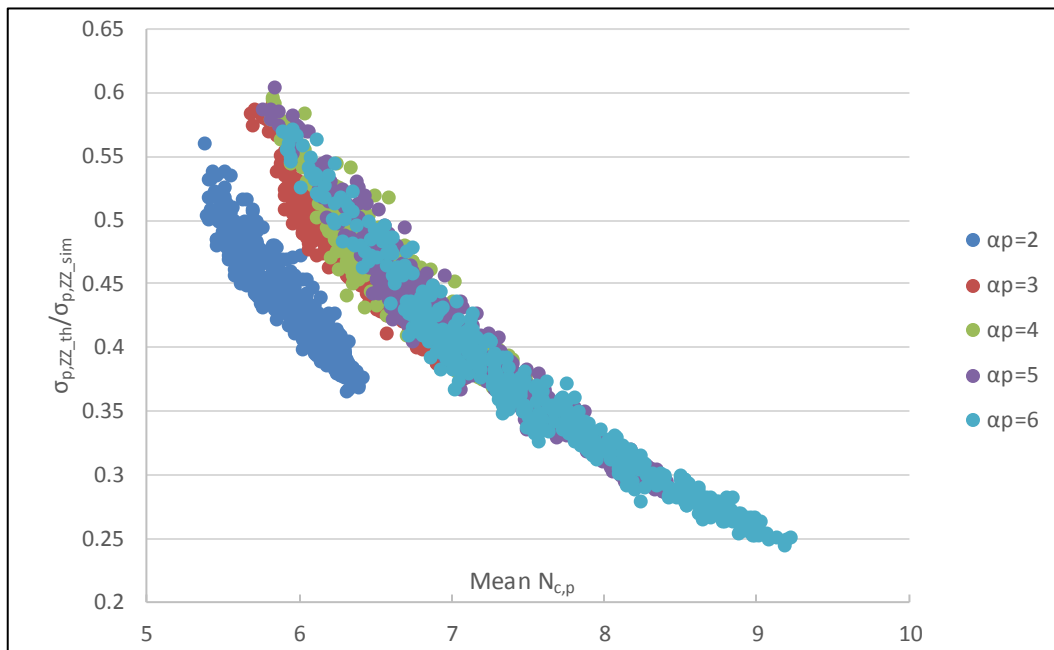


Figure 7.2.7: Ratio between the theoretical and the recorded mean particles bending stress $\bar{\sigma}_{p,ZZ_{th}}/\bar{\sigma}_{p,ZZ_{sim}}$ in shearing phase simulations, given by the mean number of contacts on particle $\bar{N}_{c,p}$ for the different aspect ratios α_p .

The slight offset observed for aspect ratio $\alpha_p = 2$ in uniaxial compression (see Figure 7.2.6) is also present for the shearing phase data.

7.2.2.3 Model Fitting

A modification of the model predicting the particle bending stress (see Equation 7.2.17) is needed to consider the phenomenon of particle stability related to the mean number of contacts on particle $\bar{N}_{c,p}$.

Chapter 7: Prediction of Particles Internal Stress for Agitated Drying Conditions

The ratio between the theoretical and recorded mean particles bending stress is inversely proportional to $\bar{N}_{c,p}$, such as:

$$\bar{\sigma}_{p,ZZ_{sim}} = \bar{\sigma}_{p,ZZ_{th}} \cdot f(\bar{N}_{c,p}) \quad 7.2.18$$

$$f(\bar{N}_{c,p}) = c \cdot \bar{N}_{c,p}^d \quad 7.2.19$$

Where a power law is assumed, with c and d dimensionless.

So, the final model for the prediction of the mean particles bending stress $\bar{\sigma}_{p,ZZ}$ is:

$$\bar{\sigma}_{p,ZZ} = \frac{8 \cdot \alpha_p \cdot \sigma \cdot \sqrt{1 + \varphi^2} \cdot \left(a \left(\frac{4\pi\alpha_p r_p^3}{\bar{N}_{c,p} \cdot f_s} \right)^{2/3} + b \right)}{\pi r_p^2 (\bar{N}_{c,p} + 1)} \cdot c \cdot \bar{N}_{c,p}^d \quad 7.2.20$$

This model is fitted on all simulation data and the fitting parameters are given in Table 7.2.3. An inter-dependency of parameter c with parameters a and b would be found if the model was fine-tuned, however the three parameters are conserved to maintain the distinction between the prediction of the mean contact force and the particle stability factor.

Table 7.2.3: Fitting parameters of Equation 7.2.19 on all simulation data.

Parameters	Values	Dimension
c	0.145	\emptyset
d	1.44	\emptyset
R^2	0.81	\emptyset

This model has a good accuracy with an overall mean error of 9.62% (see Table 7.2.4). The precision of the model differs for the different aspect ratios in uniaxial compression but correctly fits the simulation data in shearing phase with a mean error at 6.98%. The case of aspect ratio $\alpha_p = 2$ is still unique with an excellent precision in uniaxial

compression and increased error in shearing phase, recalling the error reported in the prediction of the mean contact force \bar{F}_c (see Table 7.2.2) for this aspect ratio.

Table 7.2.4: Mean error for prediction of $\bar{\sigma}_{p,ZZ}$ using Equation 7.2.19 and parameters in Table 7.2.3 for different aspect ratios and stress environments.

Aspect ratio	Compression	Shearing	All
2	3.26%	16.7%	13.0%
3	22.0%	3.57%	8.60%
4	22.5%	3.36%	8.60%
5	16.7%	4.91%	8.64%
6	13.3%	6.33%	9.33%
All	15.3%	6.98%	9.62%

7.2.2.4 Discussion

A mathematical model is built and accurately predicts the mean particles bending stress $\bar{\sigma}_{p,ZZ}$ from the predicted mean contact force \bar{F}_c (see Equation 7.2.11), the particle physical properties and the mean number of contacts on particle (see Equation 7.2.20 and Table 7.2.3). The rearranged Equation 7.2.20 shows that the bending stress depends on the solid fraction and number of contacts within the bed, which is confirmed by the reported impact of different packing on the particle breakage [281], therefore on the internal stress they experience.

The modification and calibration of this model is necessary to take into account the phenomenon of stabilisation of the particles with increasing number of contacts. The singularity of the case of aspect ratio $\alpha_p = 2$ in the prediction of $\bar{\sigma}_{p,ZZ}$ is attributed to the specific error in the prediction of \bar{F}_c for this aspect ratio.

7.2.3 Bending Stress Ratio

As demonstrated in Chapter 6.4.6.1 and Chapter 6.5.6.1 the predominant type of stress experienced by particles in the performed simulations is the tensile stress, here associated with the particles bending stress. This predominance, represented by the bending stress ratio $\alpha_{\sigma,ZZ}$ (see Equation 6.4.3), correlates strongly with the particles aspect ratio α_p (see Figure 6.4.24) in the following fashion:

$$\alpha_{\sigma,ZZ} = 1 - e \cdot \alpha_p^f \quad 7.2.21$$

With e and f dimensionless.

The impact of the normal stress is considered marginal and isn't included in the model for the prediction of $\alpha_{\sigma,ZZ}$.

This model is fitted on all simulation data for the prediction of the mean bending stress ratio $\bar{\alpha}_{\sigma,ZZ}$ and the fitting parameters are given in Table 7.2.5.

Table 7.2.5: Fitting parameters of Equation 7.2.21 on all simulation data.

Parameters	Values	Dimension
e	0.373	\emptyset
f	-1.32	\emptyset
R^2	0.96	\emptyset

This model has an excellent accuracy with an overall mean error of 0.68% (see Table 7.2.6). The precision of the model is consistent for all aspect ratios and stress environments, allowing a confident prediction of the mean bending stress ratio $\bar{\alpha}_{\sigma,ZZ}$ as a function of α_p .

Table 7.2.6: Mean error for prediction of mean bending stress ratio $\bar{\alpha}_{\sigma,ZZ}$ using Equation 7.2.21 and parameters in Table 7.2.5 for different aspect ratios and stress environments.

Aspect ratio	Compression	Shearing	All
2	0.99%	0.77%	0.83%
3	0.99%	0.71%	0.79%
4	0.96%	0.47%	0.61%
5	0.80%	0.51%	0.60%
6	0.73%	0.50%	0.60%
All	0.86%	0.59%	0.68%

7.2.4 Particles Internal Stress

A model is created and predicts the mean bending stress ratio $\bar{\alpha}_{\sigma,ZZ}$ as a function of the particles aspect ratio α_p (see Equation 7.2.21) with an excellent accuracy. Therefore, the mean particles internal stress $\bar{\sigma}_p$ can be calculated from the predicted mean particles bending stress $\bar{\sigma}_{p,ZZ}$ (see Equation 7.2.20) as follows:

$$\bar{\sigma}_p = \frac{\bar{\sigma}_{p,ZZ}}{\bar{\alpha}_{\sigma,ZZ}} \quad 7.2.22$$

$$\bar{\sigma}_p = \frac{8 \cdot \alpha_p \cdot \bar{F}_c}{\pi r_p^2 (\bar{N}_{c,p} + 1)} \cdot \frac{f(\bar{N}_{c,p})}{\bar{\alpha}_{\sigma,ZZ}} \quad 7.2.23$$

With \bar{F}_c the predicted mean contact force (see Equation 7.2.11) and $f(\bar{N}_{c,p})$ the built function associated with particle stability (see Equation 7.2.21).

Thus, the final expression of the created model for the prediction of $\bar{\sigma}_p$ is:

$$\bar{\sigma}_p = \frac{8 \cdot \alpha_p \cdot \sigma \sqrt{1 + \varphi^2} \cdot \left(a \left(\frac{4\pi\alpha_p r_p^3}{\bar{N}_{c,p} \cdot f_s} \right)^{2/3} + b \right)}{\pi r_p^2 (\bar{N}_{c,p} + 1)} \cdot \frac{c \cdot \bar{N}_{c,p}^d}{1 - e \cdot \alpha_p^f} \quad 7.2.24$$

With parameters a and b given in Table 7.2.1, c and d in Table 7.2.3, and e and f in Table 7.2.5.

The accuracy of this model is quasi-identical to the one for the prediction of $\bar{\sigma}_p(Z, Z)$ (see Table 7.2.4) as the model for the prediction of $\bar{\alpha}_{\sigma,ZZ}$ is quasi-perfect (see Table 7.2.6). The overall mean error of the predictive model for $\bar{\sigma}_p$ is 9.42%, with a better accuracy for the shearing phase at 6.73% (see Table 7.2.7).

Table 7.2.7: Mean error for prediction of mean particles internal stress $\bar{\sigma}_p$ using Equation 7.2.24 for different aspect ratios and stress environments.

Aspect ratio	Compression	Shearing	All
2	3.73%	16.74%	13.21%
3	21.23%	3.36%	8.22%
4	22.17%	3.04%	8.26%
5	16.75%	4.50%	8.38%
6	13.38%	5.96%	9.15%
All	15.17%	6.73%	9.42%

7.2.5 Conclusion

A model is built from physical theory to predict the mean particles internal stress in a particle bed from the particles physical properties, the stress environment, the number of contacts and the bed solid fraction. The model is calibrated to fit the simulation data with the introduction of six fitting parameters (which can be reduced to five by

integrating parameter c into a and b), giving the model an overall error of 9.42% when predicting simulation data.

The model assumes that the bending stress is predominant in the particles internal stress, with the introduction of a function giving the bending stress ratio from the particles aspect ratio. Indeed, the bending stress ratio scales with particle elongation and this function is introduced in the model to account for this dependency.

The analysis of simulation highlighted a phenomenon of particle stability increasing with the number of contacts it experiences. The more stable a particle, the higher its internal stress, and a function proportional to the mean number of contacts on particle is introduced in the model to reflect this key aspect.

The mean bending stress is estimated using the Simple Beam Bending theory. This method calculates the bending stress of a particle in a static (or quasi-static) case from the contact forces and the distance between each contact on the particle neutral axis. The use of this theory assumes the optimal direction of forces to induce the maximum possible bending moment. This force direction factor isn't introduced in the model but could be investigated as a probability factor in a future work.

Finally, the mean contact force is estimated using a first approximation approach. The isotropic spatial distribution of contact points in the bed is assumed and the cross-sectional concentration of contacts is assessed to determine the number of points supporting the normal and tangential load applied on the bed.

The case of aspect ratio $\alpha_p = 2$ is unique and produces different accuracy of the model compared to the other particle elongations. An error propagation is noticed in the successive steps of model building, and the uniqueness of $\alpha_p = 2$ is observed from the very estimation of the mean contact force. This initial error could be due to the low values used to fit the model for this particle elongation. Indeed, the use of the residual sum of squares as fitting method could have slightly lowered the importance of data fitting for this particle elongation. Also, the cylindrical shape of particles is assumed in the prediction of the mean contact force, which would produce a larger particle volume error for shorter particles considering their actual clumped sphere shape.

In conclusion, and despite of the constraint of building a model from physical theory and the number of pre-requisite assumptions (e.g. isotropic contact distribution), the model predicts the mean particles internal stress with an acceptable physical error i.e. $< 10\%$.

7.3 Prediction of Weibull Scale Parameter

The Weibull parameter λ gives the scale factor of the particle internal stress distribution (see Chapter 6.2.1). Being able to predict λ in a particle bed allows experimental designers to estimate the quantity of stress particles experience for different process conditions.

Three models are created to estimate λ for different level of details: the first one is created from physical theory, the second is empirically built based on simulation data and the third one is empirically built from bulk parameters.

7.3.1 From Predictive Theoretical Model of Mean Particles Internal Stress

The Weibull scale parameter λ is typically related to the mean particle internal stress $\bar{\sigma}_p$. The two variables are linearly correlated with a Pearson correlation coefficient at 0.999 in simulations. The assumption of equality is here made:

$$\lambda = \bar{\sigma}_p \quad 7.3.1$$

This equality can then be used to estimate λ based on the theoretical model built for the prediction $\bar{\sigma}_p$ (see Equation 7.2.24). This method allows the prediction of λ with an overall error of 10.8% in the simulation data (see Table 7.3.1). The error is similar to the one for the prediction of $\bar{\sigma}_p$ (see Table 7.2.7) with a better accuracy for the case of shearing phase and a different precision in the case of particle aspect ratio $\alpha_p = 2$.

Table 7.3.1: Mean error between Weibull scale parameter λ and predicted mean particles internal stress $\bar{\sigma}_p$ for different aspect ratios and stress environments.

Aspect ratio	Compression	Shearing	All
2	7.08%	23.39%	18.96%
3	13.79%	6.73%	8.65%
4	18.88%	3.18%	7.47%
5	14.56%	5.70%	8.51%
6	13.70%	8.22%	10.58%
All	13.65%	9.47%	10.80%

7.3.2 Empirical Model from Simulation Data

7.3.2.1 Linear Correlation with Sum of Forces on Particle

It is observed in the analysis of simulation data (see Chapter 6.5.6.2.1) that the Weibull scale parameter λ is strongly correlated to the mean sum of absolute forces on particle \bar{s} (see Equation 6.5.1). This phenomenon is due to the stabilisation of particles with increasing number of contacts (see Chapter 6.5.4). The correlation between λ and \bar{s} is quasi-linear with a Pearson correlation coefficient of 0.98 in uniaxial compression and 0.96 in shearing phase:

$$\lambda = a \cdot \bar{s} \quad 7.3.2$$

The parameter a (in m^{-2}) is calculated for all simulation data and the mean value \bar{a} is obtained for each aspect ratio and stress environment (see Table 7.3.2). Here, \bar{a} scales with the particle aspect ratio and is slightly higher in the shearing phase.

Table 7.3.2: Mean \bar{a} (in m^{-2}) as given in Equation 7.3.2 for the different aspect ratios and stress environments.

Aspect ratio	Compression	Shearing
2	4.89E+08	5.05E+08
3	5.75E+08	6.02E+08
4	6.98E+08	7.17E+08
5	8.56E+08	8.78E+08
6	9.93E+08	1.03E+09

7.3.2.2 Linear Correlation with Particle Aspect Ratio

A linear correlation is found between the parameter a and the particles aspect ratio α_p with a Pearson correlation coefficient of 0.97 for compression and 0.98 for shearing case (see Figure 7.3.1).

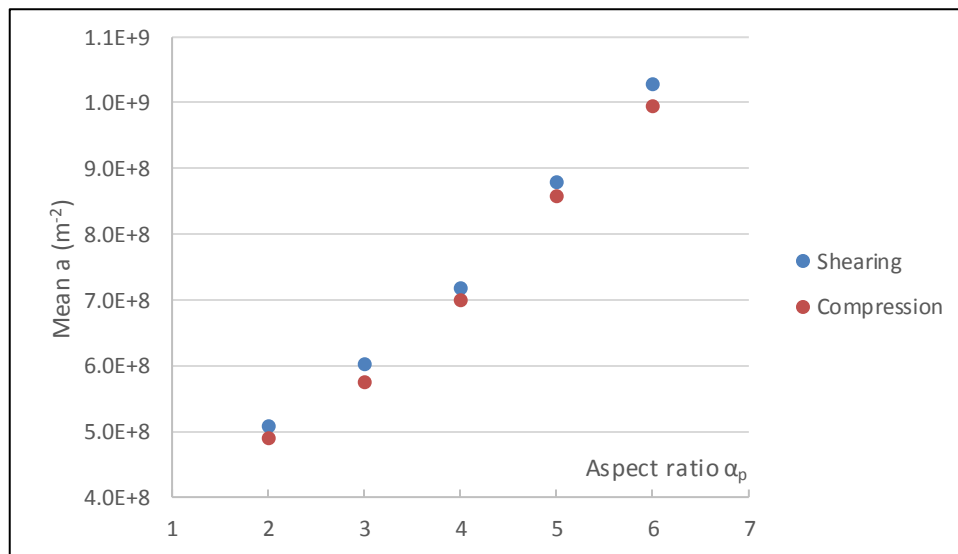


Figure 7.3.1: Mean \bar{a} (in m^{-2}) for the different aspect ratios α_p and stress environments (data in Table 7.3.2).

Indeed, shorter particles experience less internal stress than longer ones and need a greater load to be broken [55, 191]: the higher the aspect ratio of a particle, the more rapidly it breaks [53-55].

The Weibull scale parameter λ can then be obtained based on Equation 7.3.2 from the particles aspect ratio α_p and the mean sum of absolute forces on particle \bar{s} with the following equation:

$$\lambda = \bar{s}(b \cdot \alpha_p + c) \quad 7.3.3$$

With parameters b and c in m^{-2} .

b and c are obtained using the regression method of residual sum of squares on all simulation data (see Table 7.3.3), and the created linear model fits the data with a high coefficient of determination.

Table 7.3.3: Parameters of linear regression between a and aspect ratio α_p such as

$$a = b \cdot \alpha_p + c.$$

Parameters	Unit	Value
b	m^{-2}	1.31E+08
c	m^{-2}	2.17E+08
R^2	\emptyset	0.9586

The created model accurately predicts λ with an overall mean error of 4.10%, below the symbolic statistical threshold of 5%. The error is slightly reduced for shearing phase (3.36%) compared to uniaxial compression (5.66%) (see Table 7.3.4).

Table 7.3.4: Mean error of predicted λ using Equation 7.3.3 for the different aspect ratios stress environments.

Aspect ratio	Compression	Shearing	All

2	4.29%	5.19%	4.95%
3	6.58%	2.56%	3.65%
4	7.03%	3.83%	4.70%
5	6.17%	1.94%	3.28%
6	4.90%	3.29%	3.98%
All	5.66%	3.36%	4.10%

7.3.2.3 Discussion

An empirical model is built and accurately predicts the Weibull scale parameter λ from the mean sum of absolute forces on particle \bar{s} and the particles aspect ratio α_p . The creation of a model based on physical theory demonstrated that the particles internal stress is related to 3 main factors: the particles bending stress, the relative predominance of bending stress in particles internal stress and the stability of the particles.

The Simple Beam Bending theory [59] shows that the bending moment can be obtained from the contact force and the inter-contact distance on particle, whilst the bending stress ratio is related to particle elongation, and the particles stability is linked to the particles force system.

In the built empirical model, the presence of \bar{s} and α_p accounts for both contact force, number of contacts and particle elongation, which are the key elements used for the quantification of the 3 main factors detailed above. This explains the excellent accuracy of the model when fitted on simulation data.

Nevertheless, this empirical model needs a size factor to be applicable to other particle size and shape. Indeed, the sensitivity of particles to mechanical stress scales with their size [16]. This size factor for the shape and size of particles in simulations is

already present in parameters b and c . Referring to the Simple Beam bending theory, this size factor is expected to be related to the second moment of inertia of the particle and the distance from the force application (particle surface) to the particle neutral axis.

Finally, considering $\bar{s} = \bar{N}_{c,p} \cdot \bar{F}_c$, it is possible to estimate \bar{s} using the created theoretical model for the prediction of \bar{F}_c (see Equation 7.2.11) and the empirical model predicting $\bar{N}_{c,p}$ (see Equation 7.5.6) from bulk parameters.

7.3.3 Empirical Model from Bulk Parameters

7.3.3.1 Linear Correlation with Stress Environment

The theoretical model created for the prediction of Weibull scape parameter λ (see Chapter 7.2) shows that the particles internal stress scales with the stress environment in a linear fashion. Indeed, the normal stress is reported as the predominant factor impacting particle breakage [156], explaining why the breakage of particles is more important in industrial scale than laboratory scale drying [16, 165]. Moreover, the stress ratio is the main dimensionless number for the characterisation of the mechanical behaviour of a particle bed [13, 21] and accounts for the shear stress present in the bed (see Equation 2.4.6). Therefore, the stress environment is described with the normal stress σ and the stress ratio φ in the same fashion as in Chapter 7.2.1.2, and λ can then be expressed as follows:

$$\lambda = a \cdot \sigma \sqrt{1 + \varphi^2} \quad 7.3.4$$

With a dimensionless.

The parameter a is calculated for all simulation data and the mean value \bar{a} is obtained for each aspect ratio and stress environment (see Table 7.3.5). Here, \bar{a} scales with the particle aspect ratio and is higher in the shearing phase.

Table 7.3.5: Mean \bar{a} as given in Equation 7.3.4 for the different aspect ratios and stress environments.

Aspect ratio	Compression	Shearing
2	8.12	10.37
3	15.09	18.84
4	25.51	30.95
5	41.01	48.79
6	58.81	70.32

7.3.3.2 Power correlation with Particle Aspect Ratio

A power correlation is found between the parameter a and the particles aspect ratio α_p in both uniaxial compression and shearing phase (see Figure 7.3.2). Indeed, the sensitivity of a particle to mechanical stress scales with its elongation [8, 9].

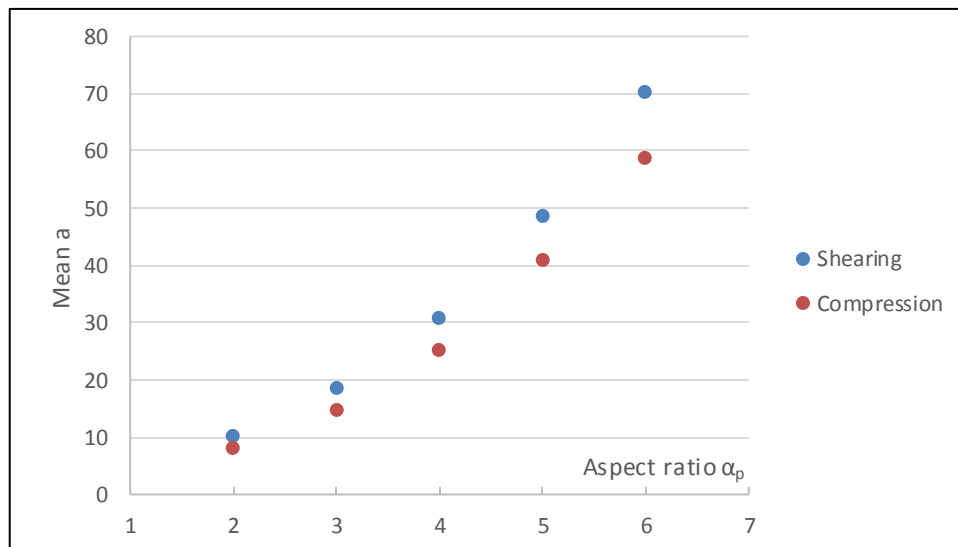


Figure 7.3.2: Mean \bar{a} for the different aspect ratios α_p and stress environments (data in Table 7.3.5).

The Weibull scale parameter λ can then be obtained based on Equation 7.3.4 from the particles aspect ratio α_p , the normal stress σ and the stress ratio φ with the following equation:

$$\lambda = b \cdot \alpha_p^c \cdot \sigma \sqrt{1 + \varphi^2} \quad 7.3.5$$

With parameters b and c dimensionless.

Parameters b and c are obtained using the regression method of residual sum of squares on all simulation data (see Table 7.3.6), and the created power model fits the data with a high coefficient of determination.

Table 7.3.6: Parameters of power regression between a and aspect ratio α_p such as

$$a = b \cdot \alpha_p^c.$$

Parameters	Unit	Value
b	\emptyset	2.28
c	\emptyset	1.87
R^2	\emptyset	0.96

The created model predicts λ with an overall mean error of 9.96% (see Table 7.3.7), with a better accuracy for shearing phase (8.23%) compared to uniaxial compression (13.66%). The precision of the model is different for particle aspect ratio $\alpha_p = 2$, a uniqueness that is also observed in the creation the theoretical model (see Chapter 7.2).

Table 7.3.7: Mean error of predicted λ using Equation 7.3.5 for the different aspect ratios stress environments.

Aspect ratio	Compression	Shearing	All

2	5.28%	19.34%	15.52%
3	18.96%	5.99%	9.52%
4	20.37%	2.84%	7.63%
5	13.60%	5.24%	7.89%
6	11.89%	7.65%	9.47%
All	13.66%	8.23%	9.96%

7.3.3.3 Discussion

An empirical model is built and predicts the Weibull scale parameter λ with an overall error below the symbolic physical margin of error of 10%. This model is based on the particles physical properties and the bulk process conditions, and therefore doesn't require simulation data.

This model has a different accuracy for the particle aspect ratio $\alpha_p = 2$, a peculiarity that has been highlighted is the creation of the theoretical model (see Chapter 7.2). Also, the parameter a (see Equation 7.3.4) has different values for shearing phase and uniaxial compression, despite of the integration of the stress ratio. It might show that the impact of the shearing aspect on the particles internal stress is not entirely represented by the presence of the stress ratio, and that there might be other phenomena to consider. The empirical model based on the forces on particle (see Chapter 7.3.2) gives equivalent results on both shearing phase and uniaxial compression, showing that the inequality of parameter a resides in the link between bulk stress components and the contact forces.

7.4 Prediction of Weibull Shape Parameter

The Weibull shape parameter k gives the shape factor of the particle internal stress distribution (see Chapter 6.2.1). The prediction of k in a particle bed allows experimental designers to estimate the uniformity of the stress experienced by particles for different process conditions: the higher the k , the narrower the distribution.

Two models are created to estimate the shape parameter k : the first one is empirically built based on simulation data and the second one is empirically created from bulk parameters.

7.4.1 Empirical Model from Simulation Data

7.4.1.1 Power Correlation with Standard Deviation of Sum of Forces on Particle

As the Weibull scale parameter λ is strongly correlated to the mean sum of absolute forces on particle \bar{s} (see Chapter 7.3.2.1), it is not surprising to observe by analogy that the Weibull shape parameter k is related to the normalised standard deviation (i.e. standard deviation divided by mean value) of s , $\sigma_{norm}(s)$, with a Spearman correlation coefficient of -0.9 (see Figure 6.4.32 & Figure 6.5.19).

A power-based correlation is found between the two variables such as:

$$k = a \cdot \sigma_{norm}(s)^b \quad 7.4.1$$

With a and b dimensionless.

The parameters a and b are obtained using the regression method of the residual sum of squares on all simulation data (see Table 7.4.1).

Table 7.4.1: Fitting parameters of Equation 7.4.1 on all simulation data.

Parameters	Units	Value
a	\emptyset	0.903

b	\emptyset	-1.07
R^2	\emptyset	0.840

This created simple power model predicts accurately k with an overall mean error of 5.07% (see Table 7.4.2). The model is slightly more precise for shearing phase and its accuracy is consistent for the different aspect ratios.

Table 7.4.2: Mean error of predicted k using Equation 7.4.1 and parameters values reported in Table 7.4.1.

Aspect ratio	Compression	Shearing	All
2	10.01%	3.66%	5.38%
3	5.22%	3.83%	4.21%
4	5.68%	4.83%	5.07%
5	8.29%	3.94%	5.32%
6	6.46%	4.39%	5.28%
All	7.07%	4.13%	5.07%

7.4.1.2 Linear Correlation between Power Parameters

The parameters a and b (see Equation 7.4.1) are obtained for each aspect ratio and stress environment using the regression method of the residual sum of squares (see Table 7.4.3). The model has a better data fitting for uniaxial compression with a higher coefficient of determination.

Table 7.4.3: Parameters of power regression as described in Equation 7.4.1 for the different aspect ratios and stress environments.

Aspect ratio	a		b		R^2	
	Compression	Shearing	Compression	Shearing	Compression	Shearing
2	0.6267	0.8627	-1.876	-1.253	0.9438	0.7988
3	0.7073	0.9107	-1.584	-1.116	0.9859	0.7864
4	0.7689	0.9601	-1.408	-0.973	0.9597	0.7841
5	0.7429	0.9451	-1.387	-0.926	0.9466	0.8247
6	0.8614	0.9449	-1.089	-0.894	0.9135	0.8418

The two power parameters a and b appear linearly correlated in the same fashion for all aspect ratios and stress environments (see Figure 7.4.1).

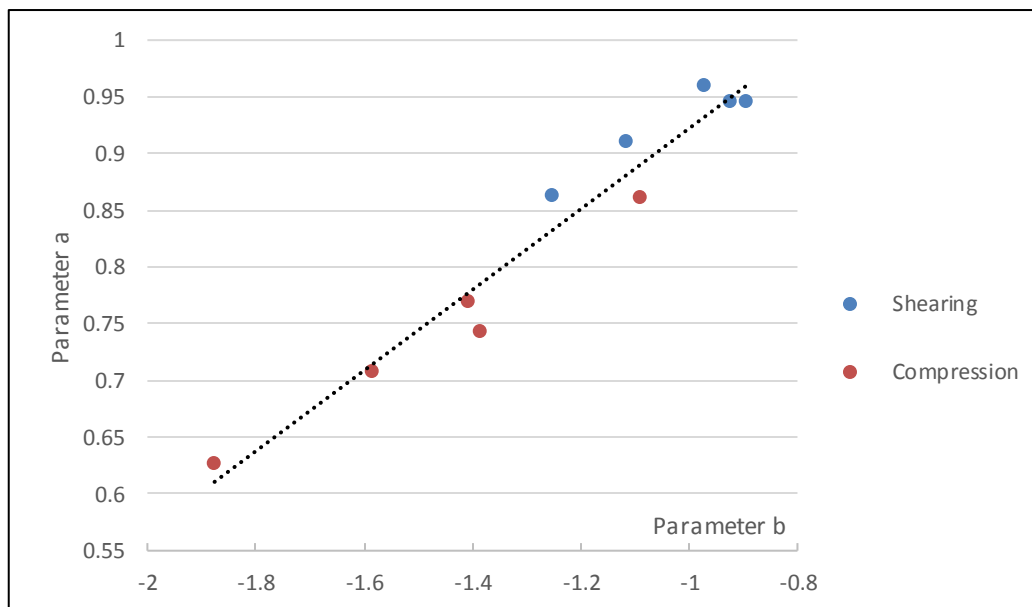


Figure 7.4.1: Parameter a plotted against parameter b (see Equation 7.4.1) for both compression and shearing cases (data in Table 7.4.3).

7.4.1.3 Correlation with Particle Aspect ratio

The power parameter b (see Equation 7.4.1) appears to scale linearly with the particles aspect ratio α_p in both uniaxial compression and shearing phase (see Figure 7.4.2).

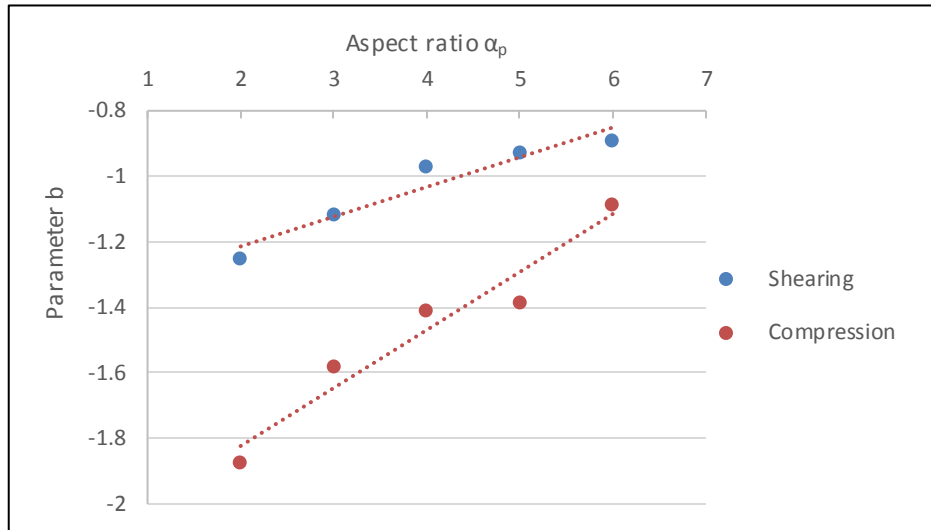


Figure 7.4.2: Parameter b (see Equation 7.4.1) for the different aspect ratios α_p and stress environments.

Thus, k is expressed as a function of $\sigma_{norm}(s)$ and α_p :

$$k = (c \cdot \alpha_p + d) \cdot \sigma_{norm}(s)^{e \cdot \alpha_p + f} \quad 7.4.2$$

With c , d , e and f dimensionless.

The four parameters are obtained by using the regression method of residual sum of squares for all simulation data (see Table 7.4.4).

Table 7.4.4: Fitting parameters of Equation 7.4.2 on all simulation data.

Parameters	Units	Value
c	\emptyset	0.02014
d	\emptyset	0.81174

e	\emptyset	0.08772
f	\emptyset	-1.4506
R^2	\emptyset	0.85494

The accuracy of the created model is excellent with an overall mean error of 4.88% (see Table 7.4.5), below the statistical threshold of 5%. The model is slightly more accurate for the shearing phase and is consistent for the different aspect ratios.

Table 7.4.5: Mean error of predicted k using Equation 7.4.2 and parameters values reported in Table 7.4.4.

Aspect ratio	Compression	Shearing	All
2	9.25%	3.35%	4.95%
3	5.21%	3.77%	4.16%
4	5.42%	5.09%	5.18%
5	7.48%	3.91%	5.04%
6	6.31%	4.08%	5.04%
All	6.69%	4.04%	4.88%

7.4.1.4 Discussion

A model is created to predict the Weibull shape parameter k from the normalised standard deviation of the sum of absolute forces on particle $\sigma_{norm}(s)$ and the particles aspect ratio α_p with an excellent overall accuracy. This model doesn't require the

calculation of particles internal stress with Euler Equation of Motion but needs simulation data to obtain $\sigma_{norm}(s)$.

The integration of α_p into the model has a minor effect, as it is shown by the low value of parameters c and e . Nevertheless, it allowed the model to reach an overall mean error of 4.88% instead of 5.07% for the simple power model (see Equation 7.4.1).

7.4.2 Empirical Model from Bulk Parameters

The analysis of simulation data has shown that the Weibull shape parameter k scales with normal stress σ applied on the particle bed for both shearing phase (see Figure 6.4.33) and uniaxial compression (see Figure 6.5.20). A logarithmic relationship is here assumed between the two variables such as:

$$k = a(\ln \sigma)^b \quad 7.4.3$$

With a and b dimensionless.

The parameters a and b are obtained using the regression method of the residual sum of squares on all simulation data (see Table 7.4.6).

Table 7.4.6: Fitting parameters of Equation 7.4.3 on all simulation data.

Parameters	Units	Value
a	\emptyset	0.252
b	\emptyset	0.762
R^2	\emptyset	0.682

Despite a low R^2 value, this logarithmic model predicts accurately the shape parameter k with an overall mean error of 7.07% (see Table 7.4.7).

Table 7.4.7: Mean error of predicted k using Equation 7.4.3 and parameters values reported in Table 7.4.6.

Aspect ratio	Compression	Shearing	All
2	8.48%	4.22%	5.38%
3	13.13%	4.15%	6.60%
4	6.57%	5.33%	5.67%
5	6.24%	8.34%	7.68%
6	5.74%	12.15%	9.39%
All	7.60%	6.83%	7.07%

An attempt to obtain a correlation between the fitting parameters and the particles aspect ratio was unsuccessful. As demonstrated in the creation of the empirical model from simulation data (see Chapter 7.4.1), the aspect ratio has a minor impact on the prediction of k . The impact of the particle size is out of scope of this study, and future work could consist of performing simulations with different particle width (i.e. element sphere radius) and observe the variation of k .

7.5 Prediction of Maximum Stress Location on Particle

The internal stress is calculated on different location within a particle using the Euler Equation of Motion (see Chapter 5.4.1.2) and the maximum value is selected as the particle internal stress. Knowing the location of this maximum stress on the particle neutral axis is essential as it represents the location of particle breakage if the particle internal stress exceeds its breakage strength [191, 192, 194].

The distribution of this location on the particle neutral axis follows a Gaussian model (see Chapter 6.2.2) with the mean value at the centre of the particle [55, 191, 192,

194, 235] and a metric standard deviation σ_{dev} . In this section, two empirical models are created to predict σ_{dev} : the first one from the simulation data, and the second one from the bulk parameters.

7.5.1 Empirical Model from Simulation Data

7.5.1.1 Power Correlation with the Mean Number of Contacts

The analysis of simulation data highlighted an inverse proportionality between the standard deviation of Gaussian model for the distribution of maximum stress location, σ_{dev} , and the mean number of contacts on particle $\bar{N}_{c,p}$ for both shearing phase (see Chapter 6.4.6.3) and uniaxial compression (see Chapter 6.5.6.3). σ_{dev} is then expressed as a function of $\bar{N}_{c,p}$:

$$\sigma_{dev} = a \cdot \bar{N}_{c,p}^b \tag{7.5.1}$$

With a in m and b dimensionless.

The parameters a and b are obtained using the regression method of the residual sum of squares for the different particle aspect ratios and stress environments (see Table 7.5.1).

Table 7.5.1: Parameters of power regression as described in Equation 7.5.1 for the different aspect ratios and stress environments.

Aspect ratio	a (in m)		b		R^2	
	Compression	Shearing	Compression	Shearing	Compression	Shearing
2	3.73E-05	4.03E-05	-0.18654	-0.24506	0.2783	0.1349
3	6.88E-05	5.78E-05	-0.42215	-0.31834	0.8482	0.1949
4	8.10E-05	7.25E-05	-0.3903	-0.32166	0.7756	0.4183

5	8.95E-05	8.30E-05	-0.31697	-0.27067	0.7962	0.585
6	1.06E-04	9.70E-05	-0.32365	-0.27355	0.8065	0.6361

7.5.1.2 Linear Correlation with Particle Aspect Ratio

Parameter a (see Equation 7.5.1) is found to scale with the particles aspect ratio α_p (see Figure 7.5.1), which corroborates the observations made during the analysis of simulation data (see Chapters 6.4.6.3 and 6.5.6.3).

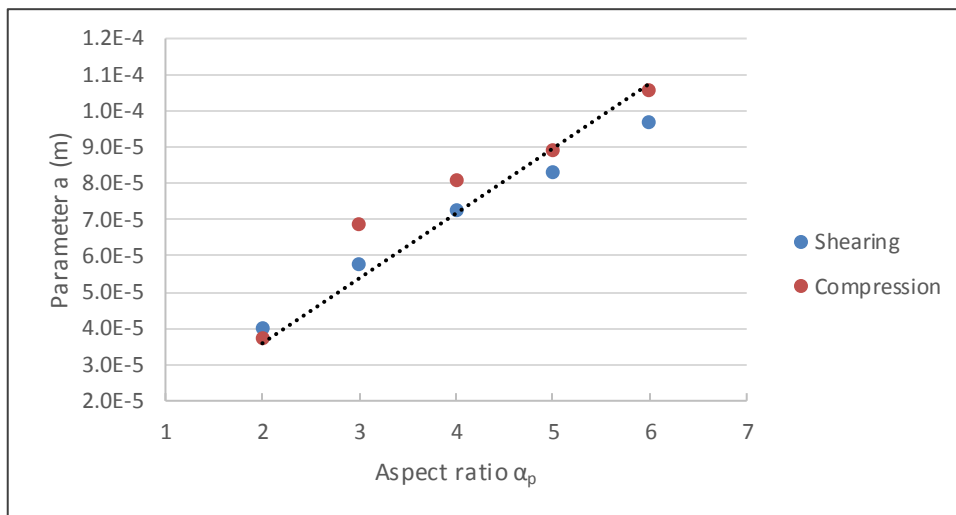


Figure 7.5.1: Parameter a (see Equation 7.5.1) for the different aspect ratios α_p and stress environments (data in Table 7.5.1). The dotted line represents the linear regression on the displayed data with an intercept at (0; 0).

Parameter a scales linearly with α_p with an intercept at (0; 0). σ_{dev} is then expressed as follows:

$$\sigma_{dev} = c \cdot \alpha_p \cdot \bar{N}_{c,p}^b \quad 7.5.2$$

With c in m and b dimensionless.

The parameters b and c are obtained using the regression method of the residual sum of squares on all simulation data (see Table 7.5.2).

Table 7.5.2: Fitting parameters of Equation 7.5.2 on all simulation data.

Parameters	Units	Value
c	m	2.42E-05
b	\emptyset	-0.466
R^2	\emptyset	0.937

7.5.1.3 Linear Correlation with Particle Size

σ_{dev} is in meter and therefore is expected to be correlated to the particle size in addition to the particle shape represented by the presence of the aspect ratio α_p in the model (see Equation 7.5.2). The value found for parameter c is quasi-equal to the particle half width i.e. an element sphere radius $r_p = 25\mu m$. The equation is modified to integrate this metric component:

$$\sigma_{dev} = r_p \cdot \alpha_p \cdot \bar{N}_{c,p}^b \quad 7.5.3$$

With b dimensionless.

The parameter b is obtained using the regression method of the residual sum of squares on all simulation data (see Table 7.5.3).

Table 7.5.3: Fitting parameters of Equation 7.5.3 on all simulation data.

Parameters	Units	Value
b	\emptyset	-0.482
R^2	\emptyset	0.937

This final power model predicts accurately σ_{dev} with an overall mean error of 6.30% (see Table 7.5.4). The error is consistent for the different particle elongation and stress environment except for particle aspect ratio $\alpha_p = 2$ which is particularly high at 18.6%. This odd value is probably due to the reduced bending stress ratio for this particle elongation (see Chapters 6.4.6.1 and 6.5.6.1) and can explain why the distribution of maximum stress location is more scattered on the particle neutral axis.

Table 7.5.4: Mean error of predicted σ_{dev} using Equation 7.5.3 and parameters values reported in Table 7.5.3.

Aspect ratio	Compression	Shearing	All
2	20.3%	18.0%	18.6%
3	2.65%	4.84%	4.24%
4	4.27%	2.51%	2.99%
5	3.71%	2.33%	2.77%
6	4.85%	2.94%	3.76%
All	6.65%	6.14%	6.30%

7.5.1.4 Discussion

An empirical model is created and predicts accurately the standard deviation of the Gaussian distribution for the location of maximum stress on particle neutral axis σ_{dev} . This model is based on the mean number of contacts a particle experienced in an inverse power fashion and the particle physical properties.

The high error of the model for particles aspect ratio $\alpha_p = 2$ can be explained by their lower bending stress ratio, which decreases the probability of the maximum stress to

be located at the centre of the particle. For aspect ratio $\alpha_p \geq 3$, the model has an excellent accuracy with a mean error below the statistical threshold of 5%.

Finally, it can be noted that only one fitting parameter is needed in this model, and this parameter b (see Table 7.5.3) is very close to $-1/2$ which could lead to a simplification of the model using a square root and give insights for the creation of a theoretical model.

7.5.2 Empirical Model from Bulk Parameters

An empirical model is created and accurately predicts σ_{dev} from simulation data (see Chapter 7.5.1). The resulting equation (see Equation 7.5.3) can be used as a basis for the creation of a model predicting σ_{dev} from bulk parameters. The mean number of contacts on particle $\bar{N}_{c,p}$ is a simulation data and therefore needs to be expressed as a function of bulk parameters. The correlations are investigated and quantified for the shearing phase only, then the built model is fine-tuned on both uniaxial compression and shearing phase data.

7.5.2.1 Linear Correlation with Solid Fraction

The analysis of simulation data highlighted a linear correlation between the mean number of contacts on particle $\bar{N}_{c,p}$ and the solid fraction f_s for both shearing phase (see Figure 6.4.9) and uniaxial compression (see Figure 6.5.9). This correlation has also been reported in DEM tri-axial compression of ellipsoids [205] and shear cell filled with spheres [270], with an inverse proportionality between coordination number and void ratio.

$\bar{N}_{c,p}$ can then be expressed as a function of f_s as follows:

$$\bar{N}_{c,p} = a \cdot f_s + b \quad 7.5.4$$

With a and b dimensionless.

The parameters a and b are obtained using the regression method of the residual sum of squares for the different particle aspect ratio α_p and normal stresses applied σ in the shearing phase (see Table 7.5.5). The regression couldn't be performed on $\alpha_p = 2$ due to the low variation of their $\bar{N}_{c,p}$ values.

Table 7.5.5: Parameters of linear regression as described in Equation 7.5.4 for the different aspect ratios α_p and normal stresses applied σ in shearing phase. The values of the coefficient of determination R^2 are in Appendix 10.

	a					b				
$\alpha_p \setminus \sigma$	1kPa	2kPa	4kPa	6.5kPa	10kPa	1kPa	2kPa	4kPa	6.5kPa	10kPa
3	9.79	14.2	16.0	17.9	17.1	0.684	-1.54	-2.29	-3.13	-2.53
4	10.3	11.6	14.2	17.4	18.6	0.880	0.450	-0.574	-2.00	-2.38
5	11.4	13.9	17.4	17.5	19.4	0.848	-0.0860	-1.46	-1.24	-1.89
6	12.8	14.8	18.9	20.4	22.1	0.655	0.0690	-1.46	-1.85	-2.30

The linear model fits the data with a greater accuracy as α_p increases – with a higher coefficient of determination R^2 (see Appendix 10) – due to a wider range of their $\bar{N}_{c,p}$ values.

7.5.2.2 Linear Correlation with Particle Aspect Ratio

The parameter a (see Equation 7.5.4) appears to be positively correlated to the particle aspect ratio α_p (see Figure 7.5.2). Indeed, the analysis of simulation data has shown that the mean number of contacts on particle $\bar{N}_{c,p}$ is proportional to α_p in a linear fashion for both shearing phase (see Figure 6.4.9) and uniaxial compression (see Figure 6.5.9). Indeed, a higher coordination number is reported to increase with aspect ratio [228].

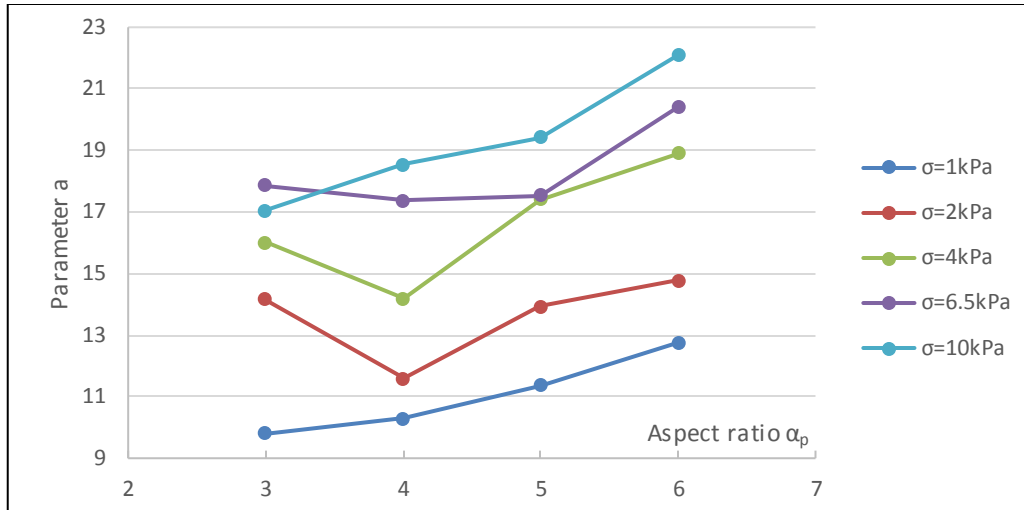


Figure 7.5.2: Parameter a as in Equation 7.5.4 obtained by linear regression for the different aspect ratios α_p and normal stresses applied σ in shearing phase. Data available in Table 7.5.5.

$\bar{N}_{c,p}$ can then be expressed as follows:

$$\bar{N}_{c,p} = (c \cdot \alpha_p + d) \cdot f_s + b \tag{7.5.5}$$

With b , c and d dimensionless.

These parameters are obtained using the regression method of the residual sum of squares for the different normal stresses applied σ in the shearing phase (see Table 7.5.6). The values of the coefficient of determination R^2 are high showing a good quality of the linear model fitting.

Table 7.5.6: Parameters of linear regression as described in Equation 7.5.5 for the different normal stresses applied σ in shearing phase.

Normal stress σ	b	c	d	R^2
1kPa	0.824	1.02	6.31	0.963
2kPa	0.0580	1.24	7.43	0.978

4kPa	-1.31	1.50	9.60	0.983
6.5kPa	-1.63	1.63	10.2	0.987
10kPa	-2.20	1.82	11.0	0.986

7.5.2.3 Logarithmic Correlation with Normal Stress

The three parameters of the model (see Equation 7.5.5) are proportional to the normal stress σ (see Table 7.5.6). Indeed, the analysis of simulation data highlighted the proportionality between the mean number of contacts on particle $\bar{N}_{c,p}$ and the normal stress σ in a logarithmic fashion for both shearing phase (see Figure 6.4.8) and uniaxial compression (see Figure 6.5.7).

The model is then modified and $\bar{N}_{c,p}$ is finally expressed as follows:

$$\bar{N}_{c,p} = (\ln \sigma)^e \cdot f_s \cdot (f \cdot \alpha_p + g) \quad 7.5.6$$

With e , f and g dimensionless.

Theses parameters are obtained using the regression method of the residual sum of squares on all simulation data (see Table 7.5.7).

Table 7.5.7: Fitting parameters of Equation 7.5.6 on all simulation data.

Parameters	Units	Value
e	\emptyset	0.598
f	\emptyset	0.403
g	\emptyset	2.10

R^2	\emptyset	0.936
-------	-------------	-------

This final logarithmic model predicts excellently $\bar{N}_{c,p}$ with an overall mean error of 2.60% (see Table 7.5.8). The error is consistent for the different particle elongation and the model fits quasi-perfectly the data for shearing phase with a mean error of 1.66%.

Table 7.5.8: Mean error of predicted $\bar{N}_{c,p}$ using Equation 7.5.6 and parameters values reported in Table 7.5.7.

Aspect ratio	Compression	Shearing	All
2	5.26%	2.02%	2.90%
3	4.46%	1.96%	2.64%
4	3.68%	1.16%	1.85%
5	4.01%	1.30%	2.16%
6	5.21%	1.84%	3.29%
All	4.62%	1.66%	2.60%

This empirical model for the prediction of $\bar{N}_{c,p}$ is finally integrated into the model created for the prediction of the Gaussian standard deviation σ_{dev} (see Equation 7.5.3):

$$\sigma_{dev} = r_p \cdot \alpha_p \cdot \left((\ln \sigma)^e \cdot f_s \cdot (f \cdot \alpha_p + g) \right)^b \quad 7.5.7$$

With b , e , f and g dimensionless.

This final model predicts accurately σ_{dev} with an overall mean error of 6.12% (see Table 7.5.9). The mean error for the different aspect ratios and stress environments is

similar to the one for the prediction of σ_{dev} from simulation (see Table 7.5.4). The usual increase in error when switching model from simulation data to bulk parameters isn't observed here, which is due to the excellent accuracy of the model predicting $\bar{N}_{c,p}$ (see Table 7.5.8).

Table 7.5.9: Mean error of predicted σ_{dev} using Equation 7.5.7 and parameters values reported in Table 7.5.3 and Table 7.5.7.

Aspect ratio	Compression	Shearing	All
2	20.8%	17.7%	18.5%
3	3.80%	4.30%	4.16%
4	4.53%	2.62%	3.14%
5	3.71%	2.19%	2.67%
6	3.76%	2.56%	3.08%
All	6.61%	5.88%	6.12%

7.5.2.4 Discussion

An empirical model is built and predicts accurately the Gaussian standard deviation σ_{dev} of the maximum stress location distribution. This estimation of σ_{dev} from the bulk parameters is rendered possible by the creation of a model predicting excellently the mean number of contacts on particle $\bar{N}_{c,p}$ from the particle aspect ratio α_p , the solid fraction of the bed and the normal stress applied. The predicted $\bar{N}_{c,p}$ is then input into another model based on simulation data, allowing the estimation of σ_{dev} .

The mean error of this model is comparable to the one for the simulation data based model due to the excellent accuracy of the model predicting $\bar{N}_{c,p}$. The error of this model is higher for aspect ratio $\alpha_p = 2$ due to their decreased bending stress ratio and

lower probability of having their maximum stress located at the centre of their neutral axis.

The model predicting $\bar{N}_{c,p}$ is dependent on the particle physical properties and is expected to vary for different particle shape in addition to different α_p . The simulations are performed in monodisperse bed and there is no doubt that $\bar{N}_{c,p}$ would change with polydispersity. Finally, the clumped sphere approach of particle modelling has shown to augment the number of in the performed simulations as two particles can enter in contact on multiple location (see Figure 6.4.11). Indeed, the sphere overlap is reported to affect the void ratio [272, 277] and the number of contacts [249, 258, 266, 272, 278] which can be twice as high for rough particles [228]. The asperity and roughness of the particles would then be a factor to consider for model refinement in further work.

7.6 Conclusion

The understanding of the existing physical and mechanical phenomena within a particle bed provided from simulation analysis (see Chapter 6) allows the creation of a theoretical model for the prediction of the particle internal stress. The mean particle internal stress is confidently assumed being equal to the Weibull scale parameter λ of the particle internal stress distribution.

Additionally, empirical models are built to predict λ , the Weibull shape parameter k and the Gaussian standard deviation σ_{dev} of the maximum stress location distribution from either the output simulation data or the bulk parameters. The error associated with bulk parameters models is slightly higher (see Table 7.6.1) but allows process designers to estimate the stress experienced by particles without the need to perform simulations.

The models usually give a better accuracy on shearing phase, which is probably due to the greater number of data points recorded from shearing simulations (see Chapter 6.3.3) and used to calibrate the models using the residual sum of squares regression method. The case of particles with aspect ratio $\alpha_p = 2$ gives different errors on most of the models created, which is potentially due to the narrower range and lower values

for their key variables, mathematically increasing their error. Moreover, the regression method used is based on squared values and thus puts the priority of the better fitting of greater variable values. Alternatively, a distinction could be operated on shorter particles for which the assumptions might be slightly different e.g. for their volume calculation based on cylindrical shape. The selected simulation parameters in Chapter 6 and the use of rigid particle are expected to have an impact on the fitting parameters obtained during the calibration of the different developed models, and their influence could be investigated in future work.

All the created models are designed to predict the key variables characterising the particles internal stress and avoid the resources and time-consuming implementation, testing and running of Euler Equation of Motion. The models are based on simulation data of monodisperse bed compression and shearing, nevertheless they could predict these key variables for polydisperse bed by applying them on sub-groups of the particles population segmented by particle size and shape.

The built models will be used in combination with the distribution of breakage strength distribution of β -LGA crystals experimentally assessed in Chapter 4 to create a probabilistic breakage kernel in Chapter 8. The kernel will be implemented in a population balance model to predict the breakage rate of particles in a lab-scale AFD.

Table 7.6.1: Summary of theoretical and empirical models created with the associated overall mean error. The list of variable description is in Chapter No.

Model type	Variable predicted	Input variables	Overall mean error	Comments
Theoretical (calibrated)	\bar{F}_c	$\sigma, \varphi, \alpha_p, r_p, \bar{N}_{c,p}, f_s$	7.41%	Odd error for $\alpha_p = 2$
	$\bar{\sigma}_{p,ZZ}$	$\sigma, \varphi, \alpha_p, r_p, \bar{N}_{c,p}, f_s$	9.62%	Odd error for $\alpha_p = 2$
	$\bar{\sigma}_p$	$\sigma, \varphi, \alpha_p, r_p, \bar{N}_{c,p}, f_s$	9.42%	Odd error for $\alpha_p = 2$
	λ	$\sigma, \varphi, \alpha_p, r_p, \bar{N}_{c,p}, f_s$	10.8%	Odd error for $\alpha_p = 2$

Chapter 7: Prediction of Particles Internal Stress for Agitated Drying Conditions

Empirical (from simulation data)	λ	\bar{s}, α_p	4.10%	Consistent error on all α_p
	k	$\alpha_p, \sigma_{norm}(s)$	4.88%	Consistent error on all α_p
	σ_{dev}	$\alpha_p, r_p, \bar{N}_{c,p}$	6.30%	Greater error for $\alpha_p = 2$
Empirical (from bulk parameters)	$\alpha_{\sigma,ZZ}$	α_p	0.68%	Excellent accuracy on all α_p
	λ	$\sigma, \varphi, \alpha_p$	9.96%	Greater error for $\alpha_p = 2$
	k	σ	7.07%	Consistent error on all α_p
	$\bar{N}_{c,p}$	σ, α_p, f_s	2.60%	Consistent error on all α_p
	σ_{dev}	$\sigma, \alpha_p, r_p, f_s$	6.12%	Greater error for $\alpha_p = 2$

8 Prediction of Particle Breakage for Agitated Drying Conditions

8.1 Introduction

In this chapter, a probabilistic approach is used to create a breakage kernel from the particle properties and the mechanical environment in which they are processed. The breakage strength distribution of a β -LGA crystal sample is assessed in Chapter 4 using an Atomic Force Microscopy method for crystal breakage [18]. Mathematical models estimating the particle internal stress distribution for different particle shape and mechanical environments are built in Chapter 7 based on the analysis of DEM shear cell simulations in Chapter 6.

The breakage kernel is then implemented into a population balance model (PBM) to estimate the breakage of particles in a lab-scale agitated filter dryer (AFD) for an increasing number of impeller rotations. The estimation is compared with experimental results for the agitation of a dry bed composed of β -LGA crystals presented in Chapter 3. A calibration is then performed on the PBM and the impact of input parameters are discussed to optimise the accuracy of the model. Finally, the calibrated model is used to predict the breakage of the β -LGA crystals for the scale-up of agitation.

8.2 Probabilistic Approach to Particle Breakage

8.2.1 Extent of Breakage

The experimental study [18] presented in Chapter 4 describes a novel technique for the assessment of particles breakage strength σ_b using Atomic Force Microscopy. It is observed that the results for a sample of β -LGA crystals are distributed and follow a Weibull model [47, 48]. Indeed, the breakage strength is highly affected by the presence of defects, especially for organic crystals [192]. Therefore the breakage strength is less a material property than a particle property, and a different distribution might be found for different beds even if their particles are made of the same material.

The cumulative density function of breakage strength σ_b for a given particle population represents then the breakage probability of one of these particles experiencing a certain internal stress. It also represents the percentage of particles with this population that would break if they were all experiencing the same internal stress.

A probabilistic approach of particle breakage is here presented where the breakage strength distribution BSD (cumulative density function) is combined with the particle internal stress distribution PISD (probability density function) to estimate the number of particles broken (see Figure 8.2.1). The BSD characterises the mechanical properties of a particle population, and the PISD is dependent on both the environment experienced by these particles and their physical properties.

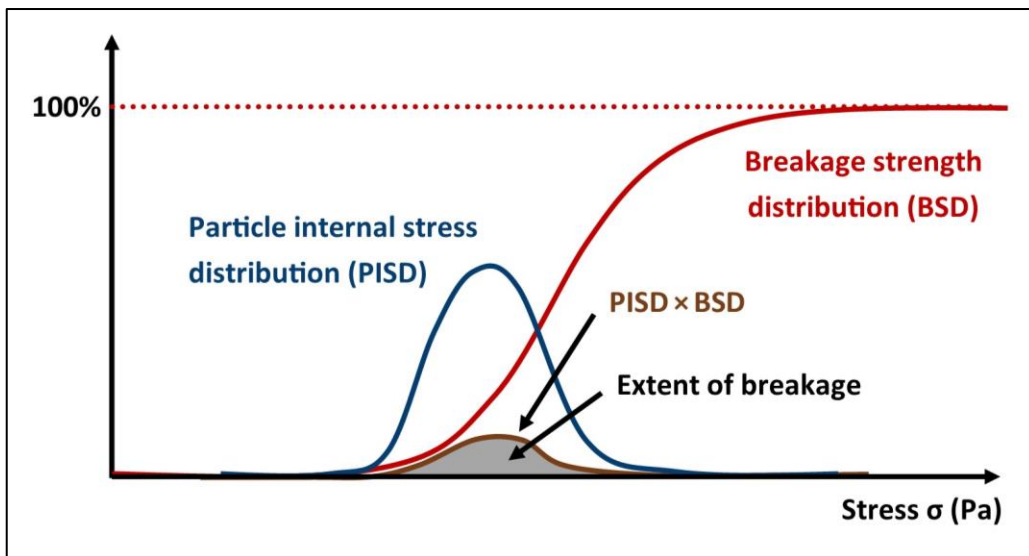


Figure 8.2.1: Particle internal stress distribution (PISD) and breakage strength distribution (BSD). The area below the joint density function ($PISD \times BSD$) is the extent of breakage.

This extent of breakage B corresponds to the area below the curve of the joint density function $PISD \times BSD$, such as:

$$B = \int_0^{+\infty} PISD(\sigma) \times BSD(\sigma) d\sigma \quad 8.2.1$$

It is demonstrated that both PISD and BSD are Weibull distribution models. B can then be written as follows:

$$B = \int_0^{+\infty} \frac{k_p}{\lambda_p} \left(\frac{\sigma}{\lambda_p} \right)^{k_p-1} e^{-(\sigma/\lambda_p)^{k_p}} \cdot \left(1 - e^{-(\sigma/\lambda_b)^{k_b}} \right) d\sigma \quad 8.2.2$$

With k_p and λ_p the Weibull parameters of the particle internal stress distribution, and k_b and λ_b the Weibull parameters of the particles breakage strength distribution (see Chapter 6.2.1). The final equation (derivation in Appendix 22) is:

$$B = \frac{k_b}{\lambda_b^{k_b}} \int_0^{+\infty} \sigma^{k_b-1} \cdot e^{-(\sigma/\lambda_b)^{k_b}} \cdot e^{-(\sigma/\lambda_p)^{k_p}} d\sigma \quad 8.2.3$$

8.2.2 Breakage Rate

The simulations have been performed without implementing a breakage kernel [232-234], therefore particles remain intact throughout the simulation regardless of the internal stress they experience. This choice allows the observation of the particle bed behaviour and particles internal stress during the simulations whilst conserving the particles size distribution, and therefore reducing the number of degrees of freedom.

Thus, the probabilistic approach developed to estimate the extent of breakage B (see Equation 8.2.3) doesn't involve time, as breakage doesn't occur in the simulations, which makes this model non-transient. This predictive model is then a breakage kernel and can be embedded in simulations to compute the breakage of particles individually based on their breakage probability. To obtain a breakage rate from the extent of breakage without performing simulations where particles would break, a time factor needs to be combined to the model. Therefore, it is essential to identify the physical phenomenon that induces an event of breakage.

If a group of particles (e.g. the particles in the simulated shear cell) are experiencing an event of breakage, the estimated percentage of particles breaking corresponds to the extent of breakage B . Once breakage is estimated, the next event of breakage occurs when this group of particles is considered as a new one. Particles packing is characterised by the relative positioning and the contacts between its particles. Indeed, the internal stress of a particle is calculated from its contact properties

resulting from the relative positioning of the particles surrounding it. The change of particles conformation is thus an appropriate key element representing an event of breakage, and the change of particles conformation in respect to time is given by the strain rate $\dot{\gamma}$ (see Equation 2.4.4). The breakage rate \dot{B} is then expressed as a function of the extent of breakage B :

$$\dot{B} = N_B \cdot B \cdot \dot{\gamma} \quad 8.2.4$$

With N_B the number of event of breakage per strain applied. Here, particles in a static bed experience only N_B events of breakage as the particles conformation remains unchanged and the same particles can only break once. On a contrary, the agitation of particles promotes their breakage at a rate determined by both the strain rate, particles mechanical properties and internal stress. In quasi-static flow regime, B is independent to $\dot{\gamma}$, in the same fashion as in the DEM shear cell simulations performed (see Chapter 5.5.2). Therefore, the probability of a particle to break in an agitated dryer increases at each strain applied γ such as:

$$P(\text{break}) = 1 - (1 - N_B \cdot B)^\gamma \quad 8.2.5$$

8.2.3 Population Balance Model

Once the breakage rate \dot{B} is determined (see Equation 8.2.4), the breakage of particles is simulated mathematically using a population balance model and the particle size distribution (PSD) is computed as the bed is sheared with increasing strain γ applied.

After each unit of strain applied, the particle population is segmented into sub-groups based on their aspect ratio α_p and the percentage of particles breaking within each sub-group corresponds to their determined extent of breakage per strain $N_B \cdot B$ (see Equation 8.2.3).

The breakage of particles is considered occurring with a cleavage plane orthogonal to the particles neutral axis and creates fragments with their aspect ratios being non-null

natural numbers $\alpha_f \in \mathbb{N}^*$. Here, the minimum particle aspect ratio is $\alpha_p = 1$ and these particles cannot break further. The size of fragments depends on the location of breakage on the particle neutral axis (see Figure 8.2.2) and is determined probabilistically using the Gaussian model for the distribution of maximum stress location (see Chapter 6.2.2).

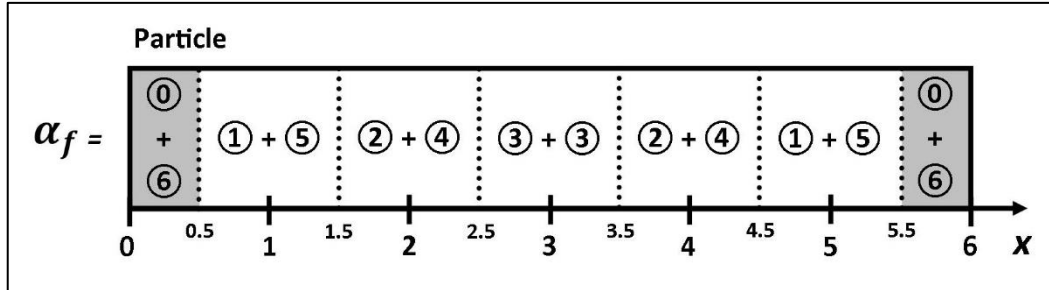


Figure 8.2.2: Aspect ratio α_f of the two created fragments (circled) for the different ranges of breakage location x in the case of a particle with $\alpha_p = 6$. No breakage occurs when $x \in [0, 0.5] \cup [5.5, 6]$.

The number of fragments n_{α_f} created having an aspect ratio α_f for the breakage of N_{α_p} particle with an aspect ratio α_p at the strain γ and at a breakage location x is given as follows:

$$n_{\alpha_f}(\alpha_p, \gamma) = n_{\alpha_p - \alpha_f}(\alpha_p, \gamma) = N_{\alpha_p}(\gamma) \cdot N_B \cdot B_{\alpha_p} \cdot 2 \cdot P(x \in [\alpha_f - 0.5, \alpha_f + 0.5]) \quad 8.2.6$$

For $\alpha_f \in \mathbb{N}^*$, $\alpha_f \in [0, \lfloor \alpha_p/2 \rfloor]$, with B_{α_p} the extent of breakage of the particle with an aspect ratio α_p , N_B the number of breakage event per unit of strain and P the probability of the breakage location x being within the corresponding range of values to create fragments with α_f . Two exceptions occur to the equation above: when $\alpha_f = 0$ the lower limit for the range of x in the probability function P is 0, and when $\alpha_f = \alpha_p/2$ the upper limit of x is $\alpha_p/2$.

The distribution of breakage location follows a Gaussian model with the mean $\bar{x} = \alpha_p/2$ and a standard deviation σ_{dev} , so that the probability function P is given as:

$$P(x \in [\alpha_f - 0.5, \alpha_f + 0.5]) = \frac{1}{2} \left(\operatorname{erf} \left(\frac{\alpha_p + 0.5 - \bar{x}}{\sigma_{dev} \sqrt{2}} \right) - \operatorname{erf} \left(\frac{\alpha_p - 0.5 - \bar{x}}{\sigma_{dev} \sqrt{2}} \right) \right) \quad 8.2.7$$

As the Gaussian cumulative density function is applicable for a real-valued variable, $P(x \in [0, \alpha_p]) \neq 1$. Therefore, the probabilities obtained for the different fragment size are normalised so that their sum equals 1.

The number of particles $N_{\alpha_p}(\gamma + 1)$ within a sub-group of α_p at a strain $\gamma + 1$ is then calculated as the number of particles $N_{\alpha_p}(\gamma)$ within this sub-group at the strain γ reduced by the number of particles breaking $N_{\alpha_p}(\gamma) \cdot N_B \cdot B_{\alpha_p}$ and augmented by the number of fragments $n_{\alpha_f = \alpha_p}(i, \gamma)$ with $\alpha_f = \alpha_p$ generated from the breakage of longer particles (i.e. $\geq \alpha_p$) at the strain γ :

$$N_{\alpha_p}(\gamma + 1) = N_{\alpha_p}(\gamma) \left(1 - N_B \cdot B_{\alpha_p} \right) + \sum_{i=\alpha_p}^{\alpha_{p,max}} n_{\alpha_f = \alpha_p}(i, \gamma) \quad 8.2.8$$

It is considered that no breakage is occurring when $x \in [0, 0.5] \cup [\alpha_p - 0.5, \alpha_p]$, so the corresponding number of fragments (i.e. $\alpha_f = \alpha_p$) is inserted back into the same α_p sub-group on the following strain $\gamma + 1$, as described in the above equation when $i = \alpha_p$.

8.3 Model Application

The probabilistic model created (see Equation 8.2.3) is applied to estimate the breakage of the studied sample of β -LGA crystals (see Chapter 4.3.1.1) in both uniaxial compression and shearing phase for different normal stresses applied σ and particles aspect ratios α_p . The analysis of DEM shear cell simulations is used to obtain the Weibull parameters of the particle internal stress distribution: the scale parameter λ_p (see Chapter 6.4.6.2.1 for shearing phase and Chapter 6.5.6.2.1 for uniaxial compression) and the shape parameter k_p (see Chapter 6.4.6.2.2 for shearing phase and Chapter 6.5.6.2.2 for uniaxial compression). The simulated particles size

distribution is monotonous with a particle width of $50\mu m$ (see Chapter 5.2.1.1). The Weibull parameters of the breakage strength distribution are obtained experimentally from the breakage of β -LGA crystals using the novel method involving Atomic Force Microscopy (see Table 4.4.1): $\lambda_b = 27.0MPa$ and $k_b = 1.95$.

In uniaxial compression, the extent of breakage is averaged for all bed conformations simulated (i.e. strain applied) for a given aspect ratio and normal stress, with a mean value \bar{B} . \bar{B} increases exponentially with both the particles aspect ratio α_p and the normal stress applied σ (see Figure 8.3.1). Here, for aspect ratio $\alpha_p = 6$, \bar{B} is multiplied by 3.43 when doubling the normal stress σ from $10kPa$ to $20kPa$. As expected, the greatest value of \bar{B} is found for the highest aspect ratio α_p and normal stress σ : when a pressure of $100kPa$ is exerted on a monodisperse bed composed of the β -LGA particles studied with an aspect ratio of 6, with a length of $300\mu m$, it is estimated that 4.5% of these particles are breaking.

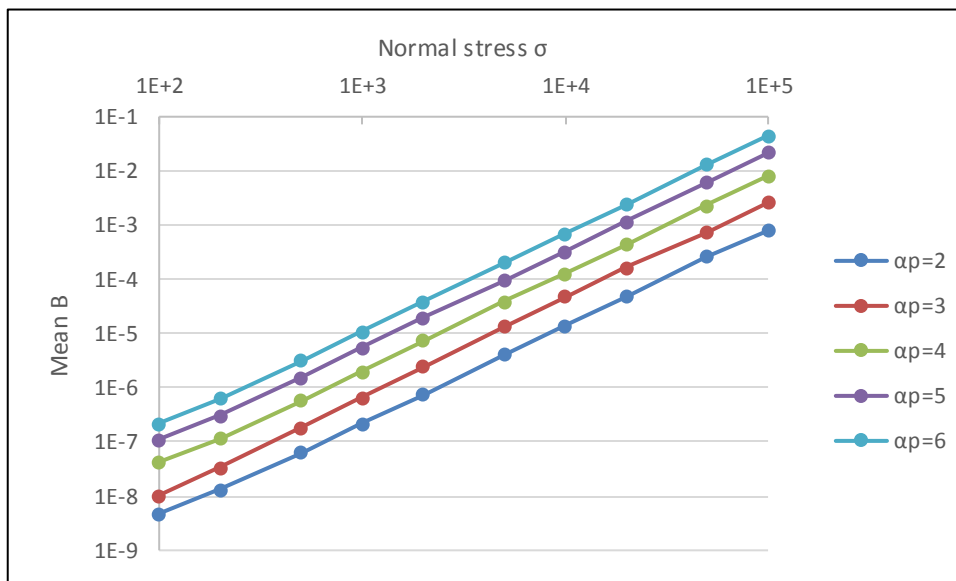


Figure 8.3.1: Mean extent of breakage \bar{B} averaged over all bed conformations in uniaxial compression for the different aspect ratios α_p and normal stresses σ .

The exponential proportionality between the extent of breakage B and both aspect ratio α_p and normal stress σ is also observed in the shearing phase (see Figure 8.3.2). The addition of the shear stress to the mechanical environment augments the extent of breakage B : for instance, the extent of breakage increases from 0.71‰ to 1.3‰ for $\alpha_p = 6$ and $\sigma = 10kPa$.

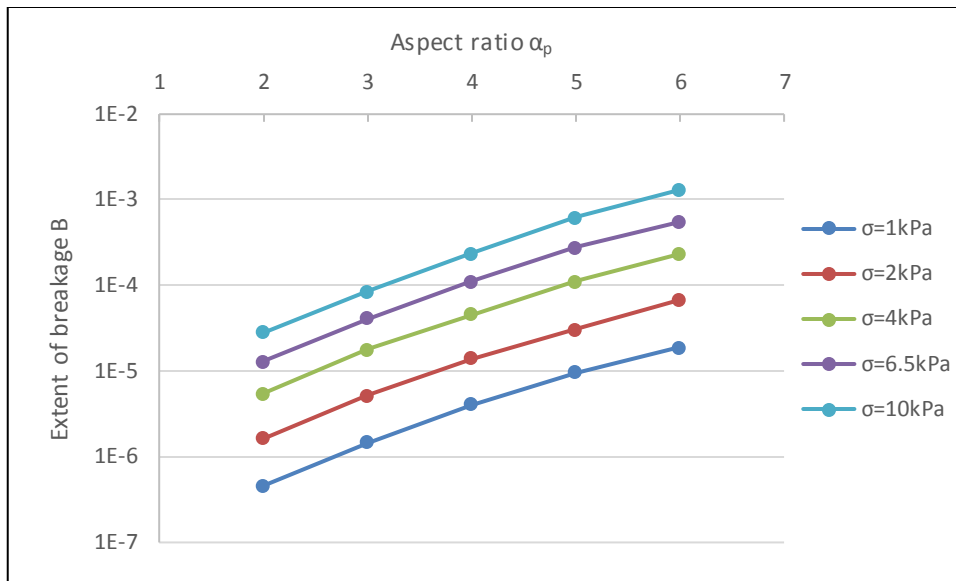


Figure 8.3.2: Extent of breakage B in steady state of shearing phase for the different aspect ratios α_p and normal stresses σ .

The created breakage kernel is implemented in a population balance model (PBM) (see Equation 8.2.8) to predict the breakage of a particle population with increasing strain applied in shearing phase and quasi-static flow regime. The initial particle size distribution (PSD) is monodispersed with cylindrical particles having an aspect ratio $\alpha_p = 6$ and a particle length $L_p = 300\mu\text{m}$. The Weibull parameters of the particles breakage strength distribution are experimentally obtained to reflect the mechanical properties of the β -LGA crystals studied. The normal stress applied remains constant at $\sigma = 4\text{kPa}$, which is typically the order of magnitude of hydrostatic pressure experienced by particles at the bottom of industrial scale dryers [1]. The extent of breakage B is previously calculated for each aspect ratio α_p and the selected normal stress σ (see Figure 8.3.2). The size of fragments is determined probabilistically using the Gaussian model parameters of maximum stress location distribution obtained from the performed simulations: the mean value is half the particle length and the standard deviation σ_{dev} is obtained for each aspect ratio α_p at the selected normal stress σ (see Figure 6.4.38). The breakage of particles is simulated following the algorithm detailed in Chapter 8.2.3. The minimum fragment aspect ratio is $\alpha_p = 1$ and these particles do not break further.

Chapter 8: Prediction of Particle Breakage for Agitated Drying Conditions

The number of particles with $\alpha_p = 6$ is quickly decreasing in a geometrical progression with a rate of 21% of particles breaking after every 1000 unit of strain applied (see Figure 8.3.3). The number of particles in the other sub-groups increases as fragments from longer particles are created, and reaches a maximum before decreasing when the loss from their breakage exceeds the feed from the breakage of longer particles. Therefore, the maximum volume fraction occurs at a larger strain for decreasing aspect ratio. The fraction for aspect ratio $\alpha_p = 1$ keeps increasing as it is not able to break with the used PBM. For an infinite strain applied, all the particles with $\alpha_p \geq 2$ are expected to break and the bed would be composed of only particles with aspect ratio $\alpha_p = 1$.

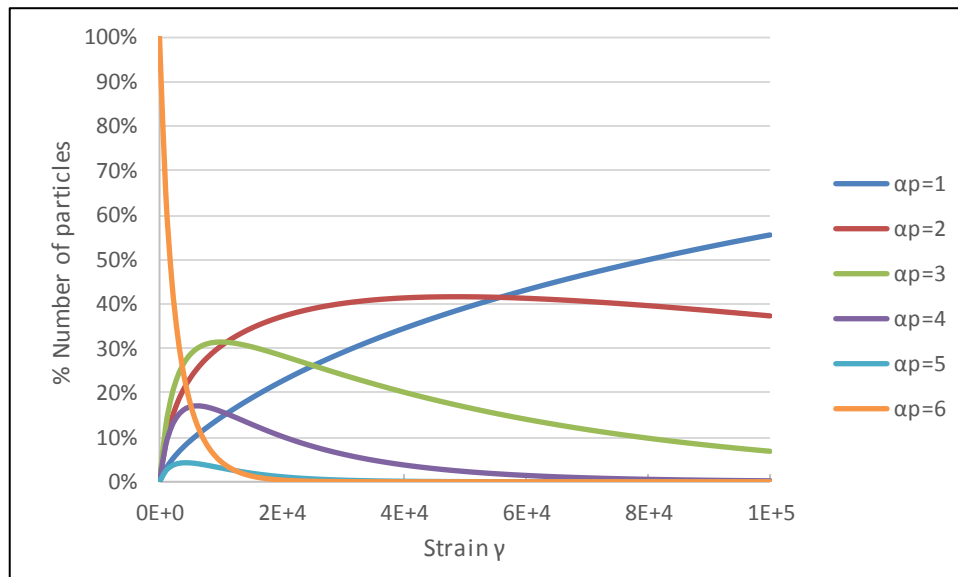


Figure 8.3.3: Fraction of particles population in the different aspect ratio α_p sub-groups, given by the strain applied γ and for a normal stress applied $\sigma = 4kPa$.

The PSD is then predicted with increasing strain applied and the corresponding volume of each particle sub-group is calculated (see Figure 8.3.4). Particles with aspect ratio $\alpha_p = 6$ represent the majority of the bed volume until a strain applied of $\gamma \approx 5500$, then the particles with aspect ratio $\alpha_p = 3$ become dominant until $\gamma \approx 27k$ when the volume for aspect ratio $\alpha_p = 2$ particles becomes predominant. It is expected that curves for aspect ratio $\alpha_p = 1$ and $\alpha_p = 2$ will be crossing with the volume for aspect ratio $\alpha_p = 1$ becoming dominant if further strain is applied beyond $100k$.

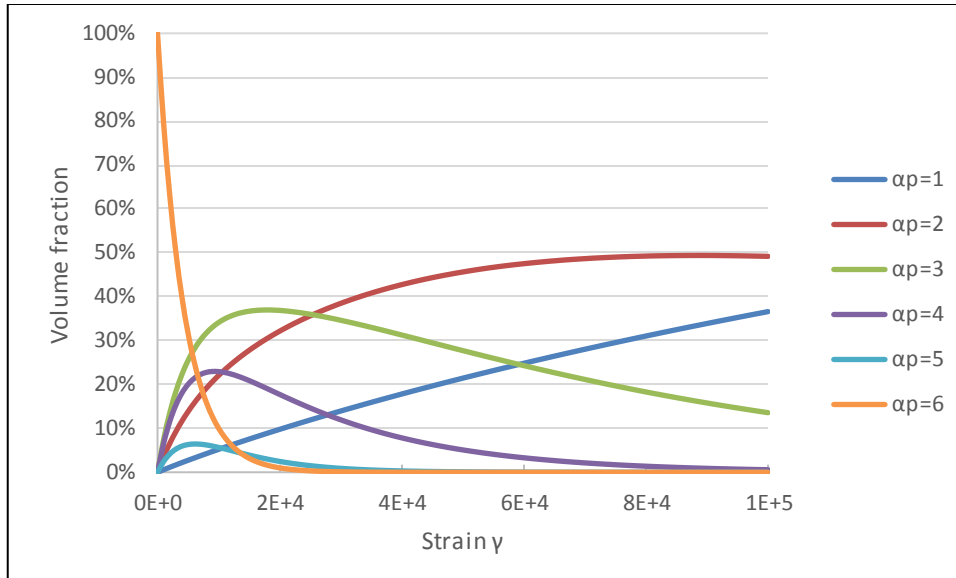


Figure 8.3.4: Volume fraction in the different aspect ratio α_p sub-groups, given by the strain applied γ and for a normal stress applied $\sigma = 4kPa$.

8.4 Model Validation against Experiments

The created breakage kernel (see Equation 8.2.4) is implemented into the PBM (see Equation 8.2.8) to predict the PSD of a dry particle bed through agitation within a lab-scale Agitated Filter Dryer (AFD).

The initial process conditions and PSD observed experimentally for the dry agitation of β -LGA crystals in Chapter 3 are input into the model and the prediction of PSD is compared with experimental measurements of particle breakage throughout agitation.

8.4.1 Bed Division into Zones

For the dry agitation experiment in Chapter 3, the height of the particle bed is measured and equals approximately $60mm$. The radius of the cylindrical bed is calculated from the information provided by the manufacturer and equals $25mm$ [337]. The volume of the impeller is neglected and the total volume of the cylindrical particle bed is then $118cm^3$. The particle bed in the AFD is divided into 9 zones of equal volume with different radial distance and height (see Figure 8.4.1) in the same fashion as in

Hare's paper [108]. All the zones have the same height at 20mm. Zones {1, 4, 7} have a cylindrical shape whilst zones {2, 3, 5, 6, 8, 9} are rings.

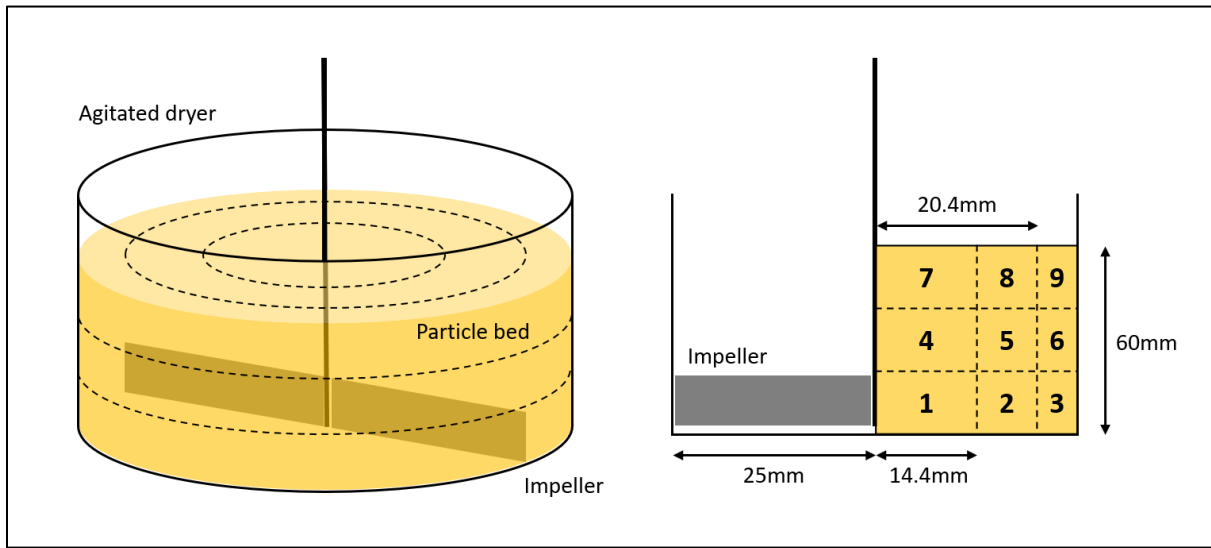


Figure 8.4.1: Particle bed in agitated filter dryer divided 9 zones of equal volume and equal height.

The radial distance of the centre of the {Inner, Middle, Outer} zones is {7.22, 17.4, 22.7} mm and the height of the centre of the {Bottom, Middle, Top} zones is {10, 30, 50} mm so that all zones have equal volumes.

8.4.2 Particle Properties

8.4.2.1 Breakage Strength

The breakage strength distribution of the particles follows the experimentally assessed distribution for the studied sample of β -LGA crystals in Chapter 4 (see Table 4.4.1) with the Weibull parameters $\lambda_b = 27.0MPa$ and $k_b = 1.95$. The β -LGA crystals involved in both Atomic Force Microscopy (AFM) experiments in Chapter 4 and AFD experiments in Chapter 3 are produced using the same crystallisation method (see Chapter 4.3.1.1) and are considered having the same breakage strength distribution.

8.4.2.2 Particle Aspect Ratio Distribution

The Particle Aspect Ratio Distribution (PAR) is the volume of the bed segmented by the particle aspect ratio α_p . Indeed, the breakage of particles is computed within each sub-groups of aspect ratio regardless of the individual particles size, as it is assumed that big particles break the same way than small particles if they have the same elongation. The volume fraction of fragments created equals the volume fraction of the broken particles and is calculated proportionally to the fragments aspect ratio α_f to conserve the same bed volume.

The initial PAR input in the model corresponds to the measured volume probability density function in the lab-scale AFD experiment on the dry bed after overnight pressure filtration (see Appendix 14). The aspect ratio ranges within the interval $\alpha_p \in [1,15]$. The same initial PAR is assigned to the 9 zones of the particle bed.

8.4.3 Breakage Model

8.4.3.1 Mechanical Environment in Zones

The results of the simulations and experiments performed in Hare's paper [108] are kindly provided by the author and allow the estimation of the strain per impeller rotation γ_{rot} and the stress ratio φ in the 9 zones of the studied AFD. Like in the paper, only the 3rd impeller rotation is considered as two rotations are necessary to reach a steady state. The data for an impeller speed of $78rpm$, at which a quasi-static flow regime has been demonstrated in the paper, is selected for the further analysis.

8.4.3.1.1 Strain per Impeller Rotation

The strain experienced by each of the 9 zones in Hare's AFD for an impeller rotation has been calculated (see Table 8.4.1). Hare's AFD is larger than the studied AFD with radial distances of the centre of the $\{Inner, Middle, Outer\}$ zones at $\{18, 33.3, 42.8\} mm$.

Chapter 8: Prediction of Particle Breakage for Agitated Drying Conditions

As it is mentioned in the paper, the strain experienced by particles in a shear cell is linearly proportional to the radial distance. Therefore, the amount of strain per impeller rotation γ_{rot} is adjusted for each of the 9 zones by cross-multiplication to correspond to the radial dimensions of the studied AFD (see Chapter 8.4.1).

Table 8.4.1: Strain per impeller rotation γ_{rot} in the 9 zones of Hare's AFD [108] and calculated for the studied AFD.

γ_{rot}	Hare et al. 2011			Studied AFD		
Height \ Radius	Inner	Middle	Outer	Inner	Middle	Outer
Top	0.905	1.04	1.90	0.364	0.545	1.01
Middle	1.30	1.69	2.61	0.523	0.885	1.38
Bottom	1.41	1.92	2.61	0.565	1.00	1.38

8.4.3.1.2 Normal Stress

The hydrostatic pressure is taken as normal stress σ and calculated in each zone of the studied AFD using Equation 2.3.1 modified to account for the bed porosity:

$$\sigma = \rho \cdot g \cdot h \cdot f_s \quad 8.4.1$$

With $\rho = 1460 \text{ kg} \cdot \text{m}^{-3}$ [323] the solid density of β -LGA crystals, h the depth into the particle bed, $g = 9.81 \text{ m} \cdot \text{s}^{-2}$ the acceleration of gravity on Earth and f_s the volume solid fraction of the bed.

The volume solid fraction is calculated from the volume $V = 118 \text{ cm}^{-3}$ (see Chapter 8.4.1) and the mass $m = 41.2 \text{ g}$ (see Chapter 3.2.1) of the particle bed:

$$f_s = \frac{m}{\rho \cdot V} \quad 8.4.2$$

The volume solid fraction is then $f_s = 0.24$.

Using the height of the centre of zones in the studied AFD (see Chapter 8.4.1), the normal stress is finally calculated and equals $\{172, 103, 34.3\} Pa$ for the $\{Bottom, Middle, Top\}$ zones.

8.4.3.1.3 Stress Ratio

The torque has been recorded experimentally in Hare's AFD [165] and the mean torque during the 3rd impeller rotation is $T = 176mN.m$.

Using the Darelus equation [152] (see Equation 2.3.4), the average shear stress τ_{ave} is calculated from the dimensions of Hare's AFD, giving $\tau_{ave} = 243Pa$.

The hydrostatic pressure of the whole bed is taken as the normal stress σ and calculated from the mass of the bed $m = 250g$ [165], the acceleration of gravity on Earth $g = 9.81m.s^{-2}$, the radius of Hare's AFD $R = 47mm$ and the radius of the impeller holder $R_{imp} = 8mm$ using the following equation:

$$\sigma = \frac{m \cdot g}{\pi(R^2 - R_{imp}^2)} \quad 8.4.3$$

The normal stress generated by the whole bed then equals $\sigma = 364Pa$.

The stress ratio φ considered in the further breakage model is finally calculated using Equation 2.4.6, resulting in $\varphi = 0.667$, which is a similar value to the stress ratio obtained in the DEM shear cell simulations (see Chapter 6.4.3).

8.4.3.2 Particle Internal Stress Distribution

The empirical models created in Chapter 7 are used to estimate the Weibull parameters of the particle internal stress distribution with bulk parameters as input. The models are built based on the DEM shear cell simulation output presented in Chapter 6 and performed in quasi-static flow regime (see Chapter 5.5.2).

8.4.3.2.1 Weibull Scale Parameter

The scale parameter λ_p is calculated in the different zones of the studied AFD using Equation 7.3.5 as a function of particle aspect ratio α_p , normal stress applied σ (see Chapter 8.4.3.1.2), stress ratio φ (see Chapter 8.4.3.1.3) and the fitting parameters of the mathematical model in Table 7.3.6.

As expected, λ_p increases with both aspect ratio α_p and normal stress σ applied (see Figure 8.4.2). The minimum value is $94Pa$ for $\alpha_p = 1$ and $\sigma = 34.3Pa$ in the top zones {7, 8, 9}, whilst the maximum value is $74.4kPa$ for $\alpha_p = 15$ and $\sigma = 172Pa$ in the bottom zones {1, 2, 3}.

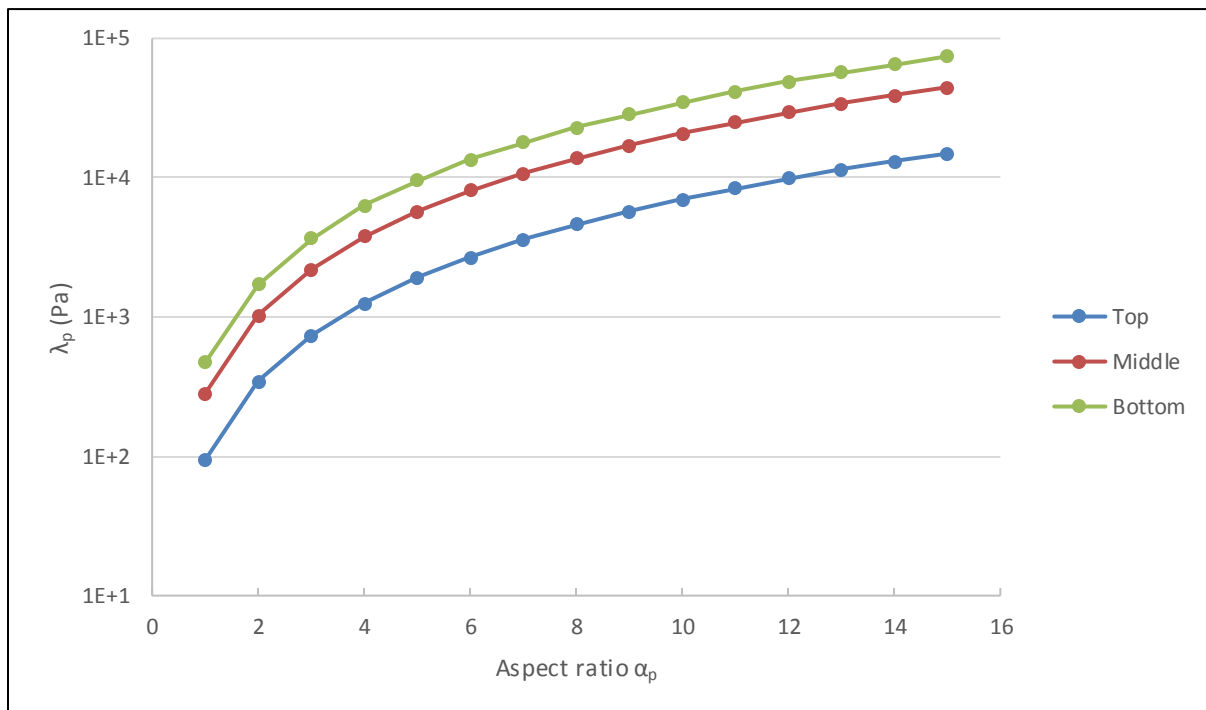


Figure 8.4.2: Weibull scale parameter λ_p for the different aspect ratios α_p and the different zones along bed height (top, middle and bottom).

8.4.3.2.2 Weibull Shape Parameter

The shape parameter k_p is calculated for the different zones of the studied AFD using Equation 7.4.3 as a function of the normal stress applied σ (see Chapter 8.4.3.1.2) and the fitting parameters in Table 7.4.6.

The value of k_p are {0.66, 0.811, 0.88} for the {*Top, Middle, Bottom*} zones.

8.4.3.2.3 Gaussian Standard Deviation

The Gaussian standard deviation σ_{dev} of the maximum stress location distribution is estimated using the built empirical model given by Equation 7.5.7 and normalised by the particle length (see Equation 7.2.15):

$$\sigma_{dev} = \frac{1}{2} \left((\ln \sigma)^e \cdot f_s \cdot (f \cdot \alpha_p + g) \right)^b \quad 8.4.4$$

Where σ_{dev} is expressed as a function of the normal stress applied σ , the particle aspect ratio α_p and the solid volume fraction $f_s = 0.24$ (see Chapter 8.4.3.1.2). The values of fitting parameters are given in Table 7.5.3 for parameter b and in Table 7.5.7 for parameters e , f and g .

σ_{dev} is inversely proportional to both aspect ratio α_p and normal stress applied σ (see Figure 8.4.3). The maximum value is 0.445 for $\alpha_p = 1$ and $\sigma = 34.3Pa$ in the top zones {7, 8, 9}, whilst the minimum value is 0.226 for $\alpha_p = 15$ and $\sigma = 172Pa$ in the bottom zones {1, 2, 3}.

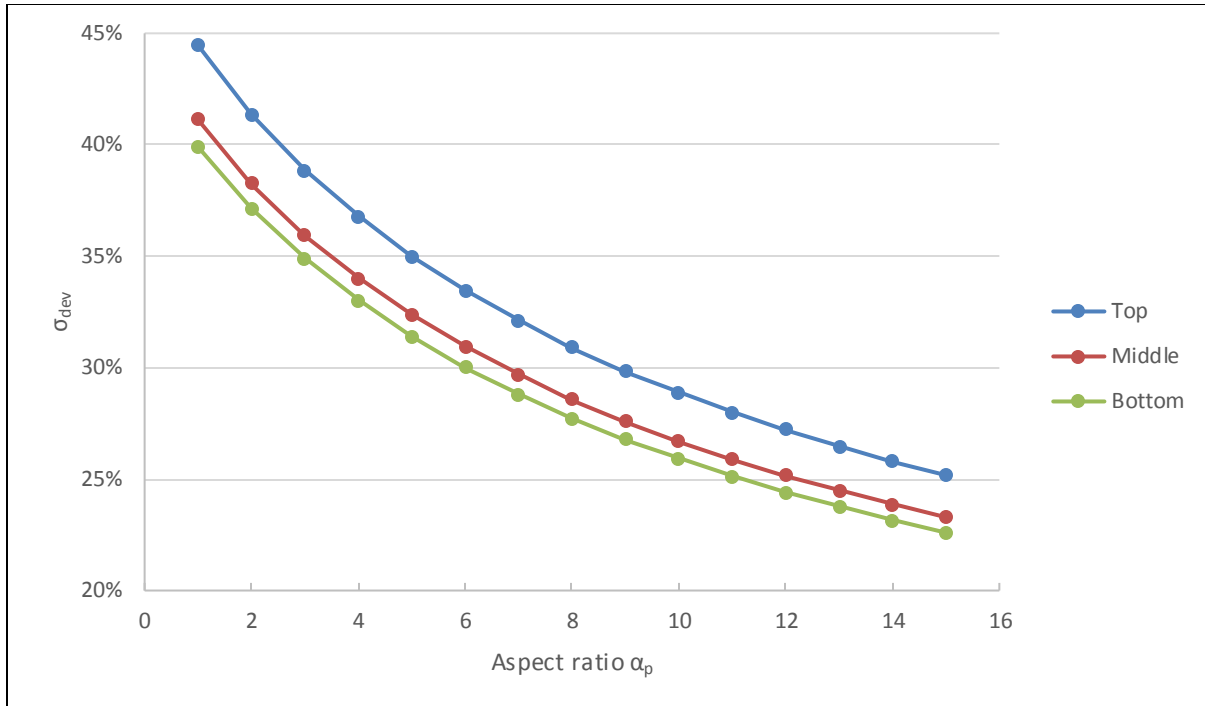


Figure 8.4.3: Gaussian standard deviation of maximum stress location for the different aspect ratios α_p and the different zones along bed height (top, middle and bottom).

8.4.3.3 Extent of Breakage

The extent of breakage B is then calculated from the experimentally measured Weibull parameters λ_b and k_b of the breakage strength distribution of the β -LGA crystals (see Chapter 8.4.2.1), and the Weibull parameters λ_p (see Chapter 8.4.3.2.1) and k_p (see Chapter 8.4.3.2.2) of the particle internal stress distribution for the different sub-groups of aspect ratio in each of the 9 zones using the created probabilistic model (see Equation 8.2.3).

The extent of breakage B increases with both aspect ratio α_p and normal stress applied σ (see Figure 8.4.4). The minimum value is $1.25E - 10$ for $\alpha_p = 1$ and $\sigma = 34.3Pa$ in the top zones $\{7, 8, 9\}$, whilst the maximum value is $2.48E - 05$ for $\alpha_p = 15$ and $\sigma = 172Pa$ in the bottom zones $\{1, 2, 3\}$.

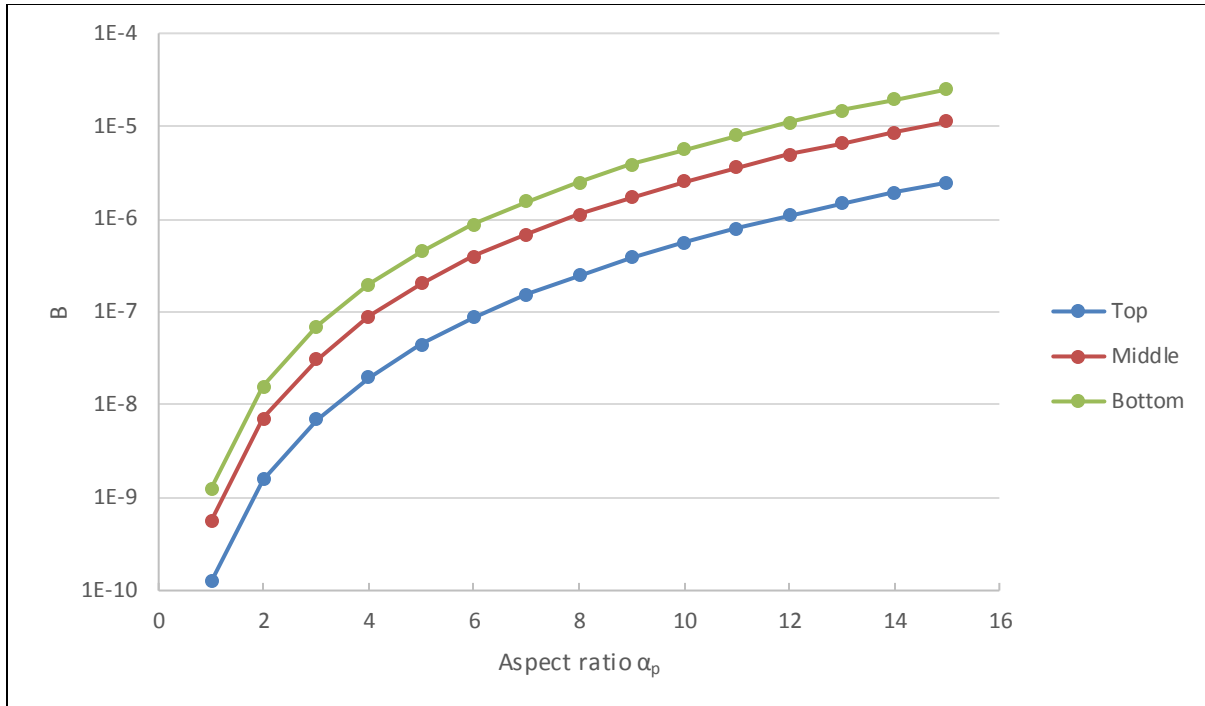


Figure 8.4.4: Extent of breakage B for the different aspect ratios α_p and the different zones along bed height (top, middle and bottom).

8.4.3.4 PARD by Impeller Rotation

The strain per impeller rotation γ_{rot} , the normal stress σ and the stress ratio φ are different for the 9 zones of the studied AFD, so the PBM is applied for each zone separately to obtain the different PARD for each unit of strain applied. The total bed PARD at I impeller rotations is then obtained by averaging the PARD of the 9 zones at the corresponding amount of strain experienced $\gamma_z(I)$ in zone z :

$$\gamma_z(I) = I \cdot \gamma_{rot,z} \quad 8.4.5$$

If the value of strain γ experienced in a zone for a given number of impeller rotations is not a natural number, an interpolation of the PARD is performed between the two closest values of γ .

8.4.4 Model Calibration

The model is calibrated against experimental AFD data by adjusting the number of events of breakage per strain N_B (see Equation 8.2.4). With a step of 10, $N_B = 220$ gives the maximum coefficient of determination $R^2 = 0.967$ (see Figure 8.4.5).

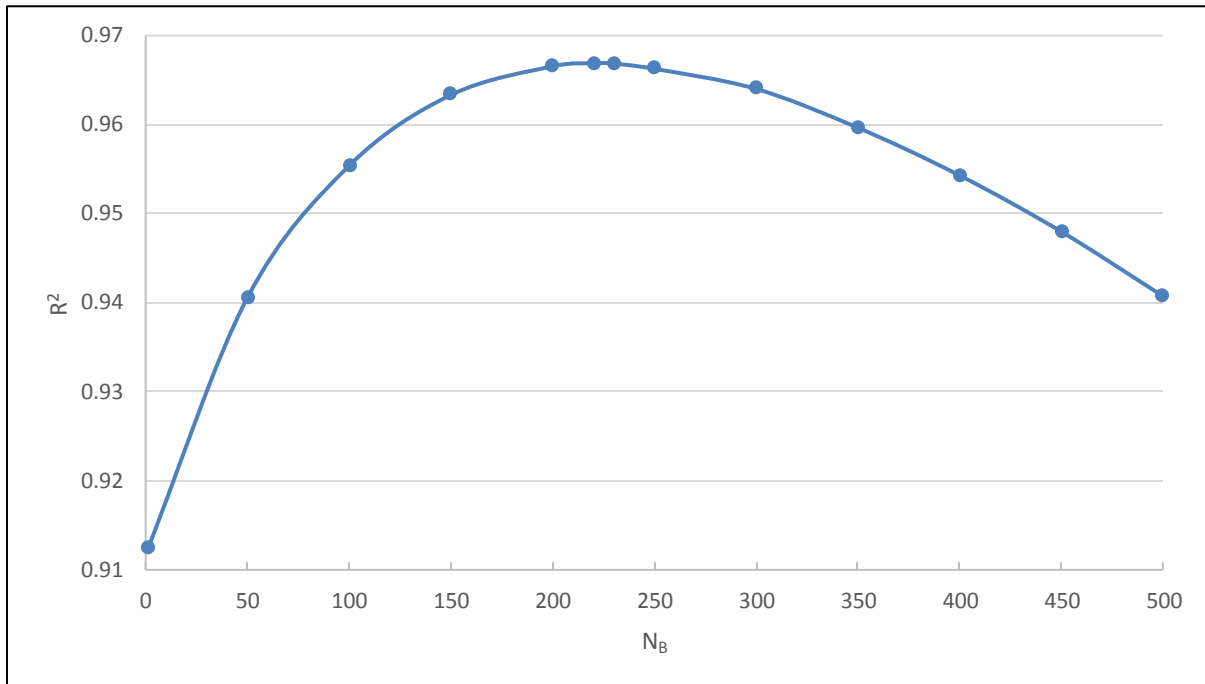


Figure 8.4.5: Coefficient of determination R^2 of the model fitting on experimental AFD data for different numbers of events of breakage per strain N_B .

The volume fraction for aspect ratio $\alpha_p = 2$ reaches a steady state in both calibrated model and experimental results (see Figure 8.4.6). Moreover, the curves of aspect ratio $\alpha_p = 1$ and $\alpha_p = 3$ cross around the same order of magnitude of impeller rotations in both cases.

Differences between the prediction and experimental results can be observed. The steady state of aspect ratio $\alpha_p = 2$ is about 54% in experiments whilst it is only 51% in the prediction. Also, the steady state of $\alpha_p = 2$ is reached earlier in experiments. Furthermore, the curves of aspect ratio $\alpha_p = 1$ and $\alpha_p = 3$ cross at a volume fraction of 20% in the model prediction, whilst it is around 17% in experiments.

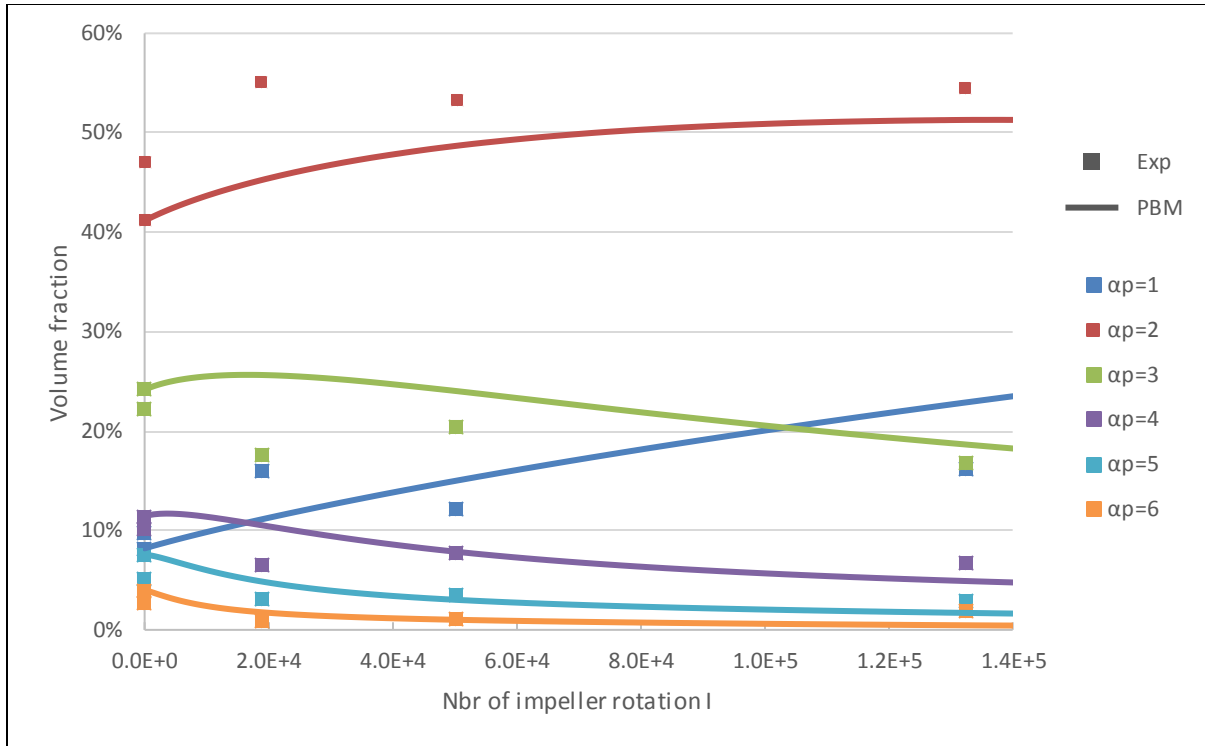


Figure 8.4.6: PARD results from calibrated model (PBM) and dry AFD experiment (Exp) for an increasing number of impeller rotations I (data are displayed for $\alpha_p \leq 6$).

Data for model-experiment comparison are in Appendix 14 & Appendix 15.

The model estimation for sub-groups with aspect ratio $\alpha_p \geq 4$ is in good agreement with experimental values, with slightly higher values for experiments. Indeed, the final volume fractions at $I \approx 140k$ impeller rotations for $\alpha_p = \{4, 5, 6\}$ are $\{6.7\%, 2.9\%, 1.9\%\}$ in experiments and $\{4.8\%, 1.6\%, 0.43\%\}$ in predictions.

8.4.5 Prediction for Process Scale-up

The model is now calibrated and can be used to predict the breakage of particles for different input parameters such as in the case of process scale-up.

The PSL Maxi Lab AFD is here considered [337] with a particle bed volume of $5L$. The cake height is $10cm$ and the cake radius is $12.6cm$. The particle bed is divided into 9 zones of equal volume in the same fashion as in Chapter 8.4.1. The radial distance of the centre of the $\{Inner, Middle, Outer\}$ zones is $\{36.4, 87.9, 115\} mm$ and the height of the centre of the $\{Bottom, Middle, Top\}$ zones is $\{16.7, 50, 83.3\} mm$.

Chapter 8: Prediction of Particle Breakage for Agitated Drying Conditions

The properties of the considered crystals are the same than the studied β -LGA sample (see Chapter 8.4.2) with the Weibull parameters of their breakage strength distribution $\lambda_b = 27.0MPa$ and $k_b = 1.95$. The initial PARD is also identical to the one measured at the beginning of the dry AFD experiment (see Appendix 14).

The amount of strain per impeller rotation γ_{rot} scales with the radial distance and is calculated for each of the 9 zones by cross-multiplication based on the values in Hare's paper [108] to correspond to the radial dimensions of the Maxi Lab in the same fashion as in Chapter (see Table 8.4.2).

Table 8.4.2: Strain per impeller rotation γ_{rot} in the 9 zones of Hare's AFD [108] and calculated for the scale-up Maxi Lab AFD.

γ_{rot}	Hare et al. 2011			Maxi Lab AFD		
Height \ Radius	Inner	Middle	Outer	Inner	Middle	Outer
Top	0.905	1.04	1.90	1.83	2.75	5.09
Middle	1.30	1.69	2.61	2.63	4.46	6.99
Bottom	1.41	1.92	2.61	2.85	5.07	6.99

The solid fraction of the bed remains unchanged at $f_s = 0.24$. Equation 8.4.1 is used to calculate the normal stress which equals $\{286, 172, 57.2\} Pa$ for the $\{Bottom, Middle, Top\}$ zones. The stress ratio is the same in all zones and the value obtained in Chapter 8.4.3.1.3 is taken with $\varphi = 0.667$.

The mathematical models used to calculate the values of the Gaussian standard deviation σ_{dev} of the maximum stress location distribution and the Weibull parameters of the particle internal stress distribution λ_p and k_p are the same than the ones used in Chapter 8.4.3.2. The calculated value of k_p are $\{0.731, 0.878, 0.944\}$ for the $\{Top, Middle, Bottom\}$ zones. The calculated values of λ_p and σ_{dev} for all aspect ratios in each zone are respectively in Appendix 17 and Appendix 18. The extent of breakage

B is calculated using the same method than in Chapter 8.4.3.3 and the values are in Appendix 19.

The predicted PARD shows that the volume fraction for particles with $\alpha_p = 2$ augments and reaches a steady state at $I = 12k$ impeller rotations before decreasing (see Figure 8.4.7). The volume fraction of particles with $\alpha_p \geq 3$ decreases before reaching a plateau after $I = 20k$ for particles with $\alpha_p \geq 4$. Whilst elongated particles are breaking, the volume fraction of particles with $\alpha_p = 1$ keeps increasing throughout agitation.

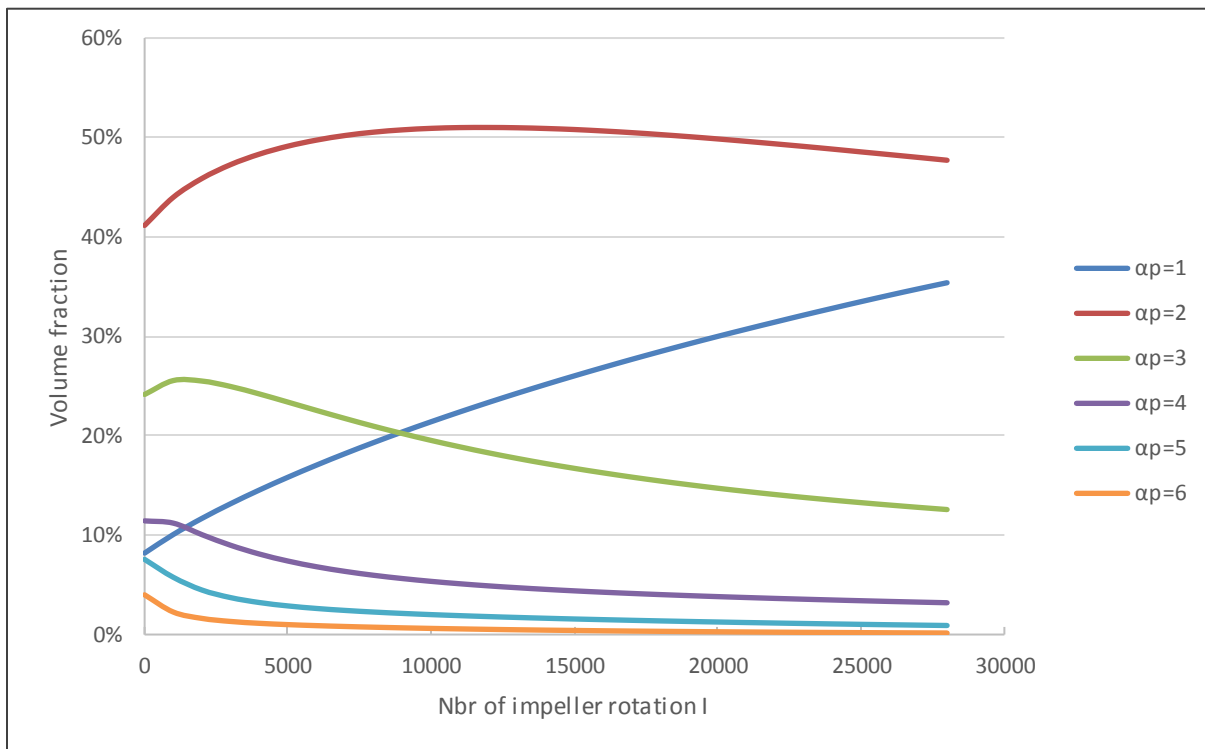


Figure 8.4.7: PARD results from the application of the calibrated model to process scale-up for an increasing number of impeller rotations I (data are displayed for $\alpha_p \leq 6$).

8.4.6 Discussion

The created PBM estimates the particle breakage in lab-scale AFD. A calibration of the breakage rate is needed and is multiplied by a factor $\times 220$ to fit the observed breakage trend in experimental data. Several assumptions have been decided at the multiple steps of the model creation which can impact the calibration factor.

8.4.6.1 Particle Properties

8.4.6.1.1 Selected Crystals for AFM Experiments

The crystals used for the assessment of the breakage strength distribution of the β -LGA sample using AFM [18] in Chapter 4 are selected for their ideal shape. Indeed, all used crystals are chosen among the biggest and most elongated ones as they are easier to handle during experiments. Due to their aspect, it is probable that these crystals haven't undergone breakage prior to the AFM experiments and have then experienced minimum fatigue compared to the other particles crystallised. Moreover, their intact aspect suggests that these crystals could be stronger than the particles casted out as no crack is visible (see Figure 4.3.5). As discussed in Chapter 4.4.2, the mean breakage strength obtained from the AFM experiments is in the order of magnitude of the reported values for this material, though slightly higher with a mean value of $29.2MPa$ in the AFM experiments (see Appendix 6) compared to $13 - 17MPa$ in MacLeod's paper [26]. Therefore, the breakage strength distribution for the β -LGA sample may have been over-estimated due to the lack of representativeness of the selected crystals regarding the particle population crystallised. A lower breakage strength would have increased the extent of breakage calculated for the different zones and aspect ratio sub-groups, which would have accelerated the breakage of particles. In fact, the extent of breakage is highly sensitive to the breakage strength distribution due to the joint density function method (see Chapter 8.2.1), and dividing the Weibull scale parameter λ_p of particle internal stress distribution by 10 multiplies the extent of breakage B by a factor $\times 89$ (see Figure 8.4.8).

If the Weibull scale parameter is selected as the average of the reported values for β -LGA crystals [26] at $\lambda_p = 15MPa$, it multiplies the extent of breakage by a factor $\times 3.2$.

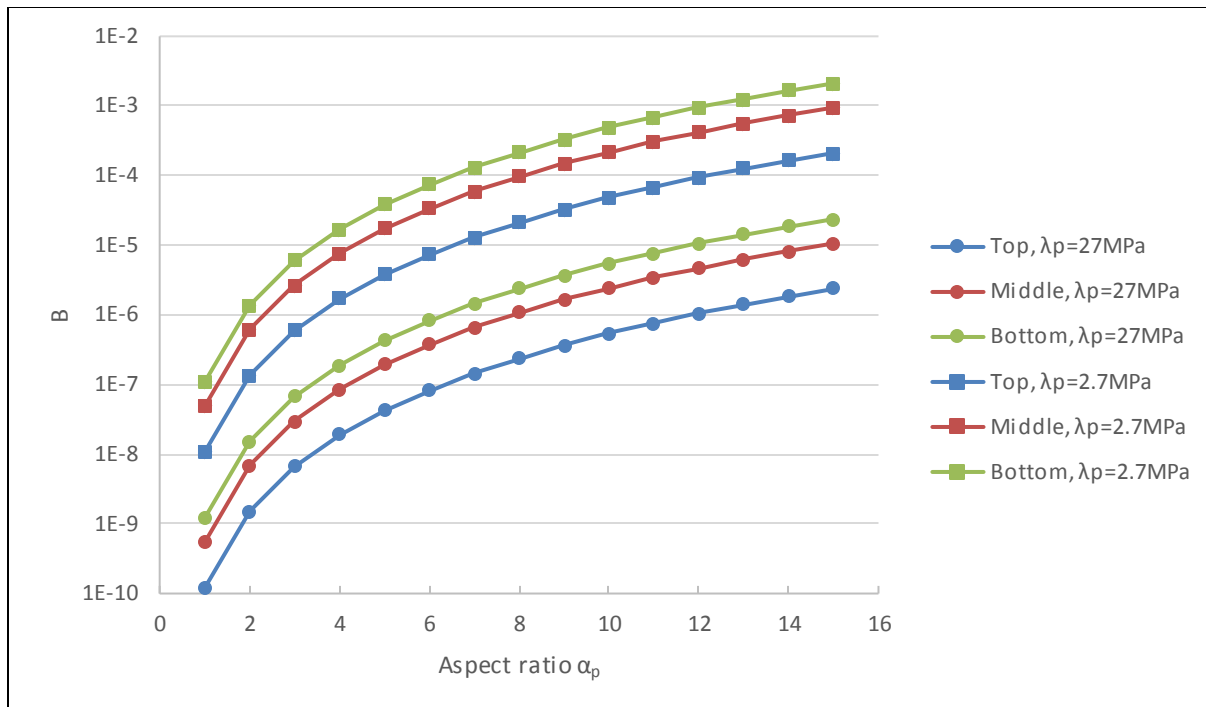


Figure 8.4.8: Extent of breakage B given by the different aspect ratios for the different zones along bed height (top, middle and bottom) and a Weibull scale parameter λ_p at 27MPa and 2.7MPa.

An alternative to the AFM single crystal breakage experiment could be to perform uniaxial compression of the β -LGA crystals both experimentally and in simulation. The extent of breakage B can be obtained by monitoring the PSD in experiments for different loads applied, and the particle internal stress distribution can be calculated in the simulations for the same conditions. Using the joint density function approach (see Chapter 8.2.1), the breakage strength distribution of the β -LGA crystals could then be determined.

8.4.6.1.2 Polydispersity

The polydispersity, observed in AFD experiments in Chapter 3, has not been investigated in the DEM shear cell simulations where the particle beds are homogeneous. Polydispersity may change the number of contacts and the contact forces on particles [211], which is likely to impact the particles internal stress. The models used in the PBM are empirical and don't account for the contact properties,

therefore this may introduce a bias in the calculation of the extent of breakage. The theoretical model built for the prediction of the Weibull scale parameter λ_p (see Equation 7.3.5) is assumed valid in polydisperse case as it accounts for both the number of contacts and the contact forces. Moreover, this model is built based on the Simple Beam Bending theory which includes a shape factor (see Chapter 5.4.1.1) and therefore is adaptive to different crystal shapes (e.g. plates, cuboids, tablets) and size.

8.4.6.1.3 Particle Size

The Hertz-Mindlin contact model [219, 220, 326] (see Chapter 5.2.1.3) used in the DEM simulations doesn't account for inter-molecular and electrostatic forces (i.e. Van der Waals, coulombic and hydrogen bonds) related to crystal surface chemistry. These forces would become significant for dry particles below a certain size (typically $< 1\mu m$) and for a strong compaction [62]. Therefore, the mathematical models built from the performed simulations may only be valid for a minimum particle size.

The analysis of correlations for experimental AFM results in Chapter 4.4.3 highlighted the fact that thinner particles have a higher breakage strength (see Table 4.4.2). Indeed, the sensitivity of a particle to mechanical stress scales with its size [16]. This size effect isn't considered in the PBM with the empirical models used and with the segmentation of particles by aspect ratio. A refined PBM prediction could be obtained by considering this size effect in the breakage kernel and analysing the particles as a PSD instead of a PARD.

8.4.6.1.4 Mechanical Properties

The extent of breakage in the PBM remains constant with agitation for each aspect ratio class: all the particles having the same aspect ratio and located in a particular zone have the same probability of breakage. Because there is a heterogeneity in the particles breakage strength, it can be argued that the weakest particles would break first, which would modify the breakage rate with applied agitation as the unbroken particles would be in average stronger than at the start of agitation. If this phenomenon

was considered in the PBM, the breakage rate would decrease with time, which is supported by AFD experiments where a steady state of PSD is achieved with sufficient work applied on the particle bed [8, 9, 28]. This isn't the case in the PBM prediction where particles would continue to break. Nevertheless, this phenomenon needs to be balanced with the fact that particles experience cracks and fatigue during agitation, which would tend to make them weaker with increasing number of impeller rotations.

The particles are also modelled as rigid in DEM shear cell simulations because their Young's modulus is significantly high (GPa) and their mechanical behaviour is reported comparable to flexible fibres with the corresponding elasticity [228]. If the particles are in the order of magnitude of $100MPa$ or lower, the use of flexible fibres in the simulations would then be more adapted and influence the particle internal stress distribution, as it is reported that the particle elastic modulus would affect the breakage rate of elongated particles [55].

8.4.6.2 Models Used in PBM

Mathematical models are created in Chapter 7 and used in the PBM for the estimation of the Weibull parameters of particle internal stress distribution (see Equation 7.3.5 and Equation 7.4.3) and the Gaussian standard deviation of the maximum stress location distribution (see Equation 8.4.4). These models are built based on the output of DEM shear cell simulations performed and analysed in Chapter 6.

The particles sheared in these simulations have a particular size and shape which have an impact on their experienced internal stress for the different mechanical environments. The clumped-sphere approach of particle modelling may have increased the number of contacts particles due to their artificially rough surfaces compared to particles made of flat surfaces [199-203]. Nevertheless, it is reported that a clumped-sphered shape creates a particle roughness that is more representative to real particles [205]. Also, a cylindrical shape of particles is assumed in the use of Euler Equation of Motion for the calculation of particle internal stress (see Chapter 5.4.1.2), whereas there is a heterogeneity of shapes in real particle bed.

The particle internal stress is calculated discretely for different locations on the particle surface using Euler Equation of Motion, and the error associated with this selection of discretisation parameters is 1.37%, which may have contributed to the error propagation.

Moreover, the accuracy of the mathematical models used in the PBM is assessed against the simulation data and there is an error associated with the use of these empirical models. The model used for the prediction of the Weibull scale parameter λ_p has an error of 9.96% whilst the error for the prediction of the Weibull shape parameter k_p is 7.07%, and 6.12% for the Gaussian standard deviation σ_{dev} .

8.4.6.3 Experimental Error

A significant difference is observed in the distribution of volume fraction by aspect ratio in the dry particle bed between the end of filtration (“*overnight filtration*”) and after 30 impeller rotations (“*1min 30rpm*”) (see Appendix 14). For example, the volume fraction of the particles with aspect ratio $\alpha_p = 2$ increases from 41% to 47%. These results, obtained from Morphologi G3 method and analysed with a dedicated script [294], suggest that an important breakage phenomenon occurred during the first 30 impeller rotations, which is not observed in the laser diffraction data (see Chapter 3.3.2). In fact, 18.8k impeller rotations are needed before observing a significant particle breakage in the laser diffraction data (see Figure 3.3.3). Thus, it is possible that this difference observed in Morphologi G3 results is due to a sampling error. If the PBM is applied with the PARD measured for “*1min 30rpm*” as initial distribution and keeping the calibrated number of events of breakage per strain $N_B = 220$, the volume fraction for the different aspect ratio sub-groups compares better with the experimental results (see Figure 8.4.9) with a higher coefficient of determination $R^2 = 0.982$.

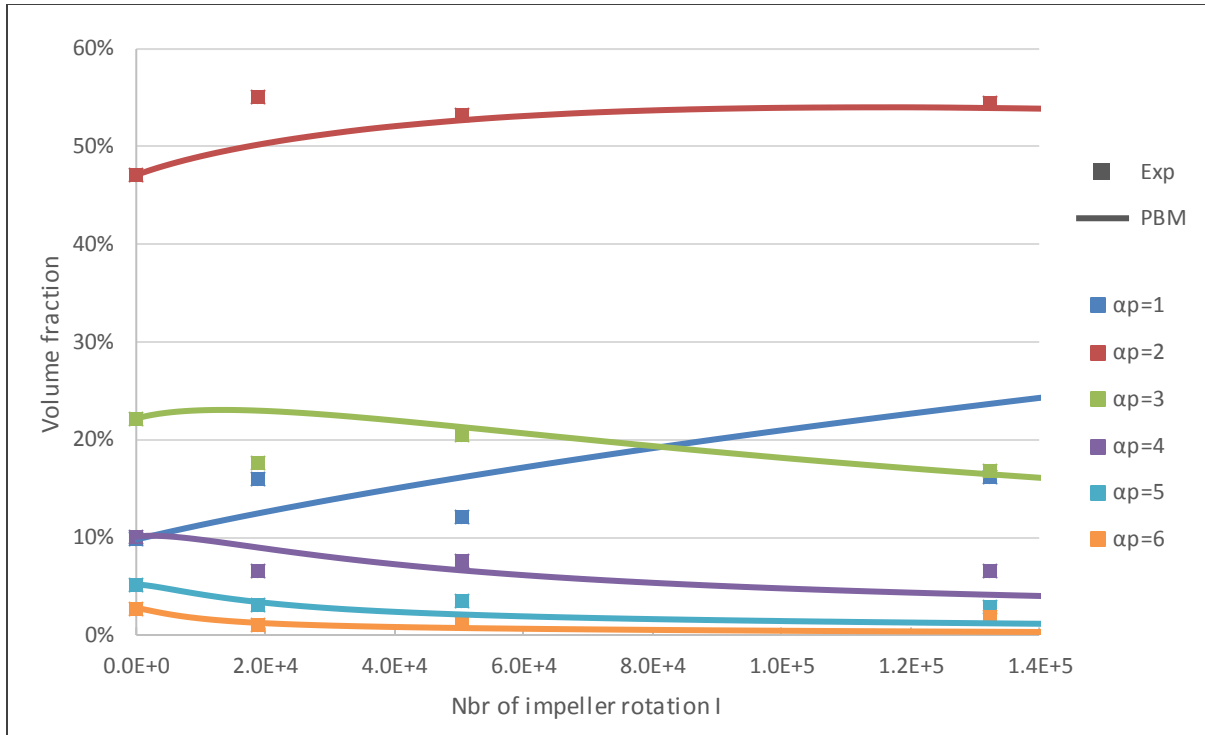


Figure 8.4.9: PARD results from calibrated model (PBM) and dry AFD experiment (Exp) for an increasing number of impeller rotation I (data are displayed for $\alpha_p \leq 6$). The initial PARD is taken as the one measured at $I = 30$. Data for model-experiment comparison are in Appendix 14 & Appendix 16.

Also, the segregation of particles by aspect ratio from Morphologi G3 data may have amplified the error of volume fractions due to the reduced number of bins: 15 in the PARD compared to a 31×31 cell grid PSD.

A possible solution is to perform several Morphologi G3 measurements at each stage of agitation to account for the sampling error. Ideally, several agitation experiments are also needed to assess the experimental error.

Moreover, the particles used in AFM and AFD experiments are both produced using the same crystallisation method, however they are not taken from the same crystallisation batch. Here, the assessment of a possible experimental error in the crystallisation process might also be needed.

8.4.6.4 Breakage Mechanisms

There are two main particle breakage mechanisms in quasi-static flow regime: fragmentation where a particle is broken into big subsequent particles and attrition when small fragments called fines are chopped from the primary particle [50]. As observed in the AFD experiments in Chapter 3, the agitation of dry particles promotes both fragmentation and attrition, whereas particles almost solely break from fragmentation in wet bed. This is due to the frictional contacts and gripping between particles in the dry case, whilst the moisture content present at inter-particulate contacts in the form of liquid bridges acts as a lubricant [26].

In the created PBM, the breakage of particles is an ideal fragmentation where the cleavage plane is normal to the particles neutral axis. The attrition isn't considered in the PBM which would affect both the final PSD and the breakage rate for the different sub-groups of aspect ratio. Moreover, this PBM doesn't compute the breakage of particles with an aspect ratio $\alpha_p = 1$ as the models used in the PBM are built to predict the breakage of elongated particles. The particles with $\alpha_p = 1$ are expected to break in reality and create fragments that would have different values of aspect ratio. This phenomenon is not included in the PBM which can explain the over-estimation of the volume fraction for $\alpha_p = 1$ and under-estimation for $\alpha_p = 2$ towards the end of agitation (see Figure 8.4.6). The analysis of PSD data from AFD experiments in Chapter 3.3.4 allowed to quantify the fines with around 3% volume fraction (see Figure 3.3.8), which is typically reported in DEM agitated dryer using breakage kernels [191].

As a solution, an attrition model such as the one presented in Hare's paper [108] could be implemented in the PBM to account for this breakage mechanism present in the agitation of dry particle bed. Considering attrition into the model is expected to increase the volume fraction of particles with aspect ratio $\alpha_p \in [1,2]$ as it is the common shape of fines.

8.4.6.5 Mechanical Environment

The normal and shear stresses used as PBM input are both determined by first approximation approach. The hydrostatic pressure is taken as the normal stress and

calculated from the weight of the particle bed at the different zone depth (see Chapter 8.4.3.1.2). The average shear stress is obtained from the measured torque and the particle bed volume (see Chapter 8.4.3.1.3) using the Darelus equation [152]. The stress ratio is then determined using Equation 2.4.6.

It has been demonstrated that the agitation promoted by the rotation of the impeller varies the stresses in the different zones of the bed depending on the angular position of the impeller [108]. Besides, both strain rate and stresses experienced by particles in zones increase in the vicinity of the impeller. Therefore, the stresses taken as PBM input may be under-estimated regarding the level of stress particles experience when most strain is applied i.e. when breakage occurs predominantly according to the model (see Chapter 8.2.2). Also, it is expected that the geometries of the impeller and the AFD have an impact on both stresses and strain in the different zones. There is no vertical movement of the impeller during agitation in the performed experiments (see Chapter 3) and this functionality of AFD can have an influence on particle breakage as it promotes shear stress in different zones of the bed.

A possible solution is to obtain the stresses and strain in the different zones for different angular rotation of the impeller from simulations like in Hare's paper [108] and apply the created PBM with fractions of impeller rotation as calculation step rather than for a full rotation. This method could increase the accuracy of the model but will require more computational power.

8.4.6.6 Particle Flow

When submitted to gravity, particles in an agitated bed segregate mechanically by size with the smallest particles migrating towards the bottom of the bed and the biggest ones towards its surface [191]. The flow of particles between the different zones aren't included in the created PBM which operates particle breakage and PARD calculation in zones as closed systems.

If a particle flow model was implemented in the PBM to account for the segregation of particles by size, the fines created would be transferred deeper in the bed to the zones with a higher normal stress. In opposite, the most elongated particles (usually among

the biggest) would be transferred the higher zones with a lower normal stress. This phenomenon would then reduce the breakage of high aspect ratio particles whilst accelerating the breakage of shorter ones. Also, both particle breakage and flow are expected to increase the solid fraction within the bed, particularly in the deeper zones, which would affect the PBM predictions as it is taken as model input.

8.4.6.7 Future Work

The created PBM predicts the distribution of volume fraction by particles aspect ratio regardless of their size. Indeed, the particles are assumed to break in the same fashion if they have the same elongation. As a future work, the PBM could be applied using the PSD grid obtained with Morphologi G3 as input to account for the particle size. If, in addition, an attrition model is implemented into the PBM, the breakage of particles could be computed along both particle width and length, which would allow a refined prediction of PSD with agitation and would reflect both aspect ratio and size reduction with particle breakage.

Also, the predictive models created in Chapter 7 are built from the analysis of DEM shear cell simulation output in Chapter 6 which are performed on dry particles only. The influence of moisture content is not investigated in this study and is a possible future work. Nevertheless, it can be assumed that the lubrication created from liquid bridges at inter-particle contacts would significantly reduce the shear stress and thus the stress ratio during agitation, as it is confirmed by an important decrease of the torque measured for AFD experiments on wet bed [1]. The addition of moisture content also increases the weight of the bed and thus the normal stress on particles calculated from the hydrostatic pressure. The actual PBM could then be used accordingly with the modified normal stress and stress ratio, and model prediction can be compared with experimental measurements.

8.5 Conclusion

A probabilistic breakage kernel is created and calculates the extent of breakage of particles for different particle properties and mechanical environments. This breakage kernel is implemented into a population balance model (PBM) to estimate the particle size distribution within an agitated filter dryer (AFD) during the agitation of elongated dry particles. The model is calibrated against experimental results and the impact of input parameters on the accuracy of the model is discussed. The calibrated model is then used for the prediction of the breakage of the same particles for the scale-up of the drying process. This method can provide insights to process operators for the selection of drying equipment to minimise particle breakage phenomenon in the manufacturing of an API.

9 Conclusions and Future Work

An innovative method combining experimental work, DEM simulations and mathematical modelling is presented to predict the particle size distribution of crystals being agitated in a dry bed.

Glutamic acid is the studied material and is crystallised into its elongated form (β -LGA). The breakage of these crystals within a lab-scale agitated filter dryer (AFD) is examined by monitoring the particle size distribution (PSD) throughout agitation for both dry and wet cases. The use of two-dimensional PSD measurement (Morphologi G3) allows the observation of the reduction of both particle size and elongation. Both particle attrition and fragmentation are detected in the dry bed whilst particles almost solely break by fragmentation in the wet case. The quasi-absence of attrition in the wet case is due to the lubrication effect caused by the presence of liquid bridges at inter-particulate contacts.

The breakage strength of a sample of β -LGA crystals is assessed using a novel published method [18] involving atomic force microscopy (AFM). The crystals are glued on a metallic support as a cantilever and the AFM probe applies an end load on the crystals individually until they break. The Euler-Bernoulli Beam theory is used to calculate the breakage strength of each crystal and a breakage strength distribution is obtained. This distribution follows a Weibull model and the two fitting parameters are determined by regression with the scale parameter $\lambda_b = 27.0MPa$ and the shape parameter $k_b = 1.95$.

A shear cell is built using distinct element modelling (DEM) and the behaviour of a sheared dry particle bed is observed in simulations. The shear cell is populated with 2000 elongated particles and periodic boundaries are used in two axes to simulate an infinite shear band. An inductive study is performed to optimise the simulation setup ensuring that the particles are sheared in a quasi-static flow regime, that the strain is effective on the whole particle bed, and that the normal stress remains constant throughout shearing. The particles touching the walls have a different behaviour from the rest of the bed and their results are not considered for further analysis. An attempt to reduce the time required to perform a simulation is made by scaling down the particles Young's modulus, however it disrupted the bed behaviour in an excessive

way. The two methods reported for the calculation of the particles internal stress are used and it is concluded that the Euler Equation of Motion is preferable to the Simple Beam Bending for the sheared particles in the performed simulations.

DEM shear cell simulations are performed for different particle shapes and mechanical environments in monodisperse bed and the internal stress is determined for each particle using the Euler Equation of Motion. An inductive study is undertaken where the aspect ratio of particles, modelled using clumped-sphere approach, and the normal stress is varied in both uniaxial compression and shearing phase. An analysis of the result data allows to identify correlations between the key variables describing the particle bed behaviour and explanations are brought based on principles of mechanical theory to support the observations. The distribution of particles internal stress within the shear cell follows a Weibull model and the fitting parameters are obtained for the different simulations. The scale parameter λ_p is impacted by both the number of contacts and contact forces, resulting in λ_p increasing with both particle aspect ratio and normal stress applied. The shape parameter k_p increases with aspect ratio and is inversely proportional to the normal stress applied. The distribution of maximum stress location on the particles neutral axis is calculated and follows a Gaussian model. The mean value of the model is half of the particle length, and the standard deviation σ_{dev} increases with the number of contacts on the particle and is inversely proportional to the particle aspect ratio.

Mathematical models are built for the prediction of the Weibull parameters of the particle internal stress distribution (λ_p and k_p) and the Gaussian standard deviation of maximum stress location on particle neutral axis (σ_{dev}). A theoretical model predicting λ_p is created based on the Simple Beam Bending equation and calibrated to fit the output data of the performed DEM shear cell simulations. A series of empirical models are also created to predict these parameters for different data inputs: some models require simulation data and are more accurate, whilst other models simply require bulk parameters and are less precise. These various models are designed for different use and allow to avoid the implementation of the resource-consuming Euler Equation of Motion. It is therefore possible to estimate the internal stress experienced by dry particles in a sheared bed directly without the need to perform simulations or using

coding to implement calculation methods. Overall, 12 models are built having a mean error ranging from 0.68% to 10.8%.

Finally, a probabilistic breakage kernel is built by calculating the joint density function of the particle internal stress distribution and the breakage strength distribution of the studied particles. The kernel is implemented into a designed population balance model (PBM) to predict the breakage of β -LGA crystals during dry agitation in a lab-scale AFD. The PBM computes the breakage of particles by fragmentation in 9 zones of a particle bed in an AFD having different radial distance and height. The Weibull parameters (λ_b and k_b) obtained from the AFM experiments on β -LGA crystals are selected for the breakage strength distribution and the created empirical mathematical models are used to obtain the Weibull parameters (λ_p and k_p) of the particle internal stress distribution for the different particle aspect ratios, normal stress, and stress ratio in the different zones. The location of breakage on a particle is determined in a probabilistic fashion using the created empirical mathematical model to obtain the Gaussian standard deviation (σ_{dev}) from the particle aspect ratio, normal stress, and solid volume fraction in the different zones. The breakage rate is expressed as a function of strain experienced by particles for an impeller rotation in each of the zones. The PBM estimates the PARD, distribution of volume fraction for the different particle aspect ratios, with increasing number of impeller rotation. The model is then calibrated against experimental results by varying the value of the number of breakage event per strain (N_B). The impact of the different input parameters on the model calibration are investigated, and it is concluded that the model is highly sensitive to its inputs (e.g. particle properties, mechanical environment) and the experimental results used for calibration. As a final step, the calibrated model is used to predict the breakage of the same β -LGA crystals for the scale-up of agitation.

In conclusion, a novel method is presented to predict the PSD during the agitation of a dry bed, and the created model is available to use by researchers and industrials to predict the breakage of particles during the drying process for any equipment and particle properties. This model could be used after calibration to predict particle breakage for the process scale-up in industry, giving insights to process operators for the selection of drying equipment to minimise the particle breakage phenomenon.

Chapter 9: Conclusions and Future Work

Possible future work is the inclusion of an attrition model to the PBM to account for the creation of fines, especially in dry particle beds. Also, DEM shear cell simulations can be performed with a different contact model to mimic the lubrication and adhesion effects of liquid bridges. The mathematical models created can then be refined to account for the moisture content in the bed allowing the PBM to compute the breakage of particles during the drying process with varying level of wetness.

10 References

1. Remy, B., et al., *Scale-up of agitated drying: Effect of shear stress and hydrostatic pressure on active pharmaceutical ingredient powder properties*. AIChE Journal, 2015. **61**(2): p. 407-418.
2. Iritani, E., H. Nagaoka, and N. Katagiri, *Determination of filtration characteristics of yeast suspension based upon multistage reduction in cake surface area under step-up pressure conditions*. Separation purification technology, 2008. **63**(2): p. 379-385.
3. Raha, S. and P.C. Kapur, *Kinetics and optimization of pressure filtration of dilute slurries by stage-wise batch tests*. International Journal of Mineral Processing, 2004. **74**(1-4): p. 169-176.
4. Hamilton, P., et al., *Investigation of factors affecting isolation of needle-shaped particles in a vacuum-agitated filter drier through non-invasive measurements by Raman spectrometry*. Chemical Engineering Science, 2013. **101**: p. 878-885.
5. Rognon, P.G., et al., *Dense flows of cohesive granular materials*. Journal of Fluid Mechanics, 2008. **596**: p. 21-47.
6. Pierrat, P., D.K. Agrawal, and H.S. Caram, *Effect of moisture on the yield locus of granular materials: theory of shift*. Powder Technology, 1998. **99**(3): p. 220-227.
7. Pierrat, P. and H.S. Caram, *Tensile strength of wet granula materials*. Powder Technology, 1997. **91**(2): p. 83-93.
8. Lekhal, A., et al., *Impact of agitated drying on crystal morphology: KCl–water system*. Powder technology, 2003. **132**(2-3): p. 119-130.
9. Lekhal, A., et al., *The effect of agitated drying on the morphology of l-threonine (needle-like) crystals*. International journal of pharmaceutics, 2004. **270**(1-2): p. 263-277.
10. Paul, E.L., H.-H. Tung, and M. Midler, *Organic crystallization processes*. Powder technology, 2005. **150**(2): p. 133-143.
11. Ansel, H.C., L.V. Allen, and N.G. Popovich, *Dosage form design: pharmaceutical and formulation considerations*, in *Ansel's Pharmaceutical Dosage Forms and Drug Delivery Systems (9th edition)*, D.B. Troy, Editor. 2005, Wolters Kluwer: Baltimore.
12. Kim, S., et al., *Control of the particle properties of a drug substance by crystallization engineering and the effect on drug product formulation*. Organic process research development, 2005. **9**(6): p. 894-901.

Chapter 10: References

13. Boton, M., et al., *Quasistatic rheology and microstructural description of sheared granular materials composed of platy particles*. Physical Review E, 2013. **87**(3): p. 032206.
14. Guo, Y., et al., *Granular shear flows of flat disks and elongated rods without and with friction*. Physics of Fluids, 2013. **25**(6): p. 063304.
15. Adamson, J., et al., *Development of suitable plant-scale drying conditions that prevent API agglomeration and dehydration*. Organic Process Research Development, 2016. **20**(1): p. 51-58.
16. Lamberto, D.J., et al., *Laboratory methods for assessing API sensitivity to mechanical stress during agitated drying*. Chemical engineering science, 2011. **66**(17): p. 3868-3875.
17. Kom, P.K., W. Cook, and E. Kougoulos, *Impact of laboratory vacuum contact drying on material drying rates and physical properties*. Organic Process Research & Development, 2011. **15**(2): p. 360-366.
18. Hallac, F.S., et al., *Micro-mechanical properties of single high aspect ratio crystals*. CrystEngComm, 2019. **21**(38): p. 5738-5748.
19. Cho, G.-C., J. Dodds, and J.C. Santamarina, *Closure to "Particle Shape Effects on Packing Density, Stiffness, and Strength: Natural and Crushed Sands" by Gye-Chun Cho, Jake Dodds, and J. Carlos Santamarina*. Journal of geotechnical geoenvironmental engineering, 2007. **133**(11): p. 1474-1474.
20. Guises, R., et al., *Granular packing: numerical simulation and the characterisation of the effect of particle shape*. Granular Matter, 2009. **11**(5): p. 281-292.
21. Matsushima, T. and C.S. Chang, *Quantitative evaluation of the effect of irregularly shaped particles in sheared granular assemblies*. Granular matter, 2011. **13**(3): p. 269-276.
22. Cundall, P.A. *A computer model for simulating progressive, large-scale movement in blocky rock system*. in *Proceedings of the International Symposium on Rock Mechanics*, 1971. 1971.
23. Pena, A., R. Garcia-Rojo, and H.J. Herrmann, *Influence of particle shape on sheared dense granular media*. Granular Matter, 2007. **9**(3-4): p. 279-291.
24. Katagiri, J., T. Matsushima, and Y. Yamada, *Simple shear simulation of 3D irregularly-shaped particles by image-based DEM*. Granular Matter, 2010. **12**(5): p. 491-497.
25. Wilson, D., et al., *Particle engineering of needle shaped crystals by wet milling and temperature cycling: Optimisation for roller compaction*. Powder technology, 2018. **339**: p. 641-650.
26. MacLeod, C.S. and F.L. Muller, *On the fracture of pharmaceutical needle-shaped crystals during pressure filtration: case studies and mechanistic*

Chapter 10: References

- understanding*. Organic Process Research & Development, 2012. **16**(3): p. 425-434.
27. Halme, A., et al., *Utilizing crystal structures for predicting impact of mechanical and surface properties on particle fracture*. Crystal Growth Design, 2019. **19**(7): p. 3670-3680.
 28. Papageorgiou, C.D., et al., *Development of a novel screening methodology for the assessment of the risk of particle size attrition during agitated drying*. Organic Process Research Development, 2020. **24**(2): p. 242-254.
 29. Kelly, R.N. and J. Kazanjian, *Commerical reference shape standards use in the study of particle shape effect on laser diffraction particle size analysis*. AAPS PharmSciTech, 2006. **7**(2): p. E126-E137.
 30. Erdoğan, S., et al., *Micrometer-scale 3-D shape characterization of eight cements: Particle shape and cement chemistry, and the effect of particle shape on laser diffraction particle size measurement*. Cement Concrete Research, 2010. **40**(5): p. 731-739.
 31. Eshel, G., et al., *Critical evaluation of the use of laser diffraction for particle-size distribution analysis*. Soil Science Society of America Journal, 2004. **68**(3): p. 736-743.
 32. Roberts, R., R. Payne, and R. Rowe, *Mechanical property predictions for polymorphs of sulphathiazole and carbamazepine*. European journal of pharmaceutical sciences, 2000. **9**(3): p. 277-283.
 33. Roberts, R. and R. Rowe, *Relationships between the modulus of elasticity and tensile strength for pharmaceutical drugs and excipients*. Journal of pharmacy & pharmacology, 1999. **51**(9): p. 975-977.
 34. Roberts, R., R. Rowe, and P. York, *The relationship between Young's modulus of elasticity of organic solids and their molecular structure*. Powder Technology, 1991. **65**(1-3): p. 139-146.
 35. Oliver, W.C. and G.M. Pharr, *An improved technique for determining hardness and elastic modulus using load and displacement sensing indentation experiments*. Journal of materials research, 1992. **7**(6): p. 1564-1583.
 36. Pollock, H.M., D. Maugis, and M. Barquins, *Characterization of submicrometre surface layers by indentation*. Microindentation Techniques in Materials Science Engineering, 1986. **889**: p. 47-71.
 37. Ennis, B.J. and G. Sunshine, *On wear as a mechanism of granule attrition*. Tribology international, 1993. **26**(5): p. 319-327.
 38. Timoshenko, S.P., *History of Strength of Materials*. 1953: Dover Publications.
 39. Simmons, G. and H. Wang, *A Handbook of Single Crystal Elastic Constants and Calculated Aggregate Properties*. 1971, MIT Press Cambridge.

40. Kitaigorodsky, A., *Molecular crystals and molecules*. Vol. 29. 2012: Elsevier.
41. Sanquer, M. and C. Ecolivet. *Dynamics of Molecular Crystals*. in *41st International Meeting of the Société Française de Chimie, Division de Chimie Physique*. 1987. Elsevier Science Limited.
42. Wang, C. and C.C. Sun, *The landscape of mechanical properties of molecular crystals*. *CrystEngComm*, 2020. **22**(7): p. 1149-1153.
43. Payne, R.S., et al., *The mechanical properties of two forms of primidone predicted from their crystal structures*. *International journal of pharmaceutics*, 1996. **145**(1-2): p. 165-173.
44. Broo, A. and S.O. Nilsson Lill, *Transferable force field for crystal structure predictions, investigation of performance and exploration of different rescoring strategies using DFT-D methods*. *Acta Crystallographica Section B: Structural Science, Crystal Engineering Materials*, 2016. **72**(4): p. 460-476.
45. Janković, B., et al., *Quantification and modeling of nanomechanical properties of chlorpropamide α , β , and γ conformational polymorphs*. *European Journal of Pharmaceutical Sciences*, 2017. **110**: p. 109-116.
46. Roberts, R., R. Rowe, and P. York, *The relationship between the fracture properties, tensile strength and critical stress intensity factor of organic solids and their molecular structure*. *International journal of pharmaceutics*, 1995. **125**(1): p. 157-162.
47. Weibull, W., *A statistical distribution function of wide applicability*. *Journal of applied mechanics*, 1951. **103**(730): p. 293-297.
48. Vogel, L. and W. Peukert, *Breakage behaviour of different materials—construction of a mastercurve for the breakage probability*. *Powder Technology*, 2003. **129**(1-3): p. 101-110.
49. Namazu, T., Y. Isono, and T. Tanaka, *Evaluation of size effect on mechanical properties of single crystal silicon by nanoscale bending test using AFM*. *Journal of Microelectromechanical Systems*, 2000. **9**(4): p. 450-459.
50. Tavares, L.M., *Chapter 1 Breakage of Single Particles: Quasi-Static*, in *Handbook of Powder Technology*. 2007. p. 3-68.
51. Boerefijn, R., M. Ghadiri, and P. Salatino, *Attrition in fluidised beds*, in *Handbook of Powder Technology*. 2007. p. 1019-1053.
52. Ho, R., et al., *Effect of milling on particle shape and surface energy heterogeneity of needle-shaped crystals*. *Pharmaceutical research*, 2012. **29**(10): p. 2806-2816.
53. de Vegt, O.M., *Jet milling from a particle perspective: predicting particle fracture based on mechanical material properties*. 2007.

Chapter 10: References

54. Shariare, M.H., et al., *Influence of solvent on the morphology and subsequent comminution of ibuprofen crystals by air jet milling*. Journal of Pharmaceutical Sciences, 2012. **101**(3): p. 1108-1119.
55. Hua, X., et al., *The internal loads, moments, and stresses in rod-like particles in a low-speed, vertical axis mixer*. Chemical Engineering Science, 2015. **134**: p. 581-598.
56. Bonakdar, T., et al., *A method for grindability testing using the Scirocco disperser*. International Journal of Pharmaceutics, 2016. **501**(1-2): p. 65-74.
57. Ghadiri, M., *Effect of shear strain rate on attrition of particulate solids in a shear cell*. Powder grains' 97, 1997: p. 127-130.
58. Ghadiri, M. and Z. Zhang, *Impact attrition of particulate solids. Part 1: A theoretical model of chipping*. Chemical Engineering Science, 2002. **57**(17): p. 3659-3669.
59. Gere, J.M., *Mechanics of Materials*. 6th Edition ed, ed. B.C.-T. Learning. 2004, Belmont, CA.
60. Subero, J. and M. Ghadiri, *Breakage patterns of agglomerates*. Powder Technology, 2001. **120**(3): p. 232-243.
61. Huang, R., et al., *Elastic Self-Doping Organic Single Crystals Exhibiting Flexible Optical Waveguide and Amplified Spontaneous Emission*. Advanced Materials, 2018. **30**(21): p. 1800814.
62. Papadakis, S.E. and R.E. Bahu, *The sticky issues of drying*. Drying Technology, 1992. **10**(4): p. 817-837.
63. Rumpf, H., in *Agglomeration*, Interscience, Editor. 1962: New York, USA.
64. Zolotarev, P.N. and N.A. Nekrasova, *On the Influence of Solvent Properties on the Structural Characteristics of Molecular Crystal Polymorphs*. J Crystal Growth Design, 2020. **20**(11): p. 7152-7162.
65. Keey, R.B., *Drying of Loose and Particulate Materials*, H. Publishing, Editor. 1992: New York, US.
66. Iveson, S.M., et al., *Nucleation, growth and breakage phenomena in agitated wet granulation processes: a review*. Powder technology, 2001. **117**(1-2): p. 3-39.
67. Begat, P., et al., *The cohesive-adhesive balances in dry powder inhaler formulations I: direct quantification by atomic force microscopy*. Pharmaceutical research, 2004. **21**(9): p. 1591-1597.
68. Willett, C.D., et al., *Capillary bridges between two spherical bodies*. Langmuir, 2000. **16**(24): p. 9396-9405.

Chapter 10: References

69. Fisher, R.A., *On the capillary forces in an ideal soil; correction of formulae given by W. B. Haines*. The Journal of Agricultural Science, 1926. **16**: p. 492-505.
70. Orr, F., L. Scriven, and A.P. Rivas, *Pendular rings between solids: meniscus properties and capillary force*. Journal of Fluid Mechanics, 1975. **67**(4): p. 723-742.
71. Simons, S. and X. Pepin, *Hardness of moist agglomerates in relation to interparticle friction, capillary and viscous forces*. Powder technology, 2003. **138**(1): p. 57-62.
72. Muguruma, Y., T. Tanaka, and Y. Tsuji, *Numerical simulation of particulate flow with liquid bridge between particles (simulation of centrifugal tumbling granulator)*. Powder Technology, 2000. **109**(1-3): p. 49-57.
73. Salman, A.D., M.J. Hounslow, and S.J.P. K, *Handbook of Powder Technology. Granulation*. Vol. 11. 2007.
74. Mason, G. and W. Clark, *Liquid bridges between spheres*. Chemical Engineering Science, 1965. **20**(10): p. 859-866.
75. Simons, S. and R. Fairbrother, *Direct observations of liquid binder-particle interactions: the role of wetting behaviour in agglomerate growth*. Powder Technology, 2000. **110**(1-2): p. 44-58.
76. Mazzone, D., G. Tardos, and R. Pfeffer, *The behavior of liquid bridges between two relatively moving particles*. Powder technology, 1987. **51**(1): p. 71-83.
77. Seville, J., C. Willett, and P. Knight, *Interparticle forces in fluidisation: a review*. Powder Technology, 2000. **113**(3): p. 261-268.
78. Schubert, H., *Kapillarität in porösen feststoffsystemen*, ed. Heidelberg. 1982, Berlin, Germany: Springer.
79. Lian, G., C. Thornton, and M.J. Adams, *A theoretical study of the liquid bridge forces between two rigid spherical bodies*. Journal of colloid interface science, 1993. **161**(1): p. 138-147.
80. Remy, B., J.G. Khinast, and B.J. Glasser, *Wet granular flows in a bladed mixer: experiments and simulations of monodisperse spheres*. AIChE Journal, 2012. **58**(11): p. 3354-3369.
81. McCarthy, J., *Micro-modeling of cohesive mixing processes*. Powder Technology, 2003. **138**(1): p. 63-67.
82. Boulogne, F., et al., *Mechanical tuning of the evaporation rate of liquid on crossed fibers*. Langmuir, 2015. **31**(10): p. 3094-3100.
83. Sauret, A., et al., *Wetting of crossed fibers: Multiple steady states and symmetry breaking*. EPL (Europhysics Letters), 2014. **105**(5): p. 56006.

Chapter 10: References

84. Sauret, A., et al., *Wetting morphologies on randomly oriented fibers*. The European Physical Journal E, 2015. **38**(6): p. 1-9.
85. Sauret, A., et al., *Wetting morphologies on an array of fibers of different radii*. Soft Matter, 2015. **11**(20): p. 4034-4040.
86. Thornton, C., *Powders & Grains* 93. 1993: AA Balkema.
87. De Bisschop, F.R. and W.J. Rigole, *A physical model for liquid capillary bridges between adsorptive solid spheres: the nodoid of plateau*. Journal of Colloid Interface Science, 1982. **88**(1): p. 117-128.
88. Frenkel, J., *Viscous flow of crystalline bodies under the action of surface tension*. J. Phys. (USSR), 1945. **9**: p. 385.
89. Ennis, B.J., G. Tardos, and R. Pfeffer, *A microlevel-based characterization of granulation phenomena*. Powder Technology, 1991. **65**(1-3): p. 257-272.
90. Keningley, S., P. Knight, and A. Marson, *An investigation into the effects of binder viscosity on agglomeration behaviour*. Powder Technology, 1997. **91**(2): p. 95-103.
91. Vialatte, L., *PhD Thesis*. 1998, Universite de Technologie de Compiègne.
92. Schæfer, T. and C. Mathiesen, *Melt pelletization in a high shear mixer. VIII. Effects of binder viscosity*. International Journal of Pharmaceutics, 1996. **139**(1-2): p. 125-138.
93. Ormos, Z., K. Pataki, and B. Stefko, *J. Ind. Chem.*, 1979. **7**: p. 131-140.
94. Johansen, A. and T. Schæfer, *Effects of interactions between powder particle size and binder viscosity on agglomerate growth mechanisms in a high shear mixer*. European Journal of Pharmaceutical Sciences, 2001. **12**(3): p. 297-309.
95. Newitt, D.M. and J.M. Conway-Jones, *A contribution to the theory and practice of granulation*. Trans IChemE, 1958. **36**: p. 422-441.
96. York, P. and R. Rowe. *Monitoring granulation size enlargement process using mixer torque rheometry*. in *First International Particle Technology Forum, Denver, USA*. 1994.
97. Yang, R., R. Zou, and A. Yu, *Numerical study of the packing of wet coarse uniform spheres*. AIChE journal, 2003. **49**(7): p. 1656-1666.
98. Anand, A., et al., *Segregation of cohesive granular materials during discharge from a rectangular hopper*. Granular Matter, 2010. **12**(2): p. 193-200.
99. Flemmer, C., *On the regime boundaries of moisture in granular materials*. Powder technology, 1991. **66**(2): p. 191-194.

Chapter 10: References

100. Schaefer, T., P. Holm, and H.G. Kristensen, *Melt pelletization in a high shear mixer. I: Effects of process variable and binder*. Acta pharmaceutica nordica, 1992. **4**(3): p. 133-140.
101. Iveson, S., J. Litster, and B. Ennis, *Fundamental studies of granule consolidation Part 1: Effects of binder content and binder viscosity*. Powder Technology, 1996. **88**(1): p. 15-20.
102. Biggs, C., et al. *Fluidised bed granulation: modelling the growth and breakage kinetics using population balances*. in *World Congress on Particle Technology*. 2002. Sydney Australia.
103. Fu, J., et al., *Impact deformation and rebound of wet granules*. Powder Technology, 2004. **140**(3): p. 248-257.
104. Pepin, X., et al., *Hardness of moist agglomerates in relation to interparticle friction, granule liquid content and nature*. Powder Technology, 2001. **117**(1-2): p. 123-138.
105. Schubert, H., *Tensile strength of agglomerates*. Powder Technology, 1975. **11**(2): p. 107-119.
106. Kendall, K., *Agglomerate strength*. Powder Metallurgy, 1988. **31**: p. 28-31.
107. Cook, E., *Drying: as much art as science*. Chemical Processing, 1999. **62**(12): p. 36-40.
108. Hare, C., M. Ghadiri, and R. Dennehy, *Prediction of attrition in agitated particle beds*. Chemical engineering science, 2011. **66**(20): p. 4757-4770.
109. Lee, T. and J. Lee, *Particle attrition by particle-surface friction in dryers*. Pharmaceutical Technology, 2003. **27**(5): p. 64-64.
110. Mujumdar, A.S., *Handbook of Industrial Drying*, ed. T.F. Group. 2007: LLC.
111. Schæfer, T., et al., *Melt pelletization in a high shear mixer. V. Effects of apparatus variables*. European Journal of Pharmaceutical Sciences, 1993. **1**(3): p. 133-141.
112. Jackson, R., *Some features of the flow of granular materials and aerated granular materials*. Journal of Rheology, 1986. **30**(5): p. 907-930.
113. Karmakar, S. and R. Kushwaha, *Development and laboratory evaluation of a rheometer for soil visco-plastic parameters*. Journal of Terramechanics, 2007. **44**(2): p. 197-204.
114. Campbell, C.S., *Granular shear flows at the elastic limit*. Journal of fluid mechanics, 2002. **465**: p. 261-291.
115. Remy, B., J.G. Khinast, and B.J. Glasser, *Discrete element simulation of free flowing grains in a four-bladed mixer*. AIChE Journal, 2009. **55**(8): p. 2035-2048.

Chapter 10: References

116. Tardos, G.I., S. McNamara, and I. Talu, *Slow and intermediate flow of a frictional bulk powder in the Couette geometry*. Powder Technology, 2003. **131**(1): p. 23-39.
117. Remy, B., *Granular flow, segregation and agglomeration in bladed mixers*. 2010: Rutgers The State University of New Jersey-New Brunswick.
118. Lekhal, A., et al., *Characterization of granular flow of wet solids in a bladed mixer*. AIChE journal, 2006. **52**(8): p. 2757-2766.
119. Goh, W.P., et al. *Stress analysis of an agitated particle bed with different particle aspect ratios by the discrete element method*. in *EPJ Web of Conferences*. 2017. EDP Sciences.
120. Herminghaus, S., *Dynamics of wet granular matter*. Advances in physics, 2005. **54**(3): p. 221-261.
121. Scheel, M., et al., *Morphological clues to wet granular pile stability*. Nature materials, 2008. **7**(3): p. 189-193.
122. Schlunder, E. *Particle heat transfer*. in *International Heat Transfer Conference Digital Library*. 1982. Begel House Inc.
123. Schlünder, E.-U. and N. Mollekopf, *Vacuum contact drying of free flowing mechanically agitated particulate material*. Chemical engineering processing: Process Intensification, 1984. **18**(2): p. 93-111.
124. Malhotra, K. and A. Mujumdar, *Particle mixing and solids flowability in granular beds stirred by paddle-type blades*. Powder Technology, 1990. **61**(2): p. 155-164.
125. Malhotra, K. and A.S. Mujumdar, *Particle flow and contact heat transfer characteristics of stirred granular beds*. Drying Technology, 1992. **10**(1): p. 51-80.
126. Sandler, N. and D. Wilson, *Prediction of granule packing and flow behavior based on particle size and shape analysis*. Journal of pharmaceutical sciences, 2010. **99**(2): p. 958-968.
127. Podczec, F. and Y. Mia, *The influence of particle size and shape on the angle of internal friction and the flow factor of unlubricated and lubricated powders*. International Journal of Pharmaceutics, 1996. **144**(2): p. 187-194.
128. Kaerger, J.S., S. Edge, and R. Price, *Influence of particle size and shape on flowability and compactibility of binary mixtures of paracetamol and microcrystalline cellulose*. European journal of pharmaceutical sciences, 2004. **22**(2-3): p. 173-179.
129. Pudasaini, N., et al., *Downstream processability of crystal habit-modified active pharmaceutical ingredient*. Organic process research development, 2017. **21**(4): p. 571-577.

Chapter 10: References

130. Miccio, F., D. Barletta, and M. Poletto, *Flow properties and arching behavior of biomass particulate solids*. Powder technology, 2013. **235**: p. 312-321.
131. Fitzpatrick, J., S. Barringer, and T. Iqbal, *Flow property measurement of food powders and sensitivity of Jenike's hopper design methodology to the measured values*. Journal of Food Engineering, 2004. **61**(3): p. 399-405.
132. Sinka, I., L. Schneider, and A. Cocks, *Measurement of the flow properties of powders with special reference to die fill*. International journal of pharmaceutics, 2004. **280**(1-2): p. 27-38.
133. Shah, U.V., et al., *Effect of crystal habits on the surface energy and cohesion of crystalline powders*. International journal of pharmaceutics, 2014. **472**(1-2): p. 140-147.
134. Feeley, J., et al., *Determination of surface properties and flow characteristics of salbutamol sulphate, before and after micronisation*. International Journal of Pharmaceutics, 1998. **172**(1-2): p. 89-96.
135. Gamble, J.F., et al., *Surface energy analysis as a tool to probe the surface energy characteristics of micronized materials—A comparison with inverse gas chromatography*. International journal of pharmaceutics, 2012. **422**(1-2): p. 238-244.
136. Shariare, M., M. De Matas, and P. York, *Effect of crystallisation conditions and feedstock morphology on the aerosolization performance of micronised salbutamol sulphate*. International journal of pharmaceutics, 2011. **415**(1-2): p. 62-72.
137. York, P., et al., *Characterisation of the surface energetics of milled dl-propranolol hydrochloride using inverse gas chromatography and molecular modelling*. International journal of pharmaceutics, 1998. **174**(1-2): p. 179-186.
138. Michaud, A., R. Peczalski, and J. Andrieu, *Optimization of crystalline powders vacuum contact drying with intermittent stirring*. Chemical Engineering Research Design, 2008. **86**(6): p. 606-611.
139. Baker, C.G., *Industrial drying of foods*. 1997: Springer Science & Business Media.
140. Hsieh, D.S., et al., *From drying kinetics, solvate structure, particle morphology, and modeling to optimal drying protocol*. Organic Process Research Development, 2017. **21**(10): p. 1509-1520.
141. Cussler, E.L., *Diffusion: mass transfer in fluid systems*. 2009: Cambridge university press.
142. Deen, W.M., *Analysis of transport phenomena*. Vol. 2. 1998: Oxford university press New York.

Chapter 10: References

143. Hsieh, D.S., et al., *The secondary drying and the fate of organic solvents for spray dried dispersion drug product*. *Pharmaceutical Research*, 2015. **32**(5): p. 1804-1816.
144. Vrentas, J.S. and C.M. Vrentas, *Diffusion and mass transfer*. 2016: CRC Press.
145. Colak, N. and A. Hepbasli, *Performance analysis of drying of green olive in a tray dryer*. *Journal of Food Engineering*, 2007. **80**(4): p. 1188-1193.
146. Iguaz, A., et al., *Mathematical modelling and simulation for the drying process of vegetable wholesale by-products in a rotary dryer*. *Journal of food engineering*, 2003. **59**(2-3): p. 151-160.
147. Rastikian, K., R. Capart, and J. Benchimol, *Modelling of sugar drying in a countercurrent cascading rotary dryer from stationary profiles of temperature and moisture*. *Journal of Food Engineering*, 1999. **41**(3-4): p. 193-201.
148. Forbert, R. and F. Heimann, *Vacuum contact drying of mechanically agitated, coarse, hygroscopic bulk material*. *Chemical Engineering Processing: Process Intensification*, 1989. **26**(3): p. 225-235.
149. Hare, C. and M. Ghadiri. *The influence of aspect ratio and roughness on flowability*. in *AIP Conference Proceedings*. 2013. AIP.
150. Remy, B., B.J. Glasser, and J.G. Khinast, *The effect of mixer properties and fill level on granular flow in a bladed mixer*. *AIChE journal*, 2010. **56**(2): p. 336-353.
151. Duran, J., *The static properties of a granular pile*. *Sands, Powders Grains*, 1999: p. 54-75.
152. Darelus, A., et al., *Measurement of the velocity field and frictional properties of wet masses in a high shear mixer*. *Chemical Engineering Science*, 2007. **62**(9): p. 2366-2374.
153. Campbell, C.S., *Granular material flows—an overview*. *Powder Technology*, 2006. **162**(3): p. 208-229.
154. Härtl, J. and J.Y. Ooi, *Numerical investigation of particle shape and particle friction on limiting bulk friction in direct shear tests and comparison with experiments*. *Powder Technology*, 2011. **212**(1): p. 231-239.
155. Ahmadian, H., *Analysis of Enzyme Dust Formation in Detergent Manufacturing Plant*, in *School of Process, Environmental and Materials Engineering*. 2008, University of Leeds. p. 293.
156. am Ende, D., et al., *Development and application of laboratory tools to predict particle properties upon scale-up in agitated filter-dryers*. *Organic Process Research Development*, 2013. **17**(10): p. 1345-1358.
157. Neil, A. and J. Bridgwater, *Attrition of particulate solids under shear*. *Powder Technology*, 1994. **80**(3): p. 207-219.

Chapter 10: References

158. Murugesan, S., P.K. Sharma, and J.E. Tabora, *Design of filtration and drying operations*. Chemical Engineering in the Pharmaceutical Industry: R&D to Manufacturing, 2010: p. 315-345.
159. Kowalski, S.J., K. Rajewska, and A. Rybicki, *Destruction of wet materials by drying*. Chemical Engineering Science, 2000. **55**(23): p. 5755-5762.
160. Chandratilleke, G.R., et al., *Effect of blade speed on granular flow and mixing in a cylindrical mixer*. Industrial engineering chemistry research, 2010. **49**(11): p. 5467-5478.
161. Stewart, R., et al., *Simulated and measured flow of granules in a bladed mixer—a detailed comparison*. Chemical engineering science, 2001. **56**(19): p. 5457-5471.
162. Zhou, Y., et al., *Microdynamic analysis of the particle flow in a cylindrical bladed mixer*. Chemical engineering science, 2004. **59**(6): p. 1343-1364.
163. Conder, E.W., et al., *The pharmaceutical drying unit operation: an industry perspective on advancing the science and development approach for scale-up and technology transfer*. Organic Process Research Development, 2017. **21**(3): p. 420-429.
164. Durak, L., et al., *Development and scale-up of a crystallization process to improve an API's physiochemical and bulk powder properties*. Organic Process Research Development, 2018. **22**(3): p. 296-305.
165. Hare, C.L., *Particle breakage in Agitated Dryers*, in *School of Process, Environmental and Materials Engineering*. 2010, University of Leeds. p. 223.
166. Zhang, S. and D.J. Lamberto, *Development of new laboratory tools for assessment of granulation behavior during bulk active pharmaceutical ingredient drying*. Journal of Pharmaceutical Sciences, 2014. **103**(1): p. 152-160.
167. Sahni, E.K., R.H. Bogner, and B. Chaudhuri, *Systematic investigation of parameters affecting the performance of an agitated filter-dryer*. Journal of pharmaceutical sciences, 2013. **102**(7): p. 2198-2213.
168. Sato, K., et al., *Two-dimensional population balance model with breakage of high aspect ratio crystals for batch crystallization*. Chemical Engineering Science, 2008. **63**(12): p. 3271-3278.
169. Wallack, D.A. and C.J. King, *Sticking and agglomeration of hygroscopic, amorphous carbohydrate and food powders*. Biotechnology Progress, 1988. **4**(1): p. 31-35.
170. Hennigs, C., T. Kockel, and T. Langrish, *New measurements of the sticky behavior of skim milk powder*. Drying technology, 2001. **19**(3-4): p. 471-484.
171. Knight, P., *Structuring agglomerated products for improved performance*. Powder technology, 2001. **119**(1): p. 14-25.

Chapter 10: References

172. Simons, S., J. Seville, and M. Adams, *An analysis of the rupture energy of pendular liquid bridges*. Chemical Engineering Science, 1994. **49**(14): p. 2331-2339.
173. Naik, S. and B. Chaudhuri, *Quantifying dry milling in pharmaceutical processing: a review on experimental and modeling approaches*. Journal of pharmaceutical sciences, 2015. **104**(8): p. 2401-2413.
174. Kumar, D., et al., *Effect of surfactant concentration on nifedipine crystal habit and its related pharmaceutical properties*. Journal of Crystal Growth, 2015. **422**: p. 44-51.
175. Kumar, D., et al., *Effect of HPMC concentration on crystal habit of nifedipine*. CrystEngComm, 2015. **17**(7): p. 1615-1624.
176. Nokhodchi, A., et al., *Crystal engineering of ibuprofen using starch derivatives in crystallization medium to produce promising ibuprofen with improved pharmaceutical performance*. RSC Advances, 2015. **5**(57): p. 46119-46131.
177. Bisker-Leib, V. and M.F. Doherty, *Modeling the crystal shape of polar organic materials: prediction of urea crystals grown from polar and nonpolar solvents*. Crystal Growth Design, 2001. **1**(6): p. 455-461.
178. Nokhodchi, A., N. Bolourtchian, and R. Dinarvand, *Crystal modification of phenytoin using different solvents and crystallization conditions*. International journal of pharmaceutics, 2003. **250**(1): p. 85-97.
179. Wang, Y. and Z. Liang, *Solvent effects on the crystal growth structure and morphology of the pharmaceutical dirithromycin*. Journal of Crystal Growth, 2017. **480**: p. 18-27.
180. Seibert, K.D., P.C. Collins, and E. Fisher, *Milling Operations in the Pharmaceutical Industry*, in *Chemical Engineering in the Pharmaceutical Industry*, D.J.a. Ende, Editor. 2011, J. Wiley & Sons, Inc: Hoboken, NJ, USA. p. 365-378.
181. Savolainen, M., et al., *Determination of amorphous content in the pharmaceutical process environment*. Journal of pharmacy pharmacology, 2007. **59**(2): p. 161-170.
182. Shah, B., V.K. Kakumanu, and A.K. Bansal, *Analytical techniques for quantification of amorphous/crystalline phases in pharmaceutical solids*. Journal of pharmaceutical sciences, 2006. **95**(8): p. 1641-1665.
183. Pazesh, S., et al., *Considerations on the quantitative analysis of apparent amorphicity of milled lactose by Raman spectroscopy*. International Journal of Pharmaceutics, 2016. **511**(1): p. 488-504.
184. Ghadiri, M., et al., *Attrition of granular solids in a shear cell*. Chemical Engineering Science, 2000. **55**(22): p. 5445-5456.

Chapter 10: References

185. Paramanathan, B. and J. Bridgwater, *Attribution of solids—I: cell development*. Chemical Engineering Science, 1983. **38**(2): p. 197-206.
186. Paramanathan, B. and J. Bridgwater, *Attrition of solids—II: material behaviour and kinetics of attrition*. Chemical Engineering Science, 1983. **38**(2): p. 207-224.
187. Pournin, L., et al., *Three-dimensional distinct element simulation of spherocylinder crystallization*. Granular Matter, 2005. **7**(2-3): p. 119-126.
188. Hua, X., et al., *The kinematics of non-cohesive, sphero-cylindrical particles in a low-speed, vertical axis mixer*. Chemical Engineering Science, 2013. **101**: p. 144-164.
189. Langston, P., A.R. Kennedy, and H. Constantin, *Discrete element modelling of flexible fibre packing*. Computational Materials Science, 2015. **96**: p. 108-116.
190. Kumar, R., et al., *Influence of normal contact force model on simulations of spherocylindrical particles*. AIChE Journal, 2018. **64**(6): p. 1986-2001.
191. Kumar, R., et al., *Breakage modeling of needle-shaped particles using the discrete element method*. Chemical Engineering Science: X, 2019. **3**: p. 100027.
192. Grof, Z., M. Kohout, and F. Štěpánek, *Multi-scale simulation of needle-shaped particle breakage under uniaxial compaction*. Chemical Engineering Science, 2007. **62**(5): p. 1418-1429.
193. Bharadwaj, R., W.R. Ketterhagen, and B.C. Hancock, *Discrete element simulation study of a Freeman powder rheometer*. Chemical Engineering Science, 2010. **65**(21): p. 5747-5756.
194. Grof, Z., et al., *Computational and experimental investigation of needle-shaped crystal breakage*. International journal of pharmaceutics, 2011. **407**(1-2): p. 12-20.
195. Kodicherla, S.P.K., et al., *The influence of particle elongations on direct shear behaviour of granular materials using DEM*. Granular Matter, 2019. **21**(4): p. 86.
196. White, J.P. and A.E. Bayly, *Simulation of Needle-shaped Crystal Breakage during Pressure Filtration using Discrete Element Method*, in *School of Chemical and Process Engineering*. 2017, University of Leeds: (Unpublished). p. 9.
197. Azéma, E. and F. Radjai, *Force chains and contact network topology in sheared packings of elongated particles*. Physical review E, 2012. **85**(3): p. 031303.
198. Favier, J., et al., *Shape representation of axi-symmetrical, non-spherical particles in discrete element simulation using multi-element model particles*. Engineering computations, 1999. **16**(4): p. 467-480.

Chapter 10: References

199. Gallas, J.A. and S. Sokolowski, *Grain non-sphericity effects on the angle of repose of granular material*. International Journal of Modern Physics B, 1993. **7**(09n10): p. 2037-2046.
200. Nolan, G. and P. Kavanagh, *Random packing of nonspherical particles*. Powder technology, 1995. **84**(3): p. 199-205.
201. Price, M., V. Murariu, and G. Morrison, *Sphere clump generation and trajectory comparison for real particles*. Proceedings of Discrete Element Modelling, 2007.
202. Kodam, M., et al., *Force model considerations for glued-sphere discrete element method simulations*. Chemical Engineering Science, 2009. **64**(15): p. 3466-3475.
203. Guo, Y., et al., *A numerical study of granular shear flows of rod-like particles using the discrete element method*. Journal of fluid Mechanics, 2012. **713**: p. 1-26.
204. Taghavi, R. *Automatic clump generation based on mid-surface*. in *Proceedings, 2nd International FLAC/DEM Symposium, Melbourne*. 2011.
205. Gong, J. and J. Liu, *Effect of aspect ratio on triaxial compression of multi-sphere ellipsoid assemblies simulated using a discrete element method*. Particuology, 2017. **32**: p. 49-62.
206. Altuhafi, F., C. O'sullivan, and I. Cavarretta, *Analysis of an image-based method to quantify the size and shape of sand particles*. Journal of Geotechnical and Geoenvironmental Engineering, 2012. **139**(8): p. 1290-1307.
207. Stahl, M. and H. Konietzky, *Discrete element simulation of ballast and gravel under special consideration of grain-shape, grain-size and relative density*. Granular Matter, 2011. **13**(4): p. 417-428.
208. Bagherzadeh-Khalkhali, A. and A.A. Mirghasemi, *Numerical and experimental direct shear tests for coarse-grained soils*. Particuology, 2009. **7**(1): p. 83-91.
209. Zhou, W., et al., *Influence of particle shape on behavior of rockfill using a three-dimensional deformable DEM*. Journal of Engineering Mechanics, 2013. **139**(12): p. 1868-1873.
210. Guo, Y. and J.S. Curtis, *Discrete element method simulations for complex granular flows*. Annual Review of Fluid Mechanics, 2015. **47**: p. 21-46.
211. Boudaghi-Khajehnohar, M., B.J. Edwards, and B. Khomami, *Effects of chain length and polydispersity on shear banding in simple shear flow of polymeric melts*. Soft Matter, 2020. **16**(28): p. 6468-6483.
212. Indraratna, B., et al., *Behavior of fresh and fouled railway ballast subjected to direct shear testing: discrete element simulation*. International Journal of Geomechanics, 2014. **14**(1): p. 34-44.

Chapter 10: References

213. Wu, Q., Z. Yang, and X. Li, *Numerical simulations of granular material behavior under rotation of principal stresses: micromechanical observation and energy consideration*. *Meccanica*, 2019. **54**(4): p. 723-740.
214. Yang, Z., J. Yang, and L. Wang, *On the influence of inter-particle friction and dilatancy in granular materials: a numerical analysis*. *Granular matter*, 2012. **14**(3): p. 433-447.
215. Yang, Z., J. Yang, and L. Wang, *Micro-scale modeling of anisotropy effects on undrained behavior of granular soils*. *Granular Matter*, 2013. **15**(5): p. 557-572.
216. Zhu, H., et al., *Discrete particle simulation of particulate systems: theoretical developments*. *Chemical Engineering Science*, 2007. **62**(13): p. 3378-3396.
217. Solutions, D. *EDEM 2.6 Theory Reference Guide*. 2014; Available from: <https://docplayer.net/101711888-Edem-2-6-theory-reference-guide.html>.
218. Tsuji, Y., T. Tanaka, and T. Ishida, *Lagrangian numerical simulation of plug flow of cohesionless particles in a horizontal pipe*. *Powder technology*, 1992. **71**(3): p. 239-250.
219. Hertz, H., *Über die Berührung fester elastischer Körper*. *Journal für die reine und angewandte Mathematik*, 1882. **92**(156-171): p. 22.
220. Mindlin, R.D. and H. Deresiewicz, *Elastic spheres in contact under varying oblique forces*. 1953.
221. Thornton, C. and K. Yin, *Impact of elastic spheres with and without adhesion*. *Powder technology*, 1991. **65**(1-3): p. 153-166.
222. Di Renzo, A. and F.P. Di Maio, *Comparison of contact-force models for the simulation of collisions in DEM-based granular flow codes*. *Chemical engineering science*, 2004. **59**(3): p. 525-541.
223. Shi, D. and J.J. McCarthy, *Numerical simulation of liquid transfer between particles*. *Powder Technology*, 2008. **184**(1): p. 64-75.
224. Mikami, T., H. Kamiya, and M. Horio, *Numerical simulation of cohesive powder behavior in a fluidized bed*. *Chemical engineering science*, 1998. **53**(10): p. 1927-1940.
225. Richefeu, V., M.S. El Youssoufi, and F. Radjai, *Shear strength properties of wet granular materials*. *Physical Review E*, 2006. **73**(5): p. 051304.
226. Yamamoto, S. and T. Matsuoka, *A method for dynamic simulation of rigid and flexible fibers in a flow field*. *The Journal of chemical physics*, 1993. **98**(1): p. 644-650.
227. Potyondy, D.O. and P. Cundall, *A bonded-particle model for rock*. *International journal of rock mechanics and mining sciences*, 2004. **41**(8): p. 1329-1364.

Chapter 10: References

228. Guo, Y., et al., *Computational study of granular shear flows of dry flexible fibres using the discrete element method*. Journal of Fluid Mechanics, 2015. **775**: p. 24-52.
229. Hibbeler, R., *Mechanics of material 6th edition Pearson prentice-hall*. Upper Saddle River, NJ, 2005.
230. Popov, E. and T. Balan, *Engineering Mechanics of Solids*. 1999, Prentice-Hall, New Jersey.
231. Potapov, A.V. and C.S. Campbell, *Computer simulation of shear-induced particle attrition*. Powder Technology, 1997. **94**(2): p. 109-122.
232. Liu, L., K. Kafui, and C. Thornton, *Impact breakage of spherical, cuboidal and cylindrical agglomerates*. Powder Technology, 2010. **199**(2): p. 189-196.
233. Antonyuk, S., S. Palis, and S. Heinrich, *Breakage behaviour of agglomerates and crystals by static loading and impact*. Powder Technology, 2011. **206**(1-2): p. 88-98.
234. Nguyen, D., et al., *Numerical modelling of breakage and adhesion of loose fine-particle agglomerates*. Chemical Engineering Science, 2014. **116**: p. 91-98.
235. Guo, Y., et al., *Predicting breakage of high aspect ratio particles in an agitated bed using the Discrete Element Method*. Chemical Engineering Science, 2017. **158**: p. 314-327.
236. Gwyn, J., *On the particle size distribution function and the attrition of cracking catalysts*. AIChE Journal, 1969. **15**(1): p. 35-39.
237. Bridgwater, J., et al., *Particle attrition due to shearing—the effects of stress, strain and particle shape*. Chemical engineering science, 2003. **58**(20): p. 4649-4665.
238. Ning, Z. and M. Ghadiri, *Distinct element analysis of attrition of granular solids under shear deformation*. Chemical engineering science, 2006. **61**(18): p. 5991-6001.
239. Kim, B.-S., S.-W. Park, and S. Kato, *Distinct element method simulation on deformation mode and stress state for specimen shape in direct shear test*. International Journal of Computational Methods, 2014. **11**(02): p. 1342004.
240. Jiang, M., et al., *Exploring the critical state properties and major principal stress rotation of sand in direct shear test using the distinct element method*. Granular Matter, 2018. **20**(2): p. 25.
241. Karion, A. and M.L. Hunt, *Wall stresses in granular Couette flows of mono-sized particles and binary mixtures*. Powder Technology, 2000. **109**(1-3): p. 145-163.
242. Campbell, C.S., *Boundary interactions for two-dimensional granular flows. Part 1. Flat boundaries, asymmetric stresses and couple stresses*. Journal of Fluid Mechanics, 1993. **247**: p. 111-136.

Chapter 10: References

243. Lun, C.K., *Granular dynamics of inelastic spheres in Couette flow*. Physics of Fluids, 1996. **8**(11): p. 2868-2883.
244. Cleary, P.W., *The effect of particle shape on simple shear flows*. Powder Technology, 2008. **179**(3): p. 144-163.
245. Lees, A. and S. Edwards, *The computer study of transport processes under extreme conditions*. Journal of Physics C: Solid State Physics, 1972. **5**(15): p. 1921.
246. Jamiolkowski, M., L. Kongsukprasert, and D.C. Lo Presti. *Characterization of gravelly geomaterials*. in *15th SEAGC, Bangkok 22-26 November 2004*. 2004. Asian Institute of Technology.
247. Wang, J. and M. Gutierrez, *Discrete element simulations of direct shear specimen scale effects*. Géotechnique, 2010. **60**(5): p. 395.
248. Huang, X., et al., *Effect of sample size on the response of DEM samples with a realistic grading*. Particuology, 2014. **15**: p. 107-115.
249. Ng, T.-T., *Triaxial test simulations with discrete element method and hydrostatic boundaries*. Journal of engineering mechanics, 2004. **130**(10): p. 1188-1194.
250. Reynolds, O., *LVII. On the dilatancy of media composed of rigid particles in contact. With experimental illustrations*. The London, Edinburgh, Dublin Philosophical Magazine Journal of Science, 1885. **20**(127): p. 469-481.
251. Reynolds, O., *Experiments showing dilatancy, a property of granular material, possibly connected with gravitation*. Proc. R. Inst. GB, 1886. **11**(354363): p. 12.
252. Johnson, K.L., *Contact mechanics*. 1987: Cambridge university press.
253. Popov, V.L., *Contact mechanics and friction*. 2010: Springer.
254. Luding, S., *Constitutive relations for the shear band evolution in granular matter under large strain*. Particuology, 2008. **6**(6): p. 501-505.
255. Christoffersen, J., M.M. Mehrabadi, and S. Nemat-Nasser, *A micromechanical description of granular material behavior*. 1981.
256. Thornton, C. and L. Zhang, *Numerical simulations of the direct shear test*. Chemical Engineering Technology: Industrial Chemistry-Plant Equipment-Process Engineering-Biotechnology, 2003. **26**(2): p. 153-156.
257. Thornton, C., *Granular dynamics, contact mechanics and particle system simulations*. A DEM study. Particle Technology Series, 2015. **24**.
258. Ng, T.T., *Particle shape effect on macro-and micro-behaviors of monodisperse ellipsoids*. International journal for numerical and analytical methods in geomechanics, 2009. **33**(4): p. 511-527.

Chapter 10: References

259. Azéma, E. and F. Radjaï, *Stress-strain behavior and geometrical properties of packings of elongated particles*. Physical Review E, 2010. **81**(5): p. 051304.
260. Kodam, M., et al. in *Particulate Processes in the Pharmaceutical Industry III*. 2012.
261. Guo, Y., et al., *Validation and time step determination of discrete element modeling of flexible fibers*. Powder technology, 2013. **249**: p. 386-395.
262. Bolton, M., *Strength and dilatancy of sands*. Geotechnique, 1986. **36**(1): p. 65-78.
263. Masson, S. and J. Martinez, *Micromechanical analysis of the shear behavior of a granular material*. Journal of engineering mechanics, 2001. **127**(10): p. 1007-1016.
264. Tian, J., et al., *Influence of particle shape on the microstructure evolution and the mechanical properties of granular materials*. Comptes Rendus Mécanique, 2018. **346**(6): p. 460-476.
265. Zhao, S., T.M. Evans, and X. Zhou, *Three-dimensional Voronoi analysis of monodisperse ellipsoids during triaxial shear*. Powder Technology, 2018. **323**: p. 323-336.
266. Donev, A., et al., *Improving the density of jammed disordered packings using ellipsoids*. Science, 2004. **303**(5660): p. 990-993.
267. Schaller, F.M., et al., *Local origin of global contact numbers in frictional ellipsoid packings*. Physical review letters, 2015. **114**(15): p. 158001.
268. Galindo-Torres, S., J. Muñoz, and F. Alonso-Marroquin, *Minkowski-Voronoi diagrams as a method to generate random packings of spheropolygons for the simulation of soils*. Physical Review E, 2010. **82**(5): p. 056713.
269. Zhao, S., et al., *Random packing of tetrahedral particles using the polyhedral discrete element method*. Particuology, 2015. **23**: p. 109-117.
270. Gong, G., et al., *DEM simulation of liquefaction for granular media under undrained axisymmetric compression and plane strain conditions*. Acta Mechanica Solida Sinica, 2012. **25**(6): p. 562-570.
271. Gong, G., *DEM (Discrete Element Method) simulations of drained and undrained behaviour*. 2008, University of Birmingham.
272. Markauskas, D., et al., *Investigation of adequacy of multi-sphere approximation of elliptical particles for DEM simulations*. Granular Matter, 2010. **12**(1): p. 107-123.
273. Abreu, C.R., F.W. Tavares, and M. Castier, *Influence of particle shape on the packing and on the segregation of spherocylinders via Monte Carlo simulations*. Powder Technology, 2003. **134**(1-2): p. 167-180.

274. Williams, S. and A. Philipse, *Random packings of spheres and spherocylinders simulated by mechanical contraction*. Physical Review E, 2003. **67**(5): p. 051301.
275. Meng, L., et al., *Shape and size effects on the packing density of binary spherocylinders*. Powder technology, 2012. **228**: p. 284-294.
276. Zhao, J., et al., *Dense random packings of spherocylinders*. Soft Matter, 2012. **8**(4): p. 1003-1009.
277. Shamsi, M.M. and A. Mirghasemi, *Numerical simulation of 3D semi-real-shaped granular particle assembly*. Powder technology, 2012. **221**: p. 431-446.
278. Donev, A., et al., *Underconstrained jammed packings of nonspherical hard particles: Ellipses and ellipsoids*. Physical Review E, 2007. **75**(5): p. 051304.
279. Buchalter, B. and R. Bradley, *Orientalional order in amorphous packings of ellipsoids*. EPL (Europhysics Letters), 1994. **26**(3): p. 159.
280. Andrienko, D., *Introduction to liquid crystals*. Journal of Molecular Liquids, 2018. **267**: p. 520-541.
281. Potapov, A.V. and C.S. Campbell, *A three-dimensional simulation of brittle solid fracture*. International Journal of Modern Physics C, 1996. **7**(05): p. 717-729.
282. Deluzarche, R. and B. Cambou, *Discrete numerical modelling of rockfill dams*. International journal for numerical and analytical methods in geomechanics, 2006. **30**(11): p. 1075-1096.
283. Abbireddy, C. and C. Clayton, *Varying initial void ratios for DEM simulations*. Géotechnique, 2010. **60**(6): p. 497.
284. Zhao, S. and J. Zhao, *A poly-superellipsoid-based approach on particle morphology for DEM modeling of granular media*. International Journal for Numerical Analytical Methods in Geomechanics, 2019. **43**(13): p. 2147-2169.
285. Radjai, F., et al., *Bimodal character of stress transmission in granular packings*. Physical review letters, 1998. **80**(1): p. 61.
286. Shi, J. and P. Guo, *Fabric evolution of granular materials along imposed stress paths*. Acta Geotechnica, 2018. **13**(6): p. 1341-1354.
287. Shi, J. and P. Guo, *Induced fabric anisotropy of granular materials in biaxial tests along imposed strain paths*. Soils Foundations, 2018. **58**(2): p. 249-263.
288. Antony, S. and N.P. Kruyt, *Role of interparticle friction and particle-scale elasticity in the shear-strength mechanism of three-dimensional granular media*. Physical Review E, 2009. **79**(3): p. 031308.
289. Bednarek, X., et al. *Calibration of DEM parameters on shear test experiments using Kriging method*. in EPJ Web of Conferences. 2017. EDP Sciences.

Chapter 10: References

290. Hossain, M., H. Zhu, and A. Yu, *Role of gravity in the flow of particles in a shear cell*. Trends in Chemical Engineering, 2017. **16**: p. 15-29.
291. Singh, A., et al., *The role of gravity or pressure and contact stiffness in granular rheology*. New journal of physics, 2015. **17**(4): p. 043028.
292. Walton, O.R., C.P. De Moor, and K.S. Gill, *Effects of gravity on cohesive behavior of fine powders: implications for processing Lunar regolith*. Granular Matter, 2007. **9**(5): p. 353-363.
293. Shier, A.P., *The Breakage of Needle-Shaped Crystals Under Pressure Filtration*. 2017, University of Leeds.
294. Mahdi, F., et al., *On the Breakage of High Aspect Ratio Crystals in Filter Beds under Continuous Percolation*. Pharmaceutical research, 2020. **37**(12): p. 1-15.
295. Hallac, F.S., et al., *Micro-mechanical properties of organic crystals*, in *Chemical Engineering*. 2017, University of Leeds.
296. Kougoulos, E., C. Chadwick, and M. Ticehurst, *Impact of agitated drying on the powder properties of an active pharmaceutical ingredient*. Powder technology, 2011. **210**(3): p. 308-314.
297. Lawrence, X.Y., *Pharmaceutical quality by design: product and process development, understanding, and control*. Pharmaceutical research, 2008. **25**(4): p. 781-791.
298. Muller, F.L., *On the rheological behaviour of batch crystallisations*. Chemical Engineering Research and Design, 2009. **87**(4): p. 627-632.
299. Taylor, L., et al., *Predictive milling of pharmaceutical materials using nanoindentation of single crystals*. Organic Process Research & Development, 2004. **8**(4): p. 674-679.
300. Kwan, C.C., et al., *Development of a novel approach towards predicting the milling behaviour of pharmaceutical powders*. European journal of pharmaceutical sciences, 2004. **23**(4-5): p. 327-336.
301. Ast, J., et al., *A review of experimental approaches to fracture toughness evaluation at the micro-scale*. Materials Design, 2019. **173**: p. 107762.
302. Ramos, K. and D. Bahr, *Mechanical behavior assessment of sucrose using nanoindentation*. Journal of materials research, 2007. **22**(7): p. 2037-2045.
303. Butt, H.-J., B. Cappella, and M. Kappl, *Force measurements with the atomic force microscope: Technique, interpretation and applications*. Surface science reports, 2005. **59**(1-6): p. 1-152.
304. Du, B., et al., *Study of elastic modulus and yield strength of polymer thin films using atomic force microscopy*. Langmuir, 2001. **17**(11): p. 3286-3291.

Chapter 10: References

305. Masterson, V.M. and X. Cao, *Evaluating particle hardness of pharmaceutical solids using AFM nanoindentation*. International journal of pharmaceutics, 2008. **362**(1-2): p. 163-171.
306. Ghosh, S., et al., *Designing Elastic Organic Crystals: Highly Flexible Polyhalogenated N-Benzylideneanilines*. Angewandte Chemie International Edition, 2015. **54**(9): p. 2674-2678.
307. O'Neil, M.J., *The Merck index: an encyclopedia of chemicals, drugs, and biologicals*. 2013: RSC Publishing.
308. Pertzoff, V.A., *The solubility of glutamic acid in water and certain organic solvents*. Journal of Biological Chemistry, 1933. **100**(1): p. 97-104.
309. Grutzik, S.J., et al., *Accurate spring constant calibration for very stiff atomic force microscopy cantilevers*. Review of Scientific Instruments, 2013. **84**(11): p. 113706.
310. Hooke, R., 1678, *De Potentia Restitutiva, or of Spring*. Explaining the Power of Springing Bodies (London: J. Martyn), 2007.
311. Lindeburg, M.R., *Mechanical engineering reference manual for the PE exam*. 2013: www. ppi2pass. com.
312. Day, G.M., S.L. Price, and M. Leslie, *Elastic constant calculations for molecular organic crystals*. Crystal Growth & Design, 2001. **1**(1): p. 13-27.
313. Matoy, K., et al., *A comparative micro-cantilever study of the mechanical behavior of silicon based passivation films*. Thin Solid Films, 2009. **518**(1): p. 247-256.
314. Descamps, M. and J.-F. Willart, *Some facets of molecular disorder in crystalline and amorphous pharmaceuticals*. Disordered Pharmaceutical Materials, 2016: p. 1-56.
315. Sherwood, J.N., *Fifty years as a crystal gazer: life as an imperfectionist*. Crystal growth & design, 2004. **4**(5): p. 863-877.
316. Fuller, C., *The Chemistry of Imperfect Crystals*. Journal of the American Chemical Society, 1964. **86**(20): p. 4514-4515.
317. Weibull, W., *Wide applicability*. Journal of applied mechanics, 1951. **103**(730): p. 293-297.
318. Saporta, G., *Probabilités, analyse des données et statistique*. 3rd Edition ed. 2011, Paris, France: Editions Technip.
319. Swadener, J., E. George, and G. Pharr, *The correlation of the indentation size effect measured with indenters of various shapes*. Journal of the Mechanics Physics of Solids, 2002. **50**(4): p. 681-694.

Chapter 10: References

320. Perkins, M., et al., *Elastic modulus measurements from individual lactose particles using atomic force microscopy*. International journal of pharmaceutics, 2007. **332**(1-2): p. 168-175.
321. Fraxedas, J., et al., *Nanoindentation: toward the sensing of atomic interactions*. Proceedings of the National Academy of Sciences, 2002. **99**(8): p. 5228-5232.
322. Park, R.J.T., *Seismic performance of steel-encased concrete piles*. 1986.
323. *L-glutamic acid*. 2017: PubChem Compound Database.
324. Laboratory, N.P., *Air Density Measurement*. 2004: Teddington, Middlesex, UK.
325. Materials, A. *ASTM A36 Mild/Low Carbon Steel*. 2012; Available from: <https://www.azom.com/article.aspx?ArticleID=6117>.
326. Mindlin, R.D., *Compliance of elastic bodies in contact*. Journal of Applied Mechanics, 1949. **16**: p. 259-268.
327. Cundall, P.A. and O.D. Strack, *A discrete numerical model for granular assemblies*. Geotechnique, 1979. **29**(1): p. 47-65.
328. Sakaguchi, H., E. Ozaki, and T. Igarashi, *Plugging of the flow of granular materials during the discharge from a silo*. International Journal of Modern Physics B, 1993. **7**(09n10): p. 1949-1963.
329. Duncan-Hewitt, W., *Predicting the relative rate of wear of pharmaceutical compacts using the mechanical properties of their constituent crystals*. Powder technology, 1990. **60**(3): p. 265-272.
330. Butcher, J.C., *Numerical methods for ordinary differential equations*. 2016: John Wiley & Sons.
331. Nørsett, S.P. and G. Wanner, *Solving ordinary differential equations: Stiff and differential-algebraic problems*. 1993: Springer-Verlag.
332. Solutions, D. *EDEM 2.4 User Guide*. 2011; Available from: <https://www.altair.com/edem/>.
333. Landau, L.D., et al., *Theory of elasticity: volume 7*. Vol. 7. 1986: Elsevier.
334. Kichenassamy, S.J.H.M., *Continued proportions and Tartaglia's solution of cubic equations*. 2015. **42**(4): p. 407-435.
335. Goswami, D.Y., *The CRC handbook of mechanical engineering*. 2004: CRC press.
336. Tenenhaus, M., *Statistique: méthodes pour décrire, expliquer et prévoir*. Vol. 680. 2007: Dunod Paris, France:.

Chapter 10: References

337. Limited, P.P.S. *GFD Brochure: The Glass Filter Dryer*. Available from: <http://www.powdersystems.com/pdf/PSL%20GFD%20brochure.pdf?gsleadDesc=Website+Glass+Filter+Dryer+Brochure+Download>.

Appendixes

Figures

Appendix 1: Vessel apparatus used for the crystallisation of glutamic acid in their elongated β form.



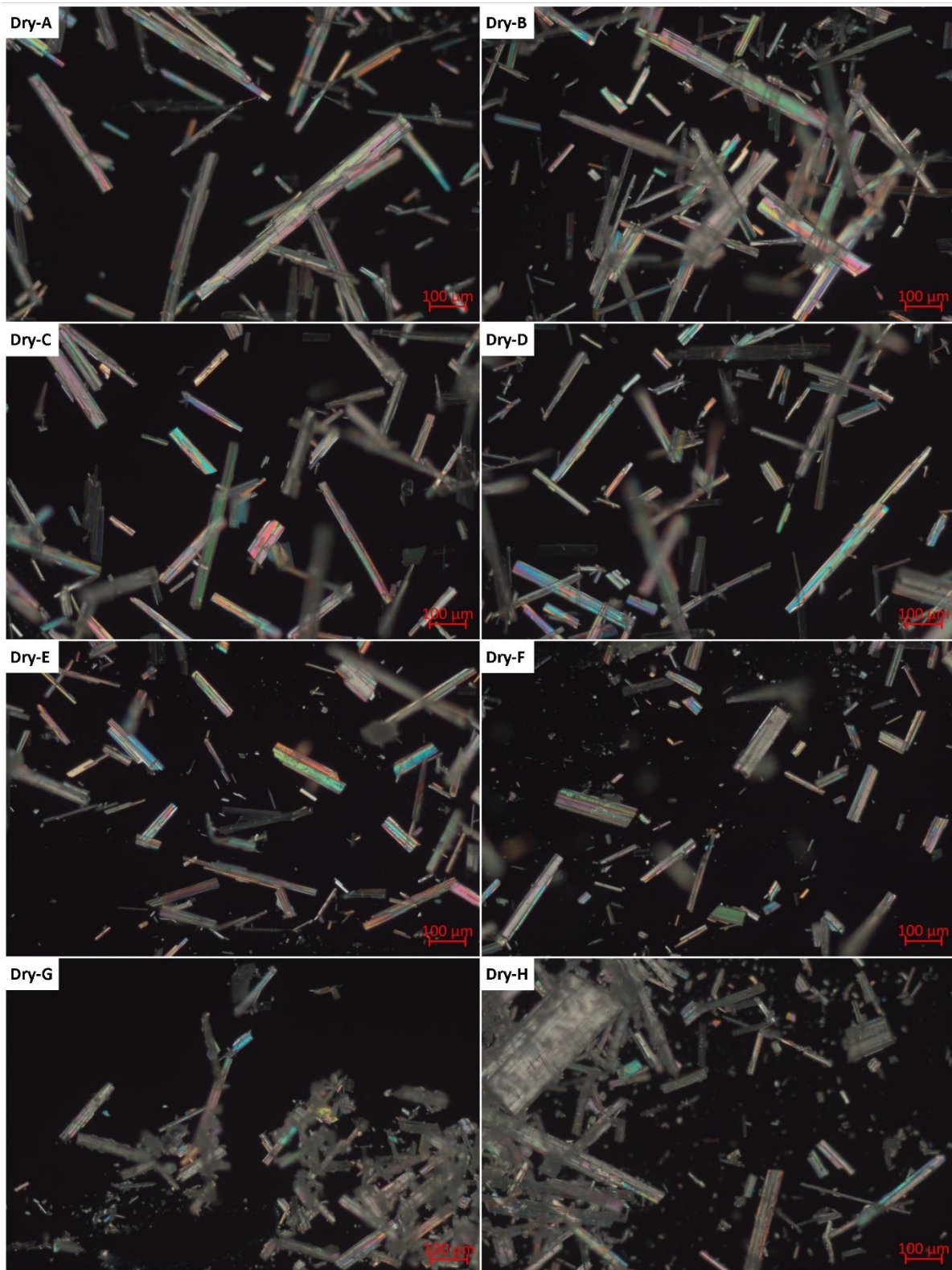
Appendixes

Appendix 2: Zeiss Axioskop 40 light microscope mounted with a Zeiss Axiocam 512 color camera used for the observation of β -LGA crystals.



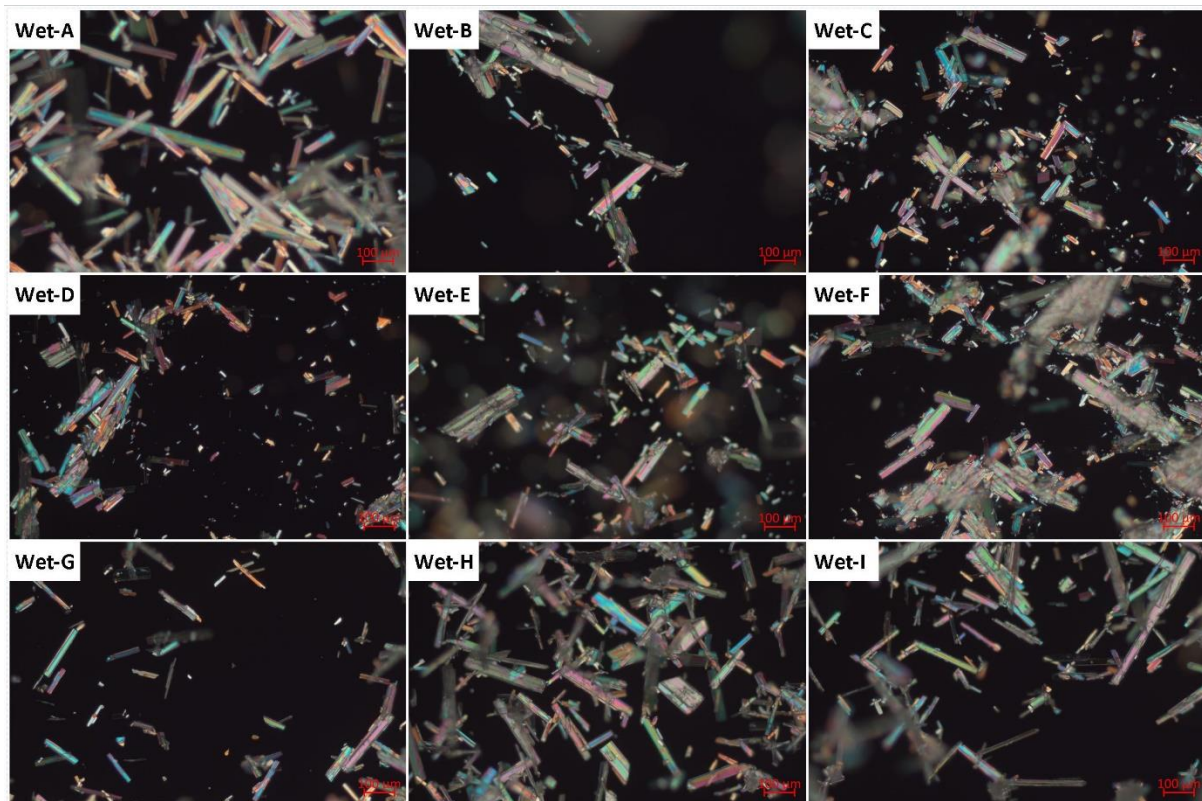
Appendixes

Appendix 3: Light microscopy images of the different samples of β -LGA crystals collected during the dry agitation experiment (see Table 3.2.1).



Appendixes

Appendix 4: Light microscopy images of the different samples of β -LGA crystals collected during the wet agitation experiment (see Table 3.2.2).



Appendixes

Tables

Appendix 5: Experimental data and calculated mechanical properties for 52 crystals.

Crystal No	Probe No	L, crystal length (m)	w, crystal width (m)	h, crystal height (m)	k_r , crystal/probe system spring (N/m)	E, Young's modulus (Pa)	n_{steps} , motor steps	L_B , crystal broken length (m)	F_B , breakage force (N)	σ_B , breakage strength (Pa)
1	1	1.71E-04	6.10E-05	1.40E-05	29.43	4.08E+09	54	1.40E-4	7.41E-04	5.18E+07
2	2	1.59E-04	8.67E-05	2.95E-05	65.63	7.07E+08	104	9.97E-5	3.18E-03	2.52E+07
3	1	2.04E-04	5.34E-05	2.95E-05	40.90	1.28E+09	56	1.87E-4	1.07E-03	2.59E+07
4	1	3.71E-04	6.76E-05	4.39E-05	21.15	8.48E+08	107	1.99E-4	1.05E-03	9.69E+06
5	1	4.85E-04	5.97E-05	3.89E-05	40.04	6.53E+09	137	4.03E-4	2.56E-03	6.86E+07
6	3	2.50E-04	6.37E-05	3.59E-05	93.63	3.74E+09	45	2.50E-4	1.96E-03	3.59E+07
7	3	1.02E-04	3.94E-05	3.69E-05	102.22	4.50E+08	69	9.37E-5	3.29E-03	3.45E+07
8	3	6.07E-04	7.66E-05	5.60E-05	32.18	2.55E+09	71	3.56E-4	1.06E-03	9.45E+06
9	3	3.94E-04	7.64E-05	4.07E-05	32.57	1.84E+09	110	3.18E-4	1.67E-03	2.51E+07
10	4	2.44E-04	7.21E-05	3.84E-05	66.47	1.42E+09	75	2.19E-4	2.32E-03	2.88E+07
11	5	1.53E-04	8.29E-05	4.07E-05	168.18	2.72E+09	57	1.21E-4	4.47E-03	2.37E+07
12	5	1.92E-04	7.05E-05	2.80E-05	118.14	5.31E+09	37	1.58E-4	2.04E-03	3.50E+07
13	5	1.45E-04	6.94E-05	2.29E-05	63.12	1.34E+09	33	1.20E-4	9.71E-04	1.92E+07
14	5	2.88E-04	4.72E-05	2.30E-05	32.77	6.54E+09	43	2.23E-4	6.57E-04	3.52E+07
15	5	2.87E-04	5.98E-05	2.54E-05	33.71	3.90E+09	40	2.21E-4	6.28E-04	2.15E+07
16	5	1.48E-04	8.26E-05	2.80E-05	179.23	1.24E+10	76	1.38E-4	6.35E-03	8.11E+07

Appendixes

17	5	1.44E-04	6.74E-05	2.87E-05	121.77	2.32E+09	24	1.39E-4	1.36E-03	2.05E+07
18	5	2.69E-04	4.50E-05	2.70E-05	38.66	4.25E+09	37	2.08E-4	6.67E-04	2.54E+07
19	5	1.14E-04	8.57E-05	4.46E-05	169.34	8.57E+08	68	1.07E-4	5.37E-03	2.01E+07
20	5	2.71E-04	5.93E-05	3.59E-05	63.57	2.68E+09	46	1.61E-4	1.36E-03	1.72E+07
21	5	1.84E-04	7.04E-05	4.20E-05	114.26	1.27E+09	43	1.32E-4	2.29E-03	1.46E+07
22	6	1.73E-04	7.16E-05	3.69E-05	136.72	2.51E+09	46	1.73E-4	2.93E-03	3.13E+07
23	6	2.34E-04	7.31E-05	2.44E-05	57.38	3.85E+09	46	2.16E-4	1.23E-03	3.65E+07
24	9	1.70E-04	5.97E-05	1.91E-05	45.01	2.73E+09	27	1.70E-4	5.66E-04	2.65E+07
25	9	2.73E-04	7.63E-05	3.69E-05	40.72	1.08E+09	47	2.73E-4	8.92E-04	1.40E+07
26	9	1.59E-04	3.28E-05	6.04E-05	53.70	1.63E+08	34	1.23E-4	8.51E-04	5.27E+06
27	10	3.31E-04	7.12E-05	3.69E-05	102.98	8.63E+09	64	2.43E-4	3.07E-03	4.63E+07
28	10	3.29E-04	4.32E-05	3.05E-05	15.05	1.88E+09	140	3.00E-4	9.82E-04	4.39E+07
29	10	1.82E-04	3.30E-05	2.67E-05	24.84	1.08E+09	66	1.39E-4	7.64E-04	2.71E+07
30	10	3.14E-04	6.51E-05	3.71E-05	17.88	7.37E+08	80	2.86E-4	6.67E-04	1.28E+07
31	10	3.04E-04	8.32E-05	4.20E-05	53.31	1.33E+09	115	3.04E-4	2.86E-03	3.55E+07
32	10	1.73E-04	2.59E-05	4.32E-05	40.81	5.10E+08	76	1.73E-4	1.45E-03	3.11E+07
33	10	3.12E-04	6.53E-05	3.30E-05	51.05	3.53E+09	64	2.60E-4	1.52E-03	3.33E+07
34	11	2.01E-04	3.87E-05	2.93E-05	56.10	2.58E+09	24	1.77E-4	6.27E-04	2.00E+07
35	11	1.91E-04	5.19E-05	3.43E-05	75.20	1.60E+09	20	1.74E-4	7.01E-04	1.20E+07
36	11	3.67E-04	9.59E-05	4.83E-05	116.82	5.12E+09	37	1.85E-4	2.01E-03	9.99E+06
37	11	1.67E-04	7.51E-05	3.31E-05	88.18	1.09E+09	34	1.67E-4	1.40E-03	1.71E+07

Appendixes

38	12	1.70E-04	6.49E-05	2.29E-05	83.39	3.60E+09	63	1.40E-4	2.45E-03	6.06E+07
39	12	5.90E-04	7.84E-05	3.44E-05	33.58	1.04E+10	120	5.33E-4	1.88E-03	6.48E+07
40	12	1.79E-04	8.09E-05	3.31E-05	173.66	1.03E+10	48	1.23E-4	3.88E-03	3.24E+07
41	12	2.02E-04	5.22E-05	2.54E-05	55.80	2.95E+09	50	1.80E-4	1.30E-03	4.16E+07
42	12	1.28E-04	7.15E-05	3.19E-05	160.59	2.96E+09	49	1.28E-4	3.67E-03	3.88E+07
43	12	1.83E-04	5.21E-05	3.31E-05	89.40	2.09E+09	32	1.60E-4	1.33E-03	2.25E+07
44	12	3.65E-04	5.87E-05	3.31E-05	24.41	2.56E+09	109	3.65E-4	1.24E-03	4.24E+07
45	12	2.86E-04	4.93E-05	3.43E-05	34.65	1.96E+09	67	2.86E-4	1.08E-03	3.19E+07
46	12	4.57E-04	6.09E-05	3.82E-05	22.79	2.89E+09	120	4.20E-4	1.27E-03	3.61E+07
47	12	1.17E-04	4.47E-05	6.36E-05	196.03	5.58E+09	50	9.02E-5	4.57E-03	1.37E+07
48	12	3.86E-04	6.99E-05	3.81E-05	52.94	4.25E+09	59	3.86E-4	1.46E-03	3.31E+07
49	12	3.24E-04	8.45E-05	3.94E-05	62.34	2.38E+09	70	2.52E-4	2.03E-03	2.34E+07
50	12	2.11E-04	3.59E-05	2.84E-05	23.87	1.24E+09	62	1.99E-4	6.90E-04	2.85E+07
51	13	1.21E-04	5.21E-05	4.26E-05	106.26	3.98E+08	22	8.66E-5	1.09E-03	6.00E+06
52	13	3.14E-04	4.51E-05	3.22E-05	13.58	1.21E+09	44	2.86E-4	2.83E-04	1.04E+07

Appendixes

Appendix 6: Descriptive statistical analysis data for the breakage experiment on the sample of 52 β -LGA crystals.

	Minimum	Maximum	Mean	Median	Standard Deviation
l , crystal length (μm)	102	607	252	208	114
l_B , crystal broken length (μm)	86.6	533	211	183	95.3
w , width (μm)	25.9	95.9	62.7	65.0	15.9
h , height (μm)	14.0	63.6	34.9	34.3	9.32
F_B , breakage force (mN)	0.283	6.35	1.84	1.36	1.31
σ_B , breakage strength (MPa)	5.27	81.1	29.2	26.8	15.8
E , Young's modulus (GPa)	0.163	12.4	3.08	2.53	2.64

Appendixes

Appendix 7: Breakage strength distribution data.

Bin Index	Bin Average Value (MPa)	Bin Average Value (Log)	N_{br}	Frequency	Cumulative N_{br}	%Cumul	Weibull %Cumul
1	6.25	6.80	2	3.8%	2	3.8%	5.57%
2	8.80	6.94	4	7.7%	6	11.5%	10.57%
3	12.4	7.09	5	9.6%	11	21.2%	19.56%
4	17.4	7.24	6	11.5%	17	32.7%	34.56%
5	24.5	7.39	12	23.1%	29	55.8%	56.24%
6	34.5	7.54	14	26.9%	43	82.7%	80.02%
7	48.6	7.69	5	9.6%	48	92.3%	95.66%
8	68.3	7.83	4	7.7%	52	100%	99.78%

Appendixes

Appendix 8: Young's modulus distribution data.

Bin Index	Bin Average Value (GPa)	Bin Average Value (Log)	N_{br}	Frequency	Cumulative N_{br}	%Cumul	Weibull %Cumul
1	0.208	8.32	1	1.9%	1	1.9%	2.84%
2	0.337	8.53	1	1.9%	2	3.8%	5.60%
3	0.545	8.74	2	3.8%	4	7.7%	10.87%
4	0.881	8.95	7	13.5%	11	21.2%	20.53%
5	1.43	9.15	8	15.4%	19	36.5%	36.80%
6	2.31	9.36	14	26.9%	33	63.5%	60.00%
7	3.74	9.57	10	19.2%	43	82.7%	83.96%
8	6.05	9.78	5	9.6%	48	92.3%	97.41%
9	9.78	9.99	4	7.7%	52	100.0%	99.93%

Appendixes

Appendix 9: Laser diffraction parameters for the different particle samples.

Sample	Description	Residual	Weighted Residual	Laser Obscuration	Valid Snaps Reported	Exhaust Vacuum Pressure (bar)
Wet-B	After Filtration	0.79	0.59	2.33	3840	0.287
Wet-C	8 Impeller Rotations	0.64	0.43	2.81	1655	0.327
Wet-D	1 min 100 rpm	0.29	0.28	0.38	168	0.364
Wet-G	142 min 100 rpm	0.21	0.17	2.5	9037	0.348
Wet-H	204 min 100 rpm	0.24	0.19	2.87	1637	0.316
Wet-I	987 min 100 rpm	0.3	0.17	2.99	7702	0.271
Dry-A	After Filtration	0.69	0.61	2.36	9182	0.412
Dry-B	Overnight Filtration	0.5	0.36	1.89	10895	0.335
Dry-B (bis)	Overnight Filtration (bis)	0.13	0.11	2.4	5078	0.329
Dry-C	8 Impeller Rotations	0.22	0.16	2.5	7541	0.359
Dry-D	1 min 30 rpm	0.28	0.19	2.45	5180	0.361
Dry-E	5 min 100 rpm	0.27	0.19	2.65	6546	0.383
Dry-F	25 min 100 rpm	0.27	0.2	2.72	10885	0.329
Dry-G	120 min 100 rpm	0.45	0.22	3.06	15178	0.305
Dry-H	165 min 100 rpm	0.43	0.25	3.5	14862	0.385
Dry-I	505 min 100 rpm	1.38	0.24	3.9	17269	0.313

Appendixes

Appendix 10: Coefficient of determination R^2 of linear regressions performed using Equation 7.5.4 for the different aspect ratios and normal stresses applied in shearing phase. Values of linear parameters given in Table 7.5.5.

$\alpha_p \setminus \sigma$	1kPa	2kPa	4kPa	6.5kPa	10kPa
3	0.521	0.710	0.752	0.767	0.756
4	0.831	0.856	0.880	0.859	0.857
5	0.902	0.939	0.929	0.937	0.924
6	0.945	0.932	0.965	0.965	0.962

Appendixes

Appendix 11: Number of data points recorded in simulations of shearing phase for the different aspect ratios α_p and normal stresses applied σ .

$\sigma \setminus \alpha_p$	2	3	4	5	6	All
1kPa	101	101	100	100	100	502
2kPa	101	101	100	100	100	502
4kPa	101	101	100	100	100	502
6.5kPa	101	101	100	100	100	502
10kPa	101	101	100	100	100	502
All	505	505	500	500	500	2510

Appendixes

Appendix 12: Number of data points recorded in simulations of uniaxial compression for the different aspect ratios α_p and strain applied γ .

$\gamma \setminus \alpha_p$	2	3	4	5	6	All
0	47	47	47	48	47	236
2	46	47				93
3					48	48
5	47	49	45	46	47	234
10		46	49	45	48	188
15	48			47	48	143
20			47	46	46	139
25					46	46
30					47	47
All	188	189	188	232	377	1174

Appendixes

Appendix 13: Statistics of particles retained and excluded for the parameters used in the script analysis of Morphologi G3 data for the different samples collected (MN: minimum neighbour).

Sample name	Description	Nbr of particles retained	Vol fraction of particles retained	Vol of particles retained (mm^3)	Nbr of particles retained	Nbr of particles excluded by MN=2	Vol fraction of particles excluded by MN=2
Wet-B	After Filtration	96%	23%	0.845	5.35E+4	28	1.16E-10
Wet-D	1 min 100 rpm	96%	22%	0.413	3.15E+4	19	2.34E-10
Wet-G	142 min 100 rpm	97%	30%	0.707	3.27E+4	18	7.62E-11
Wet-I	987 min 100 rpm	96%	66%	0.763	4.36E+4	23	1.03E-10
Dry-B	Overnight Filtration	96%	83%	0.499	3.33E+4	27	2.42E-10
Dry-D	1 min 30 rpm	96%	58%	0.498	4.69E+4	17	9.78E-11
Dry-G	120 min 100 rpm	93%	47%	0.538	1.12E+5	25	1.41E-10
Dry-H	165 min 100 rpm	95%	48%	0.765	8.29E+4	28	1.18E-10
Dry-I	505 min 100 rpm	94%	64%	0.686	1.70E+5	25	1.05E-10

Appendixes

Appendix 14: Probability density function of the different samples collected in dry and wet agitation experiments. The data is obtained using script analysis [294].

	Dry					Wet			
Sample	Overnight Filtration	1min 30rpm	120min 100rpm	165min 100rpm	505min 100rpm	After Filtration	1min 100rpm	142min 100rpm	987min 100rpm
Impeller rotations	0	30	18.8k	50.4k	132.4k	0	100	21.1k	195.2k
1	8.20%	9.78%	16.00%	12.06%	16.22%	11.16%	11.89%	8.30%	9.19%
2	41.15%	47.11%	55.08%	53.27%	54.50%	42.10%	43.44%	44.83%	49.80%
3	24.15%	22.17%	17.66%	20.46%	16.82%	21.00%	24.82%	26.27%	25.22%
4	11.43%	10.06%	6.46%	7.65%	6.65%	11.21%	9.88%	9.98%	8.20%
5	7.56%	5.16%	3.14%	3.43%	2.93%	7.38%	4.84%	5.53%	4.36%
6	3.99%	2.76%	0.98%	1.16%	1.85%	4.22%	2.98%	2.60%	1.89%
7	1.46%	1.58%	0.48%	0.78%	0.60%	1.72%	1.36%	1.18%	0.88%
8	0.99%	0.91%	0.14%	0.55%	0.23%	0.68%	0.50%	0.51%	0.25%
9	0.44%	0.28%	0.01%	0.02%	0.13%	0.33%	0.23%	0.37%	0.14%
10	0.33%	0.10%	0.02%	0.35%	0.02%	0.15%	0.02%	0.37%	0.05%
11	0.15%	0.07%	0.02%	0.28%	0.02%	0.01%	0.04%	0.04%	0.00%
12	0.14%	0.03%	0.01%		0.01%	0.04%		0.02%	0.01%
13	0.00%				0.00%	0.00%			0.00%
14	0.00%				0.01%	0.00%			0.00%
15	0.01%					0.00%			0.00%
16						0.00%			
17						0.00%			

Appendixes

Appendix 15: Estimation of probability density function from the calibrated model for different numbers of impeller rotations I and aspect ratios α_p (see Chapter 8.4.4).

$\alpha_p \setminus I$	0	30	18.8k	50.4k	132.4k
1	8.20%	8.20%	11.11%	15.01%	22.87%
2	41.15%	41.16%	45.24%	48.69%	51.29%
3	24.15%	24.16%	25.64%	24.01%	18.64%
4	11.43%	11.44%	10.53%	7.85%	4.91%
5	7.56%	7.56%	4.87%	3.02%	1.71%
6	3.99%	3.99%	1.77%	1.01%	0.46%
7	1.46%	1.46%	0.49%	0.26%	0.08%
8	0.99%	0.99%	0.23%	0.10%	0.02%
9	0.44%	0.44%	0.07%	0.02%	0.00%
10	0.33%	0.32%	0.03%	0.01%	0.00%
11	0.15%	0.15%	0.01%	0.00%	0.00%
12	0.14%	0.13%	0.00%	0.00%	0.00%
13	0.00%	0.00%	0.00%	0.00%	0.00%
14	0.00%	0.00%	0.00%	0.00%	0.00%
15	0.01%	0.01%	0.00%	0.00%	0.00%

Appendixes

Appendix 16: Estimation of probability density function from the calibrated model for different numbers of impeller rotations I and aspect ratio α_p . The initial PARD corresponds to the values for the dry AFD experiments at $I = 30$ (see Chapter 8.4.6.3).

$\alpha_p \setminus I$	30	18.8k	50.4k	132.4k
1	9.78%	12.44%	16.13%	23.67%
2	47.11%	50.20%	52.70%	53.96%
3	22.17%	22.97%	21.30%	16.46%
4	10.06%	8.96%	6.62%	4.12%
5	5.16%	3.38%	2.10%	1.20%
6	2.76%	1.25%	0.72%	0.33%
7	1.58%	0.49%	0.25%	0.08%
8	0.91%	0.19%	0.08%	0.01%
9	0.28%	0.04%	0.01%	0.00%
10	0.10%	0.01%	0.00%	0.00%
11	0.07%	0.00%	0.00%	0.00%
12	0.03%	0.00%	0.00%	0.00%
13	0.00%	0.00%	0.00%	0.00%
14	0.00%	0.00%	0.00%	0.00%
15	0.00%	0.00%	0.00%	0.00%

Appendixes

Appendix 17: Weibull scale parameter λ_p of particle internal stress distribution in Pa for the different aspect ratios α_p and in the different zones of the Maxi Lab AFD (see Chapter 8.4.5).

$\alpha_p \setminus$ Zones	Top	Middle	Bottom
1	1.57E+02	4.70E+02	7.84E+02
2	5.73E+02	1.72E+03	2.86E+03
3	1.22E+03	3.67E+03	6.11E+03
4	2.09E+03	6.28E+03	1.05E+04
5	3.18E+03	9.53E+03	1.59E+04
6	4.47E+03	1.34E+04	2.23E+04
7	5.96E+03	1.79E+04	2.98E+04
8	7.65E+03	2.30E+04	3.83E+04
9	9.54E+03	2.86E+04	4.77E+04
10	1.16E+04	3.49E+04	5.81E+04
11	1.39E+04	4.16E+04	6.94E+04
12	1.63E+04	4.90E+04	8.17E+04
13	1.90E+04	5.69E+04	9.49E+04
14	2.18E+04	6.54E+04	1.09E+05
15	2.48E+04	7.44E+04	1.24E+05

Appendixes

Appendix 18: Gaussian standard deviation σ_{dev} of the maximum stress location distribution for the different aspect ratios α_p and in the different zones of the Maxi Lab AFD (see Chapter 8.4.5).

$\alpha_p \setminus$ Zones	Top	Middle	Bottom
1	42.8%	39.9%	38.8%
2	39.8%	37.1%	36.1%
3	37.4%	34.9%	33.9%
4	35.4%	33.0%	32.1%
5	33.7%	31.4%	30.6%
6	32.2%	30.0%	29.2%
7	30.9%	28.8%	28.0%
8	29.7%	27.7%	27.0%
9	28.7%	26.8%	26.1%
10	27.8%	25.9%	25.2%
11	26.9%	25.1%	24.5%
12	26.2%	24.4%	23.8%
13	25.5%	23.8%	23.1%
14	24.8%	23.2%	22.5%
15	24.2%	22.6%	22.0%

Appendixes

Appendix 19: Extent of breakage B for the different aspect ratios α_p and in the different zones of the Maxi Lab AFD (see Chapter 8.4.5).

$\alpha_p \setminus$ Zones	Top	Middle	Bottom
1	2.39E-10	1.26E-09	2.94E-09
2	3.01E-09	1.58E-08	3.69E-08
3	1.32E-08	6.96E-08	1.62E-07
4	3.78E-08	1.99E-07	4.64E-07
5	8.55E-08	4.50E-07	1.05E-06
6	1.66E-07	8.75E-07	2.04E-06
7	2.92E-07	1.54E-06	3.58E-06
8	4.76E-07	2.50E-06	5.83E-06
9	7.31E-07	3.85E-06	8.97E-06
10	1.07E-06	5.65E-06	1.32E-05
11	1.52E-06	8.01E-06	1.87E-05
12	2.09E-06	1.10E-05	2.56E-05
13	2.80E-06	1.47E-05	3.43E-05
14	3.67E-06	1.93E-05	4.50E-05
15	4.72E-06	2.48E-05	5.79E-05

Derivations

Appendix 20: Derivation of Equation 4.3.2.

Using Hooke's law (see Equation 4.3.1) to calculate the spring constant and dividing the spring constant of the crystal by the spring constant of the probe gives:

$$\frac{k_C}{k_P} = \frac{F/\delta_C}{F/\delta_P}$$

Re-arranging the equation gives:

$$k_C = k_P \cdot \frac{\delta_P}{\delta_C}$$

Taking into account that the total displacement is equal to the sum of the crystal and the probe displacements, $\delta_T = \delta_C + \delta_P$ (see Figure 4.3.6), the equation takes the following form:

$$k_C = k_P \cdot \frac{\delta_P}{(\delta_T - \delta_P)}$$

Multiplying and dividing by δ_T gives:

$$k_C = \frac{k_P}{\delta_T} \cdot \frac{\delta_T \cdot \delta_P}{(\delta_T - \delta_P)}$$

Re-arranging the equation:

$$k_C = \frac{k_P/\delta_T}{\frac{1}{\delta_P} - \frac{1}{\delta_T}}$$

Multiplying and dividing by F gives:

$$k_C = \frac{k_P \cdot \frac{F}{\delta_T}}{\frac{F}{\delta_P} - \frac{F}{\delta_T}}$$

Considering Hooke's law (see Equation 4.3.1) results in:

Appendixes

$$k_C = \frac{k_P \cdot k_T}{k_P - k_T}$$

Appendixes

Appendix 21: Derivation of Equation 4.3.3.

Multiplying both sides of $\delta_T = \delta_C + \delta_P$ by δ_C and re-arranging gives:

$$\delta_C = \frac{\delta_T \delta_C}{\delta_C + \delta_P}$$

Dividing the numerator and the denominator of the right-hand side by F gives:

$$\delta_C = \delta_T \cdot \frac{\delta_C / F}{\frac{\delta_C}{F} + \frac{\delta_P}{F}}$$

Considering Hooke's law (see Equation 4.3.1) results:

$$\delta_C = \delta_T \cdot \frac{1/k_C}{\frac{1}{k_C} + \frac{1}{k_P}}$$

Re-arranging the equation gives:

$$\delta_C = \delta_T \cdot \frac{k_P}{k_P + k_C}$$

Appendixes

Appendix 22: Derivation of Equation 8.2.2.

Using the derivatives $(e^u)' = u' \cdot e^u$:

$$B = \int_0^{+\infty} -\left(\left(\frac{\sigma}{\lambda_p}\right)^{k_p}\right)' e^{-(\sigma/\lambda_p)^{k_p}} \cdot (1 - e^{-(\sigma/\lambda_b)^{k_b}}) d\sigma$$

$$B = \int_0^{+\infty} -\left(e^{-(\sigma/\lambda_p)^{k_p}}\right)' \cdot (1 - e^{-(\sigma/\lambda_b)^{k_b}}) d\sigma$$

Distributing the term under parenthesis:

$$B = \int_0^{+\infty} -\left(e^{-(\sigma/\lambda_p)^{k_p}}\right)' + \left(e^{-(\sigma/\lambda_p)^{k_p}}\right)' e^{-(\sigma/\lambda_b)^{k_b}} d\sigma$$

Using the linearity of integrals:

$$B = -\int_0^{+\infty} \left(e^{-(\sigma/\lambda_p)^{k_p}}\right)' d\sigma + \int_0^{+\infty} \left(e^{-(\sigma/\lambda_p)^{k_p}}\right)' e^{-(\sigma/\lambda_b)^{k_b}} d\sigma$$

Solving the first integral:

$$B = -\left[e^{-(\sigma/\lambda_p)^{k_p}}\right]_0^{+\infty} + \int_0^{+\infty} \left(e^{-(\sigma/\lambda_p)^{k_p}}\right)' e^{-(\sigma/\lambda_b)^{k_b}} d\sigma$$

$$B = 1 + \int_0^{+\infty} \left(e^{-(\sigma/\lambda_p)^{k_p}}\right)' e^{-(\sigma/\lambda_b)^{k_b}} d\sigma$$

Using the product rule of derivatives $(uv)' = uv' + u'v$:

$$B = 1 + \int_0^{+\infty} \left(e^{-(\sigma/\lambda_p)^{k_p}} \cdot e^{-(\sigma/\lambda_b)^{k_b}}\right)' - e^{-(\sigma/\lambda_p)^{k_p}} \cdot \left(e^{-(\sigma/\lambda_b)^{k_b}}\right)' d\sigma$$

Using linearity of integrals:

$$B = 1 + \int_0^{+\infty} \left(e^{-(\sigma/\lambda_p)^{k_p}} \cdot e^{-(\sigma/\lambda_b)^{k_b}}\right)' d\sigma - \int_0^{+\infty} e^{-(\sigma/\lambda_p)^{k_p}} \cdot \left(e^{-(\sigma/\lambda_b)^{k_b}}\right)' d\sigma$$

Solving the first integral:

Appendixes

$$B = 1 + \left[e^{-(\sigma/\lambda_p)^{k_p}} \cdot e^{-(\sigma/\lambda_b)^{k_b}} \right]_0^{+\infty} - \int_0^{+\infty} e^{-(\sigma/\lambda_p)^{k_p}} \cdot \left(e^{-(\sigma/\lambda_b)^{k_b}} \right)' d\sigma$$

$$B = - \int_0^{+\infty} e^{-(\sigma/\lambda_p)^{k_p}} \cdot \left(e^{-(\sigma/\lambda_b)^{k_b}} \right)' d\sigma$$

Developing the derivative, Equation 8.2.3 is finally obtained:

$$B = \frac{k_b}{\lambda_b^{k_b}} \int_0^{+\infty} \sigma^{k_b-1} \cdot e^{-(\sigma/\lambda_b)^{k_b}} \cdot e^{-(\sigma/\lambda_p)^{k_p}} d\sigma$$